https://www.sciltp.com/journals/mi
Online ISSN: 2982-2394
Volume 2, Issue 3, 2025

Materials and Interfaces

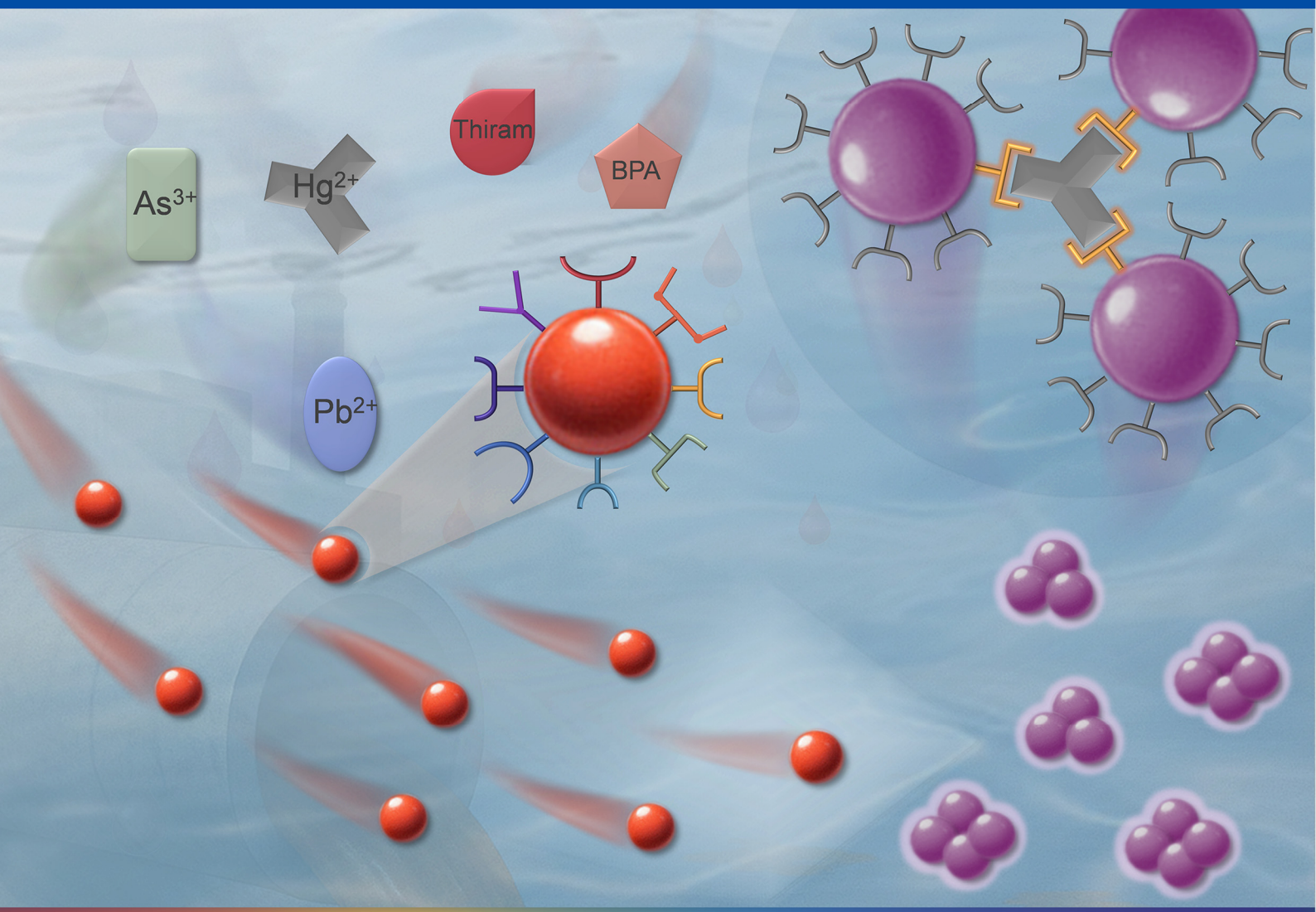

Colorimetric Plasmonic Nanosensors for Environmental Pollution Monitoring

Scilight

Contents

Vol. 2 No. 3, September 2025

Review

Colorimetric Plasmonic Nanosensors for Environmental Pollution Monitoring

Xueyong Zhang [1], Antonios G. Kanaras [2,3], and Yadong Yin [1,*]

[1] Department of Chemistry, University of California, Riverside, CA 92521, USA
[2] Department of Chemistry, School of Science, National and Kapodistrian University of Athens, Zografou, 15772 Athens, Greece
[3] School of Physics and Astronomy, University of Southampton, Highfield, Southampton SO17 1BJ, UK
* Correspondence: yadong.yin@ucr.edu

Received: 7 April 2025; Revised: 9 June 2025; Accepted: 13 June 2025; Published: 9 July 2025

Abstract: Environmental pollution, particularly water contamination by heavy metals and organic pollutants, presents a critical global challenge requiring effective monitoring solutions. Colorimetric plasmonic nanosensors, primarily utilizing gold nanoparticles (AuNPs) due to their exceptional stability and tunable optical properties, offer a promising approach for rapid, cost-effective, and label-free pollutant detection. This review highlights recent advancements in AuNP-based colorimetric plasmonic nanosensors for environmental monitoring. We explore their fundamental sensing mechanisms and critically examine their applications in detecting a broad spectrum of waterborne contaminants, including heavy metals, inorganic species, and diverse organic pollutants. By showcasing the versatility and potential of these emerging technologies, this review emphasizes their significant contribution towards developing more efficient and accessible tools for mitigating environmental pollution and protecting public health.

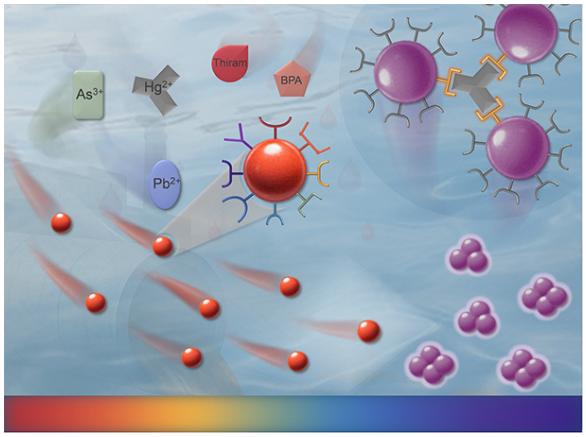

Keywords: nanosensor; pollution; surface plasmon resonance; nanoparticle; plasmonic coupling; aggregation

1. Introduction

Environmental pollution has become a critical global crisis, driven by rapid industrialization, urbanization, and unsustainable human activities [1]. Among the most pressing concerns is water pollution, which affects billions of people worldwide [2]. Over 80% of sewage is discharged into rivers and oceans without proper treatment, leading to widespread environmental degradation and increased disease prevalence [2,3]. Heavy metal contamination, particularly from toxic elements such as lead (Pb), cadmium (Cd) and mercury (Hg), poses a severe threat due to their bioaccumulative nature, resulting in long-term toxicity and ecological disruptions [4]. Additionally, organic pollutants from wastewater discharge contribute to oxygen depletion in aquatic ecosystems, elevating biochemical oxygen demand levels and endangering marine and freshwater life [5,6]. These combined factors underscore the urgent need for effective pollution control strategies to safeguard public health and the environment.

Given the growing concerns over environmental pollution, developing advanced monitoring technologies is essential for effective detection and mitigation strategies. Traditional analytical techniques, including gas chromatography [7], mass spectrometry [8], atomic absorption and emission spectroscopy [9], and high-performance liquid chromatography [10], provide high sensitivity and precision but are hindered by high costs, complex sample preparation, specialized equipment, and lengthy processing times. Furthermore, they are unsuitable for rapid, on-site monitoring, which is vital for timely pollution control. To overcome these limitations, there is growing interest in cost-effective and rapid detection methods.

Colorimetric plasmonic nanosensors offer high sensitivity, rapid response, and real-time detection capabilities [11–13], representing a class of cost-effective, label-free, and highly tunable alternatives to conventional analytical techniques for monitoring environmental pollution. Their detection mechanism relies on localized surface plasmon resonance (LSPR), where plasmonic nanoparticles, such as gold and silver nanoparticles, exhibit measurable optical shifts in response to analyte-induced changes in interparticle distance, particle size, or surface chemistry. This property enables colorimetric detection, allowing pollutants to be identified visually or with simple optical devices, eliminating the need for sophisticated laboratory settings.

Gold nanoparticles (AuNPs) are the most popular building blocks for plasmonic nanosensors due to their high stability, biocompatibility, and highly tunable surface chemistry. While silver and copper nanoparticles are also plasmonically active, they are susceptible to oxidation and degradation under environmental conditions. The high chemical stability of AuNPs ensures low toxicity and long-term sensor reliability [14]. In addition, their well-defined optical properties and ability to be functionalized with a wide range of ligands further enhance their selectivity and sensitivity toward specific pollutants. These characteristics make AuNPs particularly well-suited for the development of robust colorimetric nanosensors.

As pollution continues to pose a significant threat to ecosystems and public health, colorimetric plasmonic nanosensors offer a promising approach for rapid and accessible environmental monitoring. This review explores recent advancements in AuNP-based colorimetric plasmonic nanosensors for environmental pollution monitoring, with a specific focus on their applications in detecting heavy metals, inorganic contaminants, and a wide range of organic pollutants. By leveraging these emerging technologies, more efficient and accessible solutions can be developed to mitigate environmental pollution.

2. Fundamentals of Plasmonic Nanomaterials in Environmental Sensing

2.1. LSPR—The Basis of Colorimetric Sensing

LSPR is the fundamental principle behind colorimetric plasmonic sensors. It occurs when conduction electrons on the surface of plasmonic nanoparticles collectively oscillate in response to incident light (Figure 1A) [15]. The resonance frequency depends on several factors, including nanoparticle size, shape, interparticle distance, and the surrounding medium [16,17]. As shown in Figure 1B, for small spherical AuNPs, the primary extinction peak appears at 525 nm and progressively redshifts as the particle size increases. With larger particles, light scattering becomes more prominent, significantly influencing the overall optical properties [18]. In contrast to spherical AuNPs, gold nanorods (AuNRs) exhibit two distinct plasmonic peaks owing to their anisotropic shape: a transverse plasmon peak, which is associated with electron oscillation along the short axis, and a longitudinal plasmon peak, which occurs along the long axis. As the aspect ratio (length-to-width ratio) of AuNRs increases, the longitudinal plasmon peak redshifts significantly into the near-infrared (NIR) region, while the transverse plasmon peak remains relatively unchanged in the visible range (Figure 1C) [19]. This tunability in optical response makes AuNRs particularly useful for applications in biosensing, imaging, and photothermal therapy, where NIR light penetration is required [20,21].

Plasmonic coupling in LSPR-based sensing occurs when nanoparticles come into close proximity, leading to strong plasmonic interactions. In a well-dispersed state, individual AuNPs exhibit a distinct LSPR peak in the visible spectrum, typically producing a red-colored solution, as shown in Figure 1B. As illustrated in the electrodynamic modeling in Figure 1D, the plasmon band redshift becomes increasingly pronounced as the distance between the AuNP dimer decreases [22]. When this distance becomes smaller than the nanoparticle diameter, plasmon coupling becomes significant, resulting in a redshift of the LSPR peak due to the formation of lower-energy collective plasmonic modes [23]. Experimental results confirm this redshift, accompanied by a visible color change from red to purple (Figure 1E) [24]. The resulting spectral redshift and broadening form the basis of most aggregation-based colorimetric sensors.

2.2. Mechanisms of Colorimetric Responses in Plasmonic Sensors

The ability of AuNP-based colorimetric sensors to detect analytes relies on distinct plasmonic modulation mechanisms that induce measurable optical shifts. The most common mechanism is aggregation-based sensing, where AuNPs undergo a red-to-blue/purple color change due to interparticle plasmonic coupling when they come into proximity. In contrast, anti-aggregation mechanisms prevent nanoparticle aggregation, preserving their dispersed state and maintaining the original red color even under conditions that would otherwise promote aggregation, such as the presence of salt or interfering species. Other mechanisms, such as etching-based sensing, involve oxidative dissolution of AuNRs, causing a color fade or blue shift due to a reduction in particle size, while

growth-based sensing results in nanoparticle enlargement, shifting the LSPR peak toward longer wavelengths and intensifying the red color.

Among these, aggregation-based sensing is the most widely used due to its simplicity and strong optical response. Aggregation can be triggered through several different pathways, including crosslinking-induced aggregation, destabilization-induced aggregation, and competitive binding-induced aggregation.

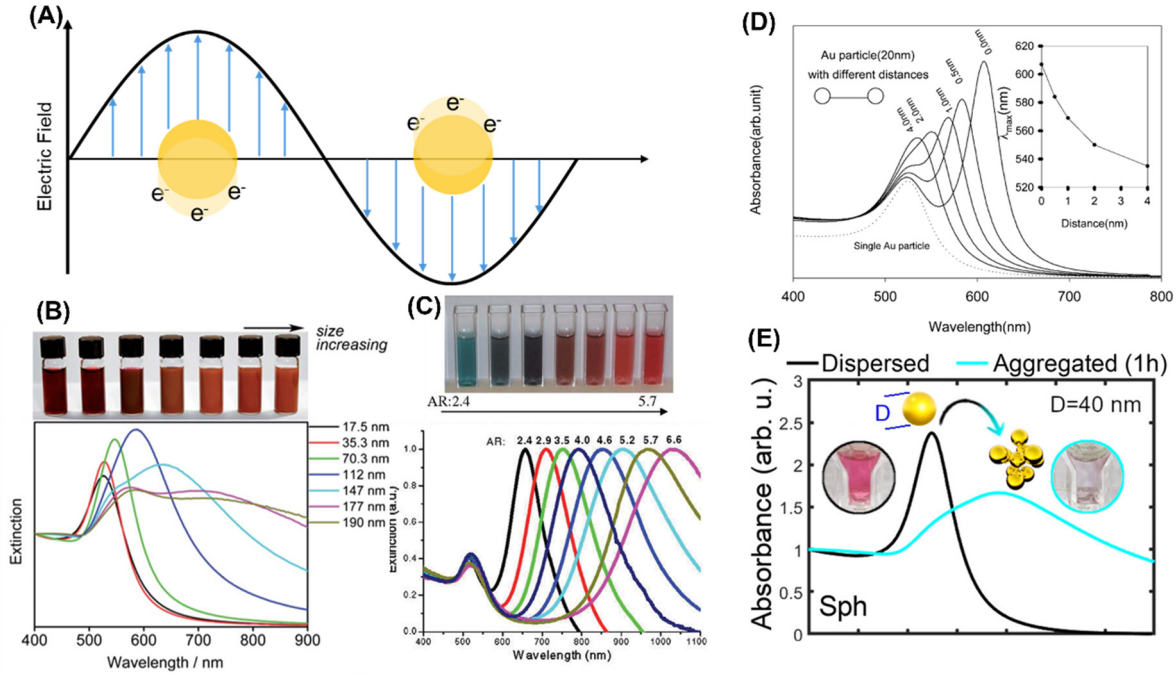

Figure 1. LSPR Principles and Spectral Shifts: Effects of Particle Size, Shape, and Aggregation in Au Nanostructures (**A**) Scheme of LSPR. (**B**) Photographic images and corresponding UV–Vis–NIR spectra of colloidal AuNPs with different particle sizes. Reproduced with permission [18]. Copyright 2012, Royal Society of Chemistry. (**C**) Photographic images and corresponding UV–Vis–NIR spectra of colloidal AuNRs with different aspect ratios. Reproduced with permission [19]. Copyright 2010, University of Cairo. (**D**) Electrodynamic simulations of 20 nm AuNP showing extinction spectra at varying interparticle distances, with the inset illustrating the corresponding plasmon peak shift as a function of spacing. Reproduced with permission [22]. Copyright 2004, American Chemical Society. (**E**) Typical spectral shift observed in colloidal sensors based on the aggregation of spherical nanoparticles with diameter D. Reproduced with permission [24]. Copyright 2023, American Chemical Society.

2.3. Aggregation-Based Colorimetric Sensing

Aggregation-induced plasmonic coupling significantly alters the optical properties of AuNPs, making this approach highly effective for colorimetric sensing. One common mechanism is crosslinking-induced aggregation, where the analyte acts as a crosslinker, binding multiple nanoparticles together. This typically occurs when the analyte has multiple binding sites that interact with AuNP surfaces, leading to the formation of large aggregates (Figure 2A). Examples include metal ions such as Pb^{2+} and Hg^{2+}, which can bridge AuNPs via specific interactions, causing a distinct red-to-blue color shift [25,26].

Another widely used mechanism is destabilization-induced aggregation, where the analyte disrupts the stabilizing ligands on the nanoparticle surface, reducing electrostatic repulsion and allowing AuNPs to aggregate. This can occur through charge screening, such as in salt-induced aggregation, where high ionic strength neutralizes the surface charge on AuNPs, leading to uncontrolled aggregation (Figure 2B). Similarly, cationic analytes like As^{3+} and Hg^{2+} can bind with the specific designed aptamers on AuNP surfaces, triggering aggregation and a corresponding color change [27,28].

Competitive binding-induced aggregation occurs when the analyte competes with existing stabilizing molecules on the AuNP surface, displacing them and promoting aggregation (Figure 2C). For example, thiol-containing molecules can replace citrate ligands on AuNPs, leading to ligand exchange and subsequent aggregation [29].

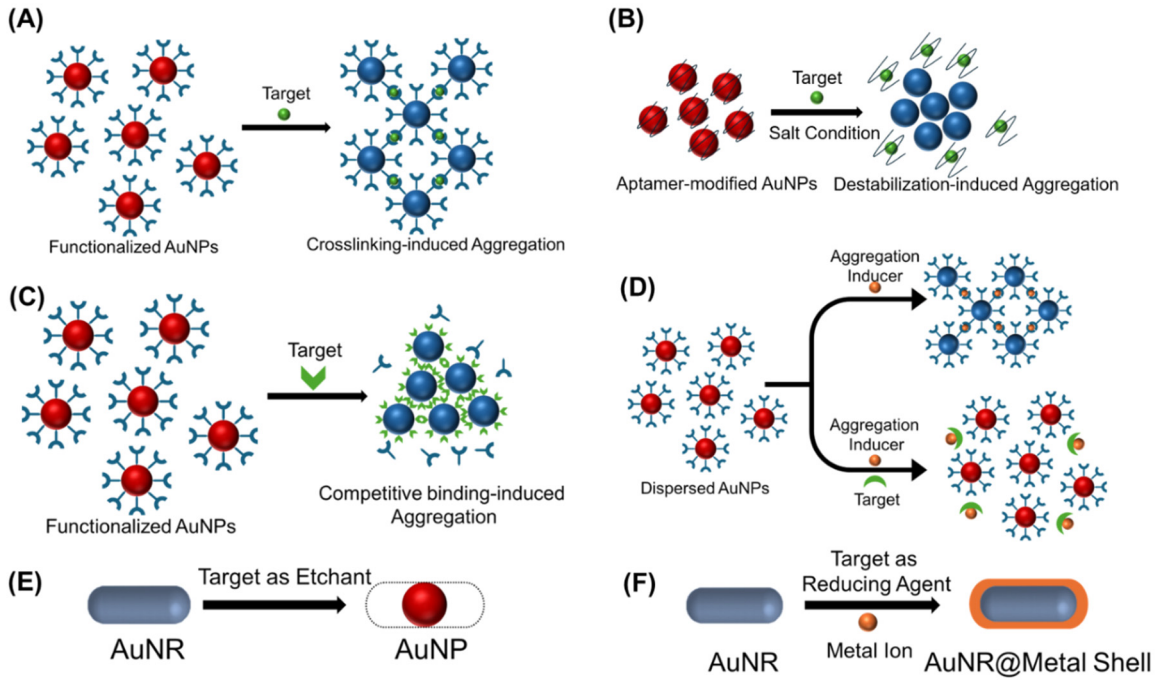

Figure 2. Mechanisms of Colorimetric Responses in Plasmonic Sensors. (**A**) Scheme for crosslinking-induced aggregation. (**B**) Scheme for destabilization-induced aggregation. (**C**) Scheme for Competitive binding -induced aggregation. (**D**) Scheme for anti-aggregation-based sensing. (**E**) Scheme for etching-based sensing. (**F**) Scheme for growth-based sensing.

2.4. Other Colorimetric Mechanisms: Anti-Aggregation, Etching and Growth

While aggregation-based sensing is the dominant strategy, other plasmonic mechanisms also contribute to colorimetric detection. Anti-aggregation-based sensing operates in the opposite manner to aggregation; here, the analyte prevents AuNPs from aggregating by stabilizing their dispersed state (Figure 2D). For example, Pb^{2+} can induce DNA strand cleavage, releasing a fragment that adsorbs onto the AuNP surface, thereby stabilizing the nanoparticles and preventing aggregation under high-salt conditions [30].

Etching-based sensing involves the oxidative dissolution of AuNPs, leading to a reduction in particle size and a corresponding shift in LSPR (Figure 2E). For example, nitrite (NO_2^-) can etch AuNRs to soluble Au species, resulting in the fading or disappearance of the original color [31].

Growth-based sensing involves the deposition of additional material onto existing AuNPs in the presence of a reducing agent, resulting in a plasmonic peak shift and a visible color change (Figure 2F). A common example is the reduction of Ag^+ by formaldehyde, which leads to silver shell growth on AuNRs and alters their optical properties, producing noticeable shifts in color depending on the extent of silver deposition [32].

2.5. Surface Functionalization of AuNPs for Colorimetric Sensing

The functionalization of AuNPs plays a crucial role in enhancing their selectivity and stability for colorimetric sensing applications. The most commonly used AuNPs are citrate-stabilized, relying on electrostatic repulsion between negatively charged citrate ligands to maintain colloidal stability [33]. However, citrate-capped AuNPs often lack sufficient selectivity [34] and sensitivity [25], prompting the need for further surface modification with specific ligands that interact selectively with target analytes. Among various strategies, thiol-based functionalization is widely employed, as thiol groups form strong Au–S bonds, enabling stable attachment of molecules such as glutathione (GSH) [35–37] and cysteine [38]. These ligands not only enhance selectivity but also improve nanoparticle stability under diverse conditions. Amine-functionalized AuNPs offer another approach, where amino groups interact with the Au surface, as seen in melamine-modified systems [39].

A highly effective strategy for achieving selective detection involves incorporating both a recognition element and a thiol group into the same molecule—allowing it to react with the target analyte while anchoring firmly onto the AuNP surface. This dual-binding design ensures both analyte recognition and nanoparticle stability, minimizing nonspecific aggregation. For instance, thiolated thymine can selectively bind Hg^{2+} [26], thiolated crown ethers target specific metal ions [40], and thiolated DNA is commonly used for specific recognition [41,42].

Tailoring the surface chemistry of AuNPs makes it possible to significantly enhance sensor performance, enabling sensitive and selective detection of a wide range of pollutants, biomolecules, and metal ions.

2.6. Synthesis of AuNPs for Colorimetric Sensing Applications

In colorimetric sensing, the Turkevich method is the most widely adopted for synthesizing AuNPs, producing citrate-stabilized AuNPs by reducing $HAuCl_4$ with trisodium citrate in boiling water [43]. These nanoparticles are widely adopted due to their simple synthesis and ease of post-synthetic functionalization. Molecules such as GSH [35], melamine [39], and aptamers [44] can readily replace the citrate ligands, enabling the introduction of selective recognition elements while maintaining colloidal stability for sensing applications. In addition to this classical approach, green synthesis methods—using reducing agents such as tannic acid [45] and gallic acid [46]—have been proposed for their environmental friendliness and biocompatibility.

AuNRs are also valuable tools for investigating etching processes and growth mechanisms. A typical seed-mediated synthesis of short AuNRs involves hexadecyltrimethylammonium bromide (CTAB), silver nitrate, and ascorbic acid. In this method, silver ions are essential for directing rod formation and minimizing spherical byproducts, with aspect ratios finely controlled through the seed-to-metal precursor ratio and reagent concentrations [47]. Building on this, the incorporation of aromatic additives into the CTAB-based system enables AuNR synthesis under reduced CTAB concentrations, while significantly enhancing monodispersity and tunability [48].

3. Detection of Inorganic Species

AuNP-based colorimetric sensing has been extensively applied to the detection of inorganic species, owing to its simplicity, high sensitivity, and visual readout. Reported systems include a wide range of analytes such as heavy metals (Pb^{2+}, As^{3+}, Hg^{2+}, Tl^{+}, Ag^{+}), other metal ions (Sc^{3+}, Cs^{+}, Al^{3+}), and anionic pollutants (CN^{-}, NO_2^{-}). In addition to single-target detection, several studies have demonstrated the simultaneous detection of multiple species using tailored surface ligands or differential response patterns, expanding the applicability of these sensors to complex environmental and biological samples.

3.1. Detection of Lead Species

Lead ion and other lead species are highly toxic, persistent, and bioaccumulative pollutants, primarily released from industrial activities, lead-based paints, batteries, and contaminated water sources [49,50]. Lead exposure poses severe health risks, particularly to the nervous system, kidneys, and cognitive development in children [51,52]. Given its environmental persistence and toxicity, effective monitoring of lead contamination is crucial for pollution control and public health protection.

Lu et al. have developed a series of DNAzyme-mediated AuNP sensors for Pb^{2+} detection, utilizing an anti-aggregation mechanism with distinct strategies [30,41,42]. In 2003, a Pb^{2+}-specific DNAzyme was employed to regulate AuNP assembly through DNA hybridization. The system consisted of AuNPs functionalized with thiol-modified DNA strands (DNA_{Au}), where the thiol end binds to the AuNP surface, along with the DNAzyme and a DNA substrate (Sub_{Au}) that hybridizes specifically to both ends of DNA_{Au} while maintaining the DNAzyme recognition portion. The hybridization between DNA_{Au} and Sub_{Au} brought the AuNPs closer together, leading to aggregation and a blue color change. In the presence of Pb^{2+}, the DNAzyme selectively cleaved the substrate strand, disrupting hybridization, preventing aggregation, and producing a red color (Figure 3A). However, this method required a two-hour heating and cooling cycle to facilitate hybridization [41]. To accelerate the process, in 2004, the design was improved by optimizing nanoparticle alignment and size, enabling faster detection in less than 10 min at room temperature [42]. Later, in 2008, Lu's group introduced a label-free sensor that eliminated the need for thiol-ended DNA to modify AuNPs and instead relied on the property of AuNPs aggregating in a high-ionic-strength environment. In this system, unmodified AuNPs and DNAzyme complex were treated under high-salt conditions. In the presence of Pb^{2+}, single-stranded DNA was released from the complex and adsorbed onto AuNPs, preventing their aggregation under high-salt conditions (Figure 3B). This approach simplified sensor fabrication, and lowered the detection limit to 3 nM, surpassing regulatory standards. Additionally, pH-controlled tunability was introduced, allowing for the adjustment of the detection range for different environmental applications [30].

The synthesis of DNA oligomers can be complex and expensive, highlighting the need for a simple and cost-effective colorimetric sensor for Pb^{2+} detection. One alternative approach relies on the aggregation mechanism, in which Pb^{2+} binds to functional groups on AuNPs, triggering their aggregation and causing a red-to-blue color shift. Frost et al. investigated the interaction between citrate-capped AuNPs and divalent heavy metal ions (Pb^{2+}, Cd^{2+}, Ni^{2+}, and Hg^{2+}), elucidating the molecular interactions responsible for Pb^{2+}-induced aggregation. ATR-FTIR and computational simulations showed that Pb^{2+} uniquely binds to both unbound carboxylate groups of citrate,

effectively neutralizing the negative charge stabilizing AuNPs. In contrast, Cd^{2+}, Ni^{2+}, and Hg^{2+} primarily interact with already-bound carboxylate groups or exhibit weaker binding, failing to fully neutralize the surface charge. This charge neutralization by Pb^{2+} was further supported by zeta potential and pH measurements, which demonstrated a reduction in AuNP surface charge from −44.3 mV to nearly neutral (−1.1 mV), leading to a significant loss of electrostatic repulsion and rapid aggregation. Additionally, Pb^{2+} caused a major pH drop (from 6.3 to 1.0), further altering surface chemistry and reinforcing nanoparticle destabilization [53]. A basic citrate-capped AuNP sensor exploits this mechanism, detecting Pb^{2+} via direct complexation with carboxyl groups, achieving a detection limit of 18 μM [25].

GSH-functionalized AuNPs (GSH-AuNPs) have been widely used for Pb^{2+} detection as a more sensitive alternative to citrate-capped AuNPs [35,36]. In this system, thiol groups in glutathione strongly bind to the AuNP surface, while carboxyl and amino groups remain available for metal ion coordination. To minimize interference from other metal ions, the amino group is protonated to ammonium by adjusting the pH to 8, ensuring that only the carboxyl groups participate in Pb^{2+} binding. This enhances Pb^{2+} selectivity and allows it to induce aggregation in a manner similar to citrate-capped AuNPs but with improved sensitivity (Figure 3C). GSH-AuNPs in the presence of salt have been successfully used to detect Pb^{2+} with a detection limit of 100 nM [35]. The aggregation of AuNPs leads to an increase in particle size, which can be more effectively detected using dynamic light scattering (DLS). By tracking these size changes, DLS-enhanced detection achieves an ultrasensitive limit of 100 ppt, making it suitable for analyzing Pb^{2+} in water, plastic toys, and paint [36].

Biocompatible materials such as tannic acid and gallic acid have been explored for AuNP functionalization [45,46,54]. Gallic acid stabilizes AuNPs through carboxylate interactions, while Pb^{2+} binds primarily to phenolic groups, inducing aggregation. The limit of detection (LOD) for Pb^{2+} using gallic acid-functionalized AuNPs is reported at the micromolar level [46]. Narrowing the size distribution and optimizing pH further reduced the LOD to 10 nM [54]. Another polyphenolic compound, tannic acid, has also been used to stabilize AuNPs, achieving an LOD of 60 ng/mL (0.29 μM) [45]. An alternative approach involves triazole-acetate-functionalized AuNPs, where a dithiol group facilitates attachment to the AuNP surface. Pb^{2+} binds to both carboxyl groups and the triazole ring, forming a stronger and more selective coordination complex (Figure 3D). This mechanism enhances selectivity over other metal ions and enables a lower detection limit of 16.7 nM [55].

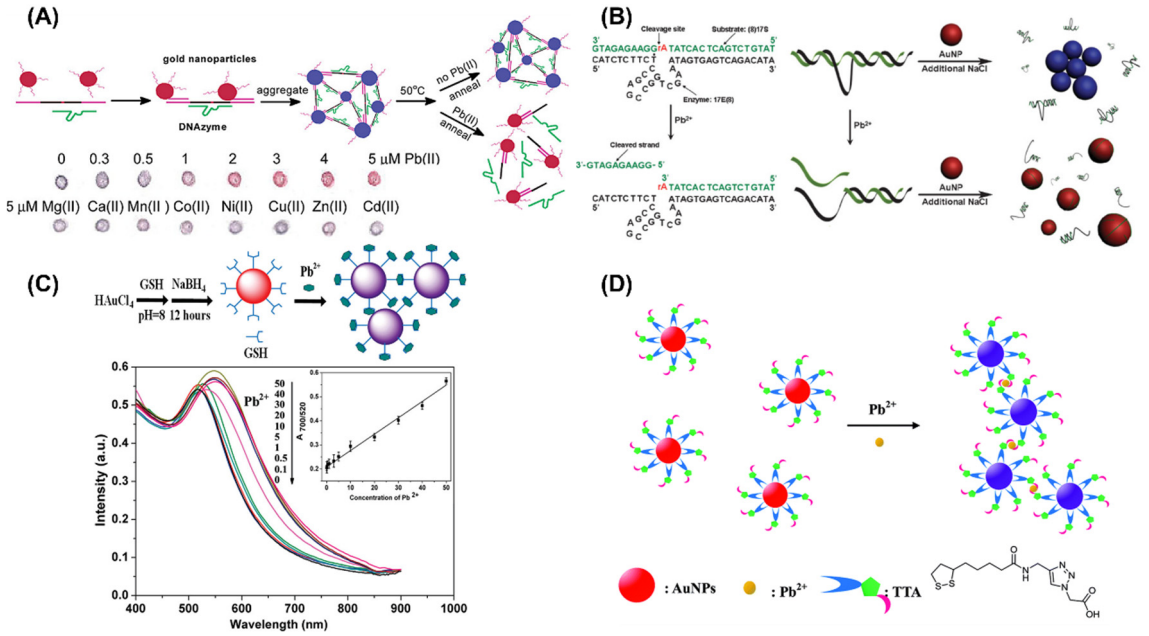

Figure 3. Colorimetric sensing strategies for Pb^{2+} detection using AuNP-based sensors. (**A**) Schematic of an anti-aggregation mechanism for Pb^{2+} detection, along with the visible color response on an alumina TLC plate at varying Pb^{2+} concentrations and in the presence of other divalent metal ions. Reproduced with permission [41]. Copyright 2003, American Chemical Society. (**B**) Anti-aggregation-based, label-free colorimetric sensing of Pb^{2+}. Reproduced with permission [30]. Copyright 2008, Wiley. (**C**) Detection of Pb^{2+} using GSH-AuNPs. Top: Schematic illustration of the sensing mechanism. Bottom: UV–vis absorption spectra of GSH-AuNPs after the addition of Pb^{2+} of varying concentrations. Reproduced with permission [35]. Copyright 2010, American Chemical Society. (**D**) Pb^{2+} detection via triazole-acetate-functionalized AuNPs. Reproduced with permission [55]. Copyright 2014, Royal Society of Chemistry.

3.2. Detection of Arsenic Species

Arsenic is a highly toxic metalloid, with its inorganic forms (As^{3+} and As^{5+}) posing the greatest hazard. As a persistent environmental pollutant, arsenic contaminates groundwater through natural geology, mining, and industrial discharge, making it a widespread concern [56]. Long-term exposure to arsenic-contaminated water leads to severe health effects, including skin lesions, peripheral neuropathy, organ damage, and an increased risk of cancer [57].

As^{3+}, like Pb^{2+}, can be detected through AuNP aggregation mechanisms, where its interaction with surface ligands triggers nanoparticle clustering and a visible red-to-blue color change. Citrate-capped AuNPs can also be used for As^{3+} detection, with As^{3+} binding to carboxyl groups to induce aggregation. Interestingly, as-synthesized citrate-capped AuNPs are not initially sensitive to As^{3+}. However, after removing excess citrate via dialysis, the detection limit improves significantly to 1.8 ppb (Figure 4A). When evaluating the selectivity of dialyzed citrate-capped AuNPs, 256 ppb (1.24 μM) of various metal ions, including Pb^{2+}, did not induce a color change [58]. However, it has been reported that Pb^{2+} requires a concentration of 18 μM to cause aggregation [25]. This suggests that while As^{3+} induces aggregation at much lower concentrations than Pb^{2+}, selectivity may become a concern at higher Pb^{2+} concentrations. Glucose, a biodegradable and biocompatible molecule, has also been used to functionalize AuNPs. It utilizes hydroxyl groups, achieving a detection limit of 0.53 ppb, with selectivity tests confirming no aggregation in the presence of Pb^{2+}, Co^{2+}, Hg^{2+}, Cd^{2+}, Ni^{2+}, or Cu^{2+} [59]. Similarly, GSH-AuNPs rely on carboxyl groups, detecting As^{3+} down to 0.12 ppb via RGB-based image quantification. However, Pb^{2+} also induces weak aggregation, indicating partial selectivity [37].

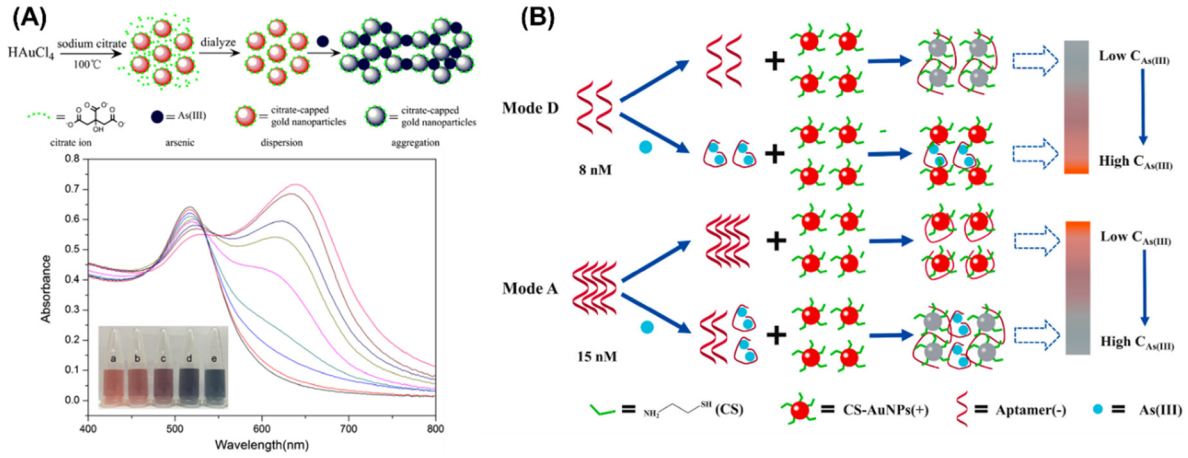

Figure 4. Colorimetric sensing strategies for As^{3+} detection using AuNP-based sensors. (**A**) Top: Schematic illustration of As^{3+} detection via dialyzed citrate-capped AuNPs. Bottom: UV–vis absorption spectra of citrate-AuNPs after the addition of As^{3+} of varying concentrations. Reproduced with permission [58]. Copyright 2017, Springer. (**B**) Bimodal detection of As^{3+} based on electrostatic attraction between positively charged AuNPs and a negatively charged As^{3+} aptamer, enabling both direct (Mode D) and amplified (Mode A) sensing modes. Reproduced with permission [27]. Copyright 2022, Elsevier.

Multifunctional groups enhance arsenic detection by providing strong binding sites for both AuNP attachment and metal coordination. GSH forms Au–S bonds via its thiol group, while its carboxyl and amino groups facilitate metal ion binding. Dithiothreitol (DTT) stabilizes AuNPs through Au–S bonds and reduces As (V) to As (III), making both oxidation states detectable. Cysteine (Cys), a thiol and amine containing amino acid, interacts with both AuNPs and metal ions, reinforcing the detection mechanism. 2,6-Pyridinedicarboxylic acid (PDCA) selectively binds to As^{3+}, further improving specificity. The GSH-DTT-Cys-PDCA functionalized AuNPs achieve a detection limit of 2.5 ppb, making them highly sensitive for arsenic detection [38].

The highest selectivity is achieved with a dual-mode aptamer-based sensor, where an As^{3+}-specific aptamer regulates nanoparticle aggregation and re-dispersion, minimizing false positives. The mechanism relies on electrostatic interactions between negatively charged aptamers and positively charged AuNPs. At low aptamer concentrations (Mode D, 8 nM), aptamers cross-link AuNPs, inducing aggregation and a red-to-blue shift. As^{3+} binding sequesters aptamers, breaking cross-links and re-dispersing AuNPs (blue-to-red shift). Conversely, at high aptamer concentrations (Mode A, 15 nM), aptamers fully coat AuNPs, preventing aggregation. As^{3+} binding removes aptamers, destabilizing AuNPs and triggering aggregation (Figure 4B). This dual-mode system enhances specificity, achieving LOD values of 0.41 ppb (Mode A) and 0.57 ppb (Mode D) for As^{3+} detection [27].

3.3. Detection of Mercury Species

Mercury is a persistent environmental pollutant released from industrial activities, coal combustion, and mining, accumulating in water bodies and soil [60]. Its highly toxic forms, particularly methylmercury, bioaccumulate in the food chain, posing serious risks to ecosystems and human health [61].

Hg^{2+} can be detected using AuNP-based colorimetric sensors through different mechanisms, primarily relying on thymine-Hg^{2+}-thymine (T-Hg^{2+}-T) coordination chemistry. One straightforward approach is to functionalize thymine with a thiol group, allowing it to attach to AuNPs via Au-S bonds. Upon Hg^{2+} addition, T-Hg^{2+}-T coordination bridges the nanoparticles, inducing aggregation and a color change (Figure 5A). This method achieves a detection limit of 2.8 nM [26]. Alternatively, Hg^{2+} can be detected without thiolation by stabilizing AuNPs with ssDNA in a high-salt environment. When Hg^{2+} is introduced, T-Hg^{2+}-T coordination induces DNA hairpin formation, destabilizing the AuNPs and leading to aggregation in the presence of salt, with a LOD of 50 nM [28]. A further variation replaces salt with the cationic polymer poly(diallyldimethylammonium chloride) (PDDA) as the aggregation inducer. In the absence of Hg^{2+}, PDDA binds to negatively charged ssDNA, preventing AuNP aggregation. However, when Hg^{2+} is introduced, ssDNA folds into a hairpin structure, releasing free PDDA, which neutralizes the AuNP surface charge and triggers aggregation (Figure 5B). This approach offers ultrasensitive detection with a LOD of 0.15 nM [62]. Beyond T-Hg^{2+}-T interactions, another method employs diethyldithiocarbamate (DDTC) as a specific ligand for Hg^{2+} detection. In this approach, Cu^{2+} in the $Cu(DDTC)_2$ complex is displaced by Hg^{2+}, releasing a thiol group that binds to AuNPs, leading to surface charge neutralization and aggregation. This method detects both Hg^{2+} (LOD: 10 nM) and methylmercury (LOD: 15 nM) [63]. In a different approach, Hg^{2+} can be detected through its direct interaction with AuNPs, forming Hg^{2+}-Au bonds that alter surface charge and stability. However, if citrate remains on AuNPs, it stabilizes them, making Hg^{2+} detection less effective. When citrate is removed, Hg^{2+} adsorption further reduces surface charge, promoting aggregation. This method is significantly less sensitive, with a LOD of 5 μM [64].

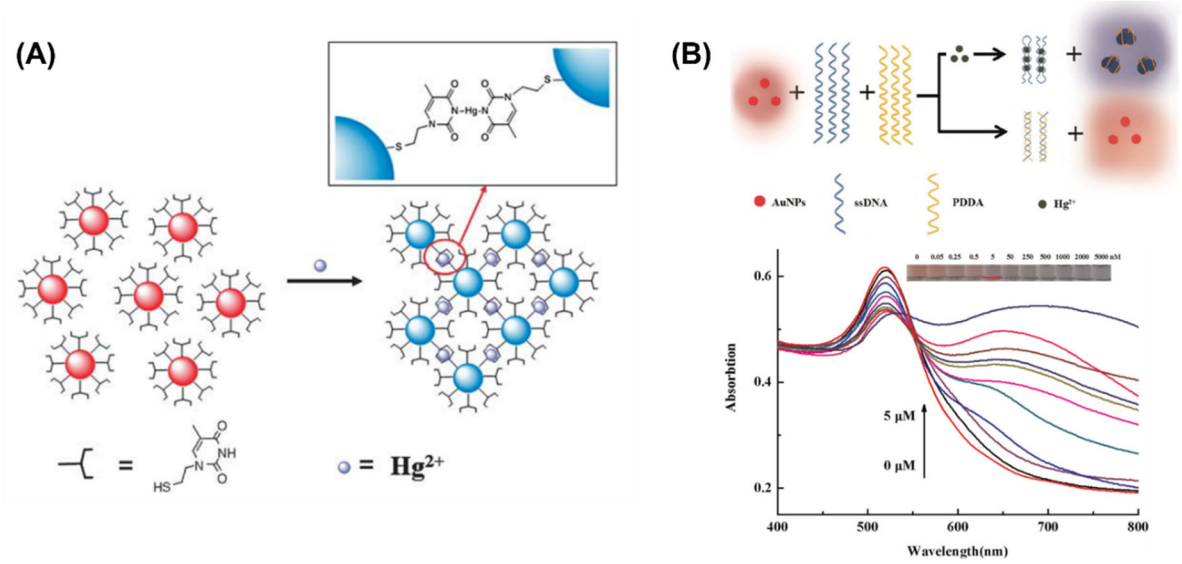

Figure 5. Colorimetric sensing strategies for Hg^{2+} detection using AuNP-based systems. (**A**) Schematic illustration of Hg^{2+} detection based on thymine–Hg^{2+}–thymine coordination chemistry. Reproduced with permission [26]. Copyright 2011, Royal Society of Chemistry. (**B**) Top: Detection mechanism of Hg^{2+} through AuNP aggregation modulated by PDDA, leveraging the specific binding between Hg^{2+} and ssDNA, along with electrostatic interactions between PDDA and ssDNA. Bottom: UV–vis absorption spectra of AuNPs after the addition of Hg^{2+} of varying concentrations. Reproduced with permission [62]. Copyright 2015, Elsevier.

3.4. Detection of Aluminum Species

Aluminum is a widespread environmental pollutant, primarily released through industrial activities, mining, and acid rain-induced leaching from soil into water sources [65]. Elevated aluminum levels in water and soil can be toxic to aquatic life, plants, and humans, and have been associated with neurodegenerative disorders, including Alzheimer's disease [66].

Citrate-capped AuNPs have also been used for Al^{3+} detection at an optimal pH of 2.9, achieving an LOD of 1.0 μM through Al^{3+} complexation with citrate ligands, which induces aggregation (Figure 6A). The pH was tuned

to eliminate interference from Fe^{3+}, while Pb^{2+} also triggered aggregation but with a longer response time. In contrast, Al^{3+} induced an immediate color change, making it more distinguishable. However, interference from Sb^{3+} and Cr^{3+} remained a challenge [34].

Beyond citrate-based detection, Al^{3+} coordination with hydroxyl groups has also been widely utilized in AuNP-based sensors. AuNPs have been functionalized with catechol ligands, including pyrocatechol, 3-(3,4-dihydroxyphenyl)propionic acid, dopamine, and levodopa, which strongly chelate with Al^{3+}. Upon Al^{3+} binding, these ligands dissociate from the AuNP surface due to their stronger affinity for Al^{3+}, leading to nanoparticle destabilization and aggregation. Among these, dopamine-functionalized AuNPs exhibited the highest sensitivity, achieving a LOD of 0.81 μM [67]. Similarly, N-lauroyltyramine has been used as a capping ligand, where Al^{3+} forms coordination complexes with hydroxyl groups, inducing AuNP aggregation with a detection limit of 1.15 μM [68]. Another approach employs Schiff base-functionalized AuNPs using N-(2-hydroxynaphthylidene)-2-aminoethanethiol (HNAET) as a chelating ligand for selective Al^{3+} detection (Figure 6B). The thiol group anchors HNAET to the AuNP surface, while the hydroxyl and imine groups strongly chelate Al^{3+}, achieving a detection limit of 0.29 μM [69].

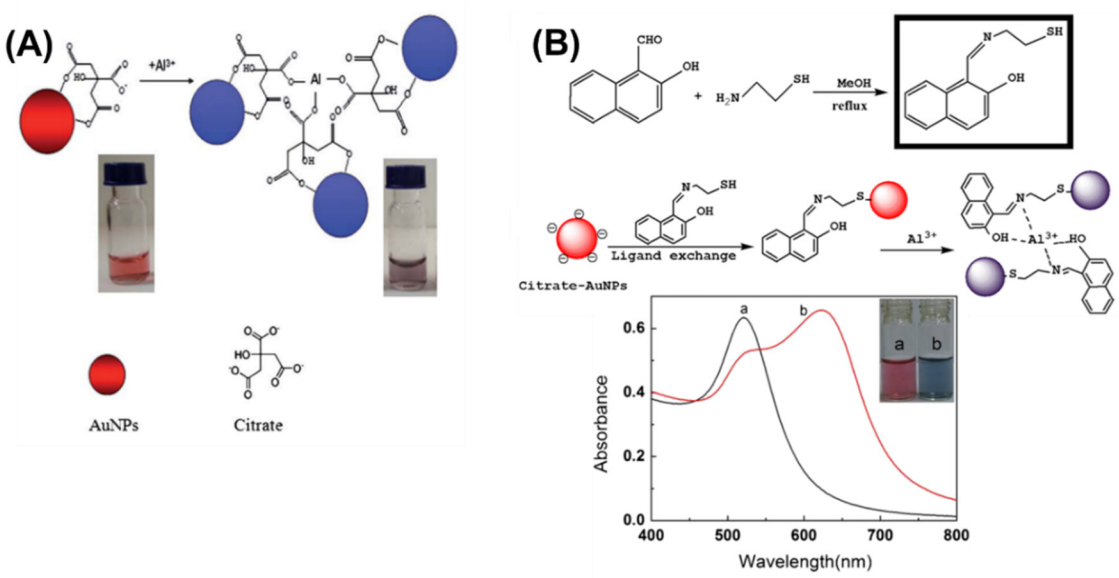

Figure 6. Colorimetric sensing strategies for Al^{3+} detection using AuNP-based sensors. (**A**) Schematic illustration of Al^{3+} sensing based on citrate-capped AuNPs. Reproduced with permission [34]. Copyright 2012, Royal Society of Chemistry. (**B**) Top: Synthesis of HNAET and the ligand exchange of HNAET onto AuNP surfaces and the corresponding signaling mechanism for Al^{3+} detection using the HNAET–AuNP probe. Bottom: UV–vis absorption spectra of citrate-AuNPs after the addition of Al^{3+}. Reproduced with permission [69]. Copyright 2016, Springer.

3.5. Detection of Cesium

Cesium primarily originates from nuclear accidents, industrial waste, and mining activities, posing environmental risks due to their long-term soil retention, and potential radiotoxicity [70].

Cs^{+} can be detected using colorimetric sensors based on nonmorphological transitions of AuNPs. Cs^{+} fits well into Prussian blue (PB) lattice and forms stable PB-Cs^{+} complex. When Prussian blue precursor (PB-P) is added to the AuNP dispersion, citric acid reduces Fe^{3+} to Fe^{2+}, leading to the formation of a PB nanoshell on the AuNP surface, causing a color change from red to blue. However, in the presence of Cs^{+}, PB-P preferentially reacts with Cs^{+}. This interaction prevents PB deposition onto AuNPs, allowing them to retain their original red color (Figure 7A). The method achieved a naked-eye detection limit of 30 μM and a UV-Vis detection limit of 19 μM [71].

3.6. Detection of Silver Species

Silver pollution arises from industrial discharge, mining, and medical waste, with excessive levels causing toxicity in aquatic ecosystems and disrupting microbial communities [72].

A three-step aggregation–dispersion–reaggregation mechanism can be utilized for Ag^{+} detection. First, AuNPs aggregate in the presence of quantum carbon dots, exhibiting a blue color. Then, upon addition of GSH, AuNPs redisperse, restoring the original red color. Finally, when Ag^{+} ions are introduced, they preferentially bind

GSH, preventing AuNP redispersion and maintaining the aggregated state (Figure 7B). This method achieves detection limits of 50 nM (UV-Vis) and 140 nM (naked-eye) [73].

3.7. Detection of Thallium Species

Thallium pollution mainly originates from mining, smelting, and industrial waste, posing severe environmental and health risks due to its high toxicity, bioaccumulation, and adverse effects on the nervous [74].

A similar three-step mechanism is employed for Tl^+ detection. Initially, positively charged thioflavin T (ThT) induces AuNP aggregation. Subsequently, the addition of negatively charged PS2.M DNA displaces ThT, redispersing the AuNPs. Finally, when Tl^+ is introduced, DNA preferentially binds Tl^+, releasing ThT, which reaggregates AuNPs (Figure 7C). This method demonstrates high selectivity and achieves a detection limit of 3.2 nM [75].

3.8. Detection of Scandium Species

Scandium, as a rare earth element, has been widely used in various industrial applications [76], leading to its extensive release into the environment through waste and emissions, which may pose risks to ecosystems and human health [77].

The three-step mechanism can also be adapted for Sc^{3+} detection. Initially, positively charged pyridoxal phosphate (PLP) aggregates negatively charged cysteamine-stabilized AuNPs. However, when Sc^{3+} is introduced, it strongly binds PLP, forming a stable complex that prevents PLP-induced aggregation, resulting in AuNP redispersion. This approach achieves high selectivity and a detection limit of 0.02 μM [78].

3.9. Detection of Cyanide

Cyanide pollution arises from industrial processes such as mining, electroplating, and chemical manufacturing, posing severe environmental and health risks due to its high toxicity, which can cause rapid aquatic life depletion [79] and human poisoning [80].

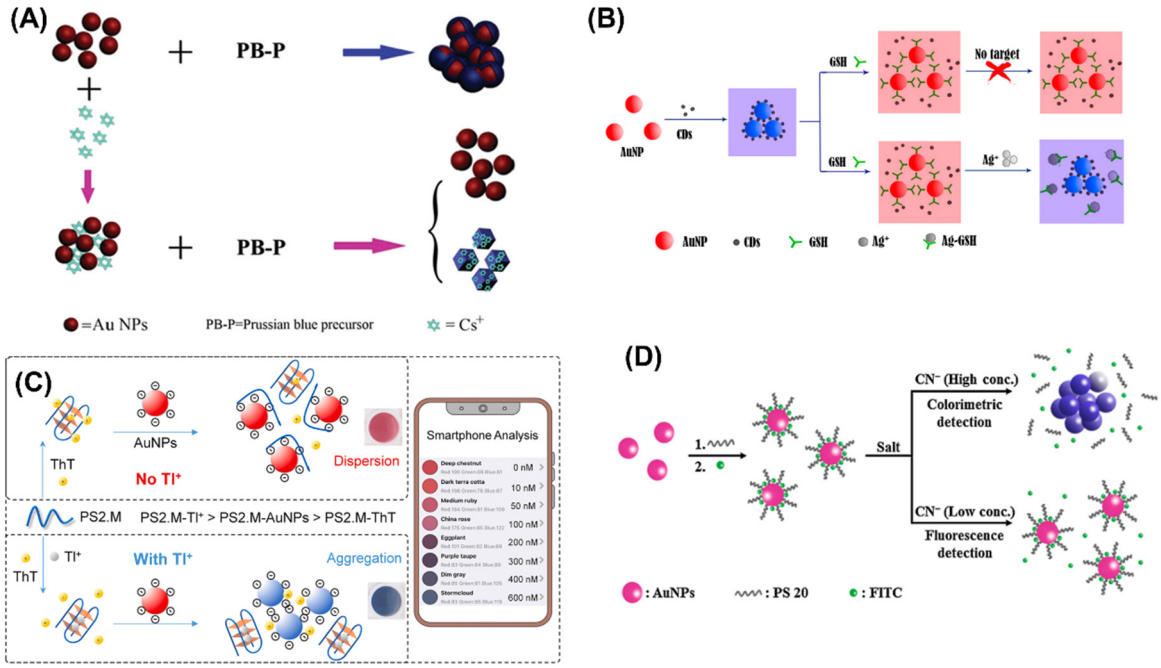

Figure 7. Colorimetric sensing strategies for Cs^+, Ag^+, Tl^+, and CN^- detection using AuNP-based probes. (**A**) Sensing mechanism for Cs^+ detection based on the interaction between AuNPs and Prussian blue (PB). Reproduced with permission [71]. Copyright 2020, Royal Society of Chemistry. (**B**) Colorimetric detection of Ag^+ via stable AuNP aggregation triggered by carbon dots in the presence of GSH. Reproduced with permission [73]. Copyright 2018, American Chemical Society. (**C**) Thioflavin T-induced charge neutralization aggregation of AuNPs for Tl^+ detection. Reproduced with permission [75]. Copyright 2022, Elsevier. (**D**) Schematic illustration of the CN^- sensing mechanism based on the dual fluorescent and colorimetric response of AuNPs. Reproduced with permission [81]. Copyright 2016, Elsevier.

Cyanide can be detected by exploiting direct reactions with the AuNP surface, beyond traditional ligand-based aggregation mechanisms. In one approach, AuNPs stabilized by polysorbate 20 (PS20) and fluorescein isothiocyanate (FITC) have been employed to detect cyanide (CN^-) through a surface-etching mechanism (Figure 7D). Initially, FITC fluorescence is quenched when attached to the AuNP surface. Upon CN^- addition, the AuNP surface is selectively etched, releasing FITC molecules into solution and restoring fluorescence intensity proportionally to the cyanide concentration (below 150 μM). At higher CN^- concentrations (>150 μM), extensive etching destabilizes the AuNPs beyond the protective capacity of PS20, leading to particle aggregation and a visible color shift from red to blue-gray, enabling naked-eye detection [81].

3.10. Detection of Nitrite

Nitrite is a harmful environmental pollutant commonly found in contaminated drinking water due to agricultural runoff and industrial waste [82]. It poses significant health risks, including methemoglobinemia and increased cancer risk, making its rapid and sensitive detection essential for water quality monitoring [83].

A highly sensitive and selective colorimetric sensor for NO_2^- was developed based on the etching of AuNRs, producing a visible color change from bluish green to red and eventually to colorless as NO_2^- concentration increases. Under acidic conditions, NO_2^- oxidizes Au to soluble species, causing preferential axial etching, which reduces the nanorod aspect ratio and induces a blue-shift in the longitudinal plasmon peak. CTAB enhances this process by stabilizing intermediate Au–Br or Au–Cl complexes. The sensor shows excellent selectivity and a detection limit of 0.5 μM and visible response at 4 μM, this system enables naked-eye detection and is promising for field applications [31].

3.11. Simultaneous Detection

While many colorimetric sensors are designed for the selective detection of a single metal ion, some approaches leverage broader interactions to enable the detection of multiple metal species.

Colorimetric sensor arrays provide effective platforms for simultaneously detecting and differentiating multiple metal ions. One array utilizes AuNPs functionalized with 11-mercaptoundecanoic acid combined with various amino acids (lysine, cysteine, histidine, tyrosine, and arginine) to detect Hg^{2+}, Cd^{2+}, Fe^{3+}, Pb^{2+}, Al^{3+}, Cu^{2+}, and Cr^{3+}. The metal–ligand interactions produce distinct responses: some ions directly induce aggregation, some modulate aggregation cooperatively with amino acids, and others form stable metal–amino acid complexes, preventing aggregation (Figure 8A). This results in unique colorimetric fingerprints, enabling simultaneous detection and differentiation of these metal ions, with detection limits in the micromolar range (approximately 2–50 μM) [84]. Another array employs AuNPs individually functionalized with cysteine, glutathione, or melamine to discriminate among Ti^{4+}, Cr^{3+}, Mn^{2+}, Fe^{3+}, Pb^{2+}, and Sn^{4+}. Each metal ion produces a distinct colorimetric fingerprint, enabling accurate differentiation and quantification through linear discriminant analysis (LDA) with high selectivity and sensitivity in the concentration range of 100–900 nM [85].

Crown ether cavities can selectively bind metal ions such as Ba^{2+}, Cd^{2+}, and Pb^{2+}. To attach crown ether (4′-aminobenzo-18-crown-6) onto AuNP surfaces, a thiol group is introduced via reaction with 3-mercaptonicotinic acid, forming stable Au–S bonds. Metal ions (Ba^{2+}, Cd^{2+}, and Pb^{2+}) interact selectively with the crown ether cavity, reducing electrostatic repulsion between AuNPs and inducing aggregation, resulting in a visible color shift (Figure 8B). Although this sensor achieves low detection limits (20 nM for Ba^{2+} and Cd^{2+}; 50 nM for Pb^{2+}), it cannot individually differentiate among these three ions, despite good selectivity over other tested metal ions [86]. Another approach employs thiolated calixarene ligands attached to AuNP surfaces, providing both aggregation-based and alloy-formation-based sensing mechanisms. In this method, Pb^{2+} ions cause AuNP aggregation by bridging nanoparticles through calixarene cavities, while Cu^{2+} ions undergo reduction upon interaction with AuNPs, forming an Au–Cu alloy shell via anti-galvanic exchange. This method achieves detection limits of 0.65 ppm for Cu^{2+} and 10 ppm for Pb^{2+} [40].

The binding between heavy metal ions and protein can also be utilized for sensing. Papain protein adsorbed on AuNPs via hydrophobic and electrostatic interactions. Metal ions bind specifically to the sulfur groups of papain's cysteine residues, reducing electrostatic repulsion and causing AuNP aggregation. This aggregation induces a visible color shift from red to blue, allowing easy, naked-eye detection. Although the sensor does not distinctly differentiate among Hg^{2+}, Pb^{2+}, and Cu^{2+} ions, it effectively discriminates them as a group from other common metal ions, with detection limits around 200 nM [87].

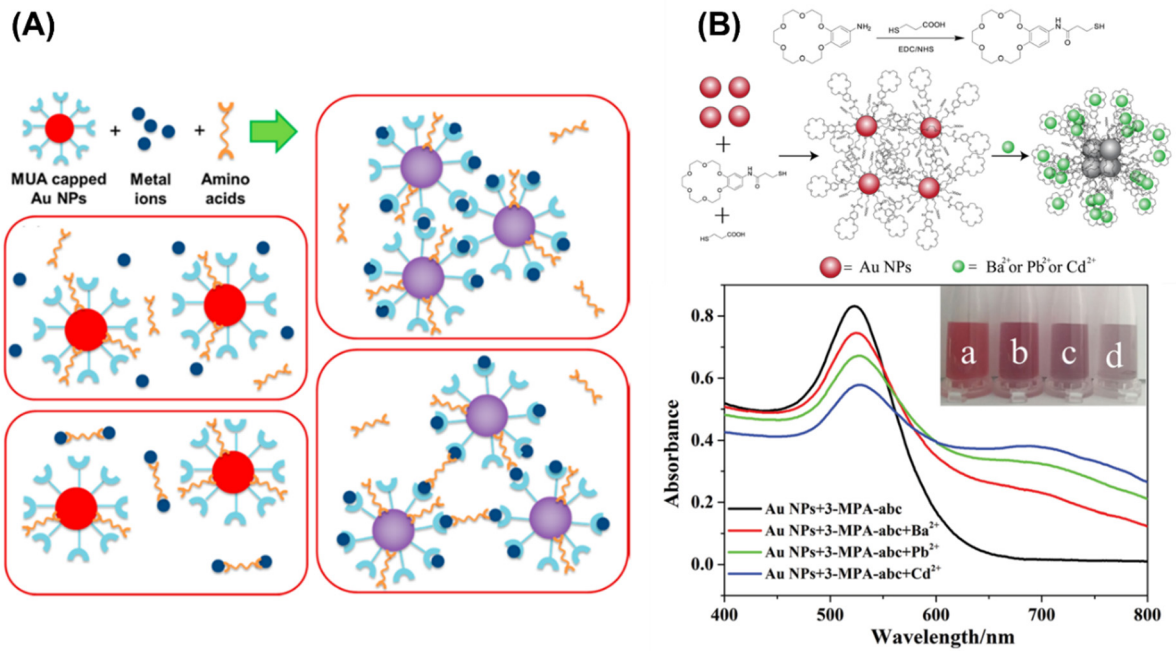

Figure 8. Simultaneous colorimetric detection of toxic metal ions using AuNP-based systems. (**A**) Schematic representation of the interactions among metal ions, amino acids, and AuNPs. Reproduced with permission [84]. Copyright 2014, American Chemical Society. (**B**) Top: Colorimetric detection mechanism of Ba^{2+}, Pb^{2+}, and Cd^{2+} using crown ether-functionalized AuNPs. Bottom: UV–vis absorption spectra crown ether-AuNPs after the addition of Ba^{2+}, Pb^{2+}, and Cd^{2+}. Reproduced with permission [86]. Copyright 2019, Royal Society of Chemistry.

4. Detection of Organic Molecules

AuNP-based colorimetric sensing has been successfully applied to the detection of organic molecules. Reported systems include a wide variety of targets such as pesticides, fungicides, antibiotics, as well as food and environmental contaminants like clenbuterol, azodicarbonamide, bisphenol A (BPA), formaldehyde, T-2 toxin, and microcystin-LR.

4.1. Detection of Pesticides and Fungicide

Pesticides and fungicides are widely used in agriculture to protect crops from pests and diseases, but their environmental impact is a growing concern. These chemicals can leach into soil and water sources, leading to contamination that affects non-target organisms, including beneficial insects, aquatic life, and soil microbiota [88,89]. Many pesticides persist in the environment, accumulating in the food chain and posing long-term ecological and health risks. Excessive exposure to certain pesticides has been linked to neurological disorders, endocrine disruption, and cancer in humans [90].

A colorimetric sensor array utilizing citrate-capped AuNPs enables the discrimination of organophosphate pesticides (OPs) through their pH- and ionic strength-dependent interactions with citrate ligands (Figure 9A). OPs induce AuNP aggregation via hydrogen bonding and electrostatic interactions, with their affinity for citrate modulated by protonation or hydrolysis under varying pH conditions (4.5, 6.5, 9.0). Additionally, increasing ionic strength (0, 5, 15 mM NaCl) weakens citrate stabilization, altering aggregation behavior and generating distinct spectral response patterns for classification via hierarchical cluster analysis and LDA, with a detection range of 120–400 ng/mL [91]. A ligand exchange-based mechanism offers an alternative approach for pesticide discrimination, where pesticides containing thiol, amine, carbonyl, or nitrile functional groups replace citrate on AuNP surfaces, leading to destabilization, aggregation, and a red-to-blue color shift. Detection is pH-dependent, with acephate (346 nM), phenthoate (3.0 nM), and profenofos (600 nM) aggregating at pH 4; acetamiprid (0.624 nM) and chlorothalonil (375 nM) at pH 6; and cartap (17 nM) at neutral pH, demonstrating high selectivity and applicability in water and food analysis [29]. Citrate-capped AuNPs have also been used to detect terbuthylazine (TBA) and dimethoate (DMT) via distinct charge-based mechanisms. TBA, carrying a strong positive charge, neutralizes citrate's negative charge, inducing aggregation and a red-to-blue color change. In contrast, DMT undergoes alkaline hydrolysis, producing negatively charged species that stabilize AuNPs, preventing aggregation and resulting in a gray-to-red color shift (Figure 9B). This sensor exhibited high selectivity, with LODs of 0.3 μM (visual) and 0.02 μM (UV-Vis) for TBA and 20 nM (visual) and 6.2 nM (UV-Vis) for DMT [92].

A label-free colorimetric assay has been developed for the detection of prothioconazole. The thiocarbonyl group in prothioconazole binds to AuNPs via Au–S interactions, while hydrogen bonding between prothioconazole molecules induces nanoparticle aggregation, resulting in a wine red-to-royal purple color shift (Figure 9C). The assay achieved a LOD of 0.38 μg/L under optimal conditions (pH 10, 1-min incubation, 0.15 M NaCl) and demonstrated high selectivity with minimal interference from other compounds [93]. A simple and rapid colorimetric sensor has been developed for the detection of tetramethylthiuram disulfide (thiram) based on the anti-aggregation of AuNPs. The detection mechanism relies on 4-aminothiophenol-functionalized AuNPs, where the thiol group anchors to the AuNP surface, and the amine group coordinates with Ag^+, inducing aggregation. However, in the presence of thiram, its strong binding affinity for Ag^+ captures the ions, preventing AuNP aggregation and restoring the original red color (Figure 9D). This system enables naked-eye detection within 15 min, with a detection limit of 0.04 μM. The sensor demonstrates high selectivity against other pesticides and metal ions and has been successfully applied to apple and soil samples [94].

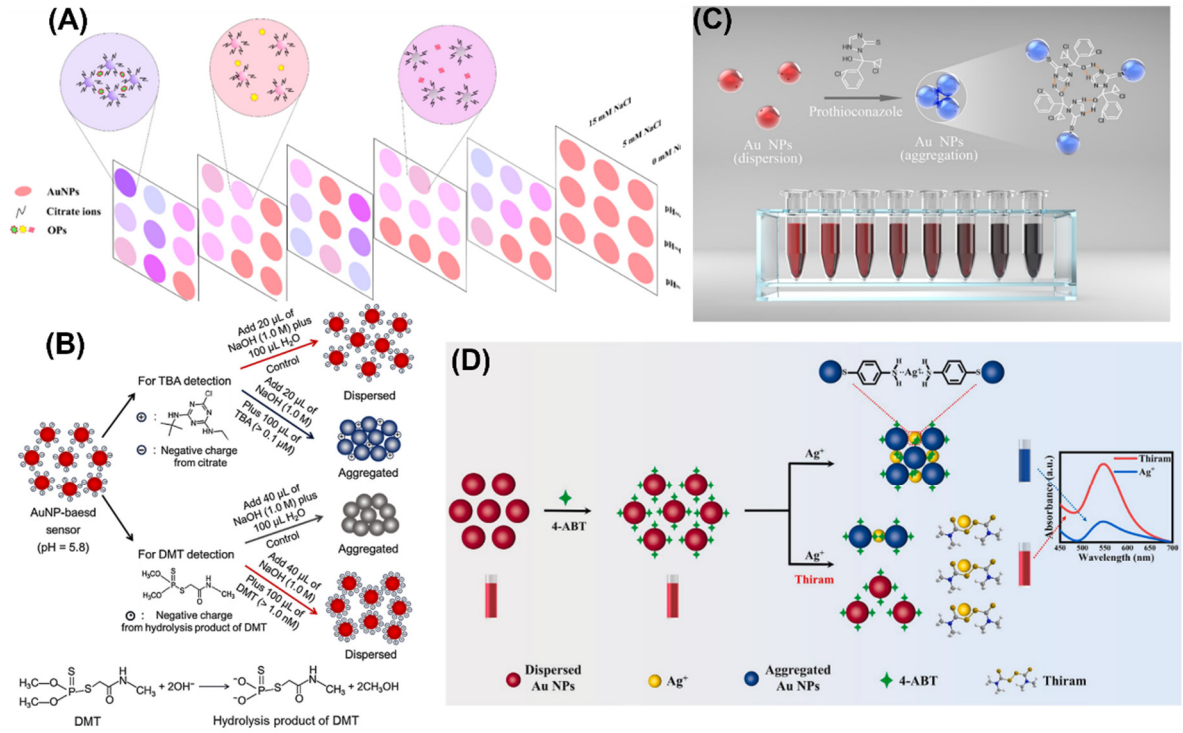

Figure 9. Colorimetric sensing strategies for pesticide and fungicide detection using AuNP-based probes. (**A**) Diagram of a colorimetric sensor array and detection principle for OPs based on citrate-stabilized AuNPs. Reproduced with permission [91]. Copyright 2016, American Chemical Society. (**B**) Schematic illustration of the detection mechanism for TBA and DMT, along with the reaction equation of DMT under alkaline conditions. Reproduced with permission [92]. Copyright 2018, Elsevier. (**C**) Prothioconazole-induced colorimetric response of AuNPs. Reproduced with permission [93]. Copyright 2020, American Chemical Society. (**D**) Schematic illustration of thiram detection using 4-aminothiophenol-functionalized AuNPs. Reproduced with permission [94]. Copyright 2022, Elsevier.

4.2. Detection of Veterinary Drug Residues

Clenbuterol, a strictly regulated growth promoter in livestock, can contaminate meat products and pose serious health risks to consumers, including cardiovascular complications, and metabolic disturbances [95,96].

A rapid and selective colorimetric sensor for CB detection has been developed using cysteamine-modified AuNPs. In this system, the thiol group of cysteamine binds to the AuNP surface, while the amine group remains exposed, enabling hydrogen bonding interactions with the hydroxyl, chloride, and amine groups of clenbuterol. These interactions induce AuNP aggregation, leading to a wine red-to-blue-gray color change, which is detectable by naked-eye observation or UV-vis spectroscopy. This sensor achieves a detection limit of 50 nM, demonstrating excellent selectivity against common food components [97]. Similarly, melamine-functionalized AuNPs have been employed for CB detection, where hydrogen bonding interactions between CB and melamine trigger AuNP aggregation, resulting in a wine red-to-blue color shift (Figure 10A). This method achieves an ultra-low detection limit of 2.8×10^{-11} M, offering a highly sensitive and cost-effective approach for clenbuterol analysis [39].

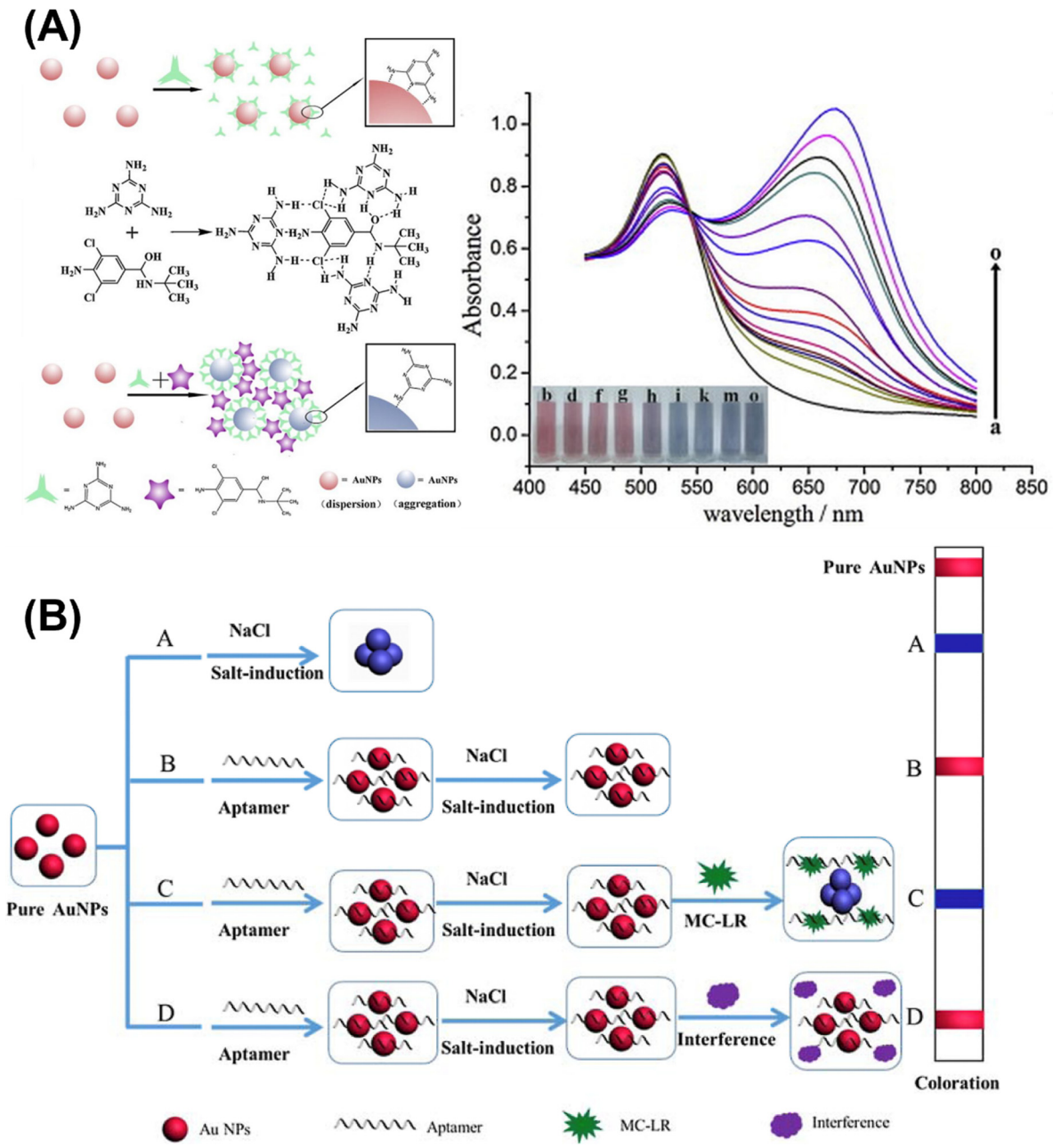

Figure 10. Colorimetric sensing strategies for CB and microcystin-LR using AuNP-based systems. (**A**) Left: Schematic illustration of the detection procedure for CB using melamine functionalized AuNPs. Right: UV–vis absorption spectra of AuNPs after the addition of CB of varying concentrations. Reproduced with permission [39]. Copyright 2012, Elsevier. (**B**) Schematic representation of the colorimetric sensing mechanism for the analytical determination of microcystin-LR. Reproduced with permission [106]. Copyright 2015, Elsevier.

4.3. Detection of Antibiotics

Antibiotics enter the environment through pharmaceutical waste, livestock runoff, and wastewater discharge, leading to contamination of soil and water systems [98,99]. Their persistent presence promotes the development of antibiotic-resistant bacteria, posing serious risks to ecosystems and public health by reducing the effectiveness of essential medical treatments [100].

Hydrogen bonding interactions are also utilized for antibiotic detection. Kanamycin, an aminoglycoside antibiotic, contains multiple amino and hydroxyl groups capable of forming hydrogen bonds. To exploit this property, AuNPs are functionalized with 4-amino-3-hydrazino-5-mercapto-1,2,4-triazole (AHMT), where the thiol group anchors onto the AuNP surface. Upon kanamycin addition, hydrogen bonding interactions between kanamycin and AHMT facilitate nanoparticle aggregation, leading to a visible red-to-deep purple color shift. This sensor achieves a detection limit of 0.004 μM, demonstrating high sensitivity and selectivity [101]. Another approach to detect antibiotics is using aptamers. The AuNPs are first stabilized with aptamers in high salt condition

while with the tetracycline (TET) and chloramphenicol (CAP), the antibiotics selectively bind to aptamers and this binding reduces the aptamer's ability to stabilize the AuNPs, leading to the detachment of the recognized fragment and subsequent AuNP aggregation causing aggregation in high-salt conditions. The sensor demonstrates high selectivity and sensitivity, achieving detection limits of 32.9 nM for TET and 7.0 nM for CAP [102].

4.4. Detection of Industrial and Natural Contaminants in Food and Water

Microcystin-LR is a potent hepatotoxin produced by cyanobacteria in contaminated water sources [103]. T-2 toxin is a mycotoxin from Fusarium fungi, contaminating food and feed, causing immunotoxic and cytotoxic effects [104]. Bisphenol A (BPA) is an industrial chemical used in plastics, acting as an endocrine disruptor with potential health risks [105].

Aptamers can also be utilized for both natural toxins and chemical contaminants detection. In this approach, aptamers first stabilize AuNPs in a high-salt environment, preventing aggregation. Upon introduction of target, the aptamers selectively bind to their targets, undergo conformational changes, and detach from the AuNP surface, triggering nanoparticle aggregation and a visible color shift (Figure 10B). This method enables the detection of microcystin-LR (LOD: 0.37 nM) [106], T-2 toxin (LOD: 57.8 pg/mL) [107], and bisphenol A (LOD: 0.004 nM) [108], demonstrating high sensitivity and specificity.

Azodicarbonamide (ADA), used as a food additive and dough conditioner, can contribute to environmental pollution through industrial emissions and wastewater discharge, potentially forming harmful byproducts that impact air and water quality [109]. ADA can be detected using an anti-aggregation mechanism. Unlike previously introduced methods, GSH is used to induce AuNP aggregation post-synthesis. GSH binds to AuNP surfaces via Au–S bonding, while its zwitterionic groups promote aggregation through electrostatic interactions. Upon introduction of ADA, GSH undergoes oxidation, leading to thiol dimerization and the formation of glutathione disulfide. This modification prevents GSH from cross-linking AuNPs, reducing aggregation and restoring the red color. The sensor achieves a visual detection limit of 0.33 μM (38.3 ppb) and a spectrophotometric detection limit of 0.23 μM (26.7 ppb) [110].

4.5. Detection of Formaldehyde

Formaldehyde (HCHO) is a toxic environmental pollutant commonly released from industrial emissions, building materials, and household products [111]. It poses serious health risks, including respiratory irritation, allergic asthma, and increased cancer risk with long-term exposure [112].

An ultra-sensitive colorimetric sensor for HCHO was developed based on its ability to reduce Ag^{+}, forming Au@Ag core–shell nanorods. Ag^{0} selectively deposits on the tips of AuNRs, where CTAB shields the sides, increasing the aspect ratio and inducing a redshift in the longitudinal plasmon band accompanied by a visible color change. The sensor achieves a detection limit as low as 6.3×10^{-11} g/mL, offering a rapid, label-free, and selective method suitable for on-site environmental monitoring [32].

5. Colorimetric Sensors Beyond AuNPs

Although AuNPs are the most used plasmonic materials in colorimetric sensors, other plasmonic nanoparticles, such as silver and copper nanoparticles (AgNPs and CuNPs), have also been explored. AgNPs exhibit a color change from yellow to red upon aggregation and, like AuNPs, citrate-capped AgNPs have been used to detect Ni^{2+} via crosslinking-induced aggregation [113]. Similarly, GSH-capped AgNPs show Ni^{2+}-induced aggregation behavior [114]. Green-synthesized AgNPs have also demonstrated detection capability for ions such as Hg^{2+}, Pb^{2+}, and Zn^{2+} [115]. In the case of Cu, L-cysteine [116] and citrate-capped nanoparticles [117] have been used for Hg^{2+} detection. Together, AgNPs and CuNPs expand the colorimetric sensing toolkit beyond AuNPs, enabling complementary detection strategies for environmental pollutants.

In addition to plasmonic nanosensors, other colorimetric sensing strategies have also been widely explored for environmental pollutant detection. Intramolecular charge transfer transitions enable highly selective sensing of Cu^{2+}, resulting in a visible color change from yellow to blue [118]. Fluorescence resonance energy transfer between donor and acceptor molecules allows for highly sensitive detection of Hg^{2+}, accompanied by a shift from greenish-yellow to orange [119]. Specific recognition between small-molecule ligands and various metal ions enables distinct color responses for multimetal ion identification [120]. Fluorescence quenching between Fe^{3+} and nitrogen-doped graphene quantum dots demonstrates excellent sensitivity and selectivity [121]. Metal–organic frameworks with nitro-functionalized linkers also show promise as dual-mode sensors, exhibiting luminescent turn-off or turn-on responses for MnO_4^{-} and Hg^{2+}, respectively [122]. The synthesis routes and detection mechanisms of these sensors vary significantly from system to system. In contrast, most AuNP-based

colorimetric sensors rely on aggregation-induced color change, with AuNPs serving as readily available and tunable templates. Notably, many non-plasmonic colorimetric sensors incorporate fluorescence-based detection, often requiring UV illumination for visual readout. In these systems, the design and synthesis of the sensing molecule play a central role in performance. Additionally, non-plasmonic systems often produce a wider range of color transitions, whereas AuNP-based sensors typically shift from red to purple (or vice versa). While differing in mechanism and design, these sensor types offer complementary strengths, and integrating plasmonic platforms with other colorimetric approaches may further enhance the performance and adaptability of future sensing systems.

6. Summary and Outlook

AuNP-based colorimetric sensing has emerged as a powerful platform for the rapid, sensitive, and visual detection of a wide range of analytes. This review highlights the diverse mechanisms underlying AuNP-based colorimetric sensing, including aggregation-based strategies such as classical aggregation, anti-aggregation, and ligand exchange, along with non-aggregation mechanisms like growth and etching, which alter the optical properties of AuNPs through changes in size, shape, or surface composition. These approaches enable the detection of various inorganic species, such as metal ions and anions, as well as organic targets, including pesticides, antibiotics, industrial additives, and toxins. Table 1 summarizes the key sensing attributes of representative colorimetric nanosensors, including analyte type, LOD, dynamic range, selectivity, response time, and notable sensor characteristics. The strength of AuNP-based sensors lies in their simplicity, low cost, and ease of interpretation via visible color changes without the need for sophisticated instrumentation. Furthermore, the surface chemistry of AuNPs is highly adaptable, allowing selective recognition through various chemistries and providing a flexible foundation for designing highly tailored sensing systems.

Despite significant advances, several practical challenges remain. While many sensing systems claim selectivity, most studies still rely on simplified interference tests with metal ion mixtures, and only a few have demonstrated reliable performance in complex sample matrices such as milk, urine, or paint extracts. Additionally, although the visual nature of colorimetric sensing is appealing, quantifying subtle color variations remains difficult without external instrumentation. Some approaches address this by incorporating smartphone-based RGB analysis, UV-vis spectrometry, or even fluorescence and DLS—but these additions often compromise the simplicity that makes colorimetric methods attractive in the first place. Lowering the detection limit has been a major focus, with aptamer-based sensors showing impressive sensitivity. However, the high cost and structural complexity of DNA-based components limit their widespread application.

Looking ahead, more efforts should focus on bridging the gap between laboratory demonstrations and real-world usability. Many studies still lack rigorous validation in real sample matrices, and reproducibility is often underreported or unsupported by statistical analysis. While colorimetric methods are valued for their simplicity, consistently and quantitatively interpreting color changes remains challenging. Current strategies using RGB values or UV-vis absorbance ratios can be inconsistent or dependent on lighting and instrumentation. To address this, incorporating hue-based color models could provide a more standardized approach to quantifying visual responses [24]. Future work should emphasize developing robust, low-cost, and user-friendly analysis tools—such as smartphone apps with hue extraction—and validating sensor performance under practical conditions.

Overall, AuNP-based colorimetric sensing remains a dynamic and evolving field with broad potential across environmental monitoring, food safety, and beyond. Realizing its full potential will depend on continued innovation in surface chemistry, signal quantification, and device integration—ultimately paving the way for practical, on-site, and user-friendly sensing solutions.

Table 1. Key sensing attributes of representative sensors.

Refs.	Analytes	LOD	Dynamic Range	Selectivity Over	Response Time	Features/Limitations
[41]	Pb^{2+}	0.1 μM	100 nM–4 μM	Mg^{2+}, Ca^{2+}, Mn^{2+}, Co^{2+}, Ni^{2+}, Cu^{2+}, Zn^{2+}, Cd^{2+}	2 h	Long incubation time
[42]	Pb^{2+}	0.4 μM	0.4–2 μM	Co^{2+}, Zn^{2+}, Cd^{2+}, Mn^{2+}, Ni^{2+}, Ca^{2+}, Mg^{2+}	10 min	High sensitivity; fast detection
[30]	Pb^{2+}	pH 7.2: 3 nM pH 5.5: 120 nM	pH 7.2: 3 nM–12 μM pH 5.5: 120 nM–20 μM	Zn^{2+}, Mn^{2+}, Co^{2+}, Ni^{2+}, Cd^{2+}, Ca^{2+}, Mg^{2+}, Hg^{2+}	6 min	High sensitivity; label-free Au NPs
[25]	Pb^{2+}	18 μM	18–100 μM	Zn^{2+}, Ni^{2+}, Cu^{2+}, Mg^{2+}, Se^{4+}, Cr^{6+}, As^{5+}, Hg^{2+}, Fe^{3+}, Al^{3+}, Ca^{2+}, Li^{+}, Sn^{2+}, Cd^{2+}	0 min	Low sensitivity; fast response
[35]	Pb^{2+}	100 nM	0.1–50 μM	Hg^{2+}, Mg^{2+}, Zn^{2+}, Ni^{2+}, Cu^{2+}, Co^{2+}, Ca^{2+}, Mn^{2+}, Fe^{2+}, Cd^{2+}, Ba^{2+}, Cr^{3+}	0 min	Fast response
[36]	Pb^{2+}	100 ppt	100–25,000 ppt	Mg^{2+}, Ca^{2+}, Hg^{2+}, Mn^{2+}, Fe^{2+}, Cu^{2+}, Ni^{2+}, Co^{2+}, Zn^{2+}, Cd^{2+}	20 min	High sensitivity (DLS-enabled)
[54]	Pb^{2+}	10 nM	10–1000 nM	Li^{+}, Na^{+}, K^{+}, Mg^{2+}, Ca^{2+}, Sr^{2+}, Ba^{2+}, Mn^{2+}, Fe^{2+}, Fe^{3+}, Co^{2+}, Ni^{2+}, Au^{3+}, Cu^{2+}, Zn^{2+}, Cd^{2+}, Hg^{2+}, Pb^{2+}	20 min	High sensitivity; broad selectivity testing
[45]	Pb^{2+}	0.29 μM	80 ng/mL–25 μg/ml	Ni^{2+}, Co^{2+}, Mg^{2+}, Ca^{2+}, Zn^{2+}, Fe^{3+}	5 min	Low sensitivity and selectivity
[55]	Pb^{2+}	16.7 nM	0.5–8 μM	Ag^{+}, Al^{3+}, Ca^{2+}, Cd^{2+}, Co^{2+}, Cr^{3+}, Cr^{6+}, Cu^{2+}, Fe^{2+}, Fe^{3+}, Hg^{2+}, Mg^{2+}, Mn^{2+}, Ni^{2+}, Pb^{2+}, Zn^{2+}	10 min	High sensitivity
[58]	As^{3+}	1.8 ppb	4–100 ppb	K^{+}, Cu^{2+}, Mn^{2+}, Zn^{2+}, Mg^{2+}, Na^{+}, Hg^{2+}, Fe^{2+}, Fe^{3+}, Ca^{2+}, Ni^{2+}, Pb^{2+}, Cd^{2+}, Cr^{3+}, Al^{3+}, As^{5+}, CH_4AsNaO_3, $(CH_3)_2AsO_2H$	6 min	High sensitivity via dialyzed citrate-Au NPs
[59]	As^{3+}	0.53 ppb	1–114 ppb	As^{3+}, Pb^{2+}, Co^{2+}, Hg^{2+}, Cd^{2+}, Ni^{2+}, Cu^{2+}	5 min	Green synthesis with glucose
[37]	As^{3+}	0.12 ppb	0.12–1 ppb	Fe^{3+}, Co^{2+}, Ni^{2+}, K^{+}, Na^{+}, Mg^{2+}, Ca^{2+}, Cu^{2+}, Hg^{2+}, Pb^{2+}	1 h	RGB quantification; narrow range
[38]	As^{5+}, As^{3+}	2.5 μg/L	0.25–20 μg/L	Cu^{2+}, Ni^{2+}, Co^{2+}, Ca^{2+}, Mg^{2+}, Na^{+}	N/A	As^{5+} detection
[27]	As^{3+}	Mode D: 0.57 ppb Mode A: 0.41 ppb	Mode D: 2–240 ppb Mode A: 2–40 ppb	Pb^{2+}, Ag^{+}, Fe^{3+}, Zn^{2+}, Cd^{2+}, Cu^{2+}, Ni^{2+}, Cr^{3+}, Bi^{3+}, K^{+}, Na^{+}, Mg^{2+}, Al^{3+}, Ba^{2+}, Sn^{2+}, Ca^{2+}, As^{5+}, CH_4AsNaO_3, $(CH_3)_2AsO_2H$	35 min	High sensitivity
[26]	Hg^{2+}	2.8 nM	5 nM–1000 nM	Cd^{2+}, Mg^{2+}, Co^{2+}, Zn^{2+}, Pb^{2+}, Mn^{2+}, Ni^{2+}, Cr^{3+}, Cu^{2+}, Fe^{2+}, Fe^{3+}, Na^{+}	5 min	Broad dynamic range
[28]	Hg^{2+}	50 nM	25–750 nM	Co^{2+}, Mn^{2+}, Pb^{2+}, Ca^{2+}, Cd^{2+}, Cr^{3+}, Zn^{2+}, Cu^{2+}, Ni^{2+},	40 min	Long incubation time
[62]	Hg^{2+}	0.15 nM	0.25–500 nM	Zn^{2+}, Mg^{2+}, Cu^{2+}, Mn^{2+}, Cd^{2+}, Ni^{2+}, Pb^{2+}	3 min	High sensitivity
[63]	Hg^{2+}, CH_3Hg^{+}	Hg^{2+}: 10 nM CH_3Hg^{+}:15 nM	Hg^{2+}:10 nM–1.5μM CH_3Hg^{+}:15 nM–0.8 μM	Cd^{2+}, Pb^{2+}, Mg^{2+}, Mn^{2+}, Co^{2+}, Ba^{2+}, Zn^{2+}, Ag^{+}	2 min	CH_3Hg^{+} detection
[64]	Hg^{2+}	5 μM	N/A	Cu^{2+}, Zn^{2+}, Co^{2+}, Mg^{2+}, Ni^{2+}, Ba^{2+}	20 min	Low sensitivity
[34]	Al^{3+}	1 μM	N/A	Hg^{2+}, Fe^{3+}, Cd^{2+}, Ag^{+}, Cu^{2+}, Ni^{2+}, Zn^{2+}, Mn^{2+}, Co^{2+}, Pb^{2+}, Al^{3+}	0 min	Low sensitivity; fast response; Sb^{3+}/Cr^{3+} interference
[67]	Al^{3+}	0.81 μM	1–3.5 μM	Ag^{+}, Mg^{2+}, Ca^{2+}, Mn^{2+}, Co^{2+}, Ni^{2+}, Cu^{2+}, Zn^{2+}, Cd^{2+}, Hg^{2+}, Pb^{2+}, Fe^{2+}, Fe^{3+}, Cr^{3+}	1 min	Narrow dynamic range
[68]	Al^{3+}	1.15 μM	1.15–12 μM	K^{+}, Ag^{+}, Na^{+}, Ba^{2+}, Cd^{2+}, Ca^{2+}, Cu^{2+}, Pb^{2+}, Mn^{2+}, Mg^{2+}, Hg^{2+}, Ni^{2+}, Pt^{2+}, Sn^{2+}, Zn^{2+}, Al^{3+}, Co^{3+}, Cr^{3+}, Au^{3+}, Fe^{3+}	1 min	Low sensitivity
[69]	Al^{3+}	0.29 μM	9–23 μM	Ag^{+}, Cd^{2+}, Co^{2+}, Al^{3+}, Cr^{3+}, Cu^{2+}, Fe^{3+}, Hg^{2+}, Mg^{2+}, Mn^{2+}, Ni^{2+}, Pb^{2+}, Ba^{2+}, Zn^{2+}	10 s	Relatively high sensitivity
[71]	Cs^{+}	19 μM	19–70 μM	Li^{+}, Na^{+}, K^{+}, Ca^{2+}, Al^{3+}, Mn^{2+}, Fe^{2+}, Mg^{2+}, NH_4^{+}, PO_4^{3-}, Cl^{-}	23 min	Low sensitivity
[73]	Ag^{+}	50 nM	100–4000 nM	Cd^{2+}, Fe^{3+}, Ca^{2+}, Mn^{2+}, Cu^{2+}, Co^{2+}, Ni^{2+}, Al^{3+}, Zn^{2+}, Pb^{2+}	10 min	High sensitivity
[75]	Tl^{+}	3.2 nM	0.01–0.6 μM	K^{+}, Na^{+}, Mg^{2+}, Ca^{2+}, Al^{3+}, Co^{2+}, Ni^{2+}, Mn^{2+}, Cu^{2+}, Zn^{2+}, Fe^{3+}, Cr^{3+}, Cd^{2+}, Ag^{+}, Pb^{2+}, Hg^{2+}	10 min	High sensitivity
[78]	Sc^{3+}	0.02 μM	0.1–3 μM	Ce^{3+}, Pr^{3+}, Nd^{3+}, Sm^{3+}, Eu^{3+}, Gd^{3+}, Tb^{3+}, Dy^{3+}, Ho^{3+}, Er^{3+}, Tm^{3+}, Yb^{3+}, Lu^{3+}, Y^{3+}, La^{3+}	1 min	Narrow dynamic range
[81]	CN^{-}	0.1 μM	0.1–50 μM	Cl^{-}, Br^{-}, BrO_3^{3-}, $C_6H_5O_7^{-}$, NO_3^{-}, CO_3^{2-}, PO_4^{3-}, F^{-}, SO_3^{2-}, $S_2O_8^{-}$, SO_4^{2-}, ClO_4^{-}, CH_3COO^{-}, Li^{+}, Mg^{2+}, K^{+}, Ca^{2+}, Cr^{3+}, Mn^{2+}, Fe^{2+}, Co^{2+}, Ni^{2+}, Cu^{2+}, Cd^{2+}, Zn^{2+}, Hg^{2+}, Pb^{2+}	30 min	High selectivity
[31]	NO_2^{-}	4 μM	1.0–15.0 μM	NO_3^{-}, SO_4^{2-}, PO_4^{3-}, Ac^{-}, Br^{-}, SCN^{-}, ClO_4^{-}, S^{2-}, Cu^{2+}, Pb^{2+}, Mg^{2+}, Hg^{2+}, Cd^{2+}, Zn^{2+}, Al^{3+}, Mn^{2+}, Ag^{+}, Cr^{3+}	10 min	Narrow dynamic range
[84]	Hg^{2+}, Cd^{2+}, Fe^{3+}, Pb^{2+}, Al^{3+}, Cu^{2+}, Cr^{3+}	Pb^{2+}, Hg^{2+}:2 μM Fe^{3+}:10 μM	2–50 μM	Ag^{+}, Ca^{2+}, Zn^{2+}, Co^{2+}, Ni^{2+}, Sr^{2+}, K^{+}, Na^{+}, Fe^{2+}	15 min	Multi-metal-ion discrimination; Low sensitivity

Table 1. *Cont.*

Refs.	Analytes	LOD	Dynamic Range	Selectivity Over	Response Time	Features/Limitations
[85]	Ti^{4+}, Cr^{3+}, Mn^{2+}, Pb^{2+}, Sn^{4+}, Fe^{3+}	100 nM for all	Ti^{4+}, Cr^{3+} Mn^{2+}, Pb^{2+}: 100−900 nM Sn^{4+}:100−1000 nM Fe^{3+}:100−800 nM	N/A	20 min	No selectivity testing
[86]	Ba^{2+} Cd^{2+} Pb^{2+}	Ba^{2+}: 20 nM Cd^{2+}: 20 nM Pb^{2+}: 50 nM	Ba^{2+}: 0.02–22 µM Cd^{2+}: 0.02–10µM Pb^{2+}: 0.05–10µM	NH_4^+, SO_4^{2-}, CO_3^{2-}, PO_4^{3-}, Al^{3+}, Zn^{2+}, Cs^+, Rb^+, K^+, Li^+, Fe^{3+}, Fe^{2+}, Na^+, Mg^{2+}, Cu^{2+}, Ni^{2+}, Ca^{2+}, Mn^{2+}, Co^{2+}, Cr^{3+}	20 min	Cannot differentiate individual cation; high sensitivity
[40]	Pb^{2+}, Cu^{2+}	0.65 ppm Cu^{2+} 10.0 ppm Pb^{2+}	N/A	Li^+, Na^+, K^+, Ba^{2+}, Mg^{2+}, Fe^{3+}, Cs^+, Hg^{2+}, Ca^{2+}, Zn^{2+}, Cd^{2+}, Ni^{2+}, Sr^{2+}, Cu^{2+}, Pb^{2+}	N/A	Pb^{2+} vs Cu^{2+} color different; range not reported
[87]	Hg^{2+}, Pb^{2+}, Cu^{2+}	200nM for all	0.2–1 µM	Ba^{2+}, Ca^{2+}, Cd^{2+}, Co^{2+}, Fe^{3+}, Mg^{2+}, Mn^{2+}, Ni^{2+} Zn^{2+}	N/A	Cannot differentiate individual ions
[91]	Azinphosmethyl (AM) Chlorpyrifos (CP) Fenamiphos (FP) Pirimiphosmethyl (PM) Phosalone (PS)	AM: 7 ng/mL CP: 118 ng/mL FP: 7 ng/mL PM: 30 ng/mL PS: 37 ng/mL	AM: 80–400 ng/mL CP: 12–800 ng/mL FP: 80–400 ng/mL PM: 40–800 ng/mL PS: 40–320 ng/mL	carbaryl, carbofuran, methiocarb, pirimicarb, imidacloprid, thiamethoxam, tebuconazole, propiconazole	10 min	Simultaneous detection and discrimination
[29]	Acephate (AC) Phenthoate (PT) Profenofos (PF) Acetamiprid (AP) Chlorothalonil(CT)Cartap	AC: 3.46 × 10^{-7} M PT: 3.0 × 10^{-9} M PF: 6.0 × 10^{-7} M AP: 6.24 × 10^{-10} M CT: 3.75 × 10^{-7} M Cartap: 1.7 × 10^{-8} M	AC: 10–900 µM PT: 0.01–1.50 µM PF: 1.0–200 µM AP: 0.001–0.15 µM CT: 1.0–1000 µM Cartap: 0.05–1.50 µM	Na^+, K^+, Cu^{2+}, Zn^{2+}, Cd^{2+}, Fe^{2+}, Mn^{2+}, Mg^{2+}, Ba^{2+}, Cr^{3+}, Fe^{3+}, Al^{3+}, Cl^-, I^-, Br^-, NO_3^-, SO_4^{2-}, $Cr_2O_7^{2-}$	5 min	High selectivity
[92]	TBA, DMT	TBA: 0.02 µM DMT: 6.2 nM	TBA: 0.1–0.9 µM DMT: 1–40 nM	30 kinds of environmental pollutants	5 min	Broad selectivity testing
[93]	Prothioconazole	0.38 µg/L	1.33–19.99 µg/L	prothioconazole-desthio, fluxapyroxad, fluazinam, azoxystrobin, metconazole, pyraclostrobine, methoxone, diflubenzuron and cyazofamid, thiodicarb	1 min	High sensitivity; fast response
[94]	Thiram	0.04 µM	0.05–2.0 µM	ethametsulfuron, diniconazole, thiophanate, gibberellins, dinotefuran, 2mercaptobenzothiazole, nereistoxin oxalate.	12 min	Low sensitivity, narrow range
[97]	CB	0.05 µM	0.05–1 µM	alamime, phenylalanine, glycerol, vitamin, threonine, urea, cysteamine, glucose, glycine, NaCl, $CaCl_2$	15 min	Low sensitivity, narrow range
[39]	CB	2.8 × 10^{-11} M	2.8 × 10^{-10}–1.4 × 10^{-6} M	DL-epinephrine, phenylalamine, tryptohan, alamine, uric acid, glycine, glycerol, glucose, $MgCl_2$, $CaCl_2$, NaCl	2 min	Broad range, fast response
[106]	Microcystin-LR	0.37 nM	0.5 nM–7.5 µM	acetaminprid, glyphosate, dylox, atrazine, clofentezine	15 min	Broad dynamic range, high sensitivity
[107]	T-2 toxin	57.8 pg/mL	0.1 ng/mL–5000 ng/mL	aflatoxins B1, ochratoxin A, zearalenone, fumonisin B	40 min	Broad dynamic range, high sensitivity, long incubation time
[108]	Bisphenol A	1 pg/mL	0.001–1000 ng/mL	bisphenol B, bisphenol C, diphenolic acid, bisphenol AF	40 min	Broad dynamic range, high sensitivity, long incubation time
[110]	Azodicarbonamide	0.23 µM	0.12 µM–1.00 µM	dibenzoyl peroxide, potassium bromate, cysteine	2 h	Short dynamic range, low selectivity, long incubation time

Author Contributions: X.Z.: Conceptualization, Writing—original draft, Writing—review & editing. A.G.K.: Writing-review & editing. Y.Y.: Conceptualization, Writing—review & editing. All authors have read and agreed to the published version of the manuscript

Funding: This research was funded by the Office of Research and Economic Development (RED) at the University of California, Riverside, through the SoCal OASIS Internal Funding Award.

Data Availability Statement: Not applicable.

Acknowledgments: We thank the Office of Research and Economic Development (RED) at the University of California, Riverside, for the SoCal OASIS Internal Funding Award.

Declaration of Generative AI and AI-assisted Technologies in the Writing Process: During the preparation of this work, the authors used ChatGPT 4o to improve the clarity and readability of the manuscript. After using this tool, the authors reviewed and edited the content as needed and take full responsibility for the content of the publication.

Conflicts of Interest: The authors declare no conflict of interest.

References

1. Sumaira; Siddique, H.M.A. Industrialization, energy consumption, and environmental pollution: Evidence from South Asia. *Environ. Sci. Pollut. Res.* **2023**, *30*, 4094–4102. https://doi.org/10.1007/s11356-022-22317-0.
2. Lin, L.; Yang, H.; Xu, X. Effects of Water Pollution on Human Health and Disease Heterogeneity: A Review. *Front. Environ. Sci.* **2022**, *10*, 880246. https://doi.org/10.3389/fenvs.2022.880246.
3. Wen, Y.; Schoups, G.; van de Giesen, N. Organic pollution of rivers: Combined threats of urbanization, livestock farming and global climate change. *Sci. Rep.* **2017**, *7*, 43289. https://doi.org/10.1038/srep43289.
4. Boyd, R.S. Heavy metal pollutants and chemical ecology: Exploring new frontiers. *J. Chem. Ecol.* **2010**, *36*, 46–58. https://doi.org/10.1007/s10886-009-9730-5.
5. Lipczynska-Kochany, E. Humic substances, their microbial interactions and effects on biological transformations of organic pollutants in water and soil: A review. *Chemosphere* **2018**, *202*, 420–437. https://doi.org/10.1016/j.chemosphere.2018.03.104.
6. Zhu, Z.-Y.; Zhang, J.; Wu, Y.; Zhang, Y.-Y.; Lin, J.; Liu, S.-M. Hypoxia off the Changjiang (Yangtze River) Estuary: Oxygen depletion and organic matter decomposition. *Mar. Chem.* **2011**, *125*, 108–116. https://doi.org/10.1016/j.marchem.2011.03.005.
7. Santos, F.J.; Galceran, M.T. The application of gas chromatography to environmental analysis. *Trends Anal. Chem* **2002**, *21*, 672–685.
8. Richardson, S.D. Environmental Mass Spectrometry: Emerging Contaminants and Current Issues. *Anal. Chem.* **2008**, *80*, 4373–4402.
9. Pohl, P. Determination of metal content in honey by atomic absorption and emission spectrometries. *Trends Anal. Chem* **2009**, *28*, 117–128. https://doi.org/10.1016/j.trac.2008.09.015.
10. Rekhi, H.; Rani, S.; Sharma, N.; Malik, A.K. A Review on Recent Applications of High-Performance Liquid Chromatography in Metal Determination and Speciation Analysis. *Crit. Rev. Anal. Chem.* **2017**, *47*, 524–537. https://doi.org/10.1080/10408347.2017.1343659.
11. Liu, B.; Zhuang, J.; Wei, G. Recent advances in the design of colorimetric sensors for environmental monitoring. *Environ. Sci. Nano* **2020**, *7*, 2195–2213. https://doi.org/10.1039/d0en00449a.
12. Wei, H.; Hossein Abtahi, S.M.; Vikesland, P.J. Plasmonic colorimetric and SERS sensors for environmental analysis. *Environ. Sci. Nano* **2015**, *2*, 120–135. https://doi.org/10.1039/c4en00211c.
13. Tang, L.; Li, J. Plasmon-Based Colorimetric Nanosensors for Ultrasensitive Molecular Diagnostics. *ACS Sens.* **2017**, *2*, 857–875. https://doi.org/10.1021/acssensors.7b00282.
14. Balasubramanian, S.K.; Yang, L.; Yung, L.Y.; Ong, C.N.; Ong, W.Y.; Yu, L.E. Characterization, purification, and stability of gold nanoparticles. *Biomaterials* **2010**, *31*, 9023–9030. https://doi.org/10.1016/j.biomaterials.2010.08.012.
15. Willets, K.A.; Van Duyne, R.P. Localized surface plasmon resonance spectroscopy and sensing. *Annu. Rev. Phys. Chem* **2007**, *58*, 267–297. https://doi.org/10.1146/annurev.physchem.58.032806.104607.
16. Link, S.; El-Sayed, M.A. Spectral Properties and Relaxation Dynamics of Surface Plasmon Electronic Oscillations in Gold and Silver Nanodots and Nanorods. *J. Phys. Chem. B* **1999**, *103*, 8410–8426.
17. Kelly, K.L.; Coronado, E.; Zhao, L.L.; Schatz, G.C. The Optical Properties of Metal Nanoparticles: The Influence of Size, Shape, and Dielectric Environment. *J. Phys. Chem. B* **2003**, *107*, 668–677.
18. Gao, C.; Vuong, J.; Zhang, Q.; Liu, Y.; Yin, Y. One-step seeded growth of Au nanoparticles with widely tunable sizes. *Nanoscale* **2012**, *4*, 2875–2878. https://doi.org/10.1039/c2nr30300k.
19. Huang, X.; El-Sayed, M.A. Gold nanoparticles: Optical properties and implementations in cancer diagnosis and photothermal therapy. *J. Adv. Res.* **2010**, *1*, 13–28. https://doi.org/10.1016/j.jare.2010.02.002.
20. Zeng, J.; Zhang, Y.; Zeng, T.; Aleisa, R.; Qiu, Z.; Chen, Y.; Huang, J.; Wang, D.; Yan, Z.; Yin, Y. Anisotropic plasmonic nanostructures for colorimetric sensing. *Nano Today* **2020**, *32*, 100855. https://doi.org/10.1016/j.nantod.2020.100855.
21. Murphy, C.J.; Sau, T.K.; Gole, A.M.; Orendorff, C.J.; Gao, J.; Gou, L.; Hunyadi, S.E.; Li, T. Anisotropic Metal Nanoparticles: Synthesis, Assembly, and Optical Applications. *J. Phys. Chem. B* **2005**, *109*, 13857–13870.
22. Zhong, Z.; Patskovskyy, S.; Bouvrette, P.; Luong, J.H.T.; Gedanken, A. The Surface Chemistry of Au Colloids and Their Interactions with Functional Amino Acids. *J. Phys. Chem. B* **2004**, *108*, 4046–4052.
23. Jain, P.K.; Huang, W.; El-Sayed, M.A. On the Universal Scaling Behavior of the Distance Decay of Plasmon Coupling in Metal Nanoparticle Pairs: A Plasmon Ruler Equation. *Nano Lett.* **2007**, *7*, 2080–2088.

24. Montano-Priede, J.L.; Sanroman-Iglesias, M.; Zabala, N.; Grzelczak, M.; Aizpurua, J. Robust Rules for Optimal Colorimetric Sensing Based on Gold Nanoparticle Aggregation. *ACS Sens.* **2023**, *8*, 1827–1834. https://doi.org/10.1021/acssensors.3c00287.
25. Tripathi, R.M.; Park, S.H.; Kim, G.; Kim, D.-H.; Ahn, D.; Kim, Y.M.; Kwon, S.J.; Yoon, S.-Y.; Kang, H.J.; Chung, S.J. Metal-induced redshift of optical spectra of gold nanoparticles: An instant, sensitive, and selective visual detection of lead ions. *Int. Biodeter. Biodegr* **2019**, *144*, 104740. https://doi.org/10.1016/j.ibiod.2019.104740.
26. Chen, L.; Lou, T.; Yu, C.; Kang, Q.; Chen, L. N-1-(2-mercaptoethyl)thymine modification of gold nanoparticles: A highly selective and sensitive colorimetric chemosensor for Hg^{2+}. *Analyst* **2011**, *136*, 4770–4773. https://doi.org/10.1039/c1an15585g.
27. Zhang, D.; Chu, S.; Wang, L.; Zhan, X.; Zhou, P.; Zhang, D. Dual-mode colorimetric determination of As(III) based on negatively-charged aptamer-mediated aggregation of positively-charged AuNPs. *Anal. Chim. Acta* **2022**, *1221*, 340111. https://doi.org/10.1016/j.aca.2022.340111.
28. Chen, G.H.; Chen, W.Y.; Yen, Y.C.; Wang, C.W.; Chang, H.T.; Chen, C.F. Detection of mercury(II) ions using colorimetric gold nanoparticles on paper-based analytical devices. *Anal. Chem.* **2014**, *86*, 6843–6849. https://doi.org/10.1021/ac5008688.
29. Rana, K.; Bhamore, J.R.; Rohit, J.V.; Park, T.-J.; Kailasa, S.K. Ligand exchange reactions on citrate-gold nanoparticles for a parallel colorimetric assay of six pesticides. *New J. Chem.* **2018**, *42*, 9080–9090. https://doi.org/10.1039/c8nj01294f.
30. Wang, Z.; Lee, J.H.; Lu, Y. Label-Free Colorimetric Detection of Lead Ions with a Nanomolar Detection Limit and Tunable Dynamic Range by using Gold Nanoparticles and DNAzyme. *Adv. Mater.* **2008**, *20*, 3263–3267. https://doi.org/10.1002/adma.200703181.
31. Chen, Z.; Zhang, Z.; Qu, C.; Pan, D.; Chen, L. Highly sensitive label-free colorimetric sensing of nitrite based on etching of gold nanorods. *Analyst* **2012**, *137*, 5197–5200. https://doi.org/10.1039/c2an35787a.
32. Lin, J.-M.; Huang, Y.-Q.; Liu, Z.-b.; Lin, C.-Q.; Ma, X.; Liu, J.-M. Design of an ultra-sensitive gold nanorod colorimetric sensor and its application based on formaldehyde reducing Ag^{+}. *RSC Adv.* **2015**, *5*, 99944–99950. https://doi.org/10.1039/c5ra16266a.
33. Park, J.W.; Shumaker-Parry, J.S. Structural study of citrate layers on gold nanoparticles: Role of intermolecular interactions in stabilizing nanoparticles. *J Am Chem Soc* **2014**, *136*, 1907–1921. https://doi.org/10.1021/ja4097384.
34. Chen, S.; Fang, Y.M.; Xiao, Q.; Li, J.; Li, S.B.; Chen, H.J.; Sun, J.J.; Yang, H.H. Rapid visual detection of aluminium ion using citrate capped gold nanoparticles. *Analyst* **2012**, *137*, 2021–2023. https://doi.org/10.1039/c2an35129c.
35. Chai, F.; Wang, C.; Wang, T.; Li, L.; Su, Z. Colorimetric detection of Pb^{2+} using glutathione functionalized gold nanoparticles. *ACS Appl. Mater. Interfaces* **2010**, *2*, 1466–1470. https://doi.org/10.1021/am100107k.
36. Beqa, L.; Singh, A.K.; Khan, S.A.; Senapati, D.; Arumugam, S.R.; Ray, P.C. Gold nanoparticle-based simple colorimetric and ultrasensitive dynamic light scattering assay for the selective detection of Pb(II) from paints, plastics, and water samples. *ACS Appl. Mater. Interfaces* **2011**, *3*, 668–673. https://doi.org/10.1021/am101118h.
37. Zheng, B.; Li, J.; Zheng, Z.; Zhang, C.; Huang, C.; Hong, J.; Li, Y.; Wang, J. Rapid colorimetric detection of arsenic (III) by glutathione functionalized gold nanoparticles based on RGB extracting system. *Opt. Laser Technol.* **2021**, *133*, 106522. https://doi.org/10.1016/j.optlastec.2020.106522.
38. Dominguez-Gonzalez, R.; Gonzalez Varela, L.; Bermejo-Barrera, P. Functionalized gold nanoparticles for the detection of arsenic in water. *Talanta* **2014**, *118*, 262–269. https://doi.org/10.1016/j.talanta.2013.10.029.
39. Zhang, X.; Zhao, H.; Xue, Y.; Wu, Z.; Zhang, Y.; He, Y.; Li, X.; Yuan, Z. Colorimetric sensing of clenbuterol using gold nanoparticles in the presence of melamine. *Biosens. Bioelectron.* **2012**, *34*, 112–117. https://doi.org/10.1016/j.bios.2012.01.026.
40. Ravi Gunupuru; Debdeep Maity; Gopala R Bhadu; Ashish Chakraborty; Srivastava, D.N.; Paul, P. Colorimetric detection of Cu^{2+} and Pb^{2+} ions using calix[4]arene functionalized gold nanoparticles. *J. Chem. Sci.* **2014**, *126*, 627–635.
41. Liu, J.; Lu, Y. A Colorimetric Lead Biosensor Using DNAzyme-Directed Assembly of Gold Nanoparticles. *J. Am. Chem. Soc.* **2003**, *125*, 6642–6643.
42. Liu, J.; Lu, Y. Accelerated Color Change of Gold Nanoparticles Assembled by DNAzymes for Simple and Fast Colorimetric Pb^{2+} Detection. *J. Am. Chem. Soc.* **2004**, *126*, 12298–12305.
43. Turkevich, J.; Stevenson, P.C.; Hillier, J. A study of the nucleation and growth processes in the synthesis of colloidal gold. *Discuss. Faraday Soc.* **1951**, *11*, 55–75.
44. Liu, D.; Wang, Z.; Jiang, X. Gold nanoparticles for the colorimetric and fluorescent detection of ions and small organic molecules. *Nanoscale* **2011**, *3*, 1421–1433. https://doi.org/10.1039/c0nr00887g.
45. Berlina, A.N.; Sharma, A.K.; Zherdev, A.V.; Gaur, M.S.; Dzantiev, B.B. Colorimetric Determination of Lead Using Gold Nanoparticles. *Anal. Lett.* **2014**, *48*, 766–782. https://doi.org/10.1080/00032719.2014.961641.
46. Yoosaf, K.; Ipe, B.I.; Suresh, C.H.; Thomas, K.G. In Situ Synthesis of Metal Nanoparticles and Selective Naked-Eye Detection of Lead Ions from Aqueous Media. *J. Phys. Chem. C* **2007**, *111*, 12839–12847.

47. Sau, T.K.; Murphy, C.J. Seeded High Yield Synthesis of Short Au Nanorods in Aqueous Solution. *Langmuir* **2004**, *20*, 6414–6420.
48. Ye, X.; Jin, L.; Caglayan, H.; Chen, J.; Xing, G.; Zheng, C.; Doan-Nguyen, V.; Kang, Y.; Engheta, N.; Kagan, C.R.; et al. Improved Size-Tunable Synthesis of Monodisperse Gold Nanorods through the Use of Aromatic Additives. *ACS Nano* **2012**, *6*, 2804–2817.
49. Tan, M.G.; Zhang, G.L.; Li, X.L.; Zhang, Y.X.; Yue, W.S.; Chen, J.M.; Wang, Y.S.; Li, A.G.; Li, Y.; Zhang, Y.M.; et al. Comprehensive Study of Lead Pollution in Shanghai by Multiple Techniques. *Anal. Chem.* **2006**, *78*, 8044–8050.
50. Raj, K.; Das, A.P. Lead pollution: Impact on environment and human health and approach for a sustainable solution. *Environ. Chem. Ecotox* **2023**, *5*, 79–85. https://doi.org/10.1016/j.enceco.2023.02.001.
51. Collin, M.S.; Venkatraman, S.K.; Vijayakumar, N.; Kanimozhi, V.; Arbaaz, S.M.; Stacey, R.G.S.; Anusha, J.; Choudhary, R.; Lvov, V.; Tovar, G.I.; et al. Bioaccumulation of lead (Pb) and its effects on human: A review. *J. Hazard. Mater. Adv.* **2022**, *7*, 100094. https://doi.org/10.1016/j.hazadv.2022.100094.
52. Reuben, A.; Caspi, A.; Belsky, D.W.; Broadbent, J.; Harrington, H.; Sugden, K.; Houts, R.M.; Ramrakha, S.; Poulton, R.; Moffitt, T.E. Association of Childhood Blood Lead Levels With Cognitive Function and Socioeconomic Status at Age 38 Years and With IQ Change and Socioeconomic Mobility Between Childhood and Adulthood. *JAMA* **2017**, *317*, 1244–1251. https://doi.org/10.1001/jama.2017.1712.
53. Frost, M.S.; Dempsey, M.J.; Whitehead, D.E. The response of citrate functionalised gold and silver nanoparticles to the addition of heavy metal ions. *Colloids Surf. A* **2017**, *518*, 15–24. https://doi.org/10.1016/j.colsurfa.2016.12.036.
54. Huang, K.W.; Yu, C.J.; Tseng, W.L. Sensitivity enhancement in the colorimetric detection of lead(II) ion using gallic acid-capped gold nanoparticles: Improving size distribution and minimizing interparticle repulsion. *Biosens. Bioelectron.* **2010**, *25*, 984–989. https://doi.org/10.1016/j.bios.2009.09.006.
55. Lee, I.L.; Sung, Y.-M.; Wu, S.-P. Triazole-acetate functionalized gold nanoparticles for colorimetric Pb(ii) sensing. *RSC Adv.* **2014**, *4*, 25251–25256. https://doi.org/10.1039/c4ra02448f.
56. Khanna, K.; Kohli, S.K.; Kumar, P.; Ohri, P.; Bhardwaj, R.; Alam, P.; Ahmad, P. Arsenic as hazardous pollutant: Perspectives on engineering remediation tools. *Sci. Total Environ.* **2022**, *838*, 155870. https://doi.org/10.1016/j.scitotenv.2022.155870.
57. Hughes, M.F. Arsenic toxicity and potential mechanisms of action. *Toxicol. Lett.* **2002**, *133*, 1–16.
58. Gong, L.; Du, B.; Pan, L.; Liu, Q.; Yang, K.; Wang, W.; Zhao, H.; Wu, L.; He, Y. Colorimetric aggregation assay for arsenic(III) using gold nanoparticles. *Microchim. Acta* **2017**, *184*, 1185–1190. https://doi.org/10.1007/s00604-017-2122-6.
59. Boruah, B.S.; Biswas, R.; Deb, P. A green colorimetric approach towards detection of arsenic (III): A pervasive environmental pollutant. *Opt. Laser Technol.* **2019**, *111*, 825–829. https://doi.org/10.1016/j.optlastec.2018.09.023.
60. Hylander, L.D.; Goodsite, M.E. Environmental costs of mercury pollution. *Sci. Total Environ.* **2006**, *368*, 352–370. https://doi.org/10.1016/j.scitotenv.2005.11.029.
61. Bernhoft, R.A. Mercury toxicity and treatment: A review of the literature. *J. Environ. Public Health* **2012**, *2012*, 460508. https://doi.org/10.1155/2012/460508.
62. Zhu, Y.; Cai, Y.; Zhu, Y.; Zheng, L.; Ding, J.; Quan, Y.; Wang, L.; Qi, B. Highly sensitive colorimetric sensor for Hg^{2+} detection based on cationic polymer/DNA interaction. *Biosens. Bioelectron.* **2015**, *69*, 174–178. https://doi.org/10.1016/j.bios.2015.02.018.
63. Chen, L.; Li, J.; Chen, L. Colorimetric detection of mercury species based on functionalized gold nanoparticles. *ACS Appl. Mater. Interfaces* **2014**, *6*, 15897–15904. https://doi.org/10.1021/am503531c.
64. Hu, Y.; Huang, Z.; Liu, B.; Liu, J. Hg(II) Adsorption on Gold Nanoparticles Dominates DNA-Based Label-Free Colorimetric Sensing. *ACS Appl. Nano Mater.* **2021**, *4*, 1377–1384. https://doi.org/10.1021/acsanm.0c02923.
65. Alasfar, R.H.; Isaifan, R.J. Aluminum environmental pollution: The silent killer. *Environ. Sci. Pollut. Res.* **2021**, *28*, 44587–44597. https://doi.org/10.1007/s11356-021-14700-0.
66. Bonfiglio, R.; Scimeca, M.; Mauriello, A. The impact of aluminum exposure on human health. *Arch. Toxicol.* **2023**, *97*, 2997–2998. https://doi.org/10.1007/s00204-023-03581-6.
67. Luo, X.; Xie, X.; Meng, Y.; Sun, T.; Ding, J.; Zhou, W. Ligands dissociation induced gold nanoparticles aggregation for colorimetric Al^{3+} detection. *Anal. Chim. Acta* **2019**, *1087*, 76–85. https://doi.org/10.1016/j.aca.2019.08.045.
68. Megarajan, S.; Veerappan, A. A selective pink-to-purple colorimetric sensor for aluminium via the aggregation of gold nanoparticles. *Opt. Mater.* **2020**, *108*, 110177. https://doi.org/10.1016/j.optmat.2020.110177.
69. Huang, P.; Li, J.; Liu, X.; Wu, F. Colorimetric determination of aluminum(III) based on the aggregation of Schiff base-functionalized gold nanoparticles. *Microchim. Acta* **2015**, *183*, 863–869. https://doi.org/10.1007/s00604-015-1734-y.
70. Li, X.; Xu, G.; Xia, M.; Liu, X.; Fan, F.; Dou, J. Research on the remediation of cesium pollution by adsorption: Insights from bibliometric analysis. *Chemosphere* **2022**, *308*, 136445. https://doi.org/10.1016/j.chemosphere.2022.136445.

71. Qiu, J.; Fu, L.; Wang, H.; Zou, R.; Zhang, Y.; Li, X.; Wu, A. Colorimetric detection of Cs^+ based on the nonmorphological transition mechanism of gold nanoparticles in the presence of Prussian blue. *New J. Chem.* **2020**, *44*, 2241–2246. https://doi.org/10.1039/c9nj05301h.
72. Tsepina, N.; Kolesnikov, S.; Minnikova, T.; Timoshenko, A.; Kazeev, K. Soil Contamination by Silver and Assessment of Its Ecotoxicity. *Rev. Agric. Sci.* **2022**, *10*, 186–205. https://doi.org/10.7831/ras.10.0_186.
73. Wang, F.; Lu, Y.; Chen, Y.; Sun, J.; Liu, Y. Colorimetric Nanosensor Based on the Aggregation of AuNP Triggered by Carbon Quantum Dots for Detection of Ag^+ Ions. *ACS Sustain. Chem. Eng* **2018**, *6*, 3706–3713. https://doi.org/10.1021/acssuschemeng.7b04067.
74. Peter, A.L.; Viraraghavan, T. Thallium: A review of public health and environmental concerns. *Environ. Int* **2005**, *31*, 493–501. https://doi.org/10.1016/j.envint.2004.09.003.
75. Lei, F.; Ye, Z.; Dong, Z.; Zhang, X.; Wu, P. Thioflavine T-induced charge neutralization assembly of AuNPs for colorimetric sensing of thallium. *Sens. Actuators B Chem.* **2022**, *370*, 132437. https://doi.org/10.1016/j.snb.2022.132437.
76. Botelho Junior, A.B.; Espinosa, D.C.R.; Vaughan, J.; Tenório, J.A.S. Recovery of scandium from various sources: A critical review of the state of the art and future prospects. *Miner. Eng.* **2021**, *172*, 107148. https://doi.org/10.1016/j.mineng.2021.107148.
77. Tanida, E.; Usuda, K.; Kono, K.; Kawano, A.; Tsuji, H.; Imanishi, M.; Suzuki, S.; Ohnishi, K.; Yamamoto, K. Urinary scandium as predictor of exposure: Effects of scandium chloride hexahydrate on renal function in rats. *Biol. Trace Elem. Res.* **2009**, *130*, 273–282. https://doi.org/10.1007/s12011-009-8337-6.
78. Deng, H.-H.; Huang, K.-Y.; Fang, Q.-H.; Lv, Y.-P.; He, S.-B.; Peng, H.-P.; Xia, X.-H.; Chen, W. Schiff base and Lewis acid-base interaction-regulated aggregation/dispersion of gold nanoparticles for colorimetric recognition of rare-earth Sc^{3+} ions. *Sens. Actuators B Chem.* **2020**, *311*, 127925. https://doi.org/10.1016/j.snb.2020.127925.
79. Barber, T.R.; Lutes, C.C.; Doorn, M.R.J.; Fuchsman, P.C.; Timmenga, H.J.; Crouch, R.L. Aquatic ecological risks due to cyanide releases from biomass burning. *Chemosphere* **2003**, *50*, 343–348.
80. Jaszczak, E.; Polkowska, Z.; Narkowicz, S.; Namiesnik, J. Cyanides in the environment-analysis-problems and challenges. *Environ. Sci. Pollut. Res.* **2017**, *24*, 15929–15948. https://doi.org/10.1007/s11356-017-9081-7.
81. Cheng, C.; Chen, H.-Y.; Wu, C.-S.; Meena, J.S.; Simon, T.; Ko, F.-H. A highly sensitive and selective cyanide detection using a gold nanoparticle-based dual fluorescence–colorimetric sensor with a wide concentration range. *Sens. Actuators B Chem.* **2016**, *227*, 283–290. https://doi.org/10.1016/j.snb.2015.12.057.
82. Camargo, J.A.; Alonso, A. Ecological and toxicological effects of inorganic nitrogen pollution in aquatic ecosystems: A global assessment. *Environ. Int* **2006**, *32*, 831–849. https://doi.org/10.1016/j.envint.2006.05.002.
83. Picetti, R.; Deeney, M.; Pastorino, S.; Miller, M.R.; Shah, A.; Leon, D.A.; Dangour, A.D.; Green, R. Nitrate and nitrite contamination in drinking water and cancer risk: A systematic review with meta-analysis. *Environ. Res.* **2022**, *210*, 112988. https://doi.org/10.1016/j.envres.2022.112988.
84. Sener, G.; Uzun, L.; Denizli, A. Colorimetric sensor array based on gold nanoparticles and amino acids for identification of toxic metal ions in water. *ACS Appl. Mater. Interfaces* **2014**, *6*, 18395–18400. https://doi.org/10.1021/am5071283.
85. Li, X.; Li, S.; Liu, Q.; Chen, Z. Electronic-Tongue Colorimetric-Sensor Array for Discrimination and Quantitation of Metal Ions Based on Gold-Nanoparticle Aggregation. *Anal. Chem.* **2019**, *91*, 6315–6320. https://doi.org/10.1021/acs.analchem.9b01139.
86. Qiu, J.; Li, Z.; Miao, L.; Wang, H.; Zhang, Y.; Wu, S.; Zhang, Y.; Li, X.; Wu, A. Colorimetric detection of Ba^{2+}, Cd^{2+} and Pb^{2+} based on a multifunctionalized Au NP sensor. *Analyst* **2019**, *144*, 5081–5089. https://doi.org/10.1039/c9an00836e.
87. Guo, Y.; Wang, Z.; Qu, W.; Shao, H.; Jiang, X. Colorimetric detection of mercury, lead and copper ions simultaneously using protein-functionalized gold nanoparticles. *Biosens. Bioelectron.* **2011**, *26*, 4064–4069. https://doi.org/10.1016/j.bios.2011.03.033.
88. Zhang, W.; Jiang, F.; Ou, J. Global pesticide consumption and pollution: With China as a focus. *Proc. Int. Acad. Ecol. Environ. Sci.* **2011**, *1*, 125–144.
89. Jeyaseelan, A.; Murugesan, K.; Thayanithi, S.; Palanisamy, S.B. A review of the impact of herbicides and insecticides on the microbial communities. *Environ. Res.* **2024**, *245*, 118020. https://doi.org/10.1016/j.envres.2023.118020.
90. Kim, K.H.; Kabir, E.; Jahan, S.A. Exposure to pesticides and the associated human health effects. *Sci Total Environ.* **2017**, *575*, 525–535. https://doi.org/10.1016/j.scitotenv.2016.09.009.
91. Fahimi-Kashani, N.; Hormozi-Nezhad, M.R. Gold-Nanoparticle-Based Colorimetric Sensor Array for Discrimination of Organophosphate Pesticides. *Anal. Chem.* **2016**, *88*, 8099–8106. https://doi.org/10.1021/acs.analchem.6b01616.
92. Chen, N.; Liu, H.; Zhang, Y.; Zhou, Z.; Fan, W.; Yu, G.; Shen, Z.; Wu, A. A colorimetric sensor based on citrate-stabilized AuNPs for rapid pesticide residue detection of terbuthylazine and dimethoate. *Sens. Actuators B Chem.* **2018**, *255*, 3093–3101. https://doi.org/10.1016/j.snb.2017.09.134.

93. Zhou, Y.; Li, C.; Liu, R.; Chen, Z.; Li, L.; Li, W.; He, Y.; Yuan, L. Label-Free Colorimetric Detection of Prothioconazole Using Gold Nanoparticles Based on One-Step Reaction. *ACS Biomater. Sci. Eng.* **2020**, *6*, 2805–2811. https://doi.org/10.1021/acsbiomaterials.0c00208.
94. Liu, K.; Jin, Y.; Wu, Y.; Liang, J. Simple and rapid colorimetric visualization of tetramethylthiuram disulfide (thiram) sensing based on anti-aggregation of gold nanoparticles. *Food Chem.* **2022**, *384*, 132223. https://doi.org/10.1016/j.foodchem.2022.132223.
95. Barbosa, J.; Cruz, C.; Martins, J.; Silva, J.M.; Neves, C.; Alves, C.; Ramos, F.; Da Silveira, M.I. Food poisoning by clenbuterol in Portugal. *Food Addit Contam.* **2005**, *22*, 563–566. https://doi.org/10.1080/02652030500135102.
96. Kumari, S.; Pal, B.; Sahu, S.K.; Prabhakar, P.K.; Tewari, D. Adverse events of clenbuterol among athletes: A systematic review of case reports and case series. *Int. J. Leg. Med.* **2023**, *137*, 1023–1037. https://doi.org/10.1007/s00414-023-02996-1.
97. Kang, J.; Zhang, Y.; Li, X.; Miao, L.; Wu, A. A Rapid Colorimetric Sensor of Clenbuterol Based on Cysteamine-Modified Gold Nanoparticles. *ACS Appl. Mater. Interfaces* **2016**, *8*, 1–5. https://doi.org/10.1021/acsami.5b09079.
98. Martinez, J.L. Environmental pollution by antibiotics and by antibiotic resistance determinants. *Environ. Pollut* **2009**, *157*, 2893–2902. https://doi.org/10.1016/j.envpol.2009.05.051.
99. Polianciuc, S.I.; Gurzau, A.E.; Kiss, B.; Stefan, M.G.; Loghin, F. Antibiotics in the environment: Causes and consequences. *Med. Pharm. Rep.* **2020**, *93*, 231–240. https://doi.org/10.15386/mpr-1742.
100. Gothwal, R.; Shashidhar, T. Antibiotic Pollution in the Environment: A Review. *CLEAN-Soil Air Water* **2014**, *43*, 479–489. https://doi.org/10.1002/clen.201300989.
101. Qin, L.; Zeng, G.; Lai, C.; Huang, D.; Zhang, C.; Xu, P.; Hu, T.; Liu, X.; Cheng, M.; Liu, Y.; et al. A visual application of gold nanoparticles: Simple, reliable and sensitive detection of kanamycin based on hydrogen-bonding recognition. *Sens. Actuators B Chem.* **2017**, *243*, 946–954. https://doi.org/10.1016/j.snb.2016.12.086.
102. Wu, Y.Y.; Huang, P.; Wu, F.Y. A label-free colorimetric aptasensor based on controllable aggregation of AuNPs for the detection of multiplex antibiotics. *Food Chem.* **2020**, *304*, 125377. https://doi.org/10.1016/j.foodchem.2019.125377.
103. Zhang, S.; Du, X.; Liu, H.; Losiewic, M.D.; Chen, X.; Ma, Y.; Wang, R.; Tian, Z.; Shi, L.; Guo, H.; et al. The latest advances in the reproductive toxicity of microcystin-LR. *Environ. Res.* **2021**, *192*, 110254. https://doi.org/10.1016/j.envres.2020.110254.
104. Li, Y.; Wang, Z.; Beier, R.C.; Shen, J.; De Smet, D.; De Saeger, S.; Zhang, S. T-2 toxin, a trichothecene mycotoxin: Review of toxicity, metabolism, and analytical methods. *J. Agric. Food Chem.* **2011**, *59*, 3441–3453. https://doi.org/10.1021/jf200767q.
105. Rochester, J.R. Bisphenol A and human health: A review of the literature. *Reprod. Toxicol.* **2013**, *42*, 132–155. https://doi.org/10.1016/j.reprotox.2013.08.008.
106. Li, X.; Cheng, R.; Shi, H.; Tang, B.; Xiao, H.; Zhao, G. A simple highly sensitive and selective aptamer-based colorimetric sensor for environmental toxins microcystin-LR in water samples. *J. Hazard. Mater.* **2016**, *304*, 474–480. https://doi.org/10.1016/j.jhazmat.2015.11.016.
107. Zhang, W.; Wang, Y.; Nan, M.; Li, Y.; Yun, J.; Wang, Y.; Bi, Y. Novel colorimetric aptasensor based on unmodified gold nanoparticle and ssDNA for rapid and sensitive detection of T-2 toxin. *Food Chem.* **2021**, *348*, 129128. https://doi.org/10.1016/j.foodchem.2021.129128.
108. Lee, E.H.; Lee, S.K.; Kim, M.J.; Lee, S.W. Simple and rapid detection of bisphenol A using a gold nanoparticle-based colorimetric aptasensor. *Food Chem.* **2019**, *287*, 205–213. https://doi.org/10.1016/j.foodchem.2019.02.079.
109. Becalski, A.; Lau, B.P.-Y.; Lewis, D.; Seaman, S.W. Semicarbazide Formation in Azodicarbonamide-Treated Flour: A Model Study. *J. Agric. Food Chem.* **2004**, *52*, 5730−5734.
110. Chen, Z.; Chen, L.; Lin, L.; Wu, Y.; Fu, F. A Colorimetric Sensor for the Visual Detection of Azodicarbonamide in Flour Based on Azodicarbonamide-Induced Anti-Aggregation of Gold Nanoparticles. *ACS Sens.* **2018**, *3*, 2145–2151. https://doi.org/10.1021/acssensors.8b00705.
111. Bourdin, D.; Mocho, P.; Desauziers, V.; Plaisance, H. Formaldehyde emission behavior of building materials: On-site measurements and modeling approach to predict indoor air pollution. *J. Hazard. Mater.* **2014**, *280*, 164–173. https://doi.org/10.1016/j.jhazmat.2014.07.065.
112. Tang, X.; Bai, Y.; Duong, A.; Smith, M.T.; Li, L.; Zhang, L. Formaldehyde in China: Production, consumption, exposure levels, and health effects. *Environ. Int* **2009**, *35*, 1210–1224. https://doi.org/10.1016/j.envint.2009.06.002.
113. Almaquer, F.E.P.; Ricacho, J.S.Y.; Ronquillo, R.L.G. Simple and rapid colorimetric sensing of Ni(II) ions in tap water based on aggregation of citrate-stabilized silver nanoparticles. *Sustain. Environ. Res.* **2019**, *29*, 23. https://doi.org/10.1186/s42834-019-0026-3.
114. Li, H.; Cui, Z.; Han, C. Glutathione-stabilized silver nanoparticles as colorimetric sensor for Ni^{2+} ion. *Sens. Actuators B Chem.* **2009**, *143*, 87–92. https://doi.org/10.1016/j.snb.2009.09.013.
115. Karthiga, D.; Anthony, S.P. Selective colorimetric sensing of toxic metal cations by green synthesized silver nanoparticles over a wide pH range. *RSC Adv.* **2013**, *3*, 16765–16774. https://doi.org/10.1039/c3ra42308e.

116. Soomro, R.A.; Nafady, A.; Sirajuddin; Memon, N.; Sherazi, T.H.; Kalwar, N.H. L-cysteine protected copper nanoparticles as colorimetric sensor for mercuric ions. *Talanta* **2014**, *130*, 415–422. https://doi.org/10.1016/j.talanta.2014.07.023.
117. Li, Q.; Wu, F.; Mao, M.; Ji, X.; Wei, L.; Li, J.; Ma, L. A dual-mode colorimetric sensor based on copper nanoparticles for the detection of mercury-(ii) ions. *Anal. Methods* **2019**, *11*, 4014–4021. https://doi.org/10.1039/c9ay00843h.
118. Madhupriya, S.; Elango, K.P. Highly selective colorimetric sensing of Cu(II) ions in aqueous solution via modulation of intramolecular charge transfer transition of aminonaphthoquinone chemosensor. *Spectrochim Acta A Mol Biomol Spectrosc* **2012**, *97*, 100–104. https://doi.org/10.1016/j.saa.2012.05.044.
119. Petdum, A.; Panchan, W.; Sirirak, J.; Promarak, V.; Sooksimuang, T.; Wanichacheva, N. Colorimetric and fluorescent sensing of a new FRET system via [5]helicene and rhodamine 6G for Hg^{2+} detection. *New J. Chem.* **2018**, *42*, 1396–1402. https://doi.org/10.1039/c7nj04129b.
120. Chen, L.; Tian, X.; Xia, D.; Nie, Y.; Lu, L.; Yang, C.; Zhou, Z. Novel Colorimetric Method for Simultaneous Detection and Identification of Multimetal Ions in Water: Sensitivity, Selectivity, and Recognition Mechanism. *ACS Omega* **2019**, *4*, 5915–5922. https://doi.org/10.1021/acsomega.9b00312.
121. Lu, F.; Zhou, Y.-h.; Wu, L.-h.; Qian, J.; Cao, S.; Deng, Y.-f.; Chen, Y. Highly Fluorescent Nitrogen-Doped Graphene Quantum Dots' Synthesis and Their Applications as Fe(III) Ions Sensor. *Int. J. Opt.* **2019**, *2019*, 8724320. https://doi.org/10.1155/2019/8724320.
122. Li, F.; Hong, Y.-S.; Zuo, K.-X.; Sun, Q.; Gao, E.-Q. Highly selective fluorescent probe for Hg^{2+} and MnO_4^- by the two-fold interpenetrating metal-organic framework with nitro functionalized linkers. *J. Solid State Chem.* **2019**, *270*, 509–515. https://doi.org/10.1016/j.jssc.2018.12.025.

Article

Development of a Temperature-Responsive Polymer Network with Enhanced Transparency and Volume Shrinkage via Star-Shaped PEG-b-PNIPA Block Copolymer

Kai Kawabata [1], Taiki Hoshino [2,3,4], and Yukikazu Takeoka [1,*]

[1] Department of Molecular & Macromolecular Chemistry, Nagoya University, Nagoya 464-8603, Japan
[2] International Center for Synchrotron Radiation Innovation Smart, Tohoku University, 468-1 Aramaki-Aza-Aoba, Aoba-ku, Sendai 980-8572, Japan
[3] RIKEN SPring-8 Center, 1-1-1 Kouto, Sayo-cho 679-5148, Japan
[4] Institute of Multidisciplinary Research for Advanced Materials, Tohoku University, 2-1-1 Katahira, Aoba-ku, Sendai 980-8577, Japan
* Correspondence: ytakeoka1@mac.com
Received: 21 March 2025; Revised: 4 June 2025; Accepted: 1 July 2025; Published: 10 July 2025

Abstract: In this study, a temperature-responsive polymer network was successfully synthesized by using a 4-arm star-shaped polyethylene glycol (PEG) derivative as an initiator and polymerizing *N*-isopropylacrylamide (NIPA) as a secondary acrylamide. The resulting star-shaped block copolymer was used as a building block to prepare a polymer network. Detailed analysis of the polymerization process (including SEC and ^{1}H NMR) confirmed the successful synthesis and high control over the star-shaped block copolymer structure. The obtained star-shaped block copolymer was crosslinked under semi-dilute conditions via a click reaction, in which the hydrophilic PEG was incorporated in an ordered manner into the poly(*N*-isopropylacrylamide) (PNIPA) network. This network exhibits a lower critical solution temperature (LCST) behavior at 32.5 °C in water. The introduction of PEG led to unique properties, such as volume shrinkage upon heating while maintaining optical transparency, due to the effective suppression of phase separation within the network. This advancement overcomes the limitations of conventional PNIPA-based gels and expands their potential applications in optical sensors, actuators, and biomedical devices. The results highlight the promising applications of this polymer network in the development of advanced smart materials.

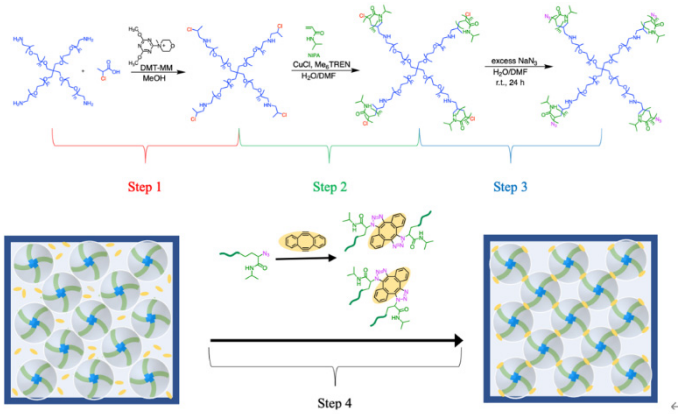

Keywords: temperature-responsive polymer gel; LCST; star-shaped block copolymer; click chemistry; optical transparency

1. Introduction

Polymer systems that exhibit a sharp change in solubility due to significant alterations in their interaction with solvents upon temperature changes have been extensively studied. In systems where the polymer does not dissolve at low temperatures but dissolves at high temperatures, the upper critical solution temperature (UCST) is observed [1,2], which intuitively correlates with the temperature-dependent solubility changes of typical substances. On the other hand, there are also systems that dissolve well at low temperatures but fail to dissolve at higher temperatures, which are classified as polymers exhibiting the lower critical solution temperature (LCST) [3,4]. Such systems are often observed in structure-forming solvents like water or ionic liquids [5].

Among polymers that exhibit LCST behavior in water, poly(*N*-isopropylacrylamide) (PNIPA), which consists of *N*-isopropylacrylamide (NIPA), has been the most studied [6]. PNIPA shows an LCST of about 32 °C in water, and its crosslinked gel, which consists of polymer chains forming a network, exhibits reversible swelling at low temperatures and contraction at high temperatures due to temperature-dependent interactions in water. This temperature responsiveness has led to extensive research into the application of PNIPA gels in sensors [7], catalysts [8], drug delivery systems [9], and actuators [10,11]. Although certain applications have shown promise, issues such as the slow rate of volume change of the gel remain a challenge, preventing widespread commercialization. Specifically, the very slow contraction rate and optical turbidity of the gel due to network phase separation prior to contraction can pose practical problems [12]. Polymer gels that undergo large volumetric changes in response to environmental stimuli can transiently enter thermodynamically unstable states under certain conditions. In such cases, the polymer chains within the network may phase-separate into aggregated and expanded domains (Figure 1). This results in the formation of refractive index fluctuations on the scale of visible wavelengths within the polymer network, leading to strong light scattering and macroscopic turbidity. Moreover, returning from the unstable state to the thermodynamically stable state can take a considerable amount of time, significantly slowing the gel's response. Such turbidity and delayed responsiveness can impair the performance or functionality of devices such as optical sensors, actuators, and biomedical systems. Therefore, it is essential to develop strategies for material design or structural control that can suppress or prevent these undesirable phenomena. To improve the contraction rate, methods such as introducing pores into the gel [13] or incorporating dangling chains that are not crosslinked at one end [14,15] have been explored. However, these methods still face the challenge of the gel losing optical transparency due to network phase separation during contraction. Therefore, if a gel can be obtained that contracts rapidly while maintaining optical transparency, it would have great potential for applications in optical sensors and other devices.

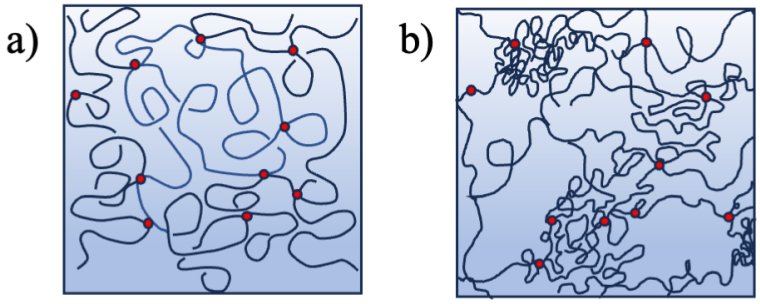

Figure 1. Conceptual diagrams showing the difference in the network structure of NIPA gel obtained from conventional free-radical polymerization, which is (**a**) fully swollen at low temperatures in water and (**b**) phase separated near the transition temperature: It segregates along regions with sparse and dense network densities, and the difference in refractive indices between these regions scatters visible light, making it appear white.

We have previously synthesized block copolymers by combining temperature-responsive PNIPA obtained through living polymerization with polymers that dissolve in water over a wide temperature range, and have explored a method of obtaining polymer networks by crosslinking their ends under appropriate conditions [16,17]. For example, after synthesizing a 4-arm star-shaped PNIPA, *N*,*N*-dimethylacrylamide (DMA), which dissolves in water over a wide temperature range, was polymerized, and the star-shaped block copolymer was crosslinked under appropriate conditions to successfully form a polymer network [18,19]. In this system, excess amounts of the crosslinking agent methylene bis-acrylamide (BIS), commonly used for gel preparation, were employed for crosslinking the star-shaped block copolymers, resulting in the formation of particles derived from BIS between the star-shaped block copolymers, as revealed by small-angle X-ray scattering (SAXS). The influence of these BIS-derived particles on the gel's properties is currently being investigated, but to accurately understand the behavior as the polymer network with an ordered structure made from the block copolymers mentioned above, it is desirable to prepare a system without the presence of BIS-derived particles. Furthermore, in order to achieve a high degree of functionality in polymer chain end-group transformations using halogenated alkyl groups, it is necessary to stabilize the halogenated chain ends during polymerization. In block copolymerization using acrylamide derivatives, it is known that the disappearance of halogenated terminal groups is significantly greater for tertiary acrylamides than for secondary acrylamides. This is due to the increase in electron density of the amide group, which results in increased alkyl substitution on the nitrogen atom, promoting the cyclization reaction of the halogenated terminal groups and leading to faster termination and the disappearance of active polymer chains. Unfortunately, polymerization using copper complexes makes it difficult to effectively activate these unstable

species, inhibiting the transformation or substitution reactions of the halogenated terminal groups. This complexity makes polymerization control difficult and hinders the desired terminal group modification. Therefore, when synthesizing block copolymers, it is preferable to choose secondary acrylamide derivatives like NIPA, as reactive halogenated alkyl groups will remain at the polymer chain ends, allowing for subsequent modification and the introduction of new polymer structures [20].

If structural challenges and synthetic inconveniences of the polymer network can be avoided, it will be possible to prepare polymer networks with a more ideally ordered structure. In this study, we used a derivative of a tetrafunctional star-shaped polymer made from polyethylene glycol (PEG), which exhibits hydrophilicity over a wide temperature range, as the initiator, and polymerized NIPA as a secondary acrylamide to synthesize a star-shaped block copolymer. Furthermore, under appropriate network formation conditions, we coupled the ends of this star-shaped block copolymer through a click reaction, introducing hydrophilic PEG into the structure of the PNIPA exhibiting LCST in an ordered manner. As a result, the obtained gel was shown to maintain optical transparency while undergoing volume reduction upon an increase in temperature.

2. Experimental Part

2.1. Materials

The 4-arm star-shaped polymer consisting of polyethylene glycol (PEG) chains, with amino groups at the ends and an average molecular weight of 2000 (4-ArmPEG-Amine), was purchased from Funakoshi (Manufacturer: Biopharma PEG Scientific, Watertown, MA, USA). 2-Chloropropionic Acid, 4-(4,6-Dimethoxy-1,3,5-triazin-2-yl)-4-methylmorpholinium Chloride (DMT-MM), Lithium bromide (LiBr), 5,6,11,12-Tetradehydrodibenzo[a,e]cyclooctene (DIBOD), and dibenzocyclooctyne-amine (DBCO-Amine) were purchased from Tokyo Chemical Industry Co., Ltd., Tokyo, Japan. Methanol (MeOH), chloroform, *N*,*N*-dimethylformamide (DMF), tetrahydrofuran (THF), acetonitrile, hydrochloric acid (HCl), copper(I) chloride (CuCl), and sodium azide (NaN_3) were purchased from Kishida Chemical Co., Ltd., Osaka, Japan. DMF used as a synthetic solvent was purified by vacuum distillation. CuCl was dissolved in concentrated hydrochloric acid, and the resulting solution was dropped into water. The precipitate was purified by suction filtration and drying. *N*-isopropylacrylamide (NIPA) was obtained from KJ Chemicals, Tokyo, Japan and tris(2-dimethylaminoethyl)amine (Me_6TREN) was provided by Mitsubishi Chemical, Tokyo, Japan. Both were purified by recrystallization and vacuum distillation. Ultrapure water was obtained by purifying tap water using a Direct-Q system (Merck) (resistivity 18.2 MΩ·cm). Ion-exchange water was obtained using a G-5C cartridge-type water purifier purchased from Organo, Chiba, Japan. Pentaerythritoltetra(2-chloropropionate) (PETCP) was synthesized on request by Tokyo Chemical Industry Co., Ltd., Tokyo, Japan.

2.2. Synthesis of Initiator from 4-ArmPEG-Amine

An amide condensation reaction using DMT-MM was employed to synthesize a 4-arm initiator containing PEG chains. 0.48 g of 4-ArmPEG-Amine, 145 μL of 2-Chloropropionic Acid, 0.93 g of DMT-MM, and 90 mL of MeOH were added to a 300 mL round-bottom flask, which was wrapped with aluminum foil to shield it from light. The synthetic scheme is shown in Figure 2, Step 1. The mixture was stirred at room temperature for 24 h. After stirring, the solvent was removed using a rotary evaporator. The crude product was purified by silica gel column chromatography ($CHCl_3$/MeOH = 2:3), yielding a viscous liquid (192.5 mg, 41% yield). The resulting sample was dissolved in $CDCl_3$ and analyzed by ^{1}H NMR.

2.3. Synthesis of End-Cl 4-Arm PEG-b-PNIPA

The 4-arm initiator containing PEG chains obtained in Section 2.2 was used to synthesize end-Cl 4-arm star-shaped PEG-b-PNIPA by living radical polymerization of NIPA. First, 1.84 g of NIPA and 192.5 mg of the 4-arm initiator were placed in a 200 mL round-bottom flask, and 5.61 mL of DMF was added under a nitrogen atmosphere in a glove box. The flask was sealed with a septum, removed from the glove box, and 3.44 mL of ultra-pure water, previously purged with nitrogen, was added using a syringe. Next, nitrogen bubbling was performed for more than 30 min at room temperature to prepare the monomer solution. Then, 29.3 mg of CuCl was placed in a 100 mL round-bottom flask, and 79.2 μL of Me_6TREN was added under nitrogen in a glove box. The solution was immersed in an ice water bath (4 °C) and stirred for 1 h to decompose the copper catalyst. The prepared monomer solution was then added via syringe (10.29 mL) under nitrogen flow, and the reaction was stirred at 4 °C for 120 min. The final monomer concentration in the reaction solution was 1.2 mol L^{-1}, and the volume ratio of DMF to water was 1:1, with a molar ratio of CuCl:Me_6TREN:NIPA:initiator = 4:4:200:1. The synthetic scheme is shown

in Figure 2, Step 2. During the polymerization, a small sample of the reaction solution was withdrawn using a syringe, and the polymerization was stopped by continuously blowing air for approximately 1 min. The sample was analyzed by ^{1}H NMR and SEC to monitor the progress of the reaction. The sample was dissolved in acetone-d_6 for ^{1}H NMR analysis. The remaining polymerization solution was diluted with THF and purified using a silica gel column to remove the copper catalyst. After catalyst removal, the solution was concentrated using a rotary evaporator. Dialysis was performed using a Spectra/Por6® Dialysis Membrane (MWCO: 1000) for 2 days in methanol, followed by 3 days in ion-exchange water. After dialysis, the product was lyophilized using a freeze dryer (FDU-1200, TOKYO RIKAKIKAI CO., LTD., Tokyo, Japan) to obtain a white solid. The final sample was dissolved in SEC elution solvent, filtered through a Millex-LCR 13 mm membrane filter (pore size 0.45 μm), and analyzed by SEC. The sample was also dissolved in acetone-d_6 for ^{1}H NMR analysis.

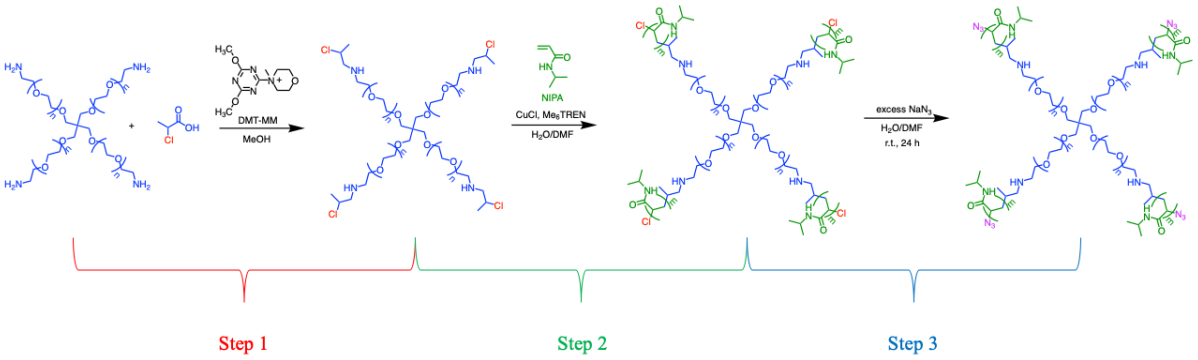

Figure 2. Synthesis of 4-ArmPEG-PNIPA with azide group at the end, Step 1: Synthesis of 4-arm initiator containing PEG, Step 2: Synthesis of end-Cl 4-arm star-shaped PEG-b-PNIPA, Step 1: Terminal azidation of tetrabranched PEG-b-PNIPA.

2.4. Synthesis of End-N_3 4-Arm Star-Shaped PEG-b-PNIPA

Referring to previously reported procedures, a 4-arm star-shaped PEG-b-PNIPA with an azide group at the end was synthesized [16–18]. The polymerization of NIPA was carried out using the same method as in 2.3, and after 80 min, 0.29 g of NaN_3 dissolved in 1.55 mL of ultrapure water was added to the reaction solution (1.03 mL). The mixture was stirred at room temperature for 24 h. The synthetic scheme is shown in Figure 2, Step 3. The reaction solution was diluted with THF, and the copper catalyst was removed by silica gel column chromatography. Dialysis was performed using a Spectra/Por 6® Dialysis Membrane (MWCO: 1000) for 2 days in methanol, followed by 3 days in ion-exchange water. After dialysis, the product was lyophilized to obtain a white solid. The final sample was analyzed by ^{1}H NMR (acetone-d_6) and infrared spectroscopy.

2.5. Azidation Reaction Efficiency of End-N_3 4-Arm Star-Shaped PEG-b-PNIPA

The azide content of the end-N_3 4-arm star-shaped PEG-b-PNIPA synthesized in 2.4 was quantified. 97.5 mg (5.0×10^{-3} mmol) of the end-N_3 4-arm star-shaped PEG-b-PNIPA was placed in a 10 mL round-bottom flask with a magnetic stirrer. Anhydrous acetonitrile (1.5 mL) and 3.6 mg of DBCO-amine were added in a nitrogen atmosphere and stirred at room temperature for 24 h. Dialysis was performed using a Spectra/Por 6® Dialysis Membrane (MWCO: 1000) for 1 day in methanol, followed by 2 days in ion-exchange water. After dialysis, the product was lyophilized to obtain a white solid. The final sample was analyzed by ^{1}H NMR (acetone-d_6) and infrared spectroscopy.

2.6. Synthesis of End-N_3 4-Arm Star-Shaped PNIPA

For comparison, end-N_3 4-arm star-shaped PNIPA was synthesized from PNIPA only, following a previously reported procedure [17]. PETCP was used as the initiator for the 4-arm structure.

2.7. Preparation of PEG-b-PNIPA Gel via End-to-End Huisgen Cycloaddition of End-N_3 4-Arm Star-Shaped PEG-b-PNIPA

To prepare a gel from end-N_3 4-arm star-shaped PEG-b-PNIPA, the conditions for achieving a semi-dilute state of the polymer in a good solvent were investigated by dynamic light scattering (DLS) measurements (described later). End-N_3 4-arm star-shaped PEG-b-PNIPA was dissolved in acetonitrile to prepare solutions with

volume fractions Φ = 0.08, 0.12, and 0.16. The mixture was treated with ultrasonic waves for 30 min and allowed to stand overnight. DIBOD, in a stoichiometric amount (2 equivalents to end-N_3 4-arm star-shaped PEG-b-PNIPA), was then added, and the mixture was stirred for about 1 min until fully dissolved. It was then left at room temperature for at least 3 days to form the gel. A similar method was used to prepare the PNIPA gel from end-N_3 4-arm star-shaped PNIPA.

2.8. Proton Nuclear Magnetic Resonance (^{1}H NMR) Measurement

Measurements were performed using a 400 MHz NMR (JEOL, Akishima City, Japan). Acetone-d_6 (Kanto Chemical, Tokyo, Japan) and chloroform-d1 (Kanto Chemical), each containing 0.03% (*v/v*) TMS as the internal standard, were used as solvents. The number of scans was set to 16.

2.9. Size Exclusion Chromatography (SEC) Measurement

2.9.1. For PEG-b-PNIPA Systems

SEC measurements were performed using an ultraviolet detector (UV-41, Shodex, Kyoto, Japan) and a differential refractive index detector (RI-101, Shodex, Kyoto, Japan). The columns used were DS-4 (Shodex) and THF solvent columns KF-803L and KF-804L (Shodex) connected in sequence. The UV detector was set to a measurement wavelength of 254 nm. Molecular weight and molecular weight distribution were calculated from the calibration curve prepared using polystyrene standards.

2.9.2. For PNIPA Systems

The measurements were conducted using a SHIMADZU LC-20AD pump, SIL-20AHT autosampler, RID-10A differential refractive index detector, and CTO-20A temperature controller. The columns used were Shodex KW-G 6B (guard column), KW-804 (two columns), and KW-802.5 (two columns) connected in sequence. LiBr was dissolved in DMF at a concentration of 5 mmol L^{-1} and stirred overnight, and the resulting solution was used as the eluent. The system was stabilized for approximately 3 h under the measurement conditions, with a flow rate of 1.0 mL/min and an oven temperature of 40 °C. The molecular weight and molecular weight distribution were calculated based on a calibration curve created from measurements of polymethyl methacrylate standards.

2.10. Infrared Absorption Spectroscopy (IR) Measurement

The measurements were conducted using a Fourier-transform infrared spectrometer, NICOLET iS50 (Thermo Scientific, Waltham, MA, USA). The scan was performed 32 times with a data interval of 0.482 cm^{-1}, and the analysis was done using OMNIC software (Spectra Version 2.2). The measurements were carried out using the KBr pellet method, where approximately 1 mg of the sample and 100 mg of KBr were finely ground in an agate mortar, placed in a pellet mold, and pressed using a small hydraulic press (Specac, Orpington, UK).

2.11. UV-Vis Transmittance Measurement

End-Cl 4-arm star-shaped PNIPA and end-Cl, N_3 4-arm star-shaped PEG-b-PNIPA were dissolved in ultrapure water to prepare 1 wt% sample solutions. The sample solutions were placed in a 1 cm path length quartz glass cell and maintained at 20 °C in a water-cooled Peltier unit. The temperature was increased from 20 °C to 50 °C, and the transmittance changes were observed (heating rate of 0.5 °C/min, observation wavelength of 500 nm). Data were collected at intervals of 0.2 °C.

2.12. Dynamic Light Scattering (DLS) Measurement

The DLS measurements were conducted using a Zetasizer Nano ZS from Malvern, Malvern, UK (He-Ne ser, beam wavelength 633 nm). The measurements were performed at a scattering angle of 173° and at 25 °C, with 12 measurements over a 10 s period.

2.12.1. DLS Measurement of End-N_3 4-Arm Star-Shaped PEG-b-PNIPA in Various Solvents

End-N_3 4-arm star-shaped PEG-b-PNIPA was dissolved at 1 wt% in 1.5 mL of MeOH, DMF, THF, and acetonitrile to prepare four different solutions. After ultrasonic treatment for 30 min, the solutions were left to stand overnight. Each polymer solution was filtered through a 0.45 μm membrane filter (Millex-LCR 13 mm), and

1–1.5 mL was injected into the measurement cell. DLS measurements were performed, and the scattering intensity was measured 12 times.

2.12.2. DLS Measurement of End-N_3 4-Arm Star-Shaped PEG-b-PNIPA

Various amounts of end-N_3 4-arm star-shaped PEG-b-PNIPA were weighed and dissolved in 1.5 mL of acetonitrile to prepare solutions with volume fractions $\Phi = 1.6 \times 10^{-3}$ to 0.200. After 30 min of ultrasonic treatment, the solutions were left to stand overnight. The obtained polymer solutions were filtered through a membrane filter (Millex-LCR 13 mm, pore size 0.45 μm), and 1–1.5 mL was injected into the measurement cell. DLS measurements were conducted, and the scattering intensity of each solution was measured 12 times. Additionally, for end-N_3 4-arm star-shaped PNIPA, solutions of varying concentrations were prepared using the same method, and the scattering intensity was evaluated through DLS measurements.

2.13. Small-Angle X-ray Scattering (SAXS) Measurement

SAXS measurements were conducted to analyze the network structure of PEG-b-PNIPA gels at the BL05XU beamline in SPring-8 (Hyogo, Japan). The prepared gels, swollen in either water or acetonitrile, were irradiated with X-rays of 0.1 nm wavelength. The scattered X-rays were detected using a PILATUS3S 1M detector (DECTRIS Ltd., Baden, Switzerland) positioned at a sample-to-detector distance of 3.9 m.

2.14. Gel Swelling Degree Test

2.14.1. Equilibrium Swelling Degree in Water and Acetonitrile

PEG-b-PNIPA gels synthesized at three different concentrations (Φ = 0.08, 0.12, 0.16) were prepared inside capillaries with an inner diameter of 1.1 mm. The gels were soaked in MeOH for several days to remove unreacted substances, then equilibrated in acetonitrile and pure water. The gel diameter, D, was measured using a digital microscope (VHX-X1, Keyence, Osaka, Japan), and the swelling degree was calculated using the following formula:

$$\text{Swelling Degree} = D/D_0 \quad (1)$$

, where D_0 is the initial diameter of 1.1 mm, and D is the diameter after solvent exchange.

2.14.2. Temperature Dependence of Equilibrium Swelling Degree

PNIPA gel (initial concentration Φ = 0.1) and PEG-b-PNIPA gel (initial concentration Φ = 0.08) were synthesized as cylindrical gels inside capillaries with an inner diameter of 1.1 mm. After soaking the gels in MeOH for several days and further soaking them in pure water for several days, they were immersed in ultrapure water in a jacketed beaker connected to a circulation temperature control unit (Lauda RE104). The temperature was gradually increased from 20 °C, and the appearance and diameter of the equilibrated gels were observed using a digital microscope (VHX-X1) approximately every day. The diameter was measured three times, and the average value was used.

3. Results and Discussion

3.1. Synthesis of Initiator

The ^{1}H NMR measurement results of the obtained product are shown in Figure S1. The integral ratios of each peak were found to be a:b:c:d = 3:1:1:52, confirming the successful synthesis of the target initiator.

3.2. Synthesis of End-Cl 4-Arm Star-Shaped PEG-b-PNIPA

To monitor the progress of the reaction, ^{1}H NMR spectra were measured for samples taken at various time points, and the conversion from monomer to polymer was calculated. The proton signal for the vinyl group of NIPA (2H, 6.2 ppm) and the aldehyde proton of the solvent DMF (1H, 8.0 ppm) were observed at distinct positions. As the reaction proceeded, the intensity of the signal from the vinyl proton of NIPA decreased (Figure S2). The integral ratio of the peak from the vinyl proton of NIPA (I_{NIPAt}) was determined with the aldehyde proton signal of DMF as the reference. Similarly, the integral ratio of the vinyl proton of NIPA in the monomer solution was calculated as I_{NIPA0}. The monomer conversion rate for each reaction time was calculated using the following equation:

$$\text{conversion}(\%) = \left(1 - \frac{I_{NIPAt}}{I_{NIPA0}}\right) \times 100 \quad (2)$$

The monomer conversion rates as a function of reaction time are shown in Figure 3a. The conversion rate exceeded 90% after 10 min and reached 99% after 120 min, indicating that the reaction was very fast and efficient.

Next, SEC results and the molecular weight and molecular weight distribution relative to the reaction rate are shown in Figure 3b,c. A narrow molecular weight distribution and polymers with molecular weights corresponding to the input ratio were obtained.

Furthermore, the obtained sample was dissolved in acetone-d_6, and ^{1}H NMR measurements were performed. The results are shown in Figure 3d. A signal (g) from the methine proton adjacent to the end-Cl of the 4-arm star-shaped PEG-b-PNIPA was observed around 4.8 ppm.

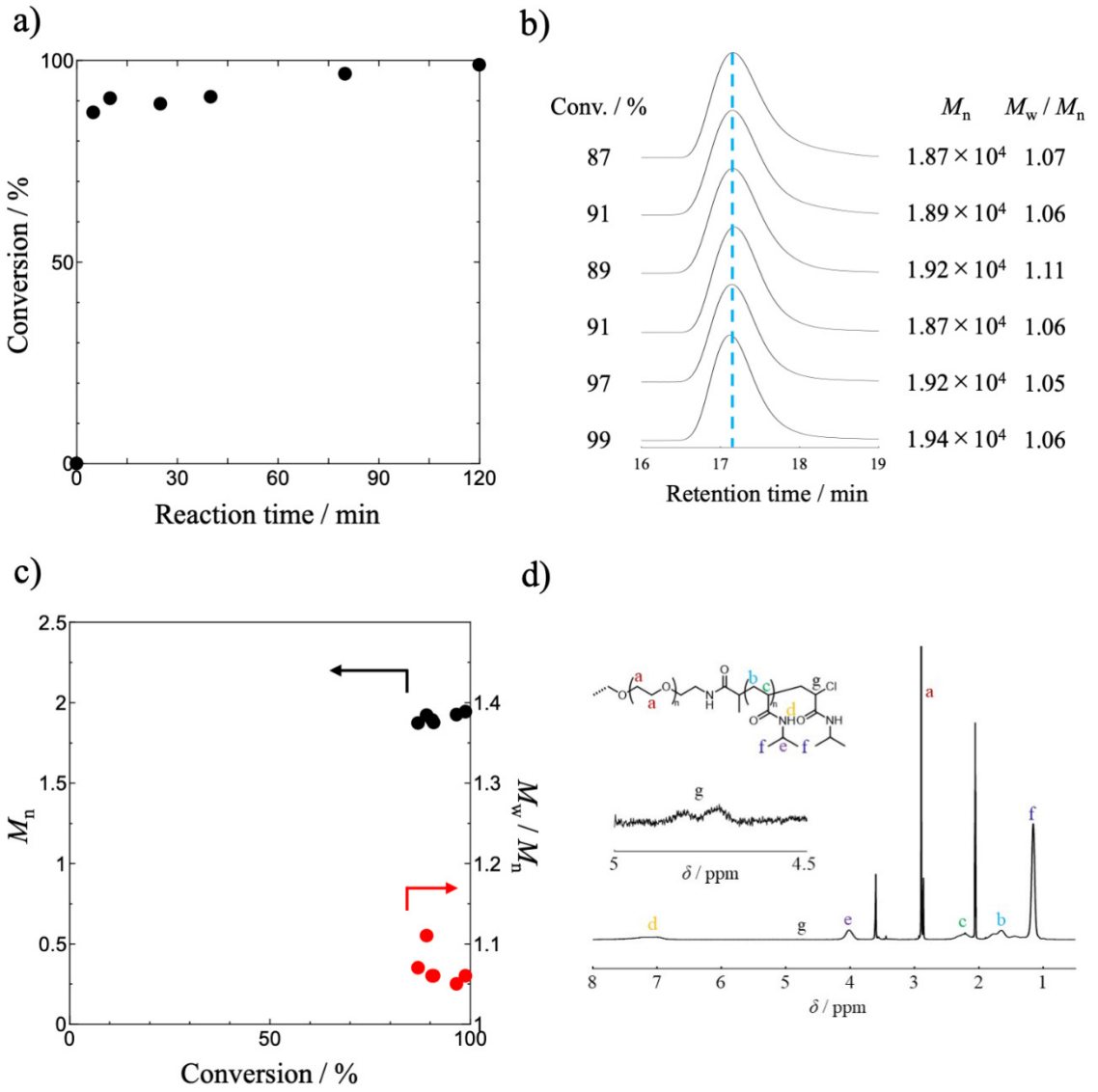

Figure 3. (**a**) Monomer conversion with polymerization time during SET-LRP of NIPA measured by ^{1}H NMR, (**b**) Evolution of SEC traces with polymerization time during SET-LRP of NIPA, (**c**) Number average molecular weight, M_n, and polydispersity index (M_w/M_n) vs. conversion plots, (**d**) ^{1}H NMR spectrum of end-Cl 4-arm star-shaped PEG-b-PNIPA.

3.3. Synthesis of End-N_3 4-Arm Star-Shaped PEG-b-PNIPA

The ^{1}H NMR measurement results for end-N_3 4-arm star-shaped PEG-b-PNIPA are shown in Figure 4a. The signal (g) from the methine proton adjacent to the end-Cl, observed in end-Cl 4-arm star-shaped PEG-b-PNIPA, was confirmed to have disappeared. However, the expected signal (h) from the methine proton adjacent to the end-N_3 was not observed in the ^{1}H NMR spectrum.

The FT-IR measurement results of end-Cl 4-arm star-shaped PEG-b-PNIPA and end-N_3 4-arm star-shaped PEG-b-PNIPA are shown in Figure 4b. After azidation, a peak at 2110 cm^{-1} was observed, which was not present before the azidation [17]. This peak, characteristic of the stretching vibration of the end-N_3 group, confirmed that azidation had occurred. From these results, it was confirmed that the end-Cl was successfully replaced with N_3 using this experimental method.

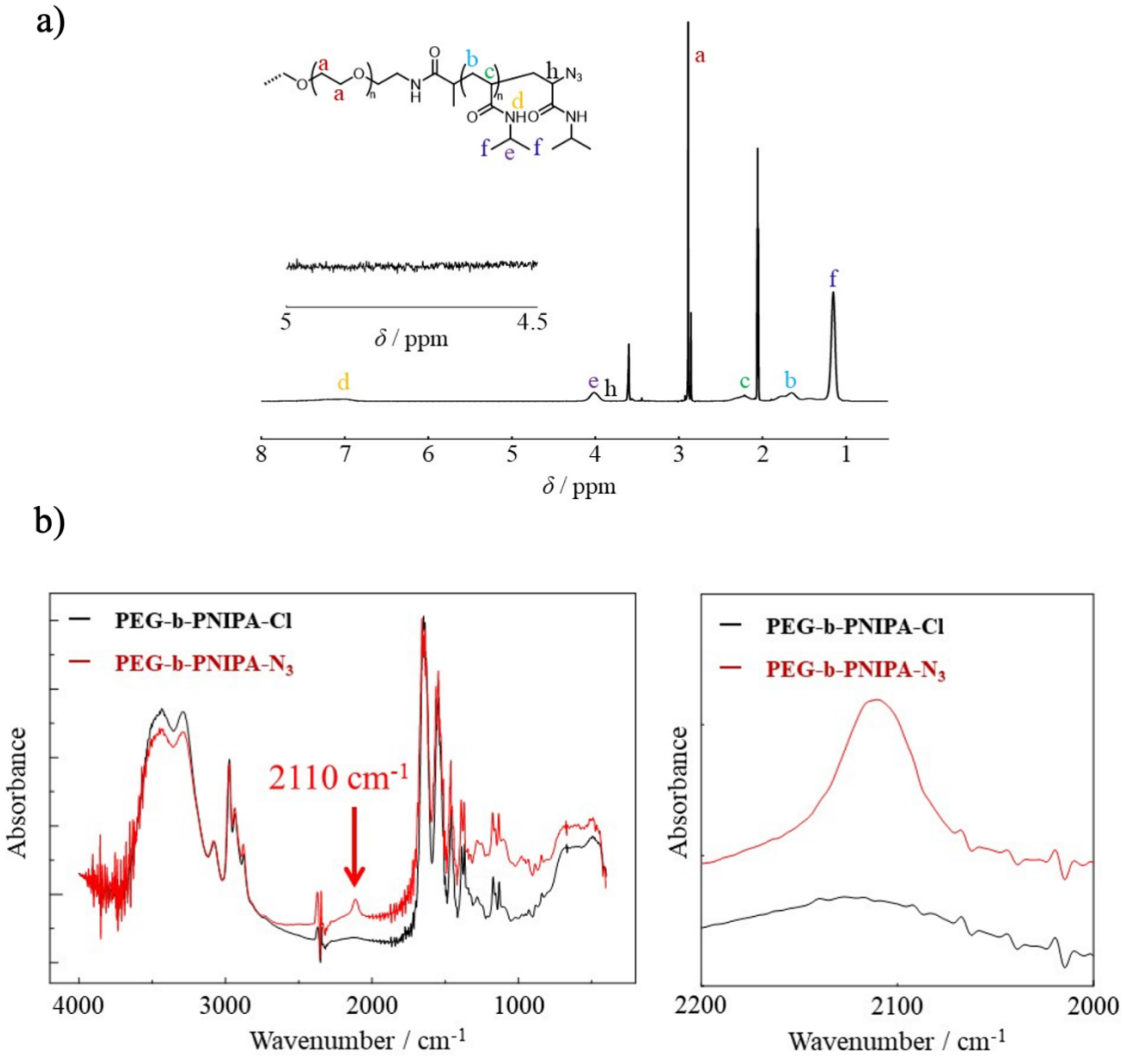

Figure 4. (**a**) ^{1}H NMR spectrum of end-N_3 4-arm star-shaped PEG-b-PNIPA, (**b**) FT-IR spectra obtained for 4-arm star-shaped PEG-b-PNIPA (black) before azidation (red) after azidaton.

3.4. Azidation Reaction Rate of End-N_3 4-Arm Star-Shaped PEG-b-PNIPA

The terminal azidation rate could not be directly evaluated from the results in Section 3.3. Therefore, DBCO-amine was introduced into the azidated end-4-arm star-shaped PEG-b-PNIPA through a click reaction, and the azidation reaction rate was determined by measuring the ^{1}H NMR of the resulting product. The results of ^{1}H NMR measurements and FT-IR are shown in Figure 5. A peak (g) corresponding to the proton of the benzene ring in DBCO-amine was observed between 7–8 ppm (Figure 5a). Thus, the ^{1}H NMR spectra before and after the click reaction, focusing on the 4–8 ppm range, are shown in Figure 5b,c. Before the click reaction, the integral ratio of peaks d and e in the PNIPA repeat unit was 1.0453:1. After the click reaction, the integral ratio of d and e, along with the peak g from the benzene ring of DBCO, was 1.1907:1. These results yield a g:e ratio of 0.1454, or e/g = 6.88. Since one arm of the 4-arm star-shaped polymer was synthesized to be 50 units long, the theoretical value for e/g is 6.25. Therefore, it was confirmed that more than 91% of the terminal azide groups were introduced. Furthermore, in FT-IR, it was confirmed that the peak from the terminal N_3 group disappeared after the reaction with DBCO-amine (Figure 5d).

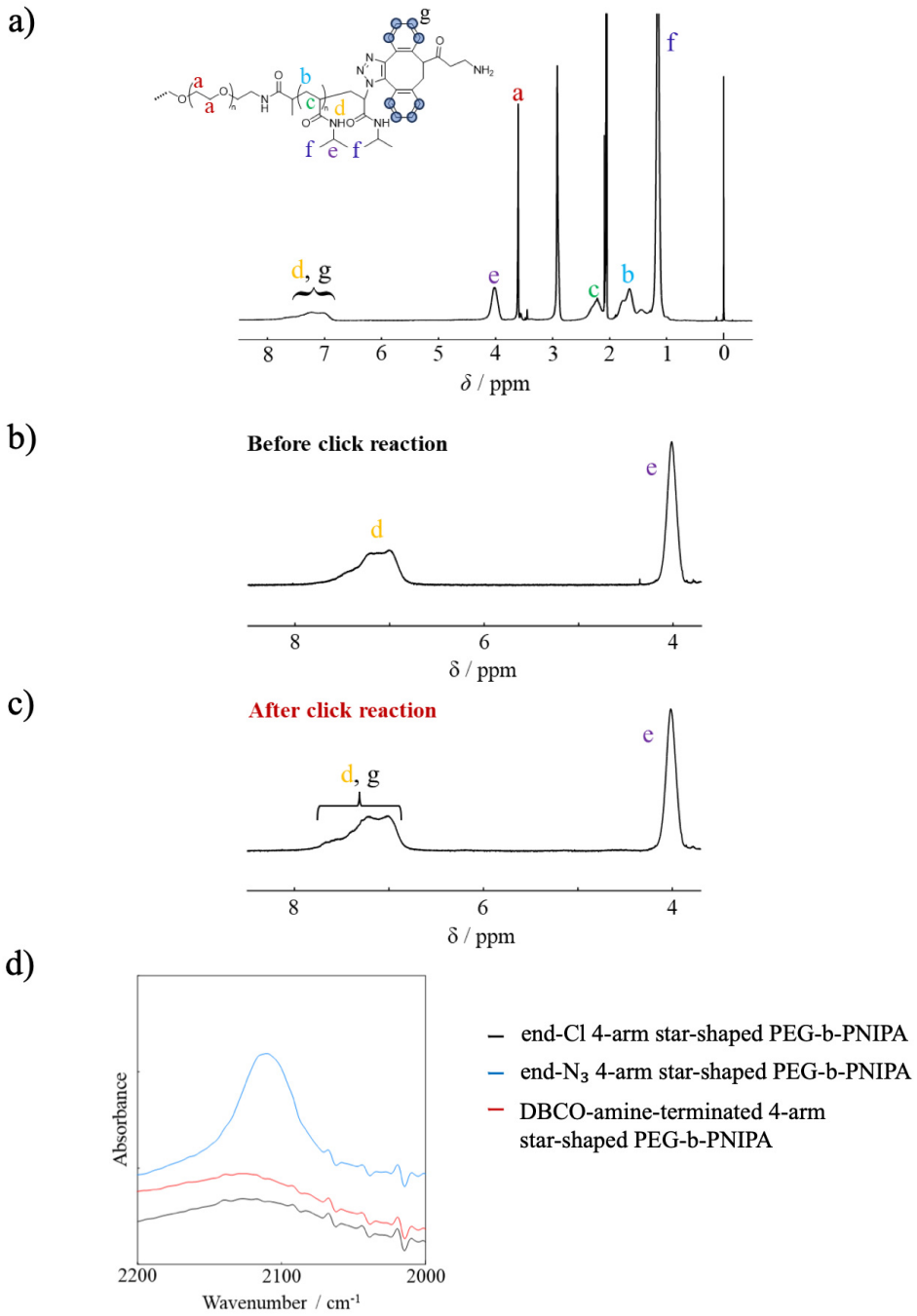

Figure 5. (**a**) ^{1}H NMR spectra of DBCO-amine-terminated 4-arm star-shaped PEG-b-PNIPA, (**b**) ^{1}H NMR of end-N_3 4-arm star-shaped PEG-b-PNIPA before reaction with DBCO-amine, (**c**) ^{1}H NMR of end-N_3 4-arm star-shaped PEG-b-PNIPA after reaction with DBCO-amine, (**d**) FT-IR spectra obtained for end-Cl 4-arm star-shaped PEG-b-PNIPA (black), end-N_3 4-arm star-shaped PEG-b-PNIPA (blue), DBCO-amine-terminated 4-arm star-shaped PEG-b-PNIPA (red).

3.5. UV-Vis Transmittance Measurement

Figure 6 shows the UV-Vis transmittance of aqueous solutions of terminal Cl 4-arm star-shaped PNIPA and terminal Cl, N_3 4-arm star-shaped PEG-b-PNIPA as a function of temperature. All polymers formed colorless and transparent solutions at low temperatures, and underwent phase separation above a certain temperature, resulting in turbid solutions. The temperatures at which the solutions of each polymer became turbid, determined from the transmittance data, are summarized in Table 1. The temperature at which the solution becomes turbid (transition temperature)—defined as the temperature where the transmittance drops below 99%—correlates with the LCST. The star-shaped polymer consisting solely of PNIPA with terminal Cl groups and without PEG segments turned turbid at 33.5 °C. This behavior is nearly identical to that of conventional linear PNIPA. In contrast, the PEG-b-PNIPA bearing Cl terminal groups and incorporating PEG segments became turbid at 37.0 °C, which is 3.5 °C

higher. This shift is attributed to the increased hydrophilicity of the polymer due to the presence of the hydrophilic PEG chains. These results also suggest that the nature of the terminal groups affects LCST behavior.

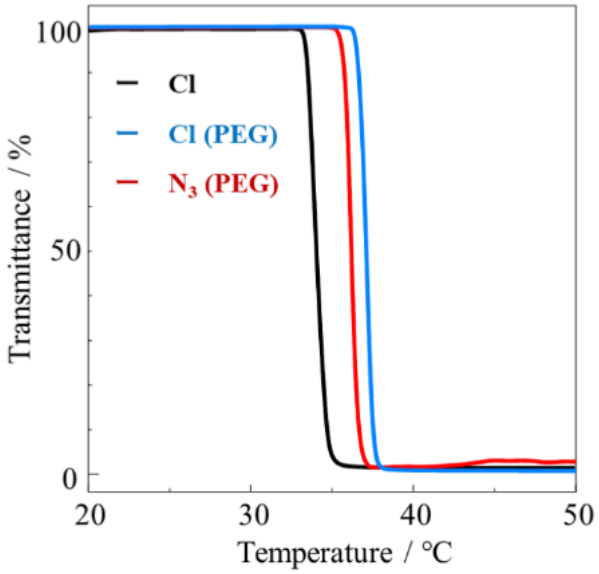

Figure 6. Dependence of transmittance on temperature of end-Cl 4-arm star-shaped PNIPA, end-Cl 4-arm star-shaped PEG-b-PNIPA, and end-N_3 4-arm star-shaped PEG-b-PNIPA in pure water.

Table 1. Transition temperature of tetra branched PNIPA and PEG-b-PNIPA.

Termination	Transition Temperature/°C
CI	33.5
CI (PEG)	37.0
N3 (PEG)	36.0

3.6. DLS Measurement of End-N_3 4-Arm Star-Shaped PEG-b-PNIPA

In order to synthesize a gel with an ordered network structure, it is essential to use a solvent with high affinity for the polymer, as well as to densely pack the polymer chains in the solution and fill the space uniformly. Therefore, we first selected an appropriate good solvent for end-N_3 4-arm star-shaped PEG-b-PNIPA. The DLS results of 1 wt% N_3 4-arm star-shaped PEG-b-PNIPA solutions dissolved in various solvents (Figure S3) were compared, and acetonitrile was selected as it showed the best dispersion properties.

Next, different volume fractions of end-N_3 4-arm star-shaped PEG-b-PNIPA were dissolved in acetonitrile, and the scattering intensity was measured to estimate the overlap volume fraction of the polymer. Since the autocorrelation functions of all polymer solutions prepared in this study exhibited sigmoid behavior, it was confirmed that no significant aggregation of the polymer occurred in these solutions (Figure S4).

The volume of the polymer in the solution (V_p) can be calculated using its molar concentration (c) with the following equation:

$$V_p = \frac{cV_sM_w}{d} \tag{3}$$

Here, V_s is the volume of the solvent (acetonitrile), M_w is the molecular weight of the polymer (the molecular weight of the end-N_3 4-arm star-shaped PEG-b-PNIPA is M_w = 2.0 × 10^4 g mol^{-1}), and d is the density of the polymer (1.34 × 10^3 g L^{-1}). Therefore, the volume fraction (Φ) of the polymer chain can be calculated using the following equation:

$$\Phi = \frac{V_p}{V_s+V_p} = \frac{\frac{cM_w}{d}}{1+\frac{cM_w}{d}} \tag{4}$$

The results of plotting the scattering intensity against the volume fraction (Φ = 1.6 × 10^{-3}~0.200) for acetonitrile solutions of end-N_3 4-arm star-shaped PEG-b-PNIPA at different concentrations, obtained by DLS measurement, are shown in Figure 7. The scattering intensity values used were corrected by subtracting the effect of the attenuator in the DLS apparatus. The region deviating from the theoretical scaling laws for dilute solutions

in a good solvent ($I \sim \Phi^1$) and semi-dilute solutions ($I \sim \Phi^{-1/4}$) was defined as the overlap region, which corresponds to the transition from the dilute region to the semi-dilute region of the polymer [21,22]. The boundary between the overlap region and the semi-dilute region, $\Phi = 0.05$, was defined as the overlap volume fraction (c^*).

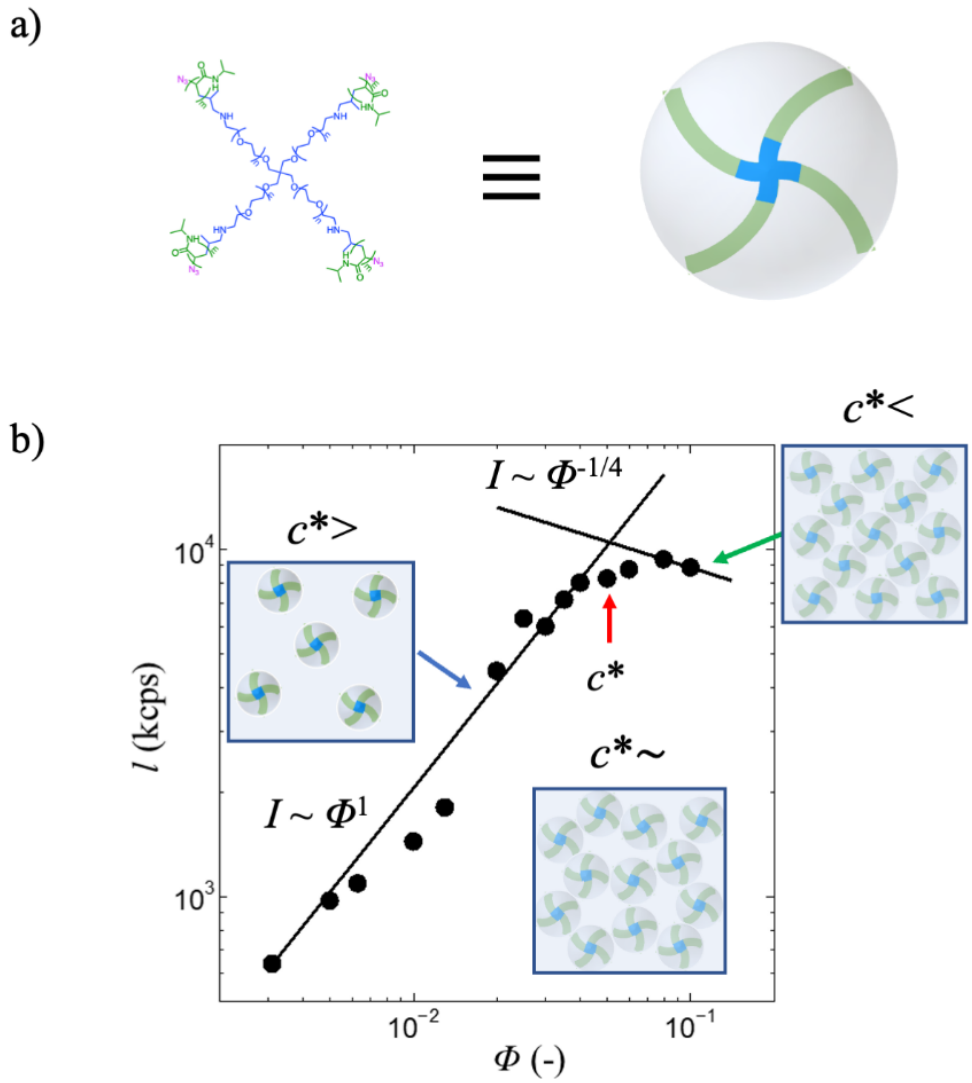

Figure 7. (**a**) Schematic of end-N_3 4-arm star-shaped PEG-b-PNIPA, (**b**) Scattering intensity (I) of end-N_3 4-arm star-shaped PEG-b-PNIPA in acetonitrile for various polymer volume fractions.

Similarly, the value of c^* for end-N_3 4-arm star-shaped PNIPA was estimated using the same method. The molecular weight of end-N_3 4-arm star-shaped PNIPA is $M_w = 2.9 \times 10^4$ g mol^{-1}, and the polymer density is 1.4×10^3 g L^{-1}. From the results shown in Figure S5, $\Phi = 0.07$ was taken as the volume fraction of c^*.

3.7. Preparation of Gel via Huisgen Cycloaddition Reaction of End-N_3 4-Arm Star-Shaped PEG-b-PNIPA or End-N_3 4-Arm Star-Shaped PNIPA

The end-N_3 4-arm star-shaped PEG-b-PNIPA acetonitrile solution, prepared at a semi-dilute concentration, was mixed with an appropriate amount of crosslinking agent (Figure 8a) and left at room temperature for 3 days. The right diagram in Figure 8a illustrates a polymer network with an ideal ordered structure, formed by the end-to-end crosslinking of four-arm star block copolymers with reactive termini, where each terminal group is connected to a different four-arm star block copolymer. The gelation process is shown in Figure 8b. In all four conditions with volume fractions $\Phi = 0.08$, 0.095, 0.12, and 0.16, the click reaction shown in Figure 8c proceeded, and the gel was formed. For comparison, the PNIPA gel was prepared at a volume fraction $\Phi = 0.1$ ($1.4c^*$).

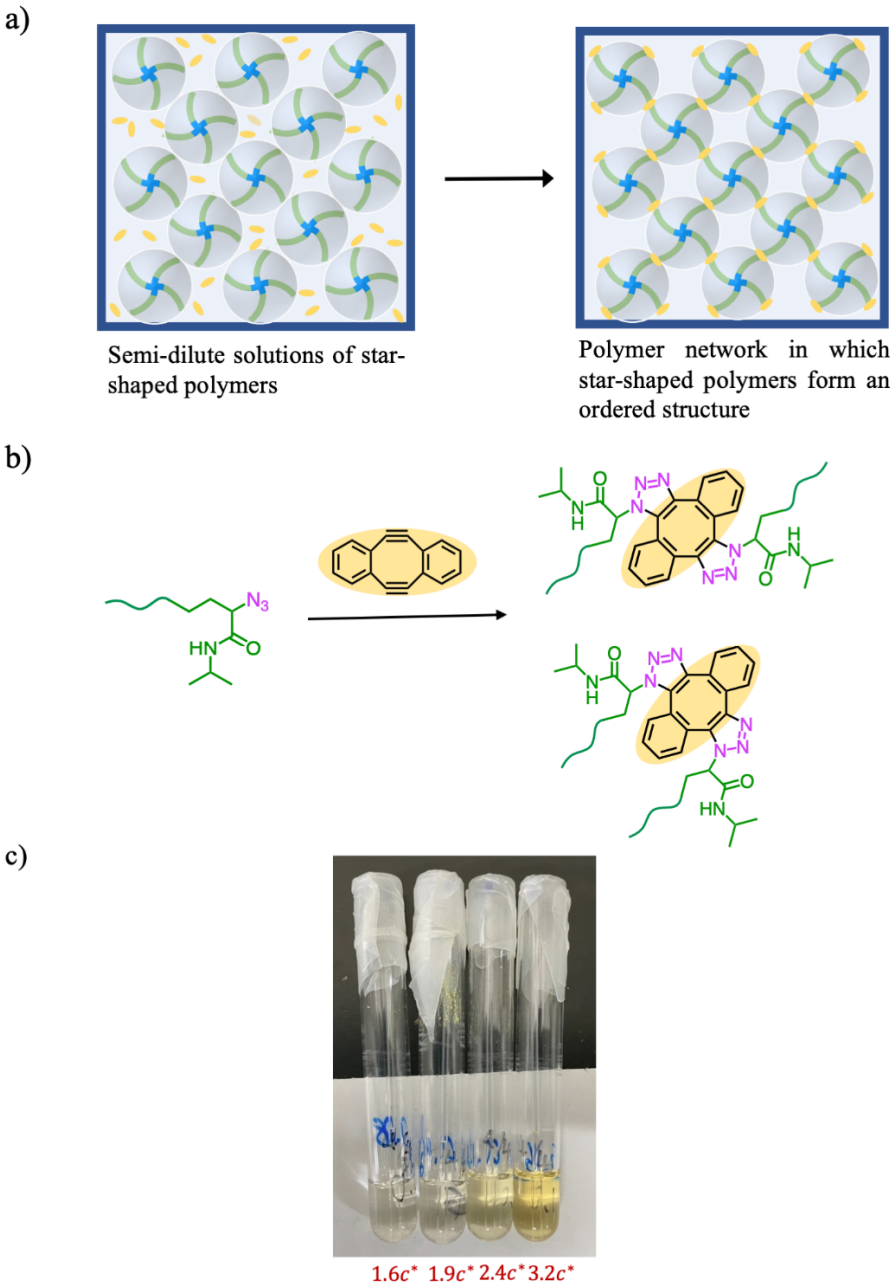

Figure 8. (**a**) Schematic of click reaction crosslinking of end-N_3 4-arm star-shaped PEG-b-PNIPA under semi-dilute conditions, (**b**) Cross-linking of end-N_3 4-arm star-shaped PEG-b-PNIPA by click reaction, (**c**) Photo of PEG-b-PNIPA gels.

3.8. Analysis of the Network Structure by SAXS

The polymer network structure of the PEG-b-PNIPA gels was analyzed using SAXS. Figure 9a shows the SAXS profiles of PEG-b-PNIPA gels with different prepared volume fractions, Φ = 0.08, 0.12, and 0.16, in pure water and acetonitrile. All the profiles are well described by the following equation [18,23,24]:

$$I(q) = \frac{I_{OZ}(0)}{1+\xi_{OZ}^2 q^2} + Cq^{-d} + I_{BKG} \quad (5)$$

The first term is the Ornstein-Zernike (OZ) function with the correlation length ξ_{OZ}. The second term, Cq^{-d}, accounts for the upturn in the low-q region, where C is a constant and d is the power-law exponent. I_{BKG} represents the q-independent background. The solid lines in Figure 9a show the fitting results using Equation (5).

The increase in intensity at low-q may indicate a two-phase structure that has a sharp interface, consistent with Porod's law ($\propto q^{-4}$). However, for the Φ = 0.08 in both water and acetonitrile, this contribution is negligible. At higher volume fractions (Φ = 0.12 and 0.16), the power law exponent d ranges from 2.3 to 3.4, suggesting the presence of a fractal structure. The low-q upturn may be therefore attributed to aggregated formation.

Figure 9b shows the Φ-dependence of ξ_{OZ}. At all volume fractions, ξ_{OZ} is larger in water than in acetonitrile, reflecting the higher degree of swelling in water. In both solvents, ξ_{OZ} decreases with increasing Φ, indicating that gels with higher prepared volume fractions possess more densely crosslinked networks.

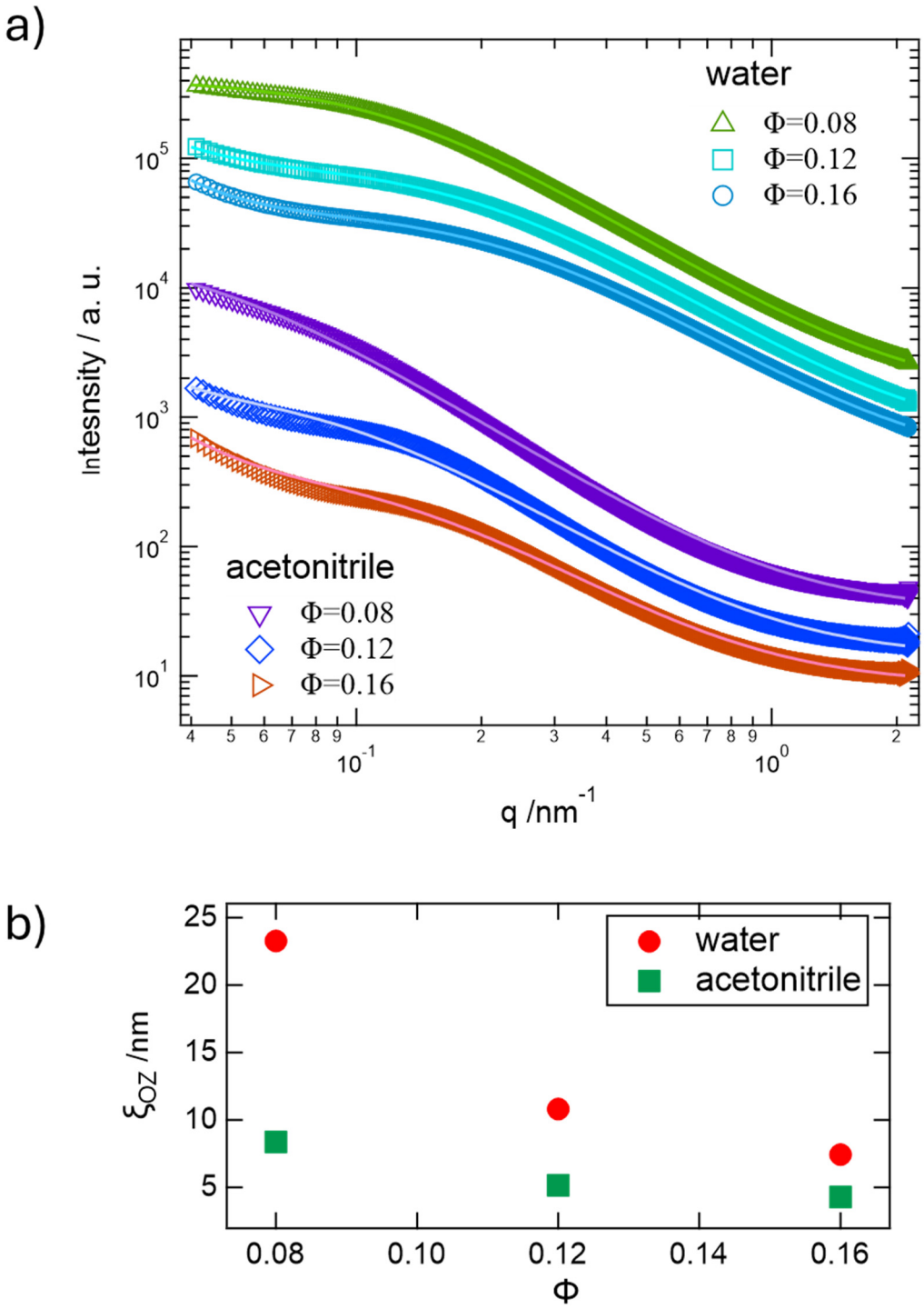

Figure 9. (**a**) SAXS profiles of PEG-b-PNIPAM gels with different prepared volume fractions, Φ = 0.08, 0.12, and 0.16, in pure water and acetonitrile. (**b**) Φ-dependence of the correlation length ξ_{OZ}.

3.9. Equilibrium Swelling Degree Measurement

3.9.1. Measurement and Comparison of Transition Temperature

The equilibrium swelling degree of the PNIPA gel (prepared at Φ = 0.1) and PEG-b-PNIPA gel (prepared at Φ = 0.08) was measured during the heating process from 20 °C to 60 °C, and the swelling curves are shown in

Figure 10. From the derivative curve of these results, the temperature where the absolute value of the slope is maximum was defined as the transition temperature.

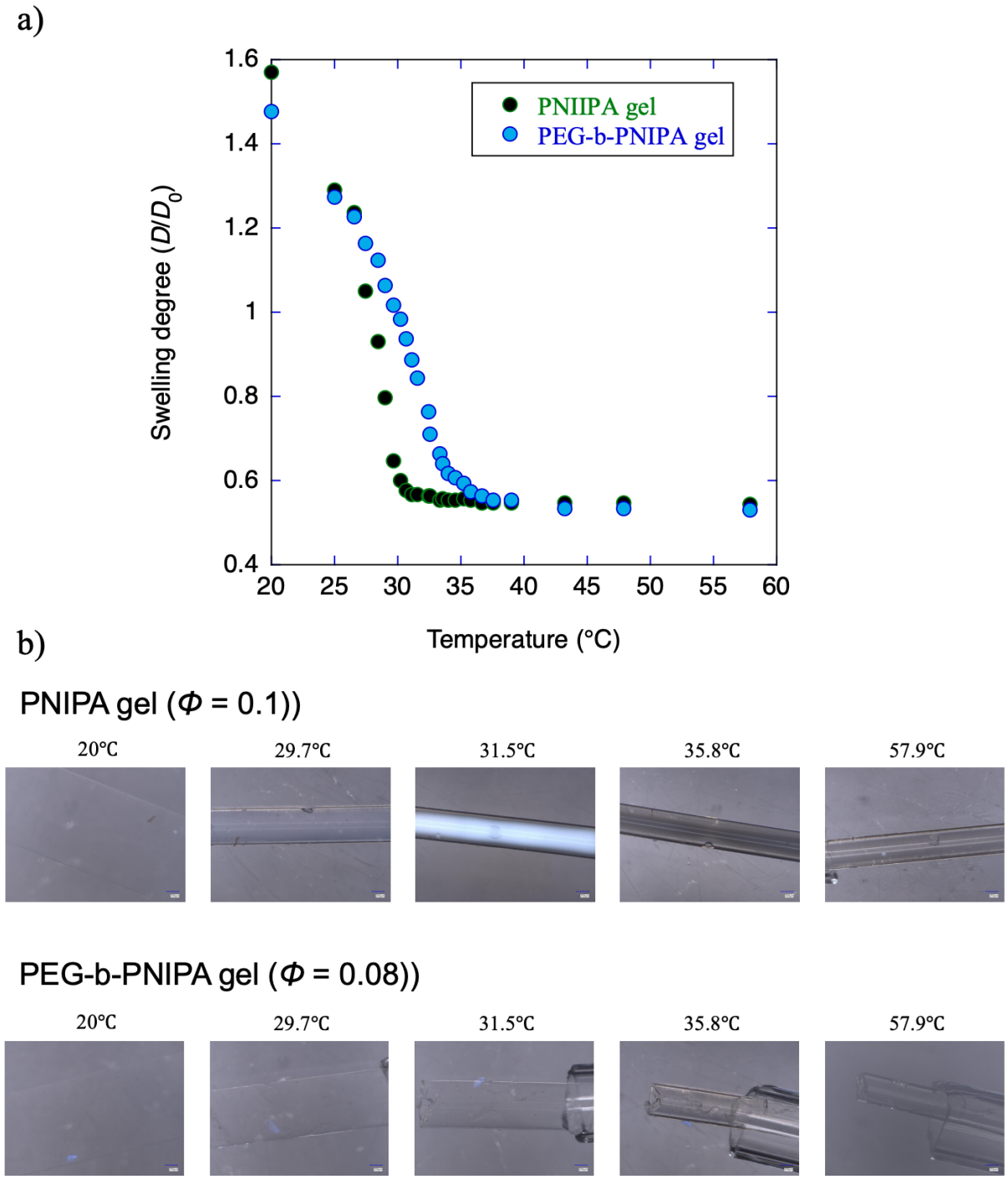

Figure 10. (**a**) Swelling curves of PNIPA gel and PEG-b-PNIPA gel, (**b**) Microscopic photographs of PNIPA gel and PEG-b-PNIPA gel observed when set at a certain temperature.

For the PNIPA gel, the transition temperature was 27 °C. Generally, the transition temperature of PNIPA gels prepared by free radical polymerization with crosslinkers like BIS is around 32.0 °C. Comparing the 4-arm star-shaped PNIPA gel crosslinked with DIBOD and the conventional PNIPA gel, a decrease of about 5 °C was observed. This decrease can be attributed to the fact that DIBOD is a hydrophobic compound with large aromatic rings. The introduction of DIBOD likely altered the hydrophilic/hydrophobic balance of the network, shifting the transition temperature to a lower temperature.

On the other hand, the PEG-b-PNIPA gel showed a transition temperature of 32.5 °C. Compared to the 4-arm star-shaped PNIPA gel, the transition temperature was 5.5 °C higher. This difference is attributed to the presence of the hydrophilic PEG. In the PEG-b-PNIPA gel, the introduction of PEG increased the overall

hydrophilicity of the network, causing the transition temperature to shift to a higher temperature. This result reflects the LCST observed in the solution, as shown in Figure 6 and Table 1.

3.9.2. Optical Changes of the Gel Near the Transition Temperature

Significant differences were observed in the state changes of the gel during the temperature increase near the transition temperature.

In the PNIPA gel, as the temperature increased, the entire gel contracted and became cloudy (Figure 10b). This behavior is similar to that observed in conventional PNIPA gels prepared by free radical polymerization, where an unstable phase is formed upon heating, and phase separation occurs within the gel. The polymer network density becomes heterogeneous, forming regions of low and high density. When the size of these regions becomes comparable to the wavelength of light, light scattering occurs, causing cloudiness. In such a state, it takes a long time to reach thermodynamic equilibrium, and the optically cloudy state tends to persist [25].

In contrast, the PEG-b-PNIPA gel maintained its transparency during the temperature rise near the transition temperature, with no cloudiness observed. This is because the hydrophilic PEG is uniformly distributed within the network, suppressing phase separation due to the temperature-responsive behavior of PNIPA and its interaction with the solvent. As a result, even though volume shrinkage occurred due to temperature changes, the gel retained its transparency and quickly reached the equilibrium state. In other words, with these properties, the shrinkage behavior of the gel can be explained by the cooperative diffusion equation, and the decrease in shrinkage rate due to phase separation, as observed in conventional PNIPA gels, will no longer occur.

4. Conclusions

In this study, a temperature-responsive polymer network was successfully synthesized by using a 4-arm star-shaped polyethylene glycol (PEG) derivative as an initiator to polymerize *N*-isopropylacrylamide (NIPA) as the secondary acrylamide. The resulting star-shaped block copolymer served as a key building block for the construction of the polymer network.

Through detailed analysis of the polymerization process, it was confirmed that the 4-arm star-shaped PEG-b-PNIPA structure was synthesized under high control. The structure was clearly verified by SEC and ^{1}H NMR measurements. Furthermore, the terminal group conversion efficiency using click chemistry was evaluated, and over 91% azidation was confirmed by ^{1}H NMR and FT-IR spectroscopy. SAXS measurements indicate that the PEG-b-PNIPA gels have a more densely cross-linked networks. Additionally, UV-Vis transmittance measurements showed that the introduction of PEG increased the LCST of the gel, enhancing its hydrophilicity and transparency.

The obtained gel exhibited unique characteristics of volume shrinkage while maintaining optical transparency upon heating. This behavior is thought to result from the effective suppression of phase separation during the shrinkage process due to the regular introduction of PEG within the polymer network. The maintenance of transparency during shrinkage overcomes the main limitation of conventional PNIPA-based gels and expands the applicability to optical sensors, actuators, and biomedical devices.

These results suggest the promising potential of this polymer network design for the development of advanced smart materials. Future research will focus on optimizing the mechanical properties of the gel and exploring its potential applications in stimulus-responsive devices. By precisely adjusting the polymer composition and crosslinking strategy, the development of next-generation materials with suitable responsiveness and durability for practical environments is aimed for.

Supplementary Materials: The following supporting information can be downloaded at: https://media.sciltp.com/articles/others/2507101000153971/MI-957-SI.pdf, Figure S1: ^{1}H NMR spectrum of initiator prepared from 4-Arm PEG-Amine; Figure S2: Time change of ^{1}H NMR spectra of the reaction solution for preparation of end-Cl 4-arm star-shaped PEG-b-PNIPA; Figure S3: Correlation coefficient of end-N_3 4-arm star-shaped PEG-b-PNIPA in various solvents (MeOH, DMF, THF, acetonitrile); Figure S4: Correlation coefficients observed from solutions of end-N_3 4-arm star-shaped PEG-b-PNIPA dissolved in various concentrations of acetonitrile; Figure S5: Scattering intensity (I) of end-N_3 4-arm star-shaped PEG-b-PNIPA in Acetonitrile for various polymer volume fractions.

Author Contributions: K.K.: Performed all experiments. Writing the original draft, conducting investigations, and generating graphs. T.H.: Performed SAXS measurements. Writing the original draft, conducting investigations, and generating graphs. Y.T.: Managing the project, acquiring funding, supervising, writing the original draft, reviewing, revising, and editing. All authors have read and agreed to the published version of the manuscript.

Funding: This work is supported by Toshiaki Ogasawara Memorial Foundation.

Data Availability Statement: Raw data will be made available upon reasonable request.

Acknowledgments: *N*-isopropylacrylamide (NIPA) was kindly obtained from KJ Chemicals. Tris(2-dimethylaminoethyl)amine (Me_6TREN) was provided by Mitsubishi Chemical.

Conflicts of Interest: The authors declare no conflict of interest.

References

1. Seuring, J.; Agarwal, S. Polymers with Upper Critical Solution Temperature in Aqueous Solution: Unexpected Properties from Known Building Blocks. *ACS Macro Lett.* **2013**, *2*, 597–600. https://doi.org/10.1021/mz400227y.
2. Zhang, Q.L.; Hoogenboom, R. Polymers with upper critical solution temperature behavior in alcohol/water solvent mixtures. *Prog. Polym. Sci.* **2015**, *48*, 122–142. https://doi.org/10.1016/j.progpolymsci.2015.02.003.
3. Cook, M.T.; Haddow, P.; Kirton, S.B.; McAuley, W.J. Polymers Exhibiting Lower Critical Solution Temperatures as a Route to Thermoreversible Gelators for Healthcare. *Adv. Funct. Mater.* **2021**, *31*, 2008123. https://doi.org/10.1002/adfm.202008123.
4. Zhang, X.; Zhang, P.P.; Lu, M.; Qi, D.M.; Müller-Buschbaum, P.; Zhong, Q. Synergistic Stain Removal Achieved by Controlling the Fractions of Light and Thermo Responsive Components in the Dual-Responsive Copolymer Immobilized on Cotton Fabrics by Cross-Linker. *ACS Appl. Mater. Interfaces* **2021**, *13*, 27372–27381. https://doi.org/10.1021/acsami.1c03290.
5. Ueki, T.; Watanabe, M. Polymers in Ionic Liquids: Dawn of Neoteric Solvents and Innovative Materials. *Bull. Chem. Soc. Jpn.* **2012**, *85*, 33–50. https://doi.org/10.1246/bcsj.20110225.
6. Das, A.; Babu, A.; Chakraborty, S.; Van Guyse, J.F.R.; Hoogenboom, R.; Maji, S. Poly(-isopropylacrylamide) and Its Copolymers: A Review on Recent Advances in the Areas of Sensing and Biosensing. *Adv. Funct. Mater.* **2024**, *34*, 2402432. https://doi.org/10.1002/adfm.202402432.
7. Jiang, L.; Qin, D.N.; Zhang, C.F.; Cui, J.B.; Xu, X.Y.; Hu, R.; Zhang, P.; Hu, L. Poly(-isopropylacrylamide) Microgel-Based Sensor for Clinical-Level X-ray Dose Measurements. *ACS Appl. Polym. Mater.* **2023**, *5*, 10073–10080. https://doi.org/10.1021/acsapm.3c01924.
8. Bergbreiter, D.E.; Case, B.L.; Liu, Y.S.; Caraway, J.W. Poly(N-isopropylacrylamide) soluble polymer supports in catalysis and synthesis. *Macromolecules* **1998**, *31*, 6053–6062. https://doi.org/10.1021/ma980836a.
9. Liu, M.; Song, X.; Wen, Y.T.; Zhu, J.L.; Li, J. Injectable Thermoresponsive Hydrogel Formed by Alginate—Poly(-isopropylacrylamide) That Releases Doxorubicin-Encapsulated Micelles as a Smart Drug Delivery System. *ACS Appl. Mater. Interfaces* **2017**, *9*, 35673–35682. https://doi.org/10.1021/acsami.7b12849.
10. Kim, T.H.; Choi, J.G.; Byun, J.Y.; Jang, Y.; Kim, S.M.; Spinks, G.M.; Kim, S.J. Biomimetic Thermal-sensitive Multi-transform Actuator. *Sci. Rep.* **2019**, *9*, 7905. https://doi.org/10.1038/s41598-019-44394-x.
11. Maeda, S.; Hara, Y.; Sakai, T.; Yoshida, R.; Hashimoto, S. Self-walking gel. *Adv. Mater.* **2007**, *19*, 3480–3484. https://doi.org/10.1002/adma.200700625.
12. Shibayama, M. Physics of polymer gels: Toyoichi Tanaka and after. *Soft Matter.* **2025**, *21*, 1995–2009. https://doi.org/10.1039/d4sm01418a.
13. Takeoka, Y.; Watanabe, M. Polymer gels that memorize structures of mesoscopically sized templates. Dynamic and optical nature of periodic ordered mesoporous chemical gels. *Langmuir* **2002**, *18*, 5977–5980. https://doi.org/10.1021/la020133t.
14. Yoshida, R.; Uchida, K.; Kaneko, Y.; Sakai, K.; Kikuchi, A.; Sakurai, Y.; Okano, T. Comb-Type Grafted Hydrogels with Rapid De-Swelling Response to Temperature-Changes. *Nature* **1995**, *374*, 240–242. https://doi.org/10.1038/374240a0.
15. Yasumoto, A.; Gotoh, H.; Gotoh, Y.; Bin Imran, A.; Hara, M.; Seki, T.; Sakai, Y.; Ito, K.; Takeoka, Y. Highly Responsive Hydrogel Prepared Using Poly(N-isopropylacrylamide)-Grafted Polyrotaxane as a Building Block Designed by Reversible Deactivation Radical Polymerization and Click Chemistry. *Macromolecules* **2017**, *50*, 364–374. https://doi.org/10.1021/acs.macromol.6b01955.
16. Jochi, Y.; Seki, T.; Soejima, T.; Satoh, K.; Kamigaito, M.; Takeoka, Y. Spontaneous synthesis of a homogeneous thermoresponsive polymer network composed of polymers with a narrow molecular weight distribution. *NPG Asia Mater.* **2018**, *10*, 840–848. https://doi.org/10.1038/s41427-018-0074-x.
17. Okaya, Y.; Jochi, Y.; Seki, T.; Satoh, K.; Kamigaito, M.; Hoshino, T.; Nakatani, T.; Fujinami, S.; Takata, M.; Takeoka, Y. Precise Synthesis of a Homogeneous Thermoresponsive Polymer Network Composed of Four-Branched Star Polymers with a Narrow Molecular Weight Distribution. *Macromolecules* **2020**, *53*, 374–386. https://doi.org/10.1021/acs.macromol.9b01616.
18. Kwon, D.; Jochi, Y.; Okaya, Y.; Seki, T.; Satoh, K.; Kamigaito, M.; Hoshino, T.; Urayama, K.; Takeoka, Y. Nonturbid Fast Temperature-Responsive Hydrogels with Homogeneous Three-Dimensional Networks by Two Types of Star Polymer Synthesis Methods. *Macromolecules* **2021**, *54*, 5750–5764. https://doi.org/10.1021/acs.macromol.1c00446.
19. Hiei, Y.; Ohshima, I.; Hara, M.; Seki, T.; Hoshino, T.; Takeoka, Y. Shrinking rates of polymer gels composed of star-shaped polymers of N-isopropylacrylamide and dimethylacrylamide copolymers: the effect of dimethylacrylamide on the

crosslinking network. *Soft Matter.* **2022**, *18*, 5204–5217. https://doi.org/10.1039/d2sm00402j.

20. Gao, G.H.; Hara, M.; Seki, T.; Takeoka, Y. Synthesis of thermo-responsive polymer gels composed of star-shaped block copolymers by copper-catalyzed living radical polymerization and click reaction. *Sci. Technol. Adv. Mater.* **2024**, *25*, 2302795. https://doi.org/10.1080/14686996.2024.2302795.
21. Rubinstein, M.; Colby, R.H. *Polymer Physics*; Oxford University Press: Oxford, UK, 2003.
22. Li, X.; Nakagawa, S.; Tsuji, Y.; Watanabe, N.; Shibayama, M. Polymer gel with a flexible and highly ordered three-dimensional network synthesized via bond percolation. *Sci. Adv.* **2019**, *5*, eaax8647. https://doi.org/10.1126/sciadv.aax8647.
23. Shibayama, M. Spatial inhomogeneity and dynamic fluctuations of polymer gels. *Macromol. Chem. Phys.* **1998**, *199*, 1–30.
24. Matsunaga, T.; Sakai, T.; Akagi, Y.; Chung, U.; Shibayama, M. Structure Characterization of Tetra-PEG Gel by Small-Angle Neutron Scattering. *Macromolecules* **2009**, *42*, 1344–1351. https://doi.org/10.1021/ma802280n.
25. Tanaka, T.; Ishiwata, S.; Ishimoto, C. Critical Behavior of Density Fluctuations in Gels. *Phys. Rev. Lett.* **1977**, *38*, 771–774. https://doi.org/10.1103/PhysRevLett.38.771.

Article

Heterojunction Engineering of All-Inorganic $CsPbI_3$ Perovskite for High-Responsivity SWIR Photodetectors Performed at Room Temperature

Sydney Schmidt [1,†], Haley Fisher [1,†], Xia Li [1], Jesse B. Brown [1], Yuqin Qian [1], Van Malmquist [1], Avetik Harutyunyan [2], Gugang Chen [2,*], and Yi Rao [1,*]

[1] Department of Chemistry and Biochemistry, Utah State University, Logan, UT 84322, USA
[2] Honda Research Institute, USA Inc., San Jose, CA 95134, USA
* Correspondence: gchen@honda-ri.com (G.C.); yi.rao@usu.edu (Y.R.)
† These authors contributed equally to this work.
Received: 20 April 2025; Revised: 10 July 2025; Accepted: 12 July 2025; Published: 30 July 2025

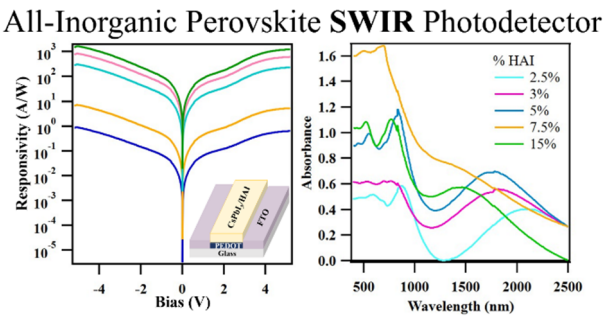

Abstract: Short-wave infrared (SWIR) light, 0.9–2.5 μm wavelengths, has widespread applications, including inspection processes, nighttime imaging, and machine vision. As such, there is increasing demand for practical and effective SWIR detectors. Many current SWIR photodetectors are based on high-cost materials and require cryogenic cooling. Perovskite materials, including $CsPbI_3$, have been effectively used as photodetectors in the UV to near IR ranges, but their large bandgaps limit their use for lower energy SWIR light. In this report we introduce an all-inorganic perovskite photodetector based on $CsPbI_3$ with heterojunction engineering for efficient and practical detection in the SWIR range at room temperature. The devices undergo a simple, solution-based fabrication process which includes spin-coating under ambient conditions and moderate annealing temperatures. Without additional cooling, the SWIR devices produce excellent results at room temperature with responsivity of 1.65×10^3 A W^{-1} and a specific detectivity of 8.0×10^{10} Jones under 0.28 mW cm^{-2} of 1310 nm light and bias of −5 V. This material shows not only high response but also high sensitivity, making it stand out in the field of SWIR photodetection with the additional benefits of low-cost production and room temperature operation.

Keywords: perovskite; short-wave IR photodetectors; Hetero-junction

1. Introduction

Short-wave infrared (SWIR) light, 0.9–2.5 μm wavelengths, has become important in many applications, such as remote sensing, communications, spectroscopy, security, and hyperspectral imaging processes [1–5]. In the communications sector, utilization of SWIR wavelengths enables free-space optical communication systems and optical wireless communications where radio frequencies are congested [6]. SWIR imaging is able to penetrate harsh weather conditions like fog better than visible light, providing usefulness in automotive applications [1,7]. Furthermore, SWIR sensors can reliably distinguish between components in the recycling process of lithium-ion batteries, increasing recycling efficiency and decreasing waste [8]. Sensors for this wavelength range have also been applied in very-high resolution satellite imaging, making possible large-scale vegetation mapping for conservation and forest management [9]. Additionally, machine vision in the SWIR is important in military applications for the identification of camouflaged materials and even the detection of landmines and chemical warfare agents [2,10]. As such, practical, affordable, and sensitive SWIR photodetectors are needed.

Current state-of-the art SWIR photodetectors are made from mixed-alloy semiconductors such InGaAs, due to their favorable sensitivities in the range of 10^3 A W^{-1} at 1550 nm with specific detectivity on the order of 10^{12} Jones [1,11–13]. However, such materials are economically and energetically expensive, often operating under

cryogenic conditions to achieve optimum results, warranting the search for new SWIR detection materials [5]. An emerging candidate for SWIR applications is colloidal quantum dot detectors, due to their tunable spectral properties, solution-processability, silicon-compatible fabrication, and low cost [10,13–15]. Lead-based quantum dots (PbS and PbSe QDs) are one of the most promising materials, having solution-processibility, being low-cost to produce, and possessing tunable bandgaps within the infrared [16]. In 2021, Kwon, et al. fabricated a solution-processed SWIR detector based on PbS QDs using conductive polymer [17]. The material had an absorption maximum at 1410 nm and achieved an ultra-high responsivity of 6 kA W^{-1} [15]. Chen et al. used a layer-by-layer spray technique to form a well-rounded PbS QD photodetector with a responsivity over 360 A W^{-1} under 1250 nm light, also yielding a detectivity on the scale of 10^{12} Jones [18]. Yet, these materials have quantum efficiency and charge transport that are low compared to epitaxial InGaAs, HgCdTe, or InSb detectors [14,15,19]. On the other hand, graphene-based technologies possess many attractive qualities as SWIR detectors [10,13–15]. Due its near-zero bandgap, graphene exhibits broadband absorption into the far infrared with fast response and high carrier mobility [1,20–22] However, graphene has very low light absorption of about 2.3% which limits its responsivity to the mA W^{-1} scale [1,13,20]. Recently, another promising candidate has emerged in the field of SWIR detection: perovskites materials [23–26]. Known for having good optoelectronic properties and simple synthesis, these materials are finding expanded applications in photodetection [23,27–30].

Perovskites are designer materials which have received enormous attention in recent years in fields spanning from catalysis to solar cells with unprecedented performance [23,31,32]. These materials take the general form ABX_3, where A is a cation such as methylammonium, B is a transition metal such as lead, and X is a halogen anion; all together it possess the same type of crystal structure as $CaTiO_3$ [23]. Perovskite photodetectors (PPDs) exhibit notable characteristics including a tunable bandgap, high carrier mobility, and solution-based coating processes which make them appealing for commercialization [28,33]. Organic-inorganic PDDs, notably methylammonium lead triiodide ($MAPbI_3$) PDDs have repeatedly shown useful response in the UV to near-IR (about 300–800 nm) regions but with highly variable responsivity, specific detectivity, and external quantum efficiency (EQE) [28,34,35]. However, the wide bandgap of these perovskite materials limits their performance in longer wavelengths, such as SWIR [28,36]. Additionally, organic-inorganic hybrid PPDs suffer from instability in oxygen and moisture, making broader application difficult [28]. Recent research from our group introduced a hydrazinium-doped methylammonium lead iodide perovskite, $[(MAI)_{1-x}(HAI)_x]_2[PbI_2]$, a mixed halide perovskite as a powerful SWIR-absorbing material, whose peak absorption was tunable based on the proportion of MAI to HAI [26]. The PPD made using this material demonstrated a broad detection range, responsivity of over 10^2 A W^{-1} at 1310 nm, good specific detectivity and high external quantum efficiency: all at ambient temperature and pressure. While this novel material showed superior stability over pure $MAPbI_3$, its relative photocurrent decreased to about 20% of its original value after 8 months [26].

Research into the application of more stable all-inorganic perovskites as photodetectors is an active field. All-inorganic lead halide perovskites offer superior stability by replacing the MA group with Cs [37]. Cs-based inorganic PDDs have shown high temperature tolerance, even maintaining 70% visible photodetection ability under 373 K heat after 9 h, showing promise for real-world use. However, this photodetector was essentially blind to wavelengths greater than 430 nm [38]. In 2021, Pintor Monroy et al. published an all-inorganic, all-evaporated $CsPbI_3$ photodetector with NiO and TiO_2 for broad-band use within the visible range. They formed a fast-responding mixed-phase $CsPbI_3$ to obtain a desirable bandgap of 1.7 eV with responsivity of 0.4 A W^{-1}, detectivity of over 10^{12} Jones, and EQE greater than 70% [39]. $CsPbBr_3$, having a bandgap of 2.3 eV, is another popular inorganic perovskite for photodetection. For example, Liu et al. fabricated a self-powered, evaporated $CsPbBr_3$ PPD without charge transport layers with the simple configuration ITO/$CsPbBr_3$/Ag [40]. The stability of this device was outstanding, along with responsivity 0.05 A W^{-1} and specific detectivity near10^{10} Jones for visible detection. Nevertheless, modifications to the perovskite must be made to decrease the bandgap and expand their usefulness to the SWIR regime.

To overcome the shortcomings of an all-inorganic $CsPbI_3$ PPD, we present here a unique preparation process by introducing hydrazinium iodide ($[NH_2NH_3^+\ I^-]$, HAI) stabilized by hydriodic acid (HI) for photodetection in the SWIR range based on the heterojunction approach of our recent organic-inorganic PPD []. With its facile synthesis and ambient-condition coating process, we developed an effective SWIR photodetector. The device achieved remarkably high responsivity and external quantum efficiency measured at room temperature.

2. Experimental Methods

2.1. Preparation of SWIR Materials

For the SWIR material, PbI_2 (Sigma Aldrich, St. Louis, MO, USA, 99.995%), CsI (Alfa Aesar, Ward Hill, MA, USA, 99.9%), HAI (synthesized in-house) [26], DMF (Sigma Aldrich, St. Louis, MO, USA, anhydrous 99.8%), DMSO (Sigma Alrich, St. Louis, MO, USA, anhydrous ≥99.9%), GBL (Aldrich, St. Louis, MO, USA, ≥99%), and HI (Alfa Aesar, Ward Hill, MA, USA, 57% *w/w* aqueous solution stabilized with 1.5% hypophosphorus acid) were used. The solution was prepared in a 2:1 of CsI/HAI and PbI_2 ratio using CsI/HAI with 15% HAI, and PbI_2. The solvent used was a mixture of DMF, DMSO, and GBL. The solution was heated while stirring for 60–120 min producing a bright yellow solution. HI was added to the vial 3–10 min before coating and returned to heat. As a result, the sample solution color deepened to a rust red. After heating the substrates to 180–200 °C, 150 µL of the rust red $CsPbI_3$ sample solution was deposited and spin coated for 30–60 s.

2.2. Fabrication of SWIR Devices

50 µm FTO-striped glass substrates were cleaned using Piranha solution (3:1 of H_2SO_4 and H_2O_2) before rinsing thoroughly and being stored in ethanol. Substrates were dried under an air stream and cleaned in an Ossila UV-ozone cleaner. Meanwhile, PEDOT:PSS (Heraeus) solution was sonicated for at least 30 min. 150 µL of PEDOT:PSS was deposited onto the substrate and spin-coated for 20–45 s. The substrates were then annealed at 145 °C under vacuum, then cooled to room temperature. After heating the substrates to 180–200 °C, the rust red $CsPbI_3$ sample solution was deposited on the PEDOT-coated device and spin coated for 30–60 s which resulted in a black coating. The device was then annealed at 100–130 °C for 20–50 min under vacuum which cooled to a pale-yellow color. This process is depicted in Figure S1.

2.3. Testing of SWIR Devices Performance

The fabricated devices were prepared for testing by scraping off excess sample from the surface, leaving a stripe of perovskite over all active cells of the substrate. The testing was performed under ambient conditions in the dark inside a dehumidified shielding box to decrease environmental effects or disturbances. The light source was a 1310 nm laser (LPSC-1310-FC, Thorlabs, Newton, NJ, USA) with a 7.1×10^{-2} cm^2 spot size and a Keithley 2401 source meter provided bias to the system and recorded current outputs. The laser output power was measured at 40.0 mW and regulated by an ND filter to desired levels. The light intensity was measured with a Newport 1916-R Optical Power Meter (Newport, Irvine, CA, USA).

2.4. Characterization of SWIR Materials and Devices

Mott Schottky measurements were performed using a Gamry Instruments potentiostat from −1 V to 1 V with an AC voltage of 10 mV and frequency of 100 Hz. Electrochemical impedance spectroscopy (EIS) was performed from 10 kHz to 2 Hz using an AC voltage of 10 mV. Transient absorption (TA) spectroscopy was performed following the procedure of Han et al. (2020) [41]. Fluorescence lifetime measurements were performing using a 515 nm light source by doubling a fundamental light from a Carbide laser (Light Conversion, Vilnius, Lithuania) and detected by a time-correlated single photon counter (PicoQuant Gmbh, Berlin, Germany).

3. Results & Discussion

We begin our analysis of the all-inorganic $CsPbI_3$ material by determining its light absorption properties. Figure 1A shows absorption spectra of the material coated at a substrate temperature of 185 °C with varied amounts of HAI included, further explanation for calculating the percentage of HAI is in the SI. Depending on the composition, each spectrum shows a broad SWIR peak 1200–2500 nm, in addition to a peak at ca. 800 nm due to the classical perovskite semiconducting material. As the HAI content increases, the SWIR peak is blue-shifted. Additionally, scanning electron microscopy (SEM) images were also taken to analyze the surface morphology of the PPDs. The SEM image in Figure 1B shows the surface of the perovskite film at 1000× magnification, demonstrating that the film was compact. In general, the images were found to be relatively homogenous but with very small holes. It also shows some self-assembled tree-branch like structures. Careful inspection of the SEM image shows topographical changes in the sample, with most of the material being spread out in florets with thicker structures being more disperse. Further optimization of the coating process may resolve the small holes and structural heterogeneity and potentially improve device performance. Figure S2 shows the XRD spectrum of our prepared $CsPbI_3$ material with HI. In comparison, Haque

et al. demonstrates that even with varied amounts of HI, the α-$CsPbI_3$ diffraction peaks which result from the 100, 110, 200, 211 and 220 Miller indices occur at approximate 2θ values of 14, 21, 28, 36 and 42, respectively. As our sample solution contains 40 μL of HI per mL of solution, it was expected that its XRD spectrum should be similar to the literature. Our spectrum contains some corresponding peaks near 21, 28, and 36, yet lacks other characteristic peaks and contains many additional peaks, making the spectrum difficult to decipher. Our XRD results are more similar–but not a perfect match– to that of δ-$CsPbI_3$ shown by Montecucco et al., with many more peaks visible including those caused by FTO. This may indicate that our compound has characteristics of both δ and non-δ $CsPbI_3$, and that the inclusion of HAI greatly affects crystal formation in the sample and warrants further investigation [3,37,42–45]. Counterintuitively, our PPD utilizes the δ phase of $CsPbI_3$ for detection of longer wavelengths than the aforementioned visible detectors, without the need for strict environmental controls. This generally undesirable form's bandgap is considered too large for visible detectors but has been reduced to accommodate SWIR wavelengths with the inclusion of HAI.

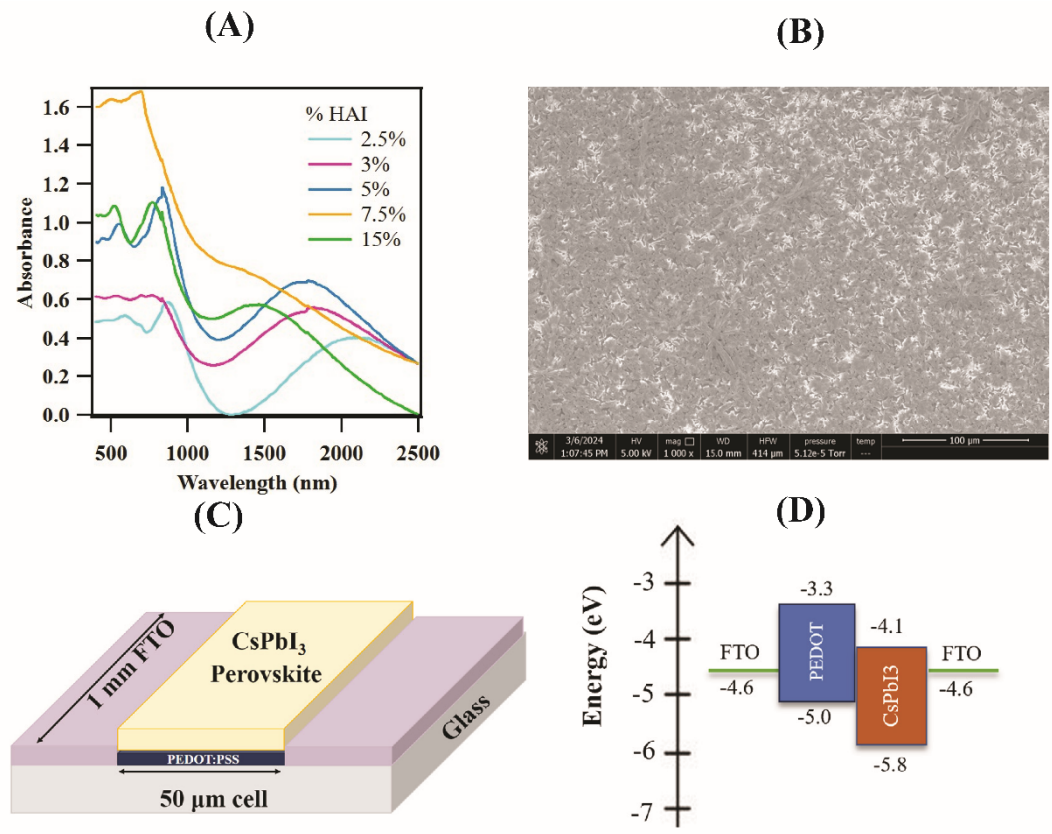

Figure 1. (**A**) Absorption spectra of $CsPbI_3$ material with different percentages of HAI. (**B**) SEM image of the perovskite surface; (**C**) Schematic of $CsPbI_3$ photodetector on FTO glass; (**D**) Energy level diagram of the perovskite photodetector.

After establishing the absorptive properties of the $CsPbI_3$ material, we turned to a simple device fabrication strategy. The as-prepared all-inorganic perovskite photodetectors consist of FTO-striped glass coated with 5×10^{-4} cm^2 layers of PEDOT:PSS and $CsPbI_3$ in the center, with FTO on either side of this stripe as shown in Figure 1C. The resulting matchup of electronic band structures using pure $CsPbI_3$ as the perovskite is shown in Figure 1D. $CsPbI_3$ has a valence band (VB) at −5.8 eV and a conduction band (CB) at −4.1 eV resulting in a bandgap of 1.7 eV [5]. Additionally, the PEDOT:PSS HTL has a bandgap of 1.7 eV as well, with the work function of commercial FTO at −4.6 eV [46,47]. The absorption spectrum of our PPD is shown in Figure S3. A local absorption peak occurs at 725 nm, corresponding to the bandgap energy of $CsPbI_3$. Interestingly, the absorption maximum for the fabricated $CsPbI_3$ device occurs at 1132 nm (1.095 eV), suggesting that notable heterojunction or intraband absorption are occurring in our HAI-doped material [15,35].

Several metrics are used to analyze the performance of photodetector devices. The first is the responsivity, *R* (A W^{-1}), which represents the ability of a photodetector to convert incoming light into useful electrical signals. Responsivity is the ratio of output current to incident light power on the active area:

$$R = \frac{I_p - I_d}{A * P} \quad (1)$$

where I_p is the photocurrent (A), I_d is the dark current (A), A is the cell area (cm^2), and P is the incident light fluence (W cm^{-2}). Additionally, the calculations for the incident light fluence are also found in the Supplementary Materials. As shown in Figure 2A, we measured the responsivity of the PPD using a 1310 nm laser with incident fluence values from 0.28 to 567 mW cm^{-2}. We observed an impressive responsivity of 1.65×10^3 A W^{-1} under 0.283 mW cm^{-2} fluence at a bias of −5 V, indicating exceptional detection even at low levels of illumination. Under the same intensity at a bias of −1 V, the responsivity still reached a value of 1.01×10^2 A W^{-1}. Overall, low fluence achieved the highest responsivities and higher fluence maintained similar response curves at lower magnitudes. We can also look at the responsivity of our device as a function of incident fluence at different applied potentials, as shown in Figure 2B. At negative potentials, the responsivity of the all-inorganic PPD decreases quickly with increased fluence and is greater for larger magnitude applied negative bias. The net photocurrent, $I_p - I_d$, remains approximately constant, such that increases in responsivity are a function of the fluence. Assuming the resistance of our material is constant, Ohm's law explains the linearity of Figure 2B.

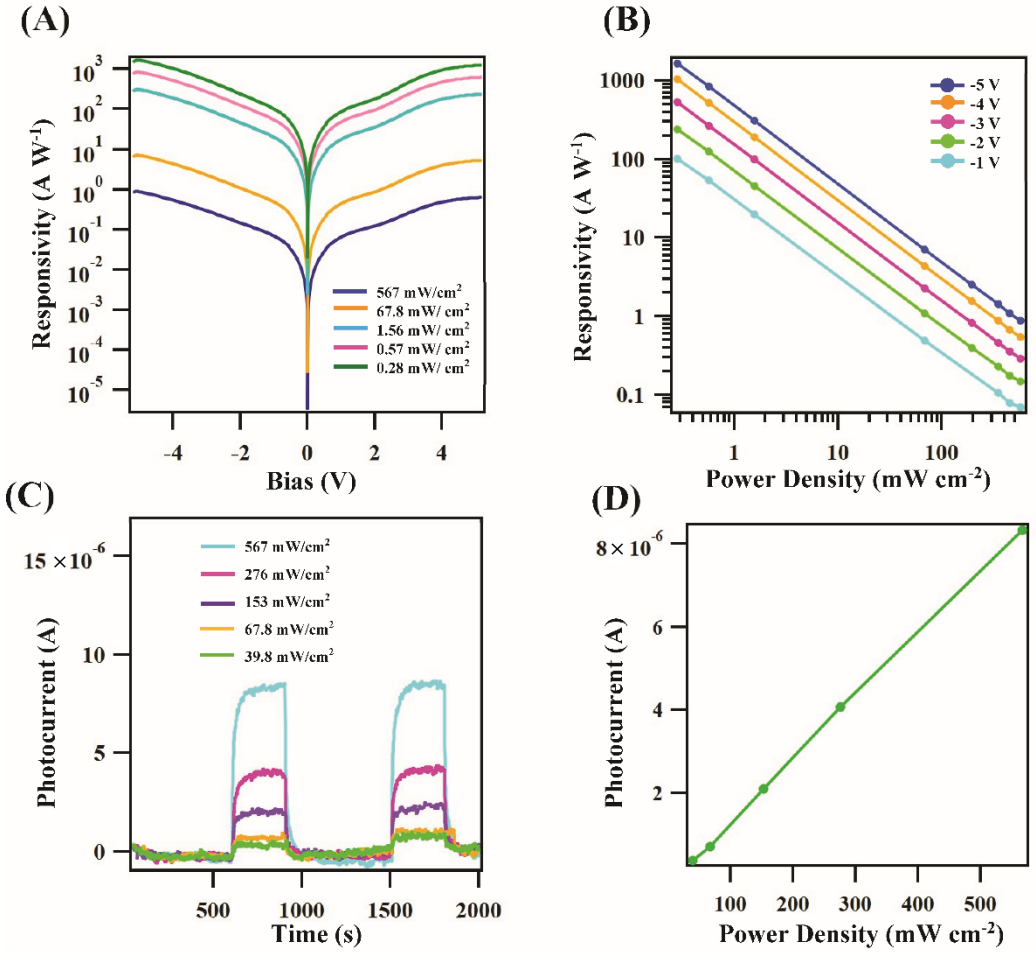

Figure 2. (**A**) Representative photoresponsivity curves at various power levels of 1310 nm illumination. (**B**) Responsivity at biases from −1 V to −5 V as a function of incident fluence. (**C**) Photocurrent through the device with 1310 nm light on and off under a bias of 3 V. (**D**) Photocurrent as a function of incident fluence.

Another important metric for photodetectors is their external quantum efficiency (EQE), which quantifies the number of free charge carriers generated from the photosensitive material per incident photon:

$$EQE = \frac{R * hc}{e\lambda} \quad (2)$$

Here, h is Planck's constant (6.626×10^{-34} J s), c is the speed of light (3×10^8 m s^{-1}), and e is the charge of a single electron (1.602×10^{-19} C). Using $R = 1.65 \times 10^3$ A W^{-1} achieved under 0.283 mW/cm^2 and −5 V bias, the EQE is found to be 1.48×10^3. Even at −1 V, the EQE is 90.7.

Next, we investigated the generated photocurrent over time at different incident intensities, as shown in Figure 2C. An increase in photocurrent is observed when the sample is irradiated with 1310 nm laser light and quickly decreases to baseline when the light is blocked. It is also apparent that the photocurrent increases with incident fluence, and the detector's response is reproducible for multiple cycles. These experiments produced a net photocurrent (I_p–I_d) up to 8.8 μA at an incident fluence of 567 mW cm^{-2}. Furthermore, we observed a linear relationship between maximum photocurrent and applied fluence, as shown in Figure 2D. This is important when implementing the photodetector to easily scale the response with incident light intensity. The theoretical photoconductive gain, *G*, is a key parameter for evaluating the efficacy of a photodetector, representing the ratio of photogenerated charge carriers to absorbed incident photons in the material:

$$G = \frac{I_p h\nu}{ePA} \tag{3}$$

Here, *v* is the frequency of the incident photon (Hz). Under a bias of −5.0 V and intensity of 0.283 mW cm^{-2}, the gain was found to be 1.43 × 10^3. Even under only −1.0 V bias, the gain is 87.08, as shown in Table S1.

Specific detectivity, *D** (Jones), is a measure of sensitivity which quantifies the ability of the photodetector to discern weak light signals from noise, and can be computed as

$$D^* = \frac{\sqrt{A\Delta f}R}{i_n} = \frac{\sqrt{A\Delta f}}{NEP} \tag{4}$$

In this equation, Δ*f* is the bandwidth (Hz), i_n is rms noise, *A* is the active area of detectors, and *NEP* denotes the noise equivalent power, or the amount of input signal required for the signal-to-noise ratio to be one [48]. Using the measurements shown in Figure S4, the specific detectivity of our device was found to be on the order of 8.0 × 10^{10} Jones under a bias from −1.0 V to −5.0 V. Specific detectivity at other biases can be found in Table S2. With these baseline metrics of the all-inorganic PPD outlined, we can perform further analyses to better understand its mechanism for excellent performance.

First, Mott-Schottky measurements were used to characterize the SWIR materials. In such an analysis, the inverse of the square of the material's measured capacitance is plotted as a function of applied bias potential. A positive slope is characteristic of an *n*-type material while a negative slope indicates a *p*-type material [49]. Figure 3A shows an inverted "V" shape, where a positive slope occurs from −1.0 to 0 V and a negative slope occurs from 0 to 1 V. This indicates that a *p*-*n* junction was formed within the perovskite material due to the HAI doping process, since $CsPbI_3$ is an inherent *p*-type semiconductor. Next, fluorescence lifetime measurements were used to investigate the lifetime of photoinduced carriers to better understand the nature of the SWIR materials. The free carrier decay can be seen in Figure 3B, after a sharp increase in free carriers is caused by a 515 nm excitation pulse. A double exponential curve fitting was performed, yielding both fast (τ_1) and slow (τ_2) decay constants to be 10.7 ± 0.1 ns and 68.2 ± 0.7 ns, respectively, with an average (τ_{avg}) of 39.5 ± 0.4 ns [50]. While there is variation in the carrier lifetime of $CsPbI_3$, these are comparable to other studies finding values between 33 and 50 ns [51–53]. These results suggest that the formed doped structures still have similar carrier lifetimes to $CsPbI_3$, allowing ample time for carrier extraction.

Last, to better understand how charge carriers flow in the heterojunction structure, transient absorption (TA) measurements were also conducted on the all-inorganic PPD. Figure 3C shows several representative TA spectra at delay times of −1, 0, 1, 10 and 100 ps between the 515 nm pump and the white light probe. A full 2D plot of this data including longer delay times is shown in Figure S5. The negative feature denotes photoinduced absorption (PIA) and is most clearly seen from 800 to 1000 nm with a shoulder at 1070 mm which decreases significantly with increasing delay as the excited state population declines. The time trace of the PIA at 1070 nm was extracted and fitted using a double exponential function, as shown in Figure 3D. The fitting yielded two fast decay time constants of 4.0 ± 0.3 ps and 25.9 ± 0.9 ps at 1070 nm, which may be due to forward and reverse charge transfer processes, respectively. These fast processes describe the processes by which the photogenerated carriers transfer between the doped and undoped perovskite.

As shown in Table 1, our heterojunction-engineered material produces SWIR responsivities far greater than other modern materials such as other perovskites [26], traditional semiconductors [54], hybrid materials [7,55], and quantum-confined systems [56] which operate at or below room temperature. Interestingly, a graphene/black phosphorus detector [57] has achieved responsivity on the same order as ours but requires meticulous fabrication where our PPD has the advantage of solution processibility and simple spin-coating fabrication.

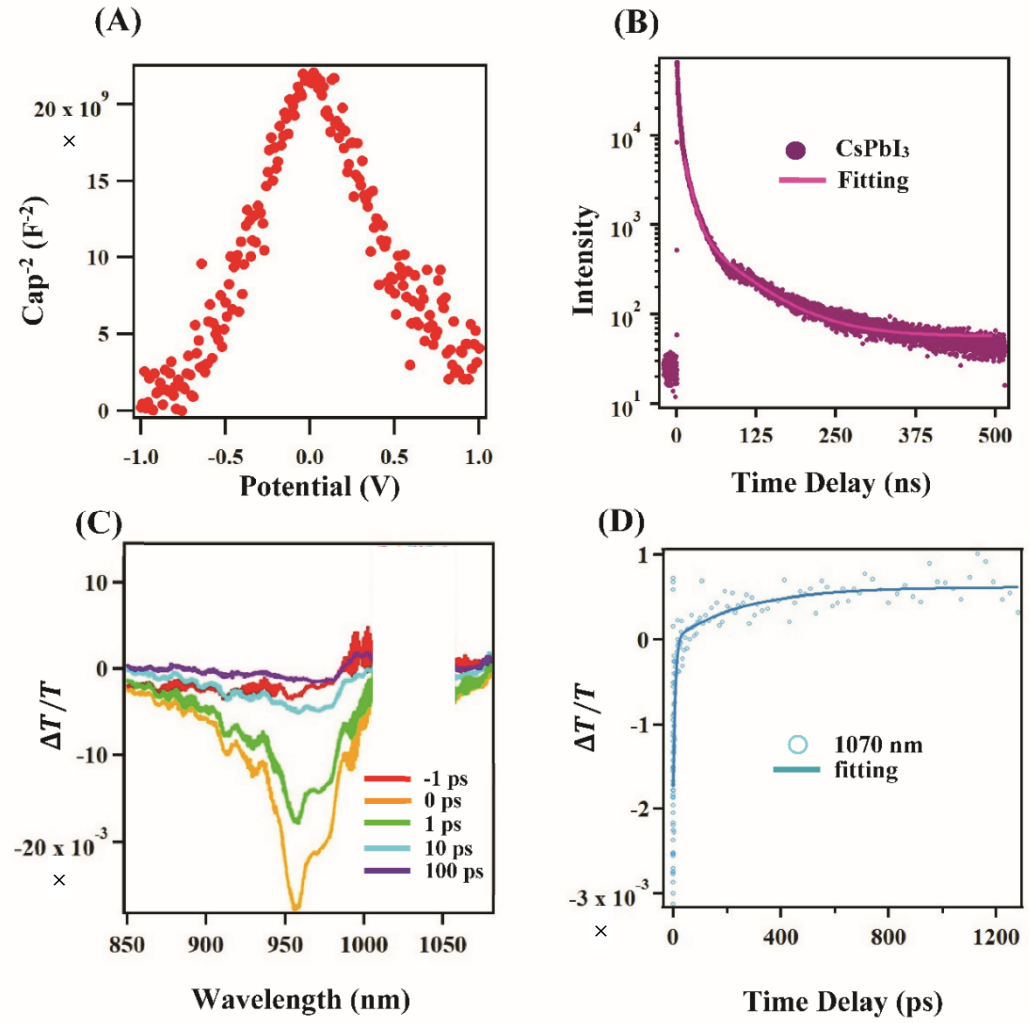

Figure 3. (**A**) Mott-Schottky plot of the fabricated all-inorganic perovskite photodetector; (**B**) Fluorescence lifetime measurements; (**C**) Transient absorption spectra of the PPD device at representative time delays; (**D**) Time traces of the TA response at 1070 nm.

Table 1. Comparison of representative SWIR detector performance based on material and operating parameters.

Material	Light Source (nm)	Bias (V)	Responsivity (A/W)	Temperature (K)	Reference
$CsPbI_3$/HAI	1310	−5	1650	Room temp.	This work
$[(MAI)_{0.835}(HAI)_{0.165}]_n[PbI_2]_1$	1310	−5	157	Room temp.	[41]
InAs/GaAs QDs	2000	−3	60.34	13	[58]
Graphene/InGaAs	1550	0–4	7.6	Room temp.	[57]
$InAs/InAs_{1-x}Sb_x/AlAs_{1-x}Sb_x$	1600	0	0.47	300	[7]
Graphene/black phosphorous	1550	1	3300	Room temp	[59]
Monolithic InSb	1550	1	0.50	77	[56]

By doping all-inorganic $CsPbI_3$ perovskite with HAI, we have extended the useful range of such photodetectors into the SWIR region through engineering a *p-n* heterojunction between the doped and undoped materials. With the introduction of this heterojunction, the effective bandgap of $CsPbI_3$ is lowered to less than 1.0 eV, which allows for response to light in the SWIR region, where perovskites have historically been blind. Our PPD achieved moderate specific detectivity, very high gain and EQE, and an excellent responsivity of 1.65×10^3 A W^{-1} at 1310 nm. A key feature of these PPDs is their ability to convert weak SWIR light to large amounts of current in ambient conditions without the need for cryogenic cooling systems. This makes our PPD especially appealing for integration into electronic systems, including low-light contexts like night vision and weather-impaired imaging, while decreasing cost and complexity.

While our $CsPbI_3$-HAI perovskite material shows potential in SWIR detection, improvements to the proof-of-concept device need to be made. One difficulty is that the absorption spectrum of the PPD was very affected by

small changes in fabrication conditions. Additionally, our experiments were implemented under ambient conditions, which resulted in poor stability, as shown in Figure S6 where the device's performance decreased over 80% in 6 days. This is most likely due to moisture and is typical for $CsPbI_3$ and other perovskites [37,52,58–60]. However, this can likely be remedied by mounting the device in a dedicated housing to ensure dry and nonreactive conditions during preparation and use as shown in the literature [61,62]. Lastly, being a Pb-containing material poses human and environmental health concerns. Proper handling and disposal must be considered if commercialization is to occur.

4. Conclusions

In summary, we produced all-inorganic SWIR materials using HAI as an additive to $CsPbI_3$ perovskite to engineer a *p-n* heterojunction within the material. We further developed simple and highly effective SWIR detectors based on the HAI-doped $CsPbI_3$ on a polymer HTL. We achieved a responsivity as high as 1.65×10^3 A W^{-1} under 1310 nm light and −5 V bias at room temperature under fluence of 0.28 mW cm^{-2}. The detector also displayed an ultra-high EQE of 1.48×10^3 and gain of 1.42×10^3 under −5 V, exemplifying its strong ability to convert incoming photons to charge carriers supplied to the external circuit, which is essential for real-world application. Additionally, a specific detectivity of 8.0×10^{10} Jones was found, demonstrating the sensitivity of this material. Our mechanistic studies show that a *p-n* junction was formed within the perovskite material between the doped and undoped phases. Fluorescence measurements characterized the carrier lifetimes in the material and TA revealed ultrafast charge transfer across the heterojunction. The performance of this material shows the potential for a new era of all-inorganic SWIR photodetectors which do not require extreme temperatures and conditions to achieve high performance, leading to important technological improvements without prohibitive costs.

Supplementary Materials: The following supporting information can be downloaded at: https://media.sciltp.com/articles/others/250730105027922 8/07-18-2025-all-inorganic-SI_Yi.pdf, Figure S1: Schematic of CsPbI3 device coating process. The main steps are preparation for PEDOT coating, PEDOT coating process, preparation for sample, and the sample coating process; Figure S2: XRD spectrum of $CsPbI_3$ material with HAI and 40 μL HI/mL; Figure S3: Absorption spectrum of prepared $CsPbI_3$ device.; Figure S4: Dark current at room temperature under a bias of −1 V (A) and −5 V (B); Figure S5: 2D plot of transient absorption spectra of the $CsPbI_3$ device with a time window of 10 ps (A) and 150 ps (B).; Figure S6: Normalized responsivity of the device over several days. Table S1: Photocurrent under 0.283 mW/cm2 illumination and corresponding gain separated by bias; Table S2: Specific detectivity at various bias if we assume $1 + 4\pi^2 f^2 \tau^2 = 1$.

Author Contributions: Y.R., G.C. and A.H. designed the project. S.S., H.F., X.L., Y.Q. and V.M. conducted experiments on material preparation, device fabrication, characterizations, analyzed the data. S.S., H.F. and J.B.B. drafted the manuscript. Y.R. and G.C. analyzed the data and revised the paper. All authors have read and agreed to the published version of the manuscript.

Funding: This research was funded by from Honda Research Institute USA, Inc. and the National Science Foundation, grant number 2045084.

Data Availability Statement: The datasets generated and/or analyzed during the current study are available from the corresponding authors on reasonable request.

Conflicts of Interest: The authors declare no conflict of interest.

References

1. Cao, F.; Liu, L.; Li, L. Short-wave infrared photodetector. *Mater. Today* **2023**, *62*, 327–349. https://doi.org/10.1016/j.mattod.2022.11.003.
2. Wu, Z.; Zhai, Y.; Kim, H.; Azoulay, J.D.; Ng, T.N. Emerging Design and Characterization Guidelines for Polymer-Based Infrared Photodetectors. *Acc. Chem. Res.* **2018**, *51*, 3144–3153. https://doi.org/10.1021/acs.accounts.8b00446.
3. Saparbaev, A.; Zhang, M.; Kuvondikov, V.; Nurumbetova, L.; Raji, I.O.; Tajibaev, I.; Yang, R. High-performance CsPbI3 perovskite solar cells without additives in air condition. *Sol. Energy* **2021**, *228*, 405–412. https://doi.org/10.1016/j.solener.2021.09.059.
4. Shimoni, M.; Haelterman, R.; Perneel, C. Hypersectral Imaging for Military and Security Applications: Combining Myriad Processing and Sensing Techniques. *IEEE Geosci. Remote Sens. Mag.* **2019**, *7*, 101–117. https://doi.org/10.1109/MGRS.2019.2902525.
5. Liu, C.; Igci, C.; Yang, Y.; Syzgantseva, O.A.; Syzgantseva, M.A.; Rakstys, K.; Nazeeruddin, M.K. Dopant-Free Hole Transport Materials Afford Efficient and Stable Inorganic Perovskite Solar Cells and Modules. *Angew. Chem. Int. Ed.* **2021**, *60*, 20489–20497. https://doi.org/10.1002/anie.202107774.
6. Jahid, A.; Alsharif, M.H.; Hall, T.J. A contemporary survey on free space optical communication: Potentials, technical challenges, recent advances and research direction. *J. Netw. Comput. Appl.* **2022**, *200*, 103311. https://doi.org/10.1016/j.jnca.2021.103311.

7. Haddadi, A.; Suo, X.V.; Adhikary, S.; Dianat, P.; Chevallier, R.; Hoang, A.M.; Razeghi, M. High-performance short-wavelength infrared photodetectors based on type-II InAs/$InAs_{1-x}Sb_x$/$AlAs_{1-x}Sb_x$ superlattices. *Appl. Phys. Lett.* **2015**, *107*, 141104. https://doi.org/10.1063/1.4932518.
8. Richter, J.; Lorenz, S.; Kaas, A.; Fuchs, M.; Röder, C.; Peuker, U.A.; Gloaguen, R. Spectral Characterization of Battery Components from Li-Ion Battery Recycling Processes. *Metals* **2024**, *14*, 147.
9. Ferreira, M.P.; Wagner, F.H.; Aragão, L.E.O.C.; Shimabukuro, Y.E.; de Souza Filho, C.R. Tree species classification in tropical forests using visible to shortwave infrared WorldView-3 images and texture analysis. *ISPRS J. Photogramm. Remote Sens.* **2019**, *149*, 119–131. https://doi.org/10.1016/j.isprsjprs.2019.01.019.
10. Tan, C.L.; Mohseni, H. Emerging technologies for high performance infrared detectors. *Nanophotonics* **2018**, *7*, 169–197. https://doi.org/10.1515/nanoph-2017-0061.
11. Liu, Z.; Luo, T.; Liang, B.; Chen, G.; Yu, G.; Xie, X.; Shen, G. High-detectivity InAs nanowire photodetectors with spectral response from ultraviolet to near-infrared. *Nano Res.* **2013**, *6*, 775–783. https://doi.org/10.1007/s12274-013-0356-0.
12. Pokharel, R.; Ramaswamy, P.; Devkota, S.; Parakh, M.; Dawkins, K.; Penn, A.; Iyer, S. Epitaxial High-Yield Intrinsic and Te-Doped Dilute Nitride GaAsSbN Nanowire Heterostructure and Ensemble Photodetector Application. *ACS Appl. Electron. Mater.* **2020**, *2*, 2730–2738. https://doi.org/10.1021/acsaelm.0c00450.
13. Zhang, F.; Zhang, X.; Li, Z.; Yi, R.; Li, Z.; Wang, N.; Fu, L. A New Strategy for Selective Area Growth of Highly Uniform InGaAs/InP Multiple Quantum Well Nanowire Arrays for Optoelectronic Device Applications. *Adv. Funct. Mater.* **2022**, *32*, 2103057. https://doi.org/10.1002/adfm.202103057.
14. Ackerman, M.M. Bringing Colloidal Quantum Dots to Detector Technologies. *Inf. Disp.* **2020**, *36*, 19–23. https://doi.org/10.1002/msid.1165.
15. Wang, Y.; Peng, L.; Schreier, J.; Bi, Y.; Black, A.; Malla, A.; Konstantatos, G. Silver telluride colloidal quantum dot infrared photodetectors and image sensors. *Nat. Photonics* **2024**, 18, 236–242. https://doi.org/10.1038/s41566-023-01345-3.
16. Wu, Z.; Ou, Y.; Cai, M.; Wang, Y.; Tang, R.; Xia, Y. Short-Wave Infrared Photodetectors and Imaging Sensors Based on Lead Chalcogenide Colloidal Quantum Dots. *Adv. Opt. Mater.* **2023**, *11*, 2201577. https://doi.org/10.1002/adom.202201577.
17. Kwon, J.B.; Han, M.; Jung, D.G.; Kong, S.H.; Jung, D. High Sensitivity Shortwave Infrared Photodetector Based on PbS QDs Using P3HT. *Nanomaterials* **2021**, *11*, 2683.
18. Chen, W.; Tang, H.; Chen, Y.; Heger, J.E.; Li, N.; Kreuzer, L.P.; Müller-Buschbaum, P. Spray-deposited PbS colloidal quantum dot solid for near-infrared photodetectors. *Nano Energy* **2020**, *78*, 105254. https://doi.org/10.1016/j.nanoen.2020.105254.
19. Yu, M.X.; Ma, J.J.; Wang, J.M.; Cai, W.G.; Zhang, Z.; Huang, B.; Tian, Z.Q. Ag_2Te Quantum Dots as Contrast Agents for Near-Infrared Fluorescence and Computed Tomography Imaging. *ACS Appl. Nano Mater.* **2020**, *3*, 6071–6077. https://doi.org/10.1021/acsanm.0c01274.
20. Hu, L.; Dong, Y.; Deng, J.; Xie, Y.; Ma, X.; Qian, F.; Xu, C. High responsivity graphene-InGaAs near-infrared photodetector realized by hole trapping and its response saturation mechanism. *Opt. Express* **2021**, *29*, 23234–23243. https://doi.org/10.1364/OE.431083.
21. Park, J.; Hwang, J.C.; Kim, G.G.; Park, J.-U. Flexible electronics based on one-dimensional and two-dimensional hybrid nanomaterials. *InfoMat* **2020**, *2*, 33–56. https://doi.org/10.1002/inf2.12047.
22. Mak, K.F.; Ju, L.; Wang, F.; Heinz, T.F. Optical spectroscopy of graphene: From the far infrared to the ultraviolet. *Solid State Commun.* **2012**, *152*, 1341–1349. https://doi.org/10.1016/j.ssc.2012.04.064.
23. Kim, J.Y.; Lee, J.-W.; Jung, H.S.; Shin, H.; Park, N.-G. High-Efficiency Perovskite Solar Cells. *Chem. Rev.* **2020**, *120*, 7867–7918. https://doi.org/10.1021/acs.chemrev.0c00107.
24. Gao, W.-H.; Chen, C. Perovskites and their constructed near-infrared photodetectors. *Nano Energy* **2024**, *128*, 109904. https://doi.org/10.1016/j.nanoen.2024.109904.
25. Jhang, A.-T.; Tsai, P.-C.; Tsai, Y.-T.; Lin, S.-Y.; Fang, M.-H. Quantum-Dots-In-Double-Perovskite for High-Gain Short-Wave Infrared Photodetector. *Adv. Opt. Mater.* **2024**, *12*, 2401252. https://doi.org/10.1002/adom.202401252.
26. Qian, Y.; Huang-Fu, Z.C.; Li, H.; Zhang, T.; Li, X.; Schmidt, S.; Rao, Y. Unleashing the Potential: High Responsivity at Room Temperature of Halide Perovskite-Based Short-Wave Infrared Detectors with Ultrabroad Bandwidth. *JACS Au* **2024**, 4, 3921–3930. https://doi.org/10.1021/jacsau.4c00621.
27. Wang, H.; Sun, Y.; Chen, J.; Wang, F.; Han, R.; Zhang, C.; Yang, J. A Review of Perovskite-Based Photodetectors and Their Applications. *Nanomaterials* **2022**, *12*, 4390.
28. Miao, J.; Zhang, F. Recent progress on highly sensitive perovskite photodetectors. *J. Mater. Chem. C* **2019**, *7*, 1741–1791. https://doi.org/10.1039/C8TC06089D.
29. Wang, F.; Zou, X.; Xu, M.; Wang, H.; Wang, H.; Guo, H.; Hu, W. Recent Progress on Electrical and Optical Manipulations of Perovskite Photodetectors. *Adv. Sci.* **2021**, *8*, 2100569. https://doi.org/10.1002/advs.202100569.
30. Li, L.; Ye, S.; Qu, J.; Zhou, F.; Song, J.; Shen, G. Recent Advances in Perovskite Photodetectors for Image Sensing. *Small* **2021**, *17*, 2005606. https://doi.org/10.1002/smll.202005606.

31. Fakharuddin, A.; Gangishetty, M.K.; Abdi-Jalebi, M.; Chin, S.H.; bin Mohd Yusoff, A.R.; Congreve, D.N.; Bolink, H.J. Perovskite light-emitting diodes. *Nat. Electron.* **2022**, *5*, 203–216. https://doi.org/10.1038/s41928-022-00745-7.
32. Liu, Y.; Xia, M.; Ren, D.; Nussbaum, S.; Yum, J.H.; Gratzel, M.; Sivula, K. Photoelectrochemical CO_2 Reduction at a Direct CuInGaS2/Electrolyte Junction. *ACS Energy Lett.* **2023**, *8*, 1645–1651. https://doi.org/10.1021/acsenergylett.3c00022.
33. Filip, M.R.; Eperon, G.E.; Snaith, H.J.; Giustino, F. Steric engineering of metal-halide perovskites with tunable optical band gaps. *Nat. Commun.* **2014**, *5*, 5757. https://doi.org/10.1038/ncomms6757.
34. Chen, S.; Teng, C.; Zhang, M.; Li, Y.; Xie, D.; Shi, G. A Flexible UV–Vis–NIR Photodetector based on a Perovskite/Conjugated-Polymer Composite. *Adv. Mater.* **2016**, *28*, 5969–5974. https://doi.org/10.1002/adma.201600468.
35. Alwadai, N.; Haque, M.A.; Mitra, S.; Flemban, T.; Pak, Y.; Wu, T.; Roqan, I. High-Performance Ultraviolet-to-Infrared Broadband Perovskite Photodetectors Achieved via Inter-/Intraband Transitions. *ACS Appl Mater Interfaces* **2017**, *9*, 37832–37838. https://doi.org/10.1021/acsami.7b09705 From NLM.
36. Pan, X.; Zhou, H.; Liu, R.; Wu, D.; Song, Z.; Tang, X.; Wang, H. Achieving a high-performance, self-powered, broadband perovskite photodetector employing MAPbI3 microcrystal films. *J. Mater. Chem. C* **2020**, *8*, 2028–2035. https://doi.org/10.1039/C9TC05668H.
37. Yao, Z.; Zhao, W.; Liu, S. Stability of the $CsPbI_3$ perovskite: From fundamentals to improvements. *J. Mater. Chem. A* **2021**, *9*, 11124–11144. https://doi.org/10.1039/D1TA01252E.
38. Li, Y.; Shi, Z.; Lei, L.; Zhang, F.; Ma, Z.; Wu, D.; Li, X. Highly Stable Perovskite Photodetector Based on Vapor-Processed Micrometer-Scale CsPbBr3 Microplatelets. *Chem. Mater.* **2018**, *30*, 6744–6755. https://doi.org/10.1021/acs.chemmater.8b02435.
39. Pintor Monroy, M.I.; Goldberg, I.; Elkhouly, K.; Georgitzikis, E.; Clinckemalie, L.; Croes, G.; Genoe, J. All-Evaporated, All-Inorganic $CsPbI_3$ Perovskite-Based Devices for Broad-Band Photodetector and Solar Cell Applications. *ACS Appl. Electron. Mater.* **2021**, *3*, 3023–3033. https://doi.org/10.1021/acsaelm.1c00252.
40. Liu, X.; Liu, Z.; Li, J.; Tan, X.; Sun, B.; Fang, H.; Liao, G. Ultrafast, self-powered and charge-transport-layer-free photodetectors based on high-quality evaporated $CsPbBr_3$ perovskites for applications in optical communication. *J. Mater. Chem. C* **2020**, *8*, 3337–3350. https://doi.org/10.1039/C9TC06630F.
41. Han, J.; Xie, Q.; Luo, J.; Deng, G.H.; Qian, Y.; Sun, D.; Rao, Y. Anisotropic Geminate and Non-Geminate Recombination of Triplet Excitons in Singlet Fission of Single Crystalline Hexacene. *J. Phys. Chem. Lett.* **2020**, *11*, 1261–1267. https://doi.org/10.1021/acs.jpclett.9b03800.
42. Haque, F.; Wright, M.; Mahmud, M.A.; Yi, H.; Wang, D.; Duan, L.; Uddin, A. Effects of Hydroiodic Acid Concentration on the Properties of CsPbI 3 Perovskite Solar Cells. *ACS Omega* **2018**, *3*, 11937–11944. https://doi.org/10.1021/acsomega.8b01589.
43. Ke, F.; Wang, C.; Jia, C.; Wolf, N.R.; Yan, J.; Niu, S.; Lin, Y. Preserving a robust $CsPbI_3$ perovskite phase via pressure-directed octahedral tilt. *Nat. Commun.* **2021**, *12*, 461. https://doi.org/10.1038/s41467-020-20745-5.
44. Luo, P.; Xia, W.; Zhou, S.; Sun, L.; Cheng, J.; Xu, C.; Lu, Y. Solvent Engineering for Ambient-Air-Processed, Phase-Stable CsPbI3 in Perovskite Solar Cells. *J. Phys. Chem. Lett.* **2016**, *7*, 3603–3608. https://doi.org/10.1021/acs.jpclett.6b01576.
45. Montecucco, R.; Quadrivi, E.; Po, R.; Grancini, G. All-Inorganic Cesium-Based Hybrid Perovskites for Efficient and Stable Solar Cells and Modules. *Adv. Energy Mater.* **2021**, *11*, 2100672. https://doi.org/10.1002/aenm.202100672.
46. Liu, D.; Li, Y.; Yuan, J.; Hong, Q.; Shi, G.; Yuan, D.; Fung, M.K. Improved performance of inverted planar perovskite solar cells with F4-TCNQ doped PEDOT:PSS hole transport layers. *J. Mater. Chem. A* **2017**, *5*, 5701–5708. https://doi.org/10.1039/C6TA10212C.
47. Yan, G.; Ji, Z.; Li, Z.; Jiang, B.; Kuang, M.; Cai, X.; Mai, W. All-inorganic $Cs_2AgBiBr_6$/CuSCN-based photodetectors for weak light imaging. *Sci. China Mater.* **2021**, *64*, 198–208. https://doi.org/10.1007/s40843-020-1358-5.
48. Wang, F.; Zhang, T.; Xie, R.; Wang, Z.; Hu, W. How to characterize figures of merit of two-dimensional photodetectors. *Nat. Commun.* **2023**, *14*, 2224. https://doi.org/10.1038/s41467-023-37635-1.
49. Naeem, R.; Ehsan, M.; Rehman, A.; Yamani, Z.; Hakeem, A.; Mazhar, M. Single step aerosol assisted chemical vapor deposition of p-n Sn(II)oxide-Ti(IV)oxide nanocomposite thin film electrodes for investigation of photoelectrochemical properties. *N. J. Chem.* **2018**, *42*, 5256–5266. https://doi.org/10.1039/C7NJ04606E.
50. Zhang, L.; Zhou, M.; Zhang, Z.; Yuan, J.; Li, B.; Wen, W.; Tian, J. Ultra-long photoluminescence lifetime in an inorganic halide perovskite thin film. *J. Mater. Chem. A* **2019**, *7*, 22229–22234. https://doi.org/10.1039/C9TA07412K.
51. Zhang, Z.; Ji, R.; Kroll, M.; Hofstetter, Y.J.; Jia, X.; Becker-Koch, D.; Vaynzof, Y. Efficient Thermally Evaporated γ-$CsPbI_3$ Perovskite Solar Cells. *Adv. Energy Mater.* **2021**, *11*, 2100299. https://doi.org/10.1002/aenm.202100299.
52. Fu, Y.; Rea, M.T.; Chen, J.; Morrow, D.J.; Hautzinger, M.P.; Zhao, Y.; Jin, S. Selective Stabilization and Photophysical Properties of Metastable Perovskite Polymorphs of $CsPbI_3$ in Thin Films. *Chem. Mater.* **2017**, *29*, 8385–8394. https://doi.org/10.1021/acs.chemmater.7b02948.
53. You, J.; Hong, Z.; Yang, Y.; Chen, Q.; Cai, M.; Song, T.B.; Yang, Y. Low-Temperature Solution-Processed Perovskite Solar Cells with High Efficiency and Flexibility. *ACS Nano* **2014**, *8*, 1674–1680. https://doi.org/10.1021/nn406020d.
54. Menon, H.; Jeddi, H.; Morgan, N.P.; Fontcuberta i Morral, A.; Pettersson, H.; Borg, M. Monolithic InSb nanostructure photodetectors on Si using rapid melt growth. *Nanoscale Adv.* **2023**, *5*, 1152–1162. https://doi.org/10.1039/D2NA00903J.

55. Yang, Q.; Wu, Q.; Luo, W.; Yao, W.; Yan, S.; Shen, J. InGaAs/graphene infrared photodetectors with enhanced responsivity. *Mater. Res. Express* **2019**, *6*, 116208. https://doi.org/10.1088/2053-1591/ab4925.
56. Deviprasad, V.P.; Ghadi, H.; Das, D.; Panda, D.; Rawool, H.; Chavan, V.; Chakrabarti, S. High performance short wave infrared photodetector using p-i-p quantum dots (InAs/GaAs) validated with theoretically simulated model. *J. Alloys Compd.* **2019**, *804*, 18–26. https://doi.org/10.1016/j.jallcom.2019.06.286.
57. Liu, Y.; Shivananju, B.N.; Wang, Y.; Zhang, Y.; Yu, W.; Xiao, S.; Bao, Q. Highly Efficient and Air-Stable Infrared Photodetector Based on 2D Layered Graphene–Black Phosphorus Heterostructure. *ACS Appl. Mater. Interfaces* **2017**, *9*, 36137–36145. https://doi.org/10.1021/acsami.7b09889.
58. Ouedraogo, N.A.N.; Chen, Y.; Xiao, Y.Y.; Meng, Q.; Han, C.B.; Yan, H.; Zhang, Y. Stability of all-inorganic perovskite solar cells. *Nano Energy* **2020**, *67*, 104249. https://doi.org/10.1016/j.nanoen.2019.104249.
59. Wang, D.; Wright, M.; Elumalai, N.K.; Uddin, A. Stability of perovskite solar cells. *Sol. Energy Mater. Sol. Cells* **2016**, *147*, 255–275. https://doi.org/10.1016/j.solmat.2015.12.025.
60. Boyd, C.C.; Cheacharoen, R.; Leijtens, T.; McGehee, M.D. Understanding Degradation Mechanisms and Improving Stability of Perovskite Photovoltaics. *Chem. Rev.* **2019**, *119*, 3418–3451. https://doi.org/10.1021/acs.chemrev.8b00336.
61. Wang, P.; Zhang, X.; Zhou, Y.; Jiang, Q.; Ye, Q.; Chu, Z.; You, J. Solvent-controlled growth of inorganic perovskite films in dry environment for efficient and stable solar cells. *Nat. Commun.* **2018**, *9*, 2225. https://doi.org/10.1038/s41467-018-04636-4.
62. Bian, H.; Bai, D.; Jin, Z.; Wang, K.; Liang, L.; Wang, H.; Liu, S.F. Graded Bandgap $CsPbI_2$+xBr_{1-x} Perovskite Solar Cells with a Stabilized Efficiency of 14.4%. *Joule* **2018**, *2*, 1500–1510. https://doi.org/10.1016/j.joule.2018.04.012.

Review

Light-Driven Soft Actuators: Materials, Designs, and Applications

Siqi Huang [1,†], Dong Zhang [1,†], and Younan Xia [1,2,*]

[1] The Wallace H. Coulter Department of Biomedical Engineering, Georgia Institute of Technology and Emory University, Atlanta, GA 30332, USA
[2] School of Chemistry and Biochemistry, Georgia Institute of Technology, Atlanta, GA 30332, USA
* Correspondence: younan.xia@bme.gatech.edu
† These authors contributed equally to this work.
Received: 16 July 2025; Revised: 23 July 2025; Accepted: 30 July 2025; Published: 11 August 2025

Abstract: Light-driven soft actuators have attracted extensive attention owning to their unique merits, including wireless remote actuation, precise spatiotemporal control, noncontact localized manipulation, as well as easily tunable properties. This review highlights recent advances in the design and fabrication of state-of-the-art light-driven soft actuators, starting from an overview of typical materials to the design strategies developed up to date, followed by discussion of their emerging applications in the contexts of biomimetic locomotion robotics, complex 3D architecture manufacturing, microfluidic systems, and biomedical research. At the end, we discuss opportunities and challenges in this rapidly growing field, together with perspectives on future directions.

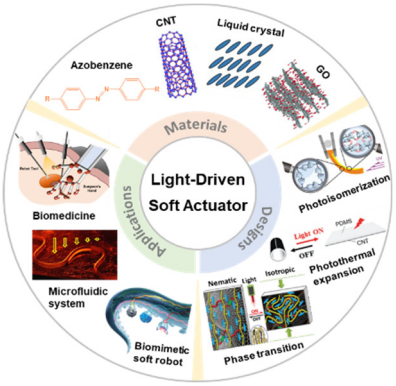

Keywords: soft actuators; light-responsive materials; biomimetics

1. Introduction

An actuator is a device capable of converting various forms of stimuli into mechanical deformation to enable movement and control of a system at macro, micro, or nanoscale levels [1–8]. The first report of an actuating system dates back to the late 1930s, when Xhiter Anckeleman came up with the first pneumatic and hydraulic actuator used for the braking system of an automobile. Since then, research into all sorts of actuators has been flourishing, including the development of novel functional materials and elucidation of driving mechanisms. Traditional hard actuators, comprised of rigid components, offer high speed, precision, and strength but often lack versatility and reconfigurability [9]. In contrast, soft actuators with flexible, lightweight, and miniaturized structures have gained significant attention in the past few decades [10,11]. Unlike their rigid counterparts, soft actuators easily perform dynamic deformation and safely interact with humans, making them ideal for applications in wearable devices, soft robotics, healthcare, micromanufacturing, and micromanipulation [12,13].

In recent years, the development of stimuli-responsive polymers has led to extensive exploration of soft actuators that can be triggered by diverse stimuli including temperature, pH value, light, ionic strength, moisture, electric field, and magnetic field. Among them, light easily stands out for its unique advantages, such as wireless remote activation, precise spatiotemporal control, and noncontact, localized manipulation [7,14]. Moreover, light-driven actuation can be finely tuned by adjusting parameters such as wavelength, intensity, polarization direction, and irradiation time [15]. As a result, light-driven soft actuators have attracted ever increasing attention [16–18].

This review focuses on the advances over the past decade in designing and fabricating light-driven soft actuators and their applications. We begin with an overview of key materials used in their fabrication, followed by discussion of the state-of-the-art design strategies and the underlying deformation and actuation mechanisms. We then highlight their emerging applications, including light-responsive biomimetic locomotion robotics, complex 3D architecture manufacturing, fabrication of microfluidic systems, and biomedicines. Finally, we address current challenges in this field and offer perspectives on future developments.

2. Typical Materials for Light-Driven Soft Actuators

Stimuli-responsive materials play a crucial role in modern materials science. In recent decades, a variety of photo-responsive materials have been developed and extensively applied to the burgeoning field of soft actuators [19,20]. In this section, we focus on three classes of materials widely used for light-driven soft actuators, including azobenzene derivatives, carbon-based materials, and liquid-crystal polymeric materials.

2.1. Azobenzene Derivatives

Among light-sensitive materials, those containing the azobenzene unit have been extensively investigated for its reversible *trans-cis* photoisomerization in response to light of different wavelengths [21–23], as illustrated in Figure 1A. Upon UV light irradiation, azobenzene transitions from a thermally stable extended *trans* state to a bent *cis* form, while exposure to visible light or thermal relaxation induces the reverse *cis* to *trans* isomerization [24]. This isomerization process results in a significant change to the dipole moment, increasing from 0 in the *trans* form to 3 Debye in the *cis* form [22,25], in additional to the dimensional change. Owning to its advantages such as ease of synthesis and good miscibility with many other polymers, azobenzene has been frequently incorporated into soft actuators with fantastic photoresponsivity. However, it also presents certain limitations. The poor thermal stability of the cis isomer restricts the operation of azobenzene-based photo-actuators to room temperature, as elevated temperatures can induce reversion to the original shape. On the other hand, its non-biodegradability and limited biocompatibility hinder its potential for in vivo biomedical applications [7].

2.2. Carbon-Based Materials

Carbon-based materials (Figure 1B), including graphene, graphite, and carbon nanotubes (CNTs), have been actively explored for use in soft actuators on account of their efficient light absorption, high thermal and electrical conductivity, good flexibility, superb mechanical properties, as well as excellent chemical stability [26–28]. Unlike photochromic azobenzene, most carbon-based materials are photothermally active. By efficiently converting light to heat and transferring the generated thermal energy to a thermal-sensitive matrix, they enable rapid photothermal actuation [26]. Research has shown that carbon-based materials can be incorporated as a filler in processable elastic polymers or used as a single layer in an asymmetric bilayer system, enhancing both photothermal response and mechanical strength of the soft actuators [29,30]. Over the last decade, advancements in fabrication techniques have significantly reduced the cost of carbon-based materials, making them increasingly feasible for commercial soft actuation products [31].

2.3. Liquid-Crystal Polymeric Materials

Liquid-crystal molecules, also known as mesogens, exhibit a unique state between the crystalline solid and isotropic liquid phases, and can be grafted to polymeric materials for fabricating soft actuators [15]. As shown in Figure 1C, there are three most widely used liquid crystal polymeric materials, i.e., liquid-crystal polymers (LCPs), liquid crystal polymer networks (LCNs), and liquid crystal elastomers (LCEs). Among them, LCEs, which are crosslinked and highly flexible, can undergo large reversible deformations, making them the most attractive for soft actuator applications [31]. In liquid crystal polymeric systems, the alignment direction of mesogens determines the phase, with the smectic and nematic phases being the typical examples. The orientation of mesogens can be readily reconfigured using external stimuli (e.g., electric, light, or heat), resulting in macroscopic shape changes. In recent years, photoinduced order–disorder phase transitions have been widely explored for triggering reversible deflections, primarily through photoisomerization or photothermal mechanisms [32–35].

3. Design Principles of Light-Driven Soft Actuators

From the perspective of device operation, most light-driven soft actuators undergo reversible deformations based upon either photochemical transformation or photothermal heating. Photochemical transformation such as photoisomerization typically involve light-sensitive substances [36], a photochemical reaction is necessary in order to trigger and control the deformation [15]. On the other hand, the photothermal effect involves light-to-heat conversion, leading to asymmetrical expansion or contraction, as well as phase transition, for the generation of deformation [30,37]. Both mechanisms have been explored in designing light-responsive soft actuator systems.

3.1. Deformation Driven by Photoisomerization

Isomerization is the chemical process by which a molecule is transformed into its isomer with the same chemical composition but a different structure or configuration [38,39]. Photochromic molecules, including azobenzene, fulgide, diarylethene, and spiropyran, display reversible photoisomerization [39–42]. In this section, we focus on two widely used moieties based on azobenzene and diarylethene.

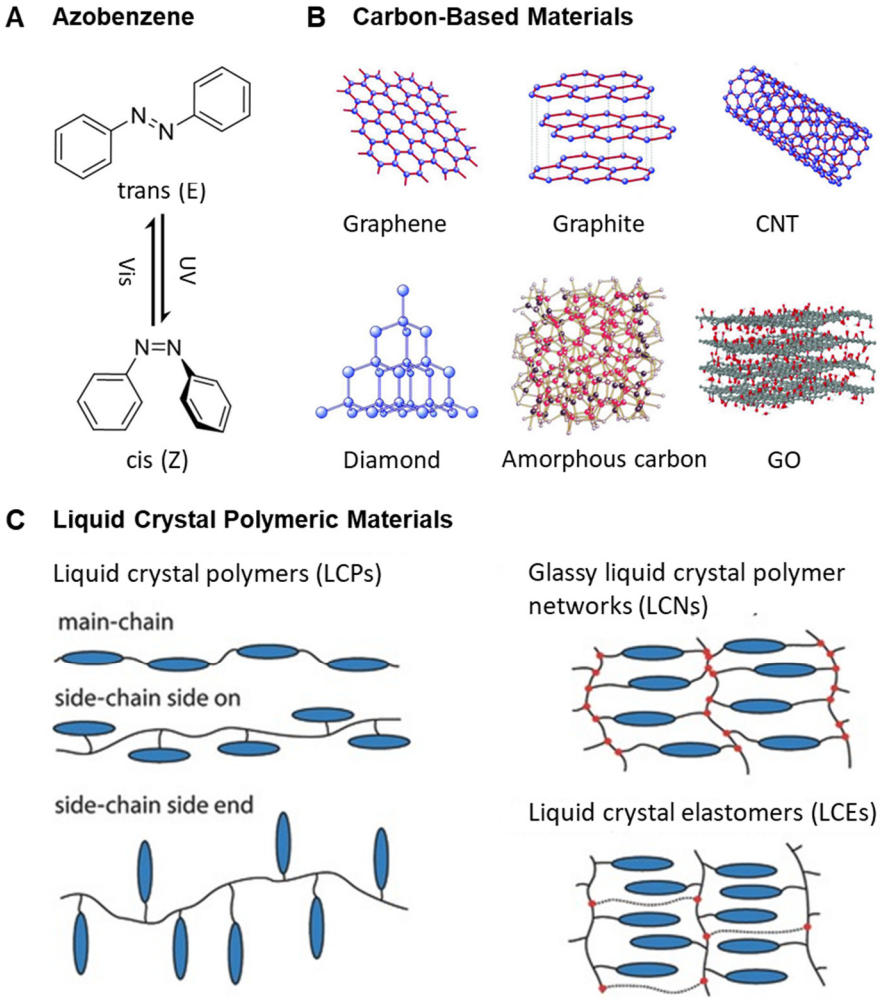

Figure 1. Representative materials for light-driven soft actuators. (**A**) Photoisomerization of azobenzene unit. (**B**) Structures of graphene, graphite, CNTs, diamond, amorphous carbon, and graphene oxide (GO). (**C**) Schematic illustration showing the distinct structures of LCPs, LCNs, and LCEs. (**A**) Reproduced with permission [23]. Copyright 2023, Wiley-VCH. (**B**) Reproduced with permission [26]. Copyright 2018, Wiley-VCH. (**C**) Reproduced with permission [31]. Copyright 2017, Wiley-VCH.

The *trans-cis* photoisomerization of azobenzene can effectively induce a rapid shape change. In one example, the azobenzene was incorporated into a liquid-crystal polymer to form a light-driven film that bends and recovers under alternating irradiation by UV and visible light (Figure 2A). As mentioned earlier, azobenzene undergo *trans-cis* isomerization, where the *trans* isomer has a length of 0.9 nm while the *cis* isomer has a length of only 0.56 nm upon UV irradiation, resulting in a macroscopic shape change due to the change in molecular dimensions. The top surface absorbs more UV light, causing the film to bend toward the UV light side [43]. Harada and coworkers developed a polymeric 4-azobenzene-based hydrogel ([c2] $AzoCD_2$) containing photoactive [c2] daisy chains (polyrotaxane double-threaded dimers) based on α-cyclodextrin hosts and azobenzene guests [44]. As shown in Figure 2B, UV irradiation induced the isomerization of azobenzene from *trans* state to *cis* state, resulting in the contraction motion of [c2] daisy chains. This conformational change led to the discharge of adsorbed water from the [c2] $AzoCD_2$ hydrogel, resulting in its shrinking in real time. Upon exposure to visible light, the hydrogel expanded as the [c2] daisy chains recovered their original conformation, restoring the hydrogel to its initial volume. The photoinduced motion of the hydrogel strip was more pronounced when it was irradiated under water, causing it to bend toward the UV light side. This bending resulted from the selective shrinkage of the exposed surface

under UV irradiation, with the unexposed side remaining unchanged. Upon exposure to visible light, the hydrogel returned to its original state (Figure 2B).

Unlike *trans-cis* photoisomerization, where the molecular conformation is simply distorted, open-closed ring photoisomerization involves the formation and breakage of covalent bonds in the intramolecular rings [24]. Typical examples include diarylethene and its derivatives. Irie et al. reported the photoinduced movement of a cocrystal of a diarylethene derivative, 1,2-bis(2-methyl-5-(1-naphthyl)-3-thienyl) perfluorocyclopentene, and perfluoronaphthalene [45]. As shown in Figure 2C, the ring in diarylethene molecule switched between open and closed state upon exposure to light of different wavelengths. Compared to the open ring form of 1,2-bis(2-methyl-5-(1-naphthyl)-3-thienyl) perfluorocyclopentene, the height of the triangle shape of the closed ring form increased from 0.534 to 0.679 nm, while the width decreased from 1.554 to 1.411 nm, leading to visible shape deformation of the cocrystal. The rectangular cocrystal plate displayed reversible bending when alternately exposed to UV and visible light, with the bending motion being repeatable over 250 cycles without any damage or fatigue.

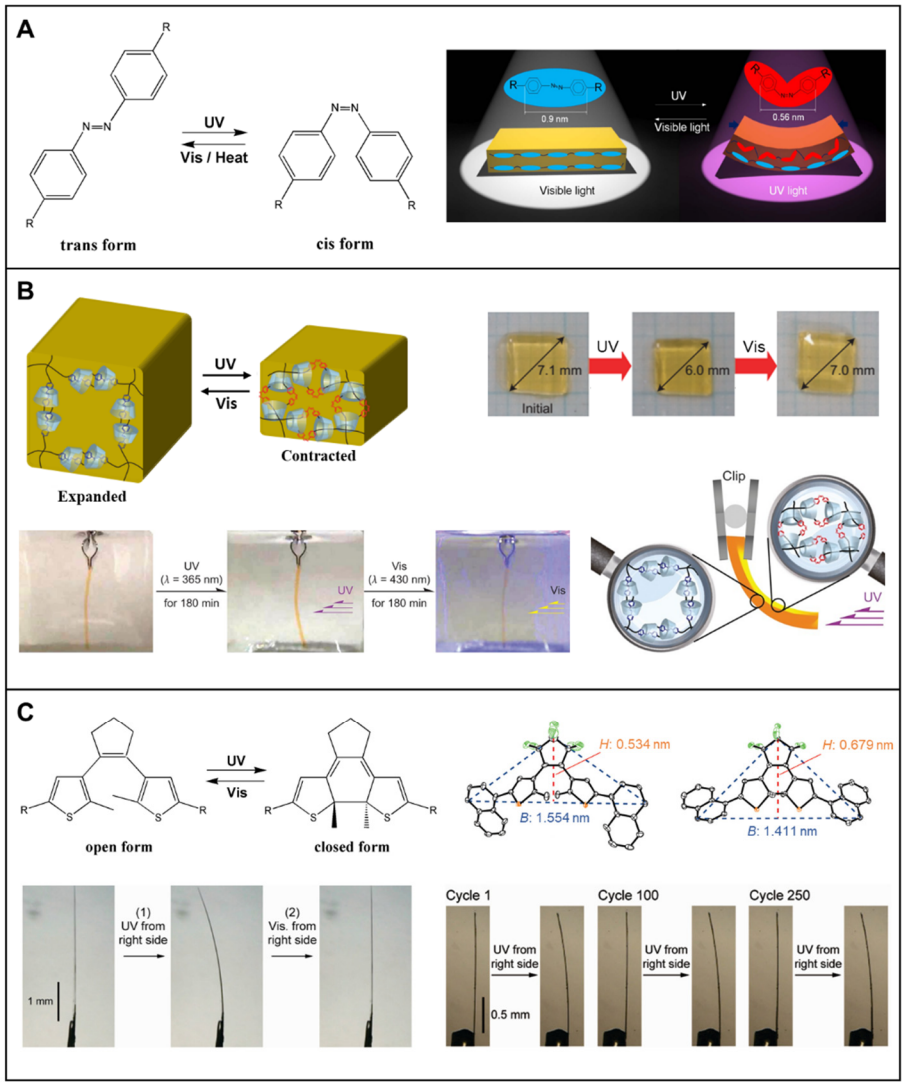

Figure 2. Photoisomerization-induced deformation based on azobenzene and diarylethene. (**A**) Chemical structures of the *trans* and *cis* isomers of azobenzene, and its *trans-cis* photoisomerization in a liquid-crystalline film. (**B**) Schematic illustration of the expansion-contraction behavior of a [c2] AzoCD$_2$ hydrogel upon photoirradiation, highlighting its bending mechanism in water. (**C**) Chemical structures of the open and closed ring isomers of diarylethene, and its open-closed ring photoisomerization in a rectangular cocrystal plate. (**A**) Reproduced with permission [43]. Copyright 2015, Nature Publishing Group. (**B**) Reproduced with permission [44]. Copyright 2016, Nature Publishing Group. (**C**) Reproduced with permission [45]. Copyright 2010, American Chemical Society.

3.2. Deformation Driven by Photothermally-Induced, Mismatched Expansion/Contraction

To convert photothermal stimulation to mechanical deformation, photothermal agents have to be incorporated into thermo-sensitive materials with an asymmetric structure, for instance, graded structure, bilayer structure, and

programmable structure, among others. In an asymmetric system, the temperature change induced by photothermal heating causes a mismatched expansion/contraction, leading to a distinct volume change and deformation.

3.2.1. Graded Structure

Chen and coworkers developed a photothermally-responsive soft actuator by loading polypyrrole (PPy) nanoparticles as a photothermal transducer into a poly(N-isopropylacrylamide) (PNIPAM) hydrogel featuring a gradient in pore size [46]. As shown in Figure 3A, NIPAM, a well-known thermo-responsive material, was first polymerized with a heterobifunctional crosslinker, 4-hydroxybutyl acrylate (4HBA), via hydrothermally-induced free radical polymerization, generating a PNIPAM-OH polymer. As the reaction progressed, the PNIPAM-OH extruded water and gradually precipitated to the bottom, and with the help of the hydrothermally induced dehydration polymerization, finally generating a hydrogel bearing a gradient in pore size. Then, PPy nanoparticles were incorporated into the hydrogel, forming a PPy-loaded photothermal-responsive soft actuator. In Figure 3B,C, the PPy-loaded hydrogel could flexibly fold or curl into a designated pattern and lift weights up in water upon NIR laser irradiation. Because of the graded distribution in pore size, the top surface of the hydrogel shrinked faster than the bottom surface when exposed to a NIR laser, resulting in noticeable bending, folding, or curling. The tunable pore size and various complex actuating behaviors make this soft actuator promising for a variety of applications, such as octopus-like swimming soft robotics and artificial muscles.

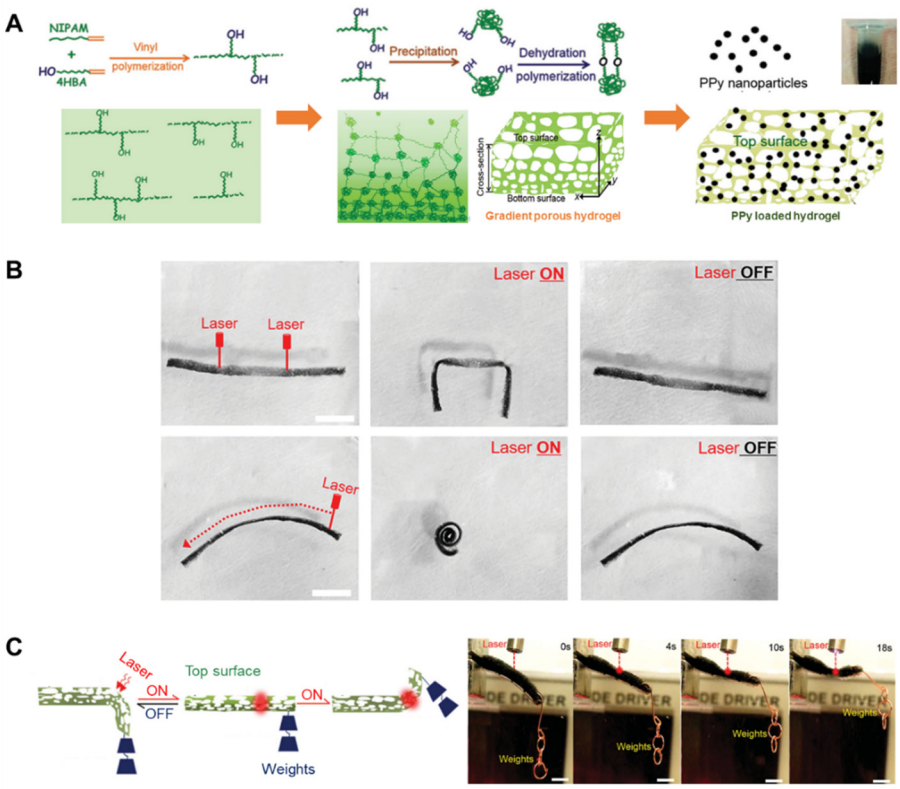

Figure 3. Photothermal-responsive hydrogel actuator with a gradient in pore size. (**A**) Schematic illustration of the three major steps involved in the fabrication of the PPy-loaded PNIPAM hydrogel. (**B**) Folding or curling the PPy-loaded hydrogel by irradiating at a designated position or moving the NIR laser across the surface. Scale bars: 1 cm. (**C**) Schematic illustration showing the PPy-loaded soft actuator lifting weights in water under NIR laser irradiation. Scale bars: 1 cm. (**A**–**C**) Reproduced with permission [46]. Copyright 2015, Wiley-VCH.

3.2.2. Bilayer Structure

The concept of bilayer design is a widely adopted and effective strategy for developing novel photothermal-responsive actuators. Hu and coworkers developed a rolled bilayer composite actuator, where the CNT layer worked for photothermal conversion, and the heat was transferred to the polydimethylsiloxane (PDMS) layer [47]. PDMS has a larger thermal expansion coefficient (3×10^{-4} K^{-1}) compared to CNT (5×10^{-6} K^{-1}), resulting in asymmetric expansion and contraction of the bilayer composite. This leads to rapid and reversible unrolling/rolling motions upon periodic light stimulation (Figure 4A). This photothermal-responsive bilayer actuator exhibited fast,

significant deformation, transitioning from a tubular to a flat shape (with an angel change > 200°), enabling various complex actuating behaviors such as somersaulting, cyclic wobbling, jumping, crawling, and grabbing.

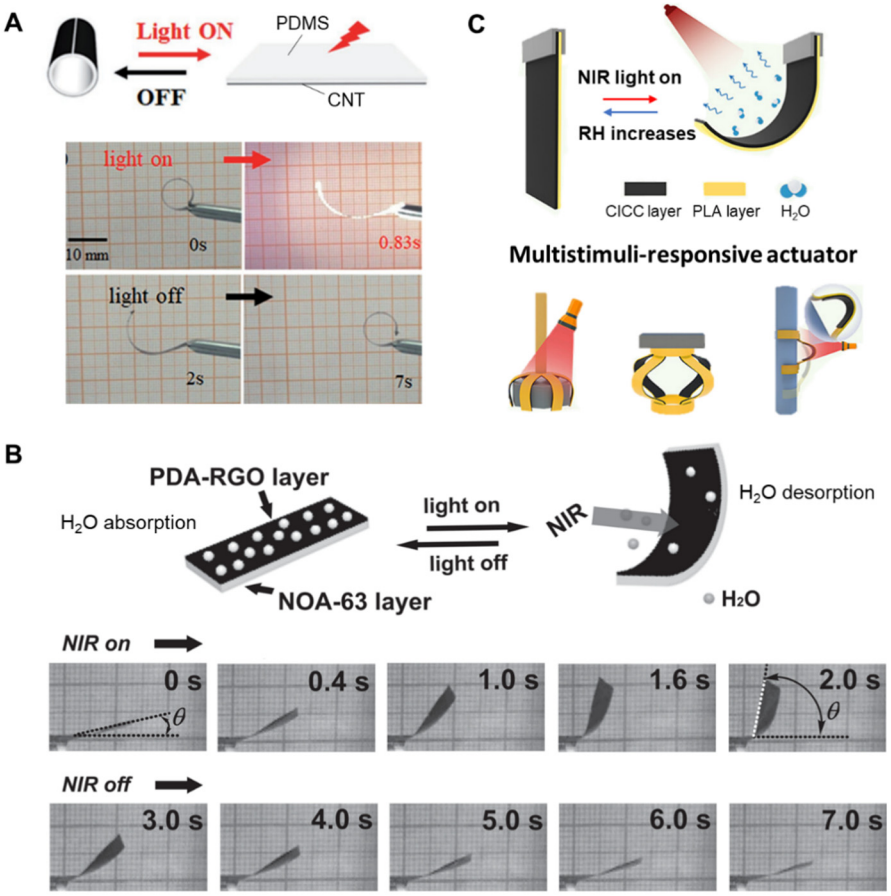

Figure 4. Photothermal-responsive actuator with a bilayer structure. Schematic illustration and real-time optical images showing (**A**) the reversible unrolling/rolling behavior of the tubular CNT/PDMS bilayer actuator under periodic light irradiation and (**B**) the reversible bending/unbending motion of the PDA-RGO/NOA-63 bilayer actuator towards the source of periodic NIR light stimulation under ambient conditions. (**C**) Schematic illustration of the actuation mechanisms of multistimuli-responsive CICC/PLA bilayer actuators under NIR light, humidity, and temperature stimuli. (**A**) Reproduced with permission [47]. Copyright 2017, Wiley-VCH. (**B**) Reproduced with permission [48]. Copyright 2014, Wiley-VCH. (**C**) Reproduced with permission [49]. Copyright 2023, American Chemical Society.

Thermal expansion refers to the change in the volume and shape of a material caused by increased molecular kinetic energy as temperature rises [26]. In addition to thermal expansion, thermal-induced water desorption can also cause shape deformation, offering another mechanism for designing photothermal-responsive actuators. To this end, Sun and coworkers constructed a NIR light-driven bilayer actuator using a NIR-absorbing and hydrophilic layer of polydopamine-modified reduced graphene oxide (PDA-RGO) and a NIR-transparent and hydrophobic layer of UV-cured Norland Optical Adhesive (NOA-63) [48]. The PDA-RGO layer, composed of hydrophilic PDA and photothermal RGO, could desorb water to shrink and reabsorb water from the environment to swell when illuminated by the NIR light. The NOA-63 layer, however, remained unchanged, resulting in asymmetric shrinking and swelling of the bilayer structure. The resultant bilayer actuator displayed reversible bending and unbending motions under periodic NIR light irradiation (Figure 4B).

Chen and co-workers proposed a high-performance biomass-based bilayer actuator (CICC/PLA) that operates based on a multistimuli-responsive actuation mechanism [49]. The cuttlefish ink nanoparticles/cellulose nanofiber (CINPs/CNF) composite (CICC) layer quickly converted the absorbed optical energy into thermal energy, causing thermal expansion to the polylactic acid (PLA) layer. Simultaneously, the increased temperature induced the desorption of water molecules from the CICC layer, resulting in its thermal shrinkage. As a result, the CICC/PLA bilayer soft actuator exhibited reversible deformation under NIR light, humidity, and temperature stimuli. Due to this multistimuli-responsive actuation mechanism, a series of untethered soft robots can be

customized for various functions, such as a grasping robot driven by NIR-light, a weightlifting robot activated by humidity, and a climbing robot inspired by monkey movement capable of climbing a vertical pole (Figure 4C).

3.2.3. Programmable Structure

Natural plants exhibit diverse mechanical motions in response to environmental stimuli, such as the two-dimensional (2D) opening and closing behavior of pinecones and the three-dimensional (3D) twisting movement of *Bauhinia variegata* pods. The alignment direction of cellulose fibrils in plant cells plays an important role in guiding motor behaviors.

Inspired by the biological systems, Peng and coworkers developed a general and effective strategy to achieve complex, tunable photothermal actuation based on a programmable aligned nanostructure [50]. In this case, they designed a CNT-wax/polyimide actuator by embedding aligned CNTs in paraffin wax on a polyimide substrate. The aligned CNT mimicked the cellulose fibrils, while the paraffin wax filled the gaps between the CNTs, resembling the amorphous fillers (e.g., hemicellulose and lignin) in the plant cell wall. By adjusting the orientation of the aligned CNTs through simple cutting of the CNT-wax/polyimide film in different directions, the actuator could achieve a variety of mechanical deformations from bending to helical buckling (Figure 5). By integrating distinct pre-programmed structures, this tunable photothermal actuator can execute sophisticated and well-controlled motions, making it a promising candidate for light-responsive robotic arms.

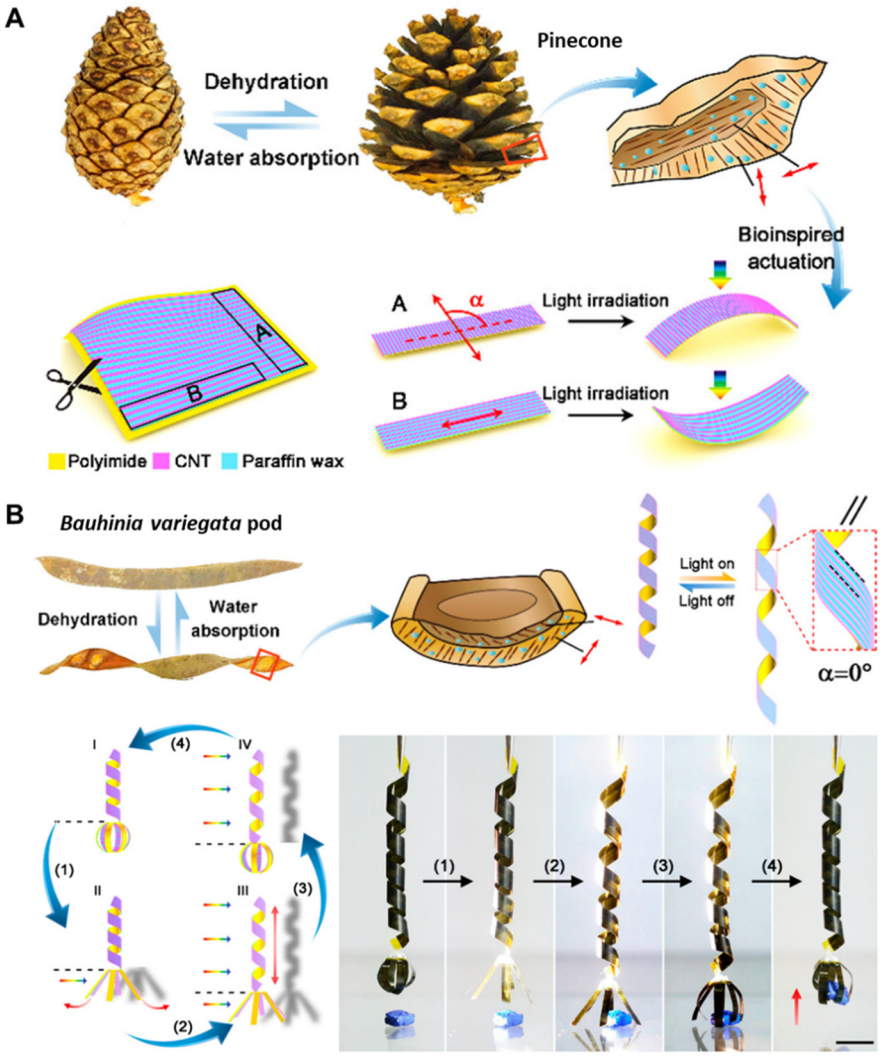

Figure 5. Photothermal-responsive actuator with a programmable structure. (**A**) Opening/closing behavior of a pinecone, and the apheliotropic/phototropic bending motion of the CNT-wax/polyimide actuator with different orientation of aligned CNTs. (**B**) Twisting movement of a *Bauhinia variegata* pod and the grasping/releasing actuation of an assembled mechanical arm utilizing several CNT-wax/polyimide actuators with different pre-programmed structures. Scale bars: 1 cm. (**A**,**B**) Reproduced with permission [50]. Copyright 2016, American Chemical Society.

3.3. Deformation Driven by Photothermally-Induced Phase Transition

Liquid crystal polymeric materials, e.g., LCNs and LCEs, contain oriented mesogens that typically maintain an ordered phase at room temperature. As the temperature increases, the ordered phase transforms into a disordered phase, realizing a dramatic volume change. In recent years, photothermal-induced order-disorder phase transition in liquid crystal-based materials has gained attention for enabling rapid and reversible deformation. Lin and coworkers explored NIR-responsive graphene/LCE nanocomposites, in which the graphene sheets were highly aligned within the nematic LCE matrix, possessing superior and tunable photomechanical actuation capabilities [51]. Upon NIR light irradiation, the aligned graphene efficiently converted light energy into thermal energy. The heat rapidly transferred to the surrounding LCE, triggering the nematic-to-isotropic phase transition, and thus induced a macroscopic contraction (Figure 6A). Over long-term cycling under NIR irradiation, the graphene/LCE nanocomposites exhibited fast response time, high actuation stress, large contraction strain, and negligible fatigue. Parmeggiani and coworkers fabricated a light-responsive microhand made of LCN with splayed alignment [52]. Under laser irradiation, the black object absorbed light and transferred heat to the splay-aligned LCN microhand (Figure 6B). The resulting heat induced the transition from the splayed alignment to a disordered phase, resulting in the bending of the microhand and enabling it to capture the object.

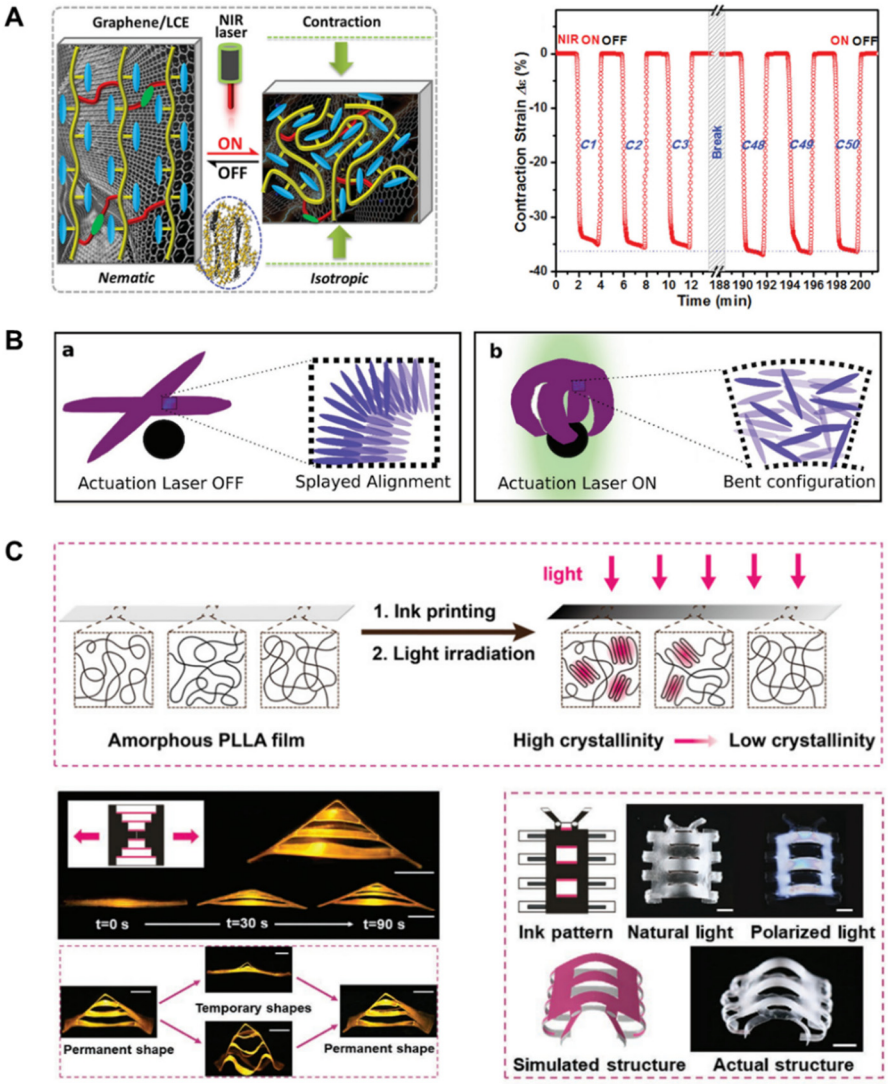

Figure 6. Photothermally-induced phase transition triggering mechanical deformation. (**A**) Schematic diagram demonstrating the nematic-isotropic phase transition in a graphene/LCE nanocomposite, and the real-time contraction strain of the graphene/LCE actuator upon cycling NIR irradiation. (**B**) Schematic diagram showing the splay-disorder phase transition in a light-responsive microhand. (**C**) Formation of a gradient crystallinity pattern induced by photothermal effect from the digital ink, and the consequent 4D transformed pyramid and worm-like structure. Scale bars: 5 mm. (**A**) Reproduced with permission [51]. Copyright 2015, Wiley-VCH. (**B**) Reproduced with permission [52]. Copyright 2017, Wiley-VCH. (C) Reproduced with permission [53]. Copyright 2020, Wiley-VCH.

In addition to order-disorder phase transition, photothermally-induced amorphous-crystallization transition offer another strategy to trigger shape deformation. For example, Xie and coworkers used photothermally-induced heterogeneous amorphous-crystallization phase transitions to achieve four-dimensional (4D) transformation [53]. In Figure 6C, an ink pattern with gradient in grayness was printed on an amorphous poly(L-lactide) (PLLA) film, which was then exposed to flood fluorescent light. The light exposure caused a gradient in crystallinity pattern due to the photothermal effect from the digital ink. The resulting heterogeneity in crystallinity reduced spatially distinct shape recovery abilities, allowing the 2D PLLA film to spontaneously evolve into a 3D shape. Using this 4D transformation strategy, complex pyramid and worm-like structures could be readily manufactured in seconds.

4. Emerging Applications

Light-driven soft actuators, with their unique advantages of wireless actuation, rapid response, and remote control, have recently sparked considerable interests for potential applications in a variety of areas. In this section, we highlight some of the most exciting applications, including light-responsive biomimetic locomotion robotics, origamis-assisted 3D architecture manufacturing, microfluidic systems, and biomedicine.

4.1. Light-Responsive Biomimetic Locomotion Robotics

In nature, many biological organisms are capable of autonomous, rapid, and self-regulated action in response to environmental stimuli, providing a continuous source of inspiration for the design of intelligent soft robotics. Mimicking the phototropism of sunflowers, He and coworkers developed an omnidirectional tracker, refer to as SunBOT, that could autonomously and instantaneously detect and track incident light in three-dimensions [54]. Sunflowers track light through photoreceptors in their stems. The incident light creates a graded distribution of auxin between the irradiated and shaded sides, leading to asymmetric stem growth that keeps the sunflower disc oriented toward the sun throughout the day. As shown in Figure 7A, SunBOT is made of a thermo-responsive PNIPAM hydrogel, together with homogeneously distributed Au nanoparticles (AuNPs) serving as both the photoreceptor and photothermal converter. When immersed in water, the asymmetric deformation between the illuminated and thereby heated side and the shaded cool side enables the SunBOT to autonomously track and aim at the incident light coming from different directions. This biomimetic phototropic device holds great promise for application in solar steam generation, achieving up to a 400% enhanced solar energy harvesting when compared with the conventional, non-tropistic materials under sunlight irradiation.

By mimicking the capture motion of Venus Flytrap, Priimagi and coworkers developed a light-driven soft gripper capable of preforming object recognition and autonomous closure [55]. They constructed a splay-aligned LCE strip attached to the tip of an optical fiber, with a transparent window at the center to allow light to pass through. As illustrated in Figure 7B, when an object entered the gripper's field of view, it reflected or scattered sufficient light onto the LCE strip, triggering the closure action to capture the object. The intensity of light reflected or scattered by the object served as optical feedback, enabling the soft gripper to distinguish between different targets and execute the corresponding actuation. This flytrap-inspired soft gripper, using optical feedback to trigger photomechanical motion, offers a new approach to autonomous, self-regulated, intelligent soft robotics.

In addition to plants, animals also exhibit remarkable capabilities to convert reversible shape deformation into macroscopic locomotion, such as slithering of snakes, swimming of fish, and telescopic motion of inchworms. In one study, Hu and coworkers reported a light-driven autonomous actuator capable of continuous self-oscillation by mimicking human sit-up motion [56]. The actuator, composed of CNT and PDMS, was shaped like a curled droplet. As shown in Figure 8A, when exposed to constant light from the right side, the curled bimorph actuator flattened (Figure 8A-i) due to the photothermal expansion of the PDMS layer. Once flat (Figure 8A-ii), reduced light intensity triggered the actuator to sit up, restoring it to its original shape. The self-shadowing-induced light-mechanical feedback loop enabled the CNT/PDMS actuator to exhibit continuous self-sustained oscillation under constant light exposure, resembling the human sit-up motion. Real-time optical images of one complete cycle of this biomimetic sit-up motion are shown in Figure 8B.

Furthermore, by mimicking phototactic locomotion of snakes (Figure 8C), Hu and coworkers fabricated a self-crawling artificial snake using the droplet-shaped CNT/PDMS actuator. This artificial snake could autonomously and continuously creep toward a light source. Infrared thermal images were recorded to investigate the phototactic locomotion mechanism of the artificial snake (Figure 8D). The friction generated during the cyclic wavelike self-oscillation facilitated the continuous forward motions toward the light. Under constant light illumination (330 mW cm^{-2}) for 30 s, the self-crawling artificial snake moved almost 6 mm (Figure 8E). Benefiting from its autonomous and continuous self-oscillation, this light-driven droplet-shaped actuator shows great potential in self-locomotive soft robotics and smart energy harvesting devices.

4.2. Origami-Assisted 3D Architectures

Traditional origami and kirigami techniques provide valuable inspiration for fabricating sophisticated 3D structures. By integrating these techniques with photo-actuation, researchers can fabricate customized 3D architectures and complex actuators with greater ease [57–59]. In one study, Lee and coworkers applied the origami concept to a graphene oxide/ethylene cellulose (GO/EC) photothermal-actuated bilayer system, enabling programmable 2D-to-3D shape morphing [58]. As illustrated in Figure 9A, 2D triangular and annular rings were transformed into intricate 3D architectures by programming the shape and relative position of the GO domains. In the case of triangular ring, GO was uniformly casted onto EC, causing its three angles to bend symmetrically inward upon light irradiation (Figure 9A(a)). For annular ring, GO was deposited on the upper surface of EC in the bare regions and on the lower surface in the shaded regions, resulting in a centrosymmetric undulatory 3D structure. These versatile, flexible, and programmable 3D architectures offer exciting opportunities for the fabrication of intelligent soft actuating devices.

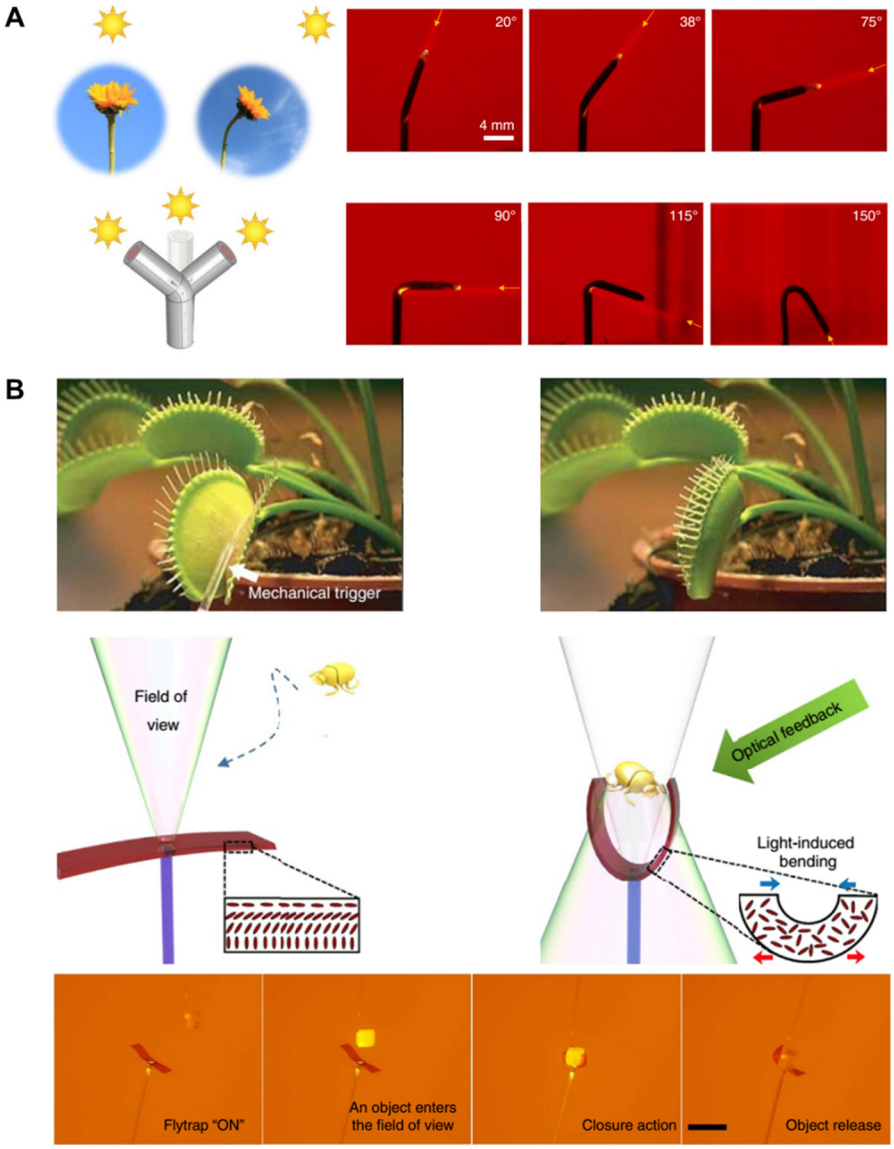

Figure 7. Light-responsive biomimetic locomotion robotics inspired by natural plants. (**A**) Sunflower-like phototropism AuNP-PNIPAM SunBOT, which autonomously tracks and aims at the laser coming from different directions (20–150°). (**B**) Flytrap-inspired, light-driven soft gripper capturing a small scattering object falling on its surface. Scale bar: 5 mm. (**A**) Reproduced with permission [54]. Copyright 2019, Nature Publishing Group. (**B**) Reproduced with permission [55]. Copyright 2017, Nature Publishing Group.

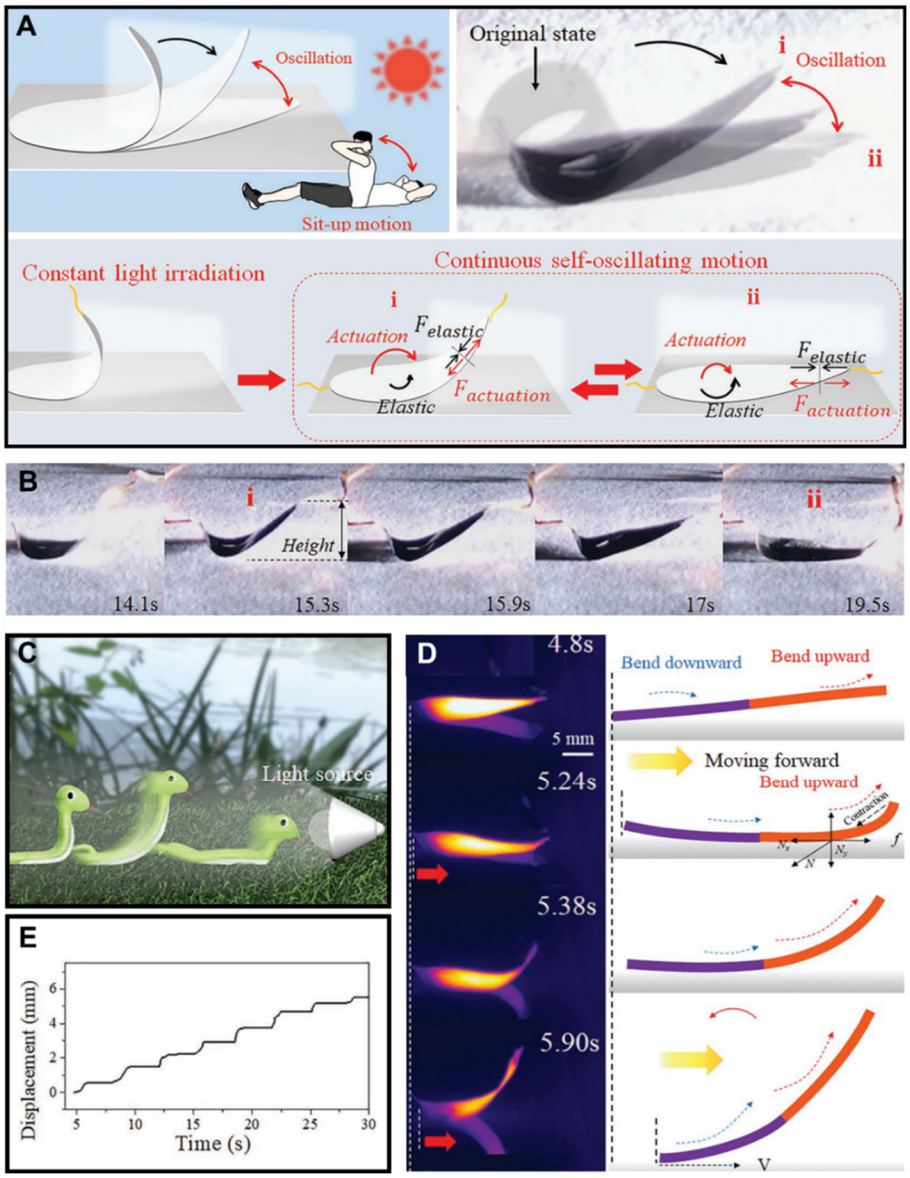

Figure 8. Light-responsive biomimetic locomotion robotics inspired by animals. (**A**) Light-driven, droplet-shaped CNT/PDMS actuator with autonomous self-oscillation, mimicking the human sit-up motion. (**B**) Real-time optical images showing one cycle of the biomimetic sit-up motion. (**C**) Schematic illustration of the phototactic locomotion of snakes. (**D**) Real-time infrared thermal images and schematic illustration showing the phototactic locomotion mechanism of the self-crawling artificial snake under constant light irradiation (330 mW cm^{-2}). (**E**) Time profile of crawling displacement under constant light illumination (330 mW cm^{-2}) for 30 s. (**A**–**E**) Reproduced with permission [56]. Copyright 2020, Wiley-VCH.

Zeng and coworkers devised a kirigami-assisted, light-fueled rolling robot using LCN and a photothermal dye [59]. As shown in Figure 9B, the fabrication process involved rolling an LCN/dye sheet into a tubular structure with triangular petals at both ends. Upon on–off switching of light (470 nm), the triangular petals exhibited blooming and closing motion. When exposed to an obliquely incident light beam, the periodic bending of the petals against the ground induced sequential rolling movements (Figure 9C). By adjusting the direction of light irradiation, the rolling robot was able to navigate along diverse trajectories. It is anticipated that integrating origami and kirigami techniques with light-responsive materials will enable the construction of complex architectures and dynamic shape morphing. This approach holds great potential in endowing soft actuators with multi-mode motions and advanced functionalities.

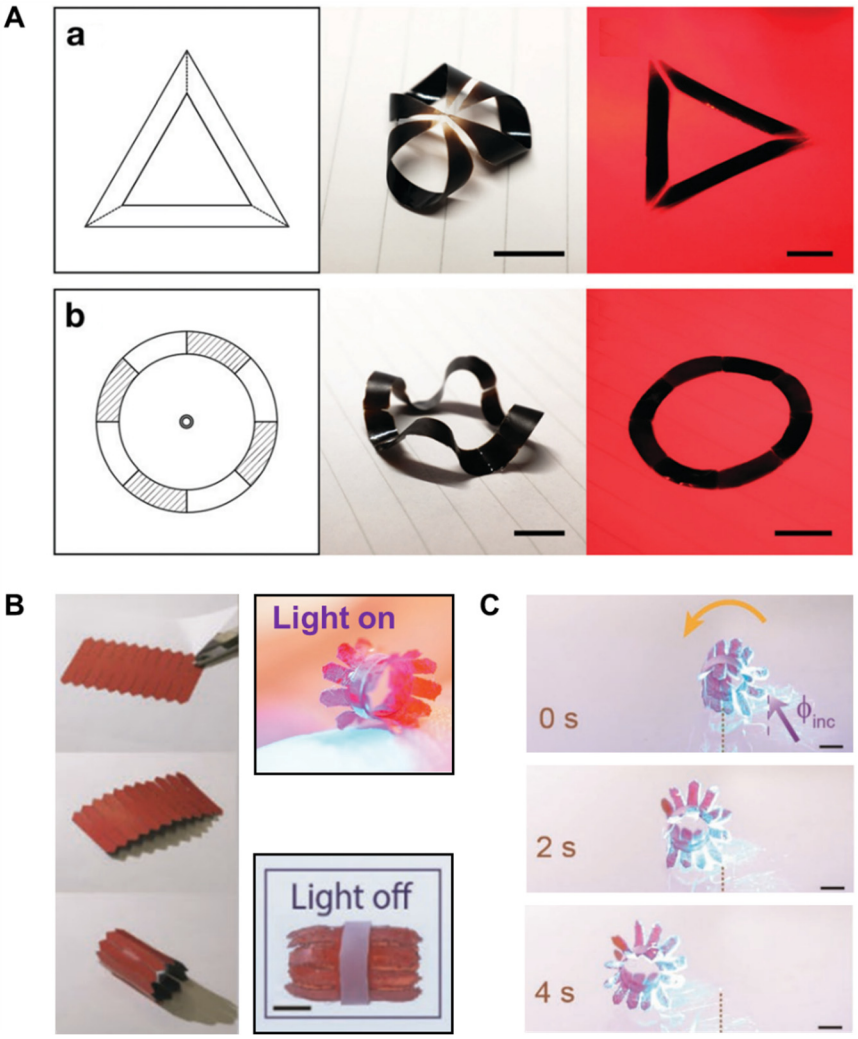

Figure 9. Origami- and kirigami-assisted 3D architectures derived from 2D patterns. (**A**) Shape morphing of an equilateral triangular ring and an annulus ring with a predesigned graphic pattern. Scale bars: 1 cm. (**B**) Fabrication of the kirigami-assisted, light-fueled rolling robot and its blooming/closing behavior under on–off light (470 nm) switching. (**C**) Real-time optical images demonstrating sequential rolling movements induced by an obliquely incident light beam (violet arrow). Scale bars: 2 mm. (**A**) Reproduced with permission [58]. Copyright 2020, Royal Society of Chemistry. (**B**,**C**) Reproduced with permission [59]. Copyright 2020, Wiley-VCH.

4.3. Microfluidic Systems

Over the past decades, microfluidic devices have attracted significant attention in microscale reactions and analyses. Integrating light-responsive actuators within microfluidic systems enables remote and precise liquid control, significantly expanding their potential applications, especially in chemical and biomedical engineering [60]. Diamond and coworkers developed a reversible light-driven hydrogel valve compatible for microfluidic systems [61]. The valve leverages the photoisomerization of a spiropyran derivative, inducing rapid and reversible shrinking and swelling to enable repeatable valve opening and closing under periodic blue LED illumination (Figure 10A). With its simplified, compact design and non-contact operation, this light-driven hydrogel valve holds promise for microfluidic applications.

In another example, Yu and coworkers reported a strategy for manipulating fluid flow using light-induced asymmetric deformation of tubular micro-actuators (TMAs) [62]. They fabricated various TMA geometries (i.e., straight, serpentine, helical, and 'Y'-shaped) using linear LCP functionalized with photoactive azobenzene (Figure 10B). When exposed to blue light with a gradient in intensity along the TMA, asymmetric deformation generated capillary force that propelled liquid toward the regions of lower light intensity. These TMAs enabled precise light-driven control of liquid transport, multiphase mixing, and microsphere capture and transport at the microscale. This strategy simplifies microfluidic systems, paving the way for intelligent, pump-free microfluidic devices.

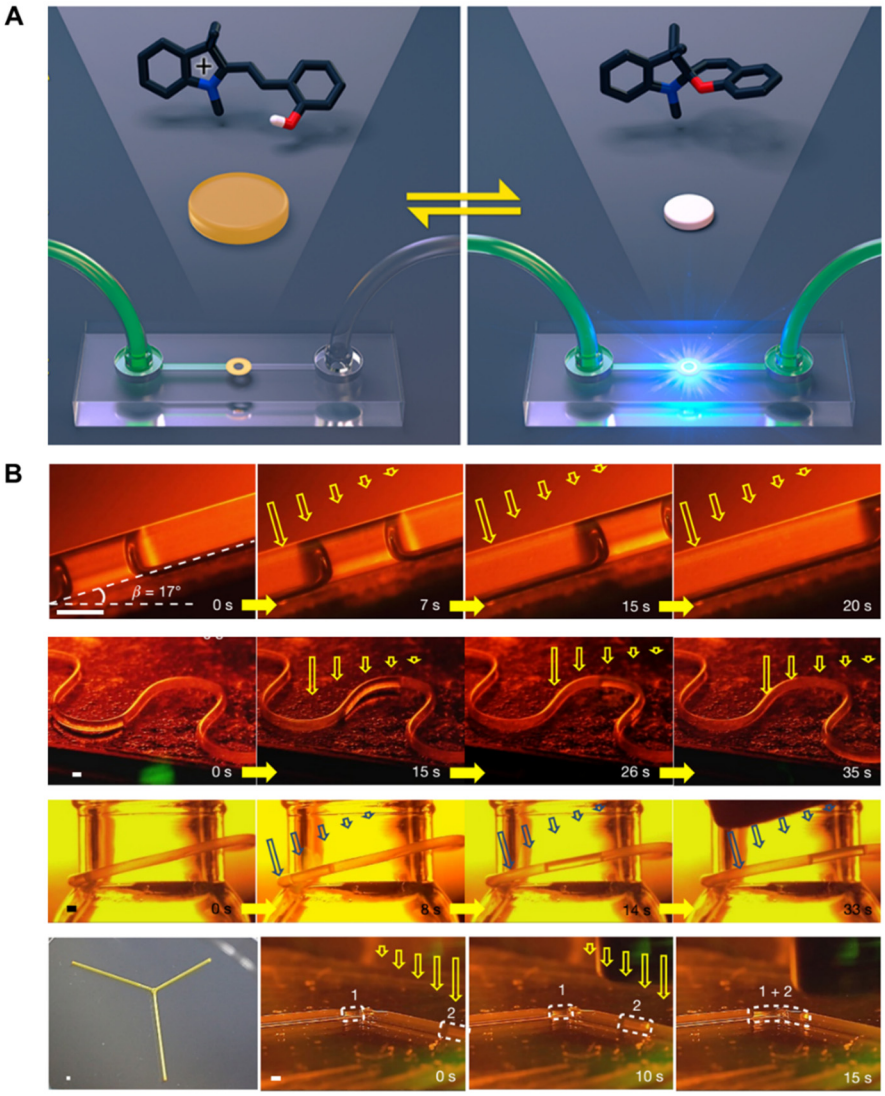

Figure 10. Light-responsive actuators in microfluidic systems. (**A**) Schematic illustration of a light-driven spiropyran-based hydrogel functioning as a smart valve in a microfluidic device. (**B**) Real-time optical images demonstrating light-driven fluid control in tubular microactuators (TMAs) with straight, serpentine, helical and 'Y'-shaped geometries. Scale bars: 0.5 mm. (**A**) Reproduced with permission [61]. Copyright 2015, American Chemical Society. (**B**) Reproduced with permission [62]. Copyright 2016, Nature Publishing Group.

4.4. Biomedical Applications

In recent years, light-responsive actuators have been increasingly pursued for diverse biomedical applications, such as drug delivery, wound closure, artificial muscle, biosensing, tissue engineering, and minimally invasive surgery [63,64]. Notable examples of their use in on-demand drug delivery and minimal invasive surgery are highlighted as follows.

4.4.1. On-Demand Drug Delivery

Biological organisms rely on specific recognition events on cellular surfaces to transfer information from extracellular to intracellular space. Inspired by cells, Thayumanavan and coworkers used the photoisomerization of azobenzene to dynamically alter interface mobility for on-demand drug delivery [65]. As shown in Figure 11A, they fabricated light-actuated vesicles with an 8 nm bilayer membrane through the self-assembly of a hydrophilic-azobenzene-hydrophobic diblock copolymer (PEG-azo-PLA). Upon light irradiation, the photo-induced *trans*-to-*cis* isomerization of azobenzene caused localized perturbation at the interface, which rapidly propagated through the entire membrane, triggering the release of the preloaded hydrophobic or hydrophilic cargos. In Figure 11B, the encased cargo was released under UV (360 nm) or blue (450 nm) light and ceased when the light was turned off. The release process could be modulated by adjusting the intensity and wavelength of the light, offering a promising strategy for controlled release.

In another example, Liu and coworkers developed biomimetic pulsating vesicles with a dual-responsive behavior, exhibiting light-triggered disassembly-reassembly and pH-tunable membrane permeability [66]. These supra-amphiphilic vesicles were formed through the self-assembly of α-cyclodextrin (α-CD) with an azobenzene-containing aromatic foldamer. α-CD selectively recognizes the *trans* isomer of azobenzene while excluding its *cis* counterpart, inducing dynamic vesicular disassembly and reassembly. Upon UV (325 nm) irradiation, the *trans*-to-*cis* isomerization of azobenzene led to vesicle rupture, facilitating the rapid release of the encased anticancer drugs (DOX). Conversely, exposure to visible light (440 nm) restored the *trans* configuration, enabling the vesicles to reassemble. This reversible transformation provides a controllable platform for drug delivery.

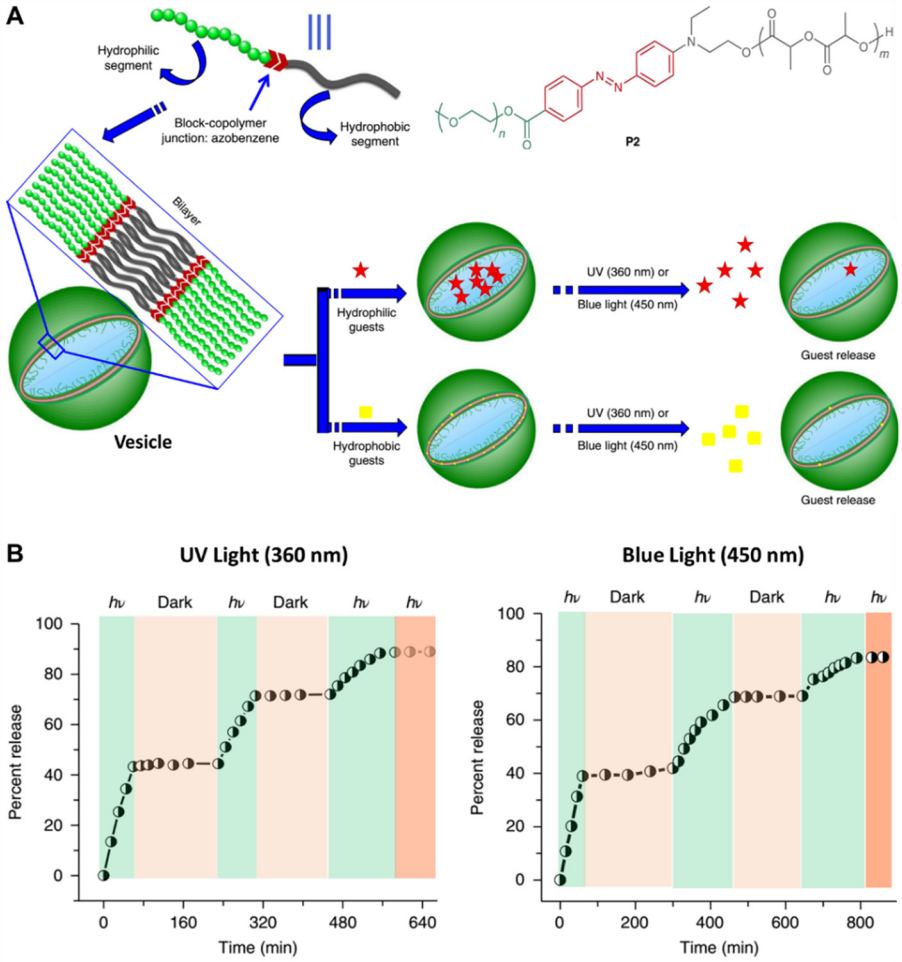

Figure 11. Light-actuated vesicles applied to on-demand drug delivery. (**A**) Schematic illustration of PEG-azo-PLA vesicles, showing their chemical structure and the encapsulation/release mechanism for hydrophilic or hydrophobic cargo molecules. (**B**) Release profiles of hydrophobic cargo molecules (DiI) from PEG-azo-PLA vesicles under alternating on–off cycles of UV (360 nm) and blue (450 nm) light, respectively. (**A**,**B**) Reproduced with permission [65]. Copyright 2018, Nature Publishing Group.

4.4.2. Minimal Invasive Surgery

Soft actuators will revolutionize minimal invasive surgery by enabling highly adaptable and less invasive operation [67]. To this end, Raquez and coworkers developed a light-responsive, fast-actuating self-tightening suture (PCL/CNC-AgNPs) composed of biocompatible poly(ε-caprolactone) and silver nanoparticle-grafted cellulose nanocrystals [68]. As shown in Figure 12A, the pre-stretched PCL/CNC-AgNPs, initially fixed in a loose knot-like shape with 100% deformation, rapidly recovered its shape under NIR irradiation, leading to self-tightened suturing within 30 s. This innovative suture, benefiting from a simple, noninvasive one-step procedure and excellent antibacterial properties, holds potential for minimally invasive surgical applications.

With rapid development of medical robotics, continuum soft robots are particularly beneficial in endoluminal diagnosis and intervention, as they can navigate confined and tortuous anatomical pathways with exceptional dexterity, flexibility, and maneuverability. Zhou and coworkers introduced a submillimeter-scale fiber robot (~1 mm) capable of decoupled macro- and micro-manipulations for endoluminal operations [69]. The design integrates thin

optical fibers that function as both mechanical tendons and light waveguides, allowing macro actuation via tendon-driven motion while simultaneously enabling micro-actuation through a built-in light-driven liquid crystal elastomer-based parallel robot. This submillimeter fiber robot, leveraging cross-scale motion several millimeters down to tens of micrometers, holds promise for delicate micro-operations in endoluminal or endocavitary interventions.

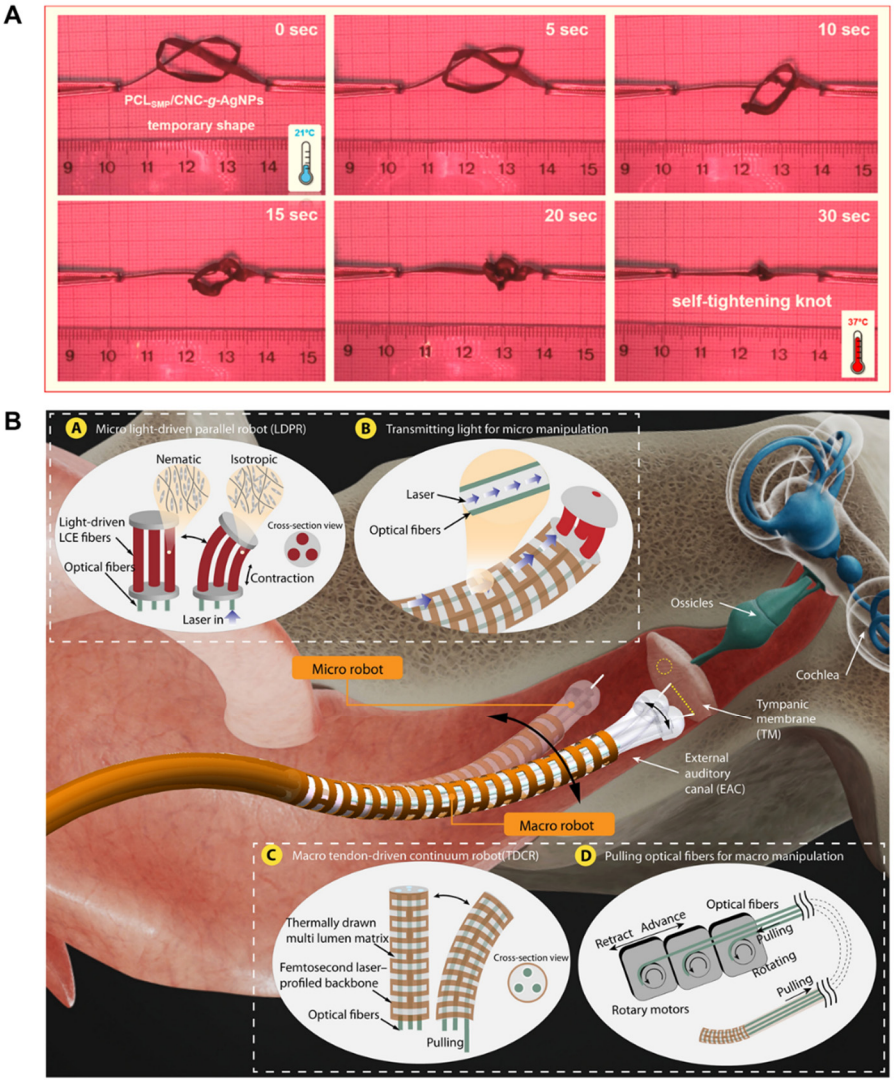

Figure 12. Light-responsive actuators applied to minimal invasive surgery. (**A**) Real-time optical images demonstrating the self-tightening process of the PCL/CNC-AgNPs suture under NIR irradiation. (**B**) A submillimeter fiber robot utilizing thin optical fibers for both tendon-driven macro motion and light-driven micro motion, facilitating cross-scale endoluminal manipulations. (**A**) Reproduced with permission [68]. Copyright 2018, American Chemical Society. (**B**) Reproduced with permission [69]. Copyright 2024, AAAS.

5. Challenges and Future Perspectives

Owning to their merits such as rapid response, flexible actuation, and remote control, light-driven soft actuators show great promise in applications ranging from soft robotics to complex 3D structure manufacturing, as well as microfluidic systems and biomedical research. Despite the rapid progress over the past decade, the soft actuators still face a set of challenges.

5.1. Integrating Multi-Mode Locomotion

Although significant progress has been made in designing light-driven actuators with sensitive and controllable actuation, there remains substantial room for advancing multi-mode locomotion. Integrating diverse locomotion behaviors, such as walking, jumping, climbing, and swimming, would enable light-driven soft robotics to operate in hazardous or inaccessible environments, reducing the need for human intervention. However, a key

challenge remains in achieving complex, sequential shape deformations and effectively translating them into diverse locomotion modes. Addressing this issue will be critical for future research in this field.

5.2. Designing Intelligent Autonomous Systems

Autonomous actuation, free of human intervention or computer control, has received increasing attention in recent years. This automation relies on the ability to independently determine when and how to move based on the feedback receiving from the environment. However, only a limited number of studies have been reported on the design of light-driven autonomous systems. As we discussed earlier, Priimagi and coworkers developed a flytrap-inspired soft gripper that utilized optical feedback based on the reflectance intensity of the object, enabling the device to distinguish and capture the targets [55]. In another example, a light-mechanical feedback loop induced autonomous and continuous self-oscillation [56]. Despite these advancements, existing autonomous systems remain limited to relatively simple and repetitive actions, with issues in terms of response speed, control accuracy, repeatability, and durability still needing to be addressed. In contrast, most natural organisms exhibit diverse self-regulated behaviors to adapt to a dynamic environment. Drawing inspiration from biological organisms could significantly advance light-driven soft actuators, paving the way for intelligent, self-regulating actuation.

5.3. Exploiting Diversified Light-Responsive Materials

Despite the extensive development of materials for light-driven soft actuators, their diversity remains limited, particularly in terms of the availability of biocompatible and biodegradable light-responsive materials for in vivo applications. Moreover, many existing photoactive components such as azobenzene, spiropyran, diarylethene, anthracene, and cinnamate, are primarily activated by UV light. However, long-term UV irradiation will accelarate materials aging, reducing their service life, and poses significant health risks, including eye damage and skin cancer [70], thereby limiting their biomedical applications. To this end, the development of materials that respond effectively to visible or NIR light is highly desirable. Advancements in diversified light-responsive materials hold great promise for breakthroughs in targeted drug delivery, surgical suturing, vascular waste scavenging, and functional scaffolds for tissue repair/regeneration.

5.4. Developing New Frontiers of Application

The defining advantages of light-driven soft actuators, including wireless operation, non-invasiveness, and spatiotemporally precise energy delivery, make them well-positioned as disruptive solutions for scenarios where conventional actuators fail. For example, light-driven soft actuators are able to travel through the unstructured, complex, or even extreme environments, allowing them to operate safely in hazardous zones (nuclear/chemical sites) without spark risks from electrical wiring and function well in vacuum (e.g., space exploration) where fluid/pneumatic systems falter. In principle, untethered soft micro-tools (e.g., photo-responsive grippers) allow for complex surgery in confined anatomy, whereas light-actuated soft microrobots can navigate through physiological barriers (e.g., blood-brain barrier) for site-specific therapeutic release, eliminating infection risks from physical connections. Furthermore, light-driven soft actuators exhibit definite superiority when interacting with human on account of their inherent flexibility and rapid photo-responsiveness, allowing breakthrough advances in wearable technology (e.g., responsive exoskeletons) and smart interfaces (e.g., brain-machine systems, dynamic haptic surfaces). Strategic focus on these application-driven advances will accelerate the transition from laboratory innovation to real-world impact where light-driven soft actuation delivers irreplaceable value.

6. Concluding Remarks

We have presented a comprehensive review of light-driven soft actuators, covering advanced light-responsive materials and innovative design principles, as well as their emerging applications in biomimetic locomotion robotics, origamis-assisted 3D architectures, microfluidic systems, and biomedical science. We also highlight the challenges in this rapidly growing field and offer perspectives on future directions. The collaborative efforts from scientists across multiple disciplines including materials science, chemistry, biomedicine, and mechanical engineering will drive the development of intelligent light-driven soft actuators, bringing them closer to practical applications in everyday life.

Author Contributions: S.H.: conceptualization, writing—original draft preparation. D.Z.: writing—reviewing and editing. Y.X.: conceptualization, supervision, writing—reviewing and editing. All authors have read and agreed to the published version of the manuscript.

Funding: The preparation of this article was supported by startup funds from the Georgia Institute of Technology. As a visiting graduate student from Beijing Forestry University, S.H. was also partially supported by a fellowship from the China Scholarship Council.

Institutional Review Board Statement: Not applicable.

Informed Consent Statement: Not applicable.

Data Availability Statement: Not applicable.

Conflicts of Interest: The authors declare no conflict of interest.

References

1. Bartlett, N.W.; Tolley, M.T.; Overvelde, J.T.B.; Weaver, J.C.; Mosadegh, B.; Bertoldi, K.; Whitesides, G.M.; Wood, R.J. A 3D-printed, functionally graded soft robot powered by combustion. *Science* **2015**, *349*, 161−165.
2. Wang, Y.; Ye, H.; He, J.; Ge, Q.; Xiong, Y. Electrothermally controlled origami fabricated by 4D printing of continuous fiber-reinforced composites. *Nat. Commun.* **2024**, *15*, 2322.
3. Iamsaard, S.; Asshoff, S.J.; Matt, B.; Kudernac, T.; Cornelissen, J.; Fletcher, S.P.; Katsonis, N. Conversion of light into macroscopic helical motion. *Nat. Chem.* **2014**, *6*, 229−235.
4. Silverberg, J.L.; Na, J.H.; Evans, A.A.; Liu, B.; Hull, T.C.; Santangelo, C.D.; Lang, R.J.; Hayward, R.C.; Cohen, I. Origami structures with a critical transition to bistability arising from hidden degrees of freedom. *Nat. Mater.* **2015**, *14*, 389–393.
5. Na, H.; Kang, Y.W.; Park, C.S.; Jung, S.; Kim, H.Y.; Sun, J.Y. Hydrogel-based strong and fast actuators by electroosmotic turgor pressure. *Science* **2022**, *376*, 301–307.
6. Marago, O.M.; Jones, P.H.; Gucciardi, P.G.; Volpe, G.A.; Ferrari, C. Optical trapping and manipulation of nanostructures. *Nat. Nanotechnol.* **2013**, *8*, 807–819.
7. Han, D.D.; Zhang, Y.L.; Ma, J.N.; Liu, Y.Q.; Han, B.; Sun, H.B. Light-mediated manufacture and manipulation of actuators. *Adv. Mater.* **2016**, *28*, 8328–8343.
8. He, Q.; Yin, R.; Hua, Y.; Jiao, W.; Mo, C.; Shu, H.; Raney, J.R. A modular strategy for distributed, embodied control of electronics-free soft robots. *Sci. Adv.* **2023**, *9*, eade9247.
9. Nocentini, S.; Parmeggiani, C.; Martella, D.; Wiersma, D.S. Optically driven soft micro robotics. *Adv. Opt. Mater.* **2018**, *6*, 1800207.
10. Jiao, D.; Zhu, Q.L.; Li, C.Y.; Zheng, Q.; Wu, Z.L. Programmable morphing hydrogels for soft actuators and robots: from structure designs to active functions. *Acc. Chem. Res.* **2022**, *55*, 1533–1545.
11. Ube, T.; Ikeda, T. Photomobile polymer materials with complex 3D deformation, continuous motions, self-regulation, and enhanced processability. *Adv. Opt. Mater.* **2019**, *7*, 1900380.
12. Park, J.; Lee, Y.; Cho, S.; Choe, A.; Yeom, J.; Ro, Y.G.; Kim, J.; Kang, D.; Lee, S.; Ko, H. Soft Sensors and Actuators for Wearable Human–Machine Interfaces. *Chem. Rev.* **2024**, *124*, 1464–1534.
13. Che, Z.; Wan, X.; Xu, J.; Duan, C.; Zheng, T.; Chen, J. Speaking without vocal folds using a machine-learning-assisted wearable sensing-actuation system. *Nat. Commun.* **2024**, *15*, 1873.
14. Di Maria, F.; Lodola, F.; Zucchetti, E.; Benfenati, F.; Lanzani, G. The evolution of artificial light actuators in living systems: from planar to nanostructured interfaces. *Chem. Soc. Rev.* **2018**, *47*, 4757–4780.
15. Stoychev, G.; Kirillova, A.; Ionov, L. Light-responsive shape-changing polymers. *Adv. Opt. Mater.* **2019**, *7*, 1900067.
16. Xu, F.; Feringa, B.L. Photoresponsive supramolecular polymers: from light-controlled small molecules to smart materials. *Adv. Mater.* **2023**, *35*, 2204413.
17. Chen, Y.; Yang, J.; Zhang, X.; Feng, Y.; Zeng, H.; Wang, L.; Feng, W. Light-driven bimorph soft actuators: design, fabrication, and properties. *Mater. Horiz.* **2021**, *8*, 728–757.
18. Yang, X.; Chen, Y.; Zhang, X.; Xue, P.; Lv, P.; Yang, Y.; Wang, L.; Feng, W. Bioinspired light-fueled water-walking soft robots based on liquid crystal network actuators with polymerizable miniaturized gold nanorods. *Nano Today* **2022**, *43*, 101419.
19. Corra, S.; Curcio, M.; Baroncini, M.; Silvi, S.; Credi, A. Photoactivated artificial molecular machines that can perform tasks. *Adv. Mater.* **2020**, *32*, 1906064.
20. Habault, D.; Zhang, H.; Zhao, Y. Light-triggered self-healing and shape-memory polymers. *Chem. Soc. Rev.* **2013**, *42*, 7244–7256.
21. Zhang, Q.M.; Li, X.; Islam, M.R.; Wei, M.; Serpe, M.J. Light switchable optical materials from azobenzene crosslinked poly (N-isopropylacrylamide)-based microgels. *J. Mater. Chem. C* **2014**, *2*, 6961–6965.
22. Hu, L.; Wan, Y.; Zhang, Q.; Serpe, M.J. Stimuli-responsive actuation: harnessing the power of stimuli-responsive polymers for actuation. *Adv. Funct. Mater.* **2020**, *30*, 2070012.
23. Jerca, F.A.; Jerca, V.V.; Hoogenboom, R. Advances and opportunities in the exciting world of azobenzenes. *Nat. Rev. Chem.* **2022**, *6*, 51-69.

24. Kuenstler, A.S.; Hayward, R.C. Light-induced shape morphing of thin films. *Curr. Opin. Colloid Interfaces Sci.* **2019**, *40*, 70–86.
25. Santer, S. Remote control of soft nano-objects by light using azobenzene containing surfactants. *J. Phys. D: Appl. Phys.* **2017**, *51*, 013002.
26. Han, B.; Zhang, Y.L.; Chen, Q.D.; Sun, H.B. Carbon-based photothermal actuators. *Adv. Funct. Mater.* **2018**, *28*, 1802235.
27. Cheng, H.; Huang, Y.; Shi, G.; Jiang, L.; Qu, L. Graphene-based functional architectures: sheets regulation and macrostructure construction toward actuators and power generators. *Acc. Chem. Res.* **2017**, *50*, 1663–1671.
28. Yu, X.; Cheng, H.; Zhang, M.; Zhao, Y.; Qu, L.; Shi, G. Graphene-based smart materials. *Nat. Rev. Mater.* **2017**, *2*, 17046.
29. Wang, E.; Desai, M.S.; Lee, S.W. Light-controlled graphene-elastin composite hydrogel actuators. *Nano. Lett.* **2013**, *13*, 2826–2830.
30. Zhang, X.; Yu, Z.B.; Wang, C.; Zarrouk, D.; Seo, J.W.T.; Cheng, J.C.; Buchan, A.D.; Takei, K.; Zhao, Y.; Ager, J.W.; et al. Photoactuators and motors based on carbon nanotubes with selective chirality distributions. *Nat. Commun.* **2014**, *5*, 2983.
31. Hines, L.; Petersen, K.; Lum, G.Z.; Sitti, M. Soft actuators for small-scale robotics. *Adv. Mater.* **2017**, *29*, 1603483.
32. Jiang, Z.C.; Xiao, Y.Y.; Zhao, Y. Shining light on liquid crystal polymer networks: preparing, reconfiguring, and driving soft actuators. *Adv. Opt. Mater.* **2019**, *7*, 1900262.
33. Ahn, S.K.; Ware, T.H.; Lee, K.M.; Tondiglia, V.P.; White, T.J. Photoinduced topographical feature development in blueprinted azobenzene-functionalized liquid crystalline elastomers. *Adv. Funct. Mater.* **2016**, *26*, 5819–5826.
34. Ikeda, T. Photomodulation of liquid crystal orientations for photonic applications. *J. Mater. Chem.* **2003**, *13*, 2037–2057.
35. Kohlmeyer, R.R.; Chen, J. Wavelength-selective, IR light-driven hinges based on liquid crystalline elastomer composites. *Angew. Chem. Int. Ed.* **2013**, *52*, 9234–9237.
36. Stumpel, J.E.; Broer, D.J.; Schenning, A. Stimuli-responsive photonic polymer coatings. *Chem. Commun.* **2014**, *50*, 15839–15848.
37. Kohlmeyer, R.R.; Lor, M.; Chen, J. Remote, local, and chemical programming of healable multishape memory polymer nanocomposites. *Nano. Lett.* **2012**, *12*, 2757–2762.
38. Dugave, C.; Demange, L. Cis–trans isomerization of organic molecules and biomolecules: implications and applications. *Chem. Rev.* **2003**, *103*, 2475–2532.
39. Xu, W.C.; Sun, S.; Wu, S. Photoinduced reversible solid-to-liquid transitions for photoswitchable materials. *Angew. Chem. Int. Ed.* **2019**, *58*, 9712–9740.
40. Bandara, H.M.D.; Burdette, S.C. Photoisomerization in different classes of azobenzene. *Chem. Soc. Rev.* **2012**, *41*, 1809–1825.
41. Irie, M.; Fukaminato, T.; Matsuda, K.; Kobatake, S. Photochromism of diarylethene molecules and crystals: memories, switches, and actuators. *Chem. Rev.* **2014**, *114*, 12174–12277.
42. Klajn, R. Spiropyran-based dynamic materials. *Chem. Soc. Rev.* **2014**, *43*, 148–184.
43. Huang, C.; Lv, J.A.; Tian, X.; Wang, Y.; Yu, Y.; Liu, J. Miniaturized swimming soft robot with complex movement actuated and controlled by remote light signals. *Sci. Rep.* **2015**, *5*, 17414.
44. Iwaso, K.; Takashima, Y.; Harada, A. Fast response dry-type artificial molecular muscles with [c2] daisy chains. *Nat. Chem.* **2016**, *8*, 625–632.
45. Morimoto, M.; Irie, M. A diarylethene cocrystal that converts light into mechanical work. *J. Am. Chem. Soc.* **2010**, *132*, 14172–14178.
46. Luo, R.; Wu, J.; Dinh, N.D.; Chen, C.H. Gradient porous elastic hydrogels with shape-memory property and anisotropic responses for programmable locomotion. *Adv. Funct. Mater.* **2015**, *25*, 7272–7279.
47. Hu, Y.; Liu, J.; Chang, L.; Yang, L.; Xu, A.; Qi, K.; Lu, P.; Wu, G.; Chen, W.; Wu, Y. Electrically and sunlight-driven actuator with versatile biomimetic motions based on rolled carbon nanotube bilayer composite. *Adv. Funct. Mater.* **2017**, *27*, 1704388.
48. Ji, M.; Jiang, N.; Chang, J.; Sun, J. Near-infrared light-driven, highly efficient bilayer actuators based on polydopamine-modified reduced graphene oxide. *Adv. Funct. Mater.* **2014**, *24*, 5412–5419.
49. Chen, Z.; Gao, B.; Li, P.; Zhao, X.; Yan, Q.; Liu, Z.; Xu, L.; Zheng, H.; Xue, F.; Ding, R.; et al. Multistimuli-responsive actuators derived from natural materials for entirely biodegradable and programmable untethered soft robots. *ACS Nano* **2023**, *17*, 23032–23045.
50. Deng, J.; Li, J.; Chen, P.; Fang, X.; Sun, X.; Jiang, Y.; Weng, W.; Wang, B.; Peng, H. Tunable photothermal actuators based on a pre-programmed aligned nanostructure. *J. Am. Chem. Soc.* **2016**, *138*, 225–230.
51. Yang, Y.; Zhan, W.; Peng, R.; He, C.; Pang, X.; Shi, D.; Jiang, T.; Lin, Z. Graphene-enabled superior and tunable photomechanical actuation in liquid crystalline elastomer nanocomposites. *Adv. Mater.* **2015**, *27*, 6376–6381.
52. Martella, D.; Nocentini, S.; Nuzhdin, D.; Parmeggiani, C.; Wiersma, D.S. Photonic microhand with autonomous action. *Adv. Mater.* **2017**, *29*, 1704047.

53. Peng, W.; Zhang, G.; Liu, J.; Nie, S.; Wu, Y.; Deng, S.; Fang, G.; Zhou, J.; Song, J.; Qian, J.; et al. Light-coded digital crystallinity patterns toward bioinspired 4D transformation of shape-memory polymers. *Adv. Funct. Mater.* **2020**, *30*, 2000522.
54. Qian, X.; Zhao, Y.; Alsaid, Y.; Wang, X.; Hua, M.; Galy, T.; Gopalakrishna, H.; Yang, Y.; Cui, J.; Liu, N.; et al. Artificial phototropism for omnidirectional tracking and harvesting of light. *Nat. Nanotechnol.* **2019**, *14*, 1048–1055.
55. Wani, O.M.; Zeng, H.; Priimagi, A. A Light-driven artificial flytrap. *Nat. Commun.* **2017**, *8*, 15546.
56. Yang, L.; Chang, L.; Hu, Y.; Huang, M.; Ji, Q.; Lu, P.; Liu, J.; Chen, W.; Wu, Y. An autonomous soft actuator with light-driven self-sustained wavelike oscillation for phototactic self-locomotion and power generation. *Adv. Funct. Mater.* **2020**, *30*, 1908842.
57. Jeon, S.J.; Hauser, A.W.; Hayward, R.C. Shape-morphing materials from stimuli-responsive hydrogel hybrids. *Acc. Chem. Res.* **2017**, *50*, 161–169.
58. Gao, D.; Lin, M.F.; Xiong, J.; Li, S.; Lou, S.N.; Liu, Y.; Ciou, J.H.; Zhou, X.; Lee, P.S. Photothermal actuated origamis based on graphene oxide–cellulose programmable bilayers. *Nanoscale Horiz.* **2020**, *5*, 730–738.
59. Cheng, Y.C.; Lu, H.C.; Lee, X.; Zeng, H.; Priimagi, A. Kirigami-based light-induced shape-morphing and locomotion. *Adv. Mater.* **2020**, *32*, 1906233.
60. Yang, T.; Chen, Y.; Minzioni, P. A review on optical actuators for microfluidic systems. *J. Micromech. Microeng.* **2017**, *27*, 123001.
61. Ter Schiphorst, J.; Coleman, S.; Stumpel, J.E.; Ben Azouz, A.; Diamond, D.; Schenning, A.P. Molecular design of light-responsive hydrogels, for in situ generation of fast and reversible valves for microfluidic applications. *Chem. Mater.* **2015**, *27*, 5925–5931.
62. Lv, J.A.; Liu, Y.; Wei, J.; Chen, E.; Qin, L.; Yu, Y. Photocontrol of fluid slugs in liquid crystal polymer microactuators. *Nature* **2016**, *537*, 179.
63. Fernandez-Villamarin, M.; Brooks, L.; Mendes, P.M. The Role of photochemical reactions in the development of advanced soft materials for biomedical applications. *Adv. Opt. Mater.* **2019**, *7*, 1900215.
64. Korde, J.M.; Kandasubramanian, B. Naturally biomimicked smart shape memory hydrogels for biomedical functions. *Chem. Eng. J.* **2020**, 3*79*, 122430.
65. Molla, M.R.; Rangadurai, P.; Antony, L.; Swaminathan, S.; de Pablo, J.J.; Thayumanavan, S. Dynamic actuation of glassy polymersomes through isomerization of a single azobenzene unit at the block copolymer interface. *Nat. Chem.* **2018**, *10*, 659–666.
66. Yan, T.; Li, F.; Tian, J.; Wang, L.; Luo, Q.; Hou, C.; Dong, Z.; Xu, J.; Liu, J. Biomimetic pulsating vesicles with both pH-tunable membrane permeability and light-triggered disassembly–re-assembly behaviors prepared by supra-amphiphilic helices. *ACS Appl. Mater. Interfaces* **2019**, *11*, 30566–30574.
67. Mu, J.; Yang, L.; Sheng, N.; Zhang, Y.; Guo, Y.; Song, X.; Jiang, H.; Zhang, Y.; Zuo, S.; Zhang, H.; et al. Advancing medical devices with soft actuators. *Innovation Mater.* **2025**, *3*, 100112.
68. Toncheva, A.; Khelifa, F.; Paint, Y.; Voué, M.; Lambert, P.; Dubois, P.; Raquez, J.M. Fast IR-actuated shape-memory polymers using in situ silver nanoparticle-grafted cellulose nanocrystals. *ACS Appl. Mater. Interfaces* **2018**, *10*, 29933–29942.
69. Zhou, C.; Xu, Z.; Lin, Z.; Qin, X.; Xia, J.; Ai, X.; Lou, C.; Huang, Z.; Huang, S.; Liu, H.; et al. Submillimeter fiber robots capable of decoupled macro-micro motion for endoluminal manipulation. *Sci. Adv.* **2024**, *10*, eadr6428.
70. Chung, H.; Dai, T.; Sharma, S.K.; Huang, Y.-Y.; Carroll, J.D.; Hamblin, M.R. The nuts and bolts of low-level laser (light) therapy. *Ann. Biomed. Eng.* **2012**, *40*, 516–533.

Review

Cell Electrospinning: Electrohydrodynamic Effects on Cell Viability and Beyond

Anne-Kathrine Kure Larsen and Menglin Chen *

Department of Biological and Chemical Engineering, Aarhus University, 8000 Aarhus C, Denmark
* Correspondence: menglin@bce.au.dk
Received: 9 June 2025; Revised: 9 August 2025; Accepted: 13 August 2025; Published: 19 August 2025

Abstract: Electrospinning is a widely used technique for creating nano- to microscale fibers that resembles the fibrous structure of the extracellular matrix (ECM) environment, crucial for tissue engineering and disease modelling. Directly incorporating living cells into the electrospinning process, 'cell electrospinning', has evolved in the last two decades as a new biofabrication method combining homogenous cell loading with the potential of single cell resolution. However, keeping cells viable and functional during the electrohydrodynamic process is an ongoing challenge. In this review, key parameters in electrospinning affecting mammalian cell viability and functionality are assessed with the goal of identifying the most critical ones in the successful production of living cell-embedded fibers. The review further outlooks the potential mechanobiological and electrophysiological effects on the cells exposed under the electrohydrodynamic condition to layout a couple unexplored applications.

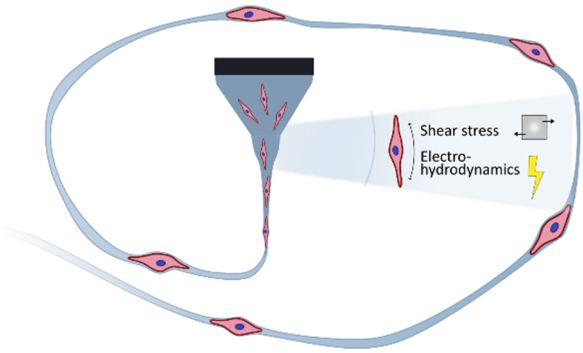

Keywords: cell electrospinning; biofabrication; tissue engineering; viability; mechanobiology; electrical stimulation

1. Introduction

Electrospinning is a versatile technique capable of generating continuous, ultrafine fibers with diameters at the nanometer to micrometer scale. The technique finds broad applications in diverse fields, including drug delivery [1], tissue engineering [2], air filtration [3], and food biosensors [4]. The underlying principle of electrospinning involves the formation of a "Taylor cone" from a charged jet of a liquid viscous solution subjected to a strong electric field, first described by Sir Geoffrey Taylor in 1964 [5]. However, it was until 1971 when Baumgarten obtained acrylic microfibers [6], electrospinning started to gain momentum as an efficient technique for the production of nano- and microfibers. In parallel with the development of electrospinning, electrospraying emerged as well. This technique, while utilizing similar principles as electrospinning, employs lower solution viscosity to generate micro- and nano-sized droplets instead of fibers [7].

In the biomedical research field, electrospinning has been widely applied to produce fibers that are capable of mimicking the fibrous morphology of the natural extracellular matrix (ECM) surrounding the cells in our bodies [2]. The ECM can differ in composition and mechanical properties, depending on the specific tissue requirement [8]. Being able to artificially mimic these fibrous ECM structures provides opportunities to study the effects of morphology, chemical composition and mechanical stiffness on cell response in a relatively controlled manner. One of the obstacles in the use of electrospun fibers for tissue engineering is the limited distribution of cells inside the volume of the densely packed fibrous matrix when seeding cells on top of an electrospun scaffold. To overcome this issue, an extension of electrospinning has emerged: Cell electrospinning. This technique involves the same principles, but instead of seeding on top of electrospun fibers, living cells are added directly into the electrospinning solution to ideally result in cell-embedded fibers [9], creating uniform and in-depth cell distribution within the fibrous matrix [10,11].

Other emerging biofabrication techniques such as 3D bioprinting, incorporating cells in the bioprinting materials, already offers a solution for in-depth cell distribution, but suffers from limited spatial resolutions, such as above 100 μm for extrusion-based bioprinting [12] and above 50 μm for light projection-based bioprinting, and subsequent suboptimal oxygen and nutrients diffusion [13,14]. Bioprinting techniques with higher resolution are highly desired for replicating physiological features at cellular scale [15]. Because of the inherent high resolution of electrospinning with fiber diameters of a few hundred nanometres to a few micrometres [16], electrospinning with living cells could potentially be a powerful tool to meet the needs of both higher resolution and better nutrient diffusion.

Cell viability is often compromised during the bioprinting process, especially in extrusion-based bioprinting where cells experience shear stresses during the extrusion [17]. Although cell viabilities above 90% have been achieved in bioprinting, a delicate balance between material stiffness, viscosity, processing parameters and resulting porosity is crucial for obtaining both high cell viability and printing fidelity [14]. Compared to bioprinting which is a much more established technology, obtaining viable cell-loaded, higher resolutions structures via cell electrospinning is still under development. While good viabilities above 90% have also been reported, some studies suffer from much lower viabilities down to 15–25% [18] and slight changes in parameters were found to influence them drastically [19,20].

Therefore, achieving high cell viability throughout the process of electrospinning is an ultimate prerequisite for the applications of cell electrospinning. There are several excellent and recent reviews on cell electrospinning, including materials (Maurmann et al. [9]), its critical processing parameters and biomedical applications (Elveren et al. [11]). Cell viability has been evaluated in some highlighted studies, emphasizing parameters important for cell fate; however, there is still ambiguity to which parameters play the most significant roles for cell survival and function during an electrospinning process. The aim of this review is to investigate the cell electrospinning process and solution parameters, and their possible interplay. This will be done through a thorough literature review with focus on discussing reported cell viabilities in relation to electrospinning parameters and resulting fiber morphologies. Cell electrospinning has been conducted on various cell types, including mammalian, bacteria and yeast cells; A few reviews have included the latter two [21–23], but in this review, we limit the scope to mammalian cell electrospinning for tissue regeneration application. The review will cover the majority of conducted studies on mammalian cell electrospinning and highlight the critical parameters focusing on their role in maintaining cell viability. We believe that a better understanding of the interplay between process parameters and cell fate will help improve the success rate for obtaining viable cell-embedded fibers, further leading to the broadening of the application of single cell-embedded fibers that may provide beyond morphological guidance.

2. Principles of Electrospinning and Cell Electrospinning

Theoretically pinned as electrohydrodynamics, which describes how an electric field influences a charged fluid, electrospinning is based on the extension of viscous liquid jet from a syringe by an applied electric field, forming sub-micron scale fibers. In the setup, the viscous liquid dispenser is placed above or next to a collector plate. While an electric field is applied across the needle and collector, and the liquid is pumped out at a controlled flow rate, a droplet emerges forming a Taylor cone [5] (Figure 1) to initiate a jet whipping into submicron fibers deposited on the collector. Various parameters affecting electrospinning performance and morphology of electrospun fibers can be modified such as the distance between needle and collector (typically 1–20 cm), the applied voltage (typically 1–20 kV), electric field strength, and the solution flow rate (Figure 1). Instead of a solid collector, the fibers can also be spun directly into a liquid coagulation bath [24].

Cell electrospinning shares the same principle and procedure, except incorporating living cells into the electrospinning solution. Cell electrospinning has been reported with a variety of components, cell types and process parameters. An overview of reported studies can be seen below (Table 1) with the most important parameters listed. In the next section, the challenges associated with cell electrospinning and the influence of the most dominant parameters on cell viability will be presented and discussed.

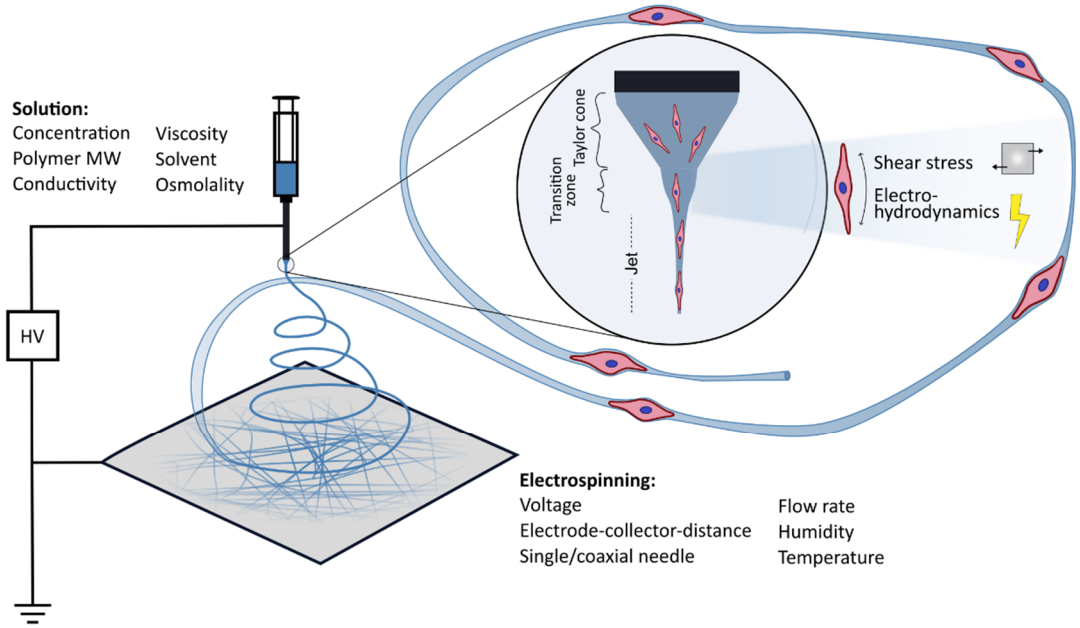

Figure 1. Illustration of Cell electrospinning, the typical electrospinning setup, crucial solution properties and operational parameters.

Table 1. Overview of publications using cell electrospinning and cell electrospraying and their parameters and highest obtained cell viabilities. Abbreviations: PDMS: Polydimethylsiloxane, PVA: Polyvinyl alcohol, PLLA: Poly(l-lactic acid), DMF: N,N-dimethyl formamide, DCM: dichloromethane, PEG: Polyethylene glycol, PEO: Poly(ethylene oxide), PCL: Polycaprolactone, FBS: Fetal Bovine Serum.

Technique	Materials	Solvent	Voltage/Collector Distance	Electric Field Strength (kV/mm)	Flow Rate (mL/h)	Cell Type	Cell Viability	Year	Reference
Electrospinning (coaxial)	Shell: PDMS, core: Cell suspension	Core: Cell medium	9 kV/105 mm	0.09	0.36/36 (core/shell)	EHDJ/1321N1 cells	67.6 ± 1.9% (after fiber dissolution)	2006	[25]
Electrospinning	8% PVA (MW = 205 kDa)	DI water/cell medium	6 kV/150 mm	0.04	0.5	3T3-L1 mouse fibroblasts	15–25%/>90% in culture medium (electrospray)	2011	[18]
Electrospinning (coaxial)	Shell: 12% PLLA (MW = 140 kDa), core: 10% PEG (MW = 35 kDa)/PEO (MW = 900 kDa) + cells	Shell: DMF/DCM, Core: Aqueous solution	20 kV/150 mm	0.133	1.2/1.5 (core/shell)	PC12 cells	NA	2012	[26]
Electrospinning	10% PVA	Milli-Q water	21 kV/150 mm	0.14	0.34	Mononuclear cells (MNCs), mesenchymal stem cells (MSCs)	8.38–19.6%	2012	[27]
Electrospinning (coaxial)	Shell: 12% PCL (MW = 70–90 kDa), Core: 2% PEO (MW = 600 kDa) + 2% FBS	Shell: Chloroform/DMF 60:40, Core: 50% FBS	NA	0.15	NA (ratio of 1:6 (core/shell))	Human umbilical vein endothelial cells (HUVEC)	NA (but 97% in PEO/FBS solution compared to 3% in PEO alone)	2014	[28]
Electrospinning (coaxial)	Matrigel rich collagen biopolymer	NA	8 kV/20 mm	0.4	NA	Primary cardiac myocytes	~80%	2014	[29]
Electrospinning	2% alginate, 2% PEO (MW = 900 kDa), 0.7% lecithin	PBS in water	11.2 kV/70 mm	0.16	0.5	MG63 cells	>80%	2015	[30]
Electrospraying	Cell suspension	Cell culture medium	15 kV/40 mm	0.375	2.60	Mesenchymal stem cells	89 ± 4.6%	2015	[31]
Electrospinning	2% alginate, 3% PEO (MW = 900 kDa)	Tri-distilled water	0.7–1.75 kV/14 mm	0.05–0.125	0.25	C2C12 myoblasts	90%	2018	[32]
Electrospinning (coaxial)	Shell: 20% PCL (MW = 70–90 kDa), core: 10% PVA (MW = 85–124 kDa)	Shell: Chloroform, Core: Cell culture medium	6 kV/60 mm	0.1	1/1 (core/shell)	PC12	>95%	2018	[33]
Electrospinning	1% Fibrinogen, 0.2% PEO	DI water w. 5% glucose	4.5 kV/80 mm	0.056	7.5	C2C12 cells as cellular aggregates	NA (estimate: ~50–60%)	2019	[34]
Electrospinning	0.5% Gelatin, 0.5% pullulan	Serum-free culture medium	8 kV/75 mm	0.107	1.8	Adipose tissue-derived stem cells (hASCs)	90%	2020	[20]

Table 1. *Cont.*

Technique	Materials	Solvent	Voltage/Collector Distance	Electric Field Strength (kV/mm)	Flow Rate (mL/h)	Cell Type	Cell Viability	Year	Reference
Electrospinning (coaxial)	Shell: 15% poly(lactic-co-glycolic acid) (82/18 molar ratio), 5% PEO (MW = 10.065 kDa), core: 6% PVA (MW = 85–146 kDa)	Shell: Chloroform, core: DI water/cell medium	10 kV/50 mm	0.2	10/50 (core/shell)	Pheochromocytoma 12 (PC12) cells	NA	2020	[35]
Electrospinning	2% Sodium alginate, 3% PEO (MW = 900 kDa)	Triple-distilled water	10.5 kV/140 mm	0.075	0.25	Human umbilical vein endothelial cells (HUVECs)	90%	2020	[36]
Electrospinning	12% Poly(vinyl) alcohol (PVA, MW = 89.000–98.000)	10:1 Deionized water/cell culture medium	1–2 kV/70–100 mm	0.029	1	MC3T3 osteoblast precursor cells	81%	2021	[37]
Electrospraying	Laminin modified Alginate	20 mM HEPES	18 kV/15 mm	1.2	0.04	Adipose derived stem cells (ADSCs)	99%	2021	[38]
Electrospraying	0.125% Gelatin, 0.125% pullulan	Serum-free media	10 + 15 kV/70 mm	0.143–0.214	12	Human adipose-derived stem cells (hASCs)	90 + 70%	2021	[39]
Electrospraying	Cell suspension	Cell culture medium	9 kV/50 mm	0.18	2	C28/12 chondrocytes, primary chondrocytes	<91%	2022	[40]
Electrospinning	2% Alginate/3% PEO (MW = 900 kDa)	Triple-distilled water	10.5 kV/140 mm	0.075	0.25	Smooth muscle cells (SMCs) and Mesenchymal stem cells (MSCs)	>90%	2023	[19]
Electrospinning	50% Gelatin (fish) (MW = 50–100 kDa)	PBS	20 kV/50 mm	0.40	2.4	Mesenchymal stem cell (MSC)	>90%	2023	[41]
Electrospinning	7.5% hydrazide functionalized POEGMA (POH), 2.5% PEO (MW = 600 kDa)	DMEM medium/PBS	10 kV/10 mm	1	0.9	3T3 fibroblasts and Psi2 12S6 epithelial cells	NA but ≈4-fold increase in cell density at day 14.	2023	[42]
Electrospinning	7.5% hydrazide functionalized POEGMA (POH), 2.5% PEO (MW = 600 kDa)	PBS:DMEM 3:1	10 kV/100 mm	0.1	0.9	C2C12 mouse myoblast	>85%	2023	[43]
Electrospinning	10% polyvinylpyrrolidone (PVP) (MW = 360 kDa)	PBS	8 kV/100 mm	0.08	NA	Human umbilical cord mesenchymal stem cells (HUCMSCs)	88 ± 4.3%	2024	[44]

3. Challenges in Cell Electrospinning

Cell electrospinning is demanding in terms of the choice of materials and solvents. The options are limited compared to conventional electrospinning where organic solvents often are used to dissolve polymers, which should naturally be avoided when incorporating living cells. In addition, the materials should be biocompatible, non-toxic, and the degradability should be considered depending on the application. Furthermore, the electrospinning parameters should be fine-tuned to maintain both viable cells and spinnability. Collectively, the spinnability of the solution and inclusion of living cells in the extruded fibers is a delicate balance [11]. The limited number of publications using cell electrospinning underlines the necessity to better understand the parameters that affect both spinnability and viability, thus obtaining fully viable and functional cells inside thin single cell-sized fibers is still an essential challenge [32,34]. In the next sections, the different parameters in cell electrospinning will be discussed and assessed for their influence on cell viability and function with examples from literature.

3.1. Solution Components

Solution composition is critical in cell electrospinning since living cells are incorporated. The main criteria to consider are the use of non-cytotoxic and biocompatible materials and water as solvent, in contrast to the typical organic solvents such as hexafluoro-isopropanol, chloroform, dichloromethane or dimethylformamide in conventional electrospinning [45]. The choice of solvent will affect spinnability of the polymer together with the resulting fiber diameter and morphology [46]. When a polymer solution is extruded as a jet into the air, fibers are formed from electrostatic tensile forces and solidification of the jet as the solvent evaporates. The behaviour of the jet is furthermore influenced by the viscosity and the viscoelasticity of the polymer solution. At high viscosities, larger jets and fibers are formed, but below a certain threshold of viscosity, the jet can start breaking into droplets resulting in electrospraying instead of spinning [46,47].

The use of aqueous solution for preserving cell viability requires hydrophilic polymers. These are often natural, biobased polymers e.g., proteins such as collagen, silk fibroin, fibrinogen or collagen-derived gelatine [48], polysaccharides like sodium alginate [49], pullulan [50] and glycosaminoglycans such as hyaluronic acid [51], or synthetic but biocompatible polymers such as poly(vinyl alcohol) (PVA). Polyelectrolytes alone have inherently low spinnability due to limited chain entanglement. This is the case for one of the most common polysaccharides in cell electrospinning, sodium alginate (SA), in which limited ability for the negatively charged alginate chains to entangle sufficiently hinders fiber formation [32]. SA is therefore usually co-electrospun together with other polymers such as poly(ethylene oxide) (PEO) as a carrier polymer to increase molecular entanglement and viscosity, and with processing agents such as lecithin [30,32,52–54]. Importantly, since the polymers are water soluble but would have to be stable in cell culture medium after cell electrospinning, rapid in situ crosslinking of the materials is needed for the fibers to maintain their structure. Various strategies have been applied varying depending on the material e.g., physical crosslinking, enzymatic crosslinking or click chemistry photocrosslinking. SA as an example, rapid ionic physical crosslinking is achieved by immersing fibers into a $CaCl_2$ solution in which Ca^{2+} ions substitute Na^{2+} ions and cause ionic bonding between Ca^{2+} and the carboxyl groups on sodium alginate [55]. Enzymatic crosslinking has, on the other hand, been performed using fibrinogen by the addition of thrombin that converts fibrinogen molecule to insoluble fibrin [34].

A way to solve the limited choices of hydrophilic polymers with rapid crosslinkability for preparing aqueous cell-loading solutions, is the use of coaxial cell electrospinning. A coaxial needle is used to separate the core and shell flows, enabling the use of polymers requiring organic solvents in the shell compartment. By retaining the cells suspended in culture medium or aqueously dissolved polymers in the core, the two solvents are immiscible during electrospinning and thus the cells are not in contact with the organic solvent which is further evaporating quickly. As a benefit, crosslinking is optional as the shell is often a hydrophobic polymer, only needed if the core material has to be crosslinked as well [26,33].

Osmolarity is also an important parameter to consider for cell viability. Aqueous cell electrospinning solutions should thus also contain surfactants, cell culture additives and salts for creating a physiological relevant environment with the correct osmolarity. As an example, in a study of Ang. et al. they observed an increased viability from 2% to 97% for HUVECs in a 2% PEO solution by addition of 50% FBS, with significant increase in viability already seen at 5% FBS. The low viability in PEO alone was suspected to be caused by the hypotonic nature of the aqueous solution in relation to the cell interior, with a low osmolality of 0.41 mOsm/kg compared to physiological osmolality of 270–290 mOsm/kg, causing water influx across the cell membrane. Besides its nutritious effect, the addition of FBS to the cell-containing electrospinning solution was anticipated to increase osmolality closer to physiological conditions and also demonstrated enhanced cell survival [28]. 5% glucose has been used as an alternative to an ionic buffer such as PBS in order to match cellular osmolarity while keeping the

solution at low ionic concentrations to maintain conductivity suited for electrospinning and decrease the current on the cells [34]. These examples highlight the importance of considering physiological osmolarity for obtaining viable cells in electrospinning and other biofabrication processes.

The ability of a polymer to facilitate cell adhesion is also important for cell survival. For example, PVA has limited cell adhesion owing to the low protein adsorption, so various biopolymers such as gelatin and chitosan have often been co-electrospun with PVA as electrospun scaffolds, resulting in increased cell adhesion and survival upon seeding [56,57]. Porcine and fish gelatin have been popular choices in both conventional electrospinning and cell electrospinning, owing to its natural collagen origin, biocompatibility, low cost and cell adhesion properties. In both studies listed here, a very good viability has been obtained for electrospun fibers including gelatin of either fish or porcine origin [20,41]. Gelatins from different animal sources are different in their chemical structure, resulting in different sol-gel transition temperature. Fish gelatin has been proposed as an alternative to the commonly used porcine gelatin as cold-water fish gelatin has a lower sol-gel transition temperature, below ambient temperature opposed to porcine gelatin that gels at room temperature, requiring extra control over ambient temperature during electrospinning [58]. On the other hand, crosslinking leads to very different storage moduli, 723–7340 Pa for porcine and 294–464 Pa for fish gelatin, which could ultimately influence the behaviour of cells embedded in electrospun fibers [59].

3.2. Electric Field Strength

The electric field strength, determined by the ratio of applied voltage to the distance between the electrode and the collector, is a critical parameter in electrospinning. However, while the main limit to the strength of the electric fields is directed by the range yielding good spinnability and suitable fiber diameters and morphologies in conventional electrospinning, the parameter seem to be more crucial in cell electrospinning. Excessive electric field strength has been stated to negatively affect cell viability as a too strong electric field can disrupt the cellular membrane [32,60,61], however no definite quantitative relationship between electric field strength or time and cell viability has been established yet.

It is well-known from the use of electroporation in DNA delivery methods, that cells can sustain a certain electric field, with electroporation typically using electric pulses at 0.5–1 kV/cm [62]. It is noteworthy that there is usually a fraction of the electroporated cells that do not survive it [63]. There may be similar effect in cell electrospinning, even though considerable differences in electric field strengths have been reported throughout the listed studies (Table 1), varying from 0.029 to 0.4 kV/mm (only taking into account the studies that reported viability results). For electrospraying, the electric fields are often much stronger and better tolerated by cells, however it fails to facilitate continuous fiber production. Yang et al. successfully produced laminin-alginate microspheres using cell electrospraying with a strong field at 1.2 kV/mm and resulting 99% viability of adipose derived stem cells [64]. It was already reported by Jayasinghe et al. as one of the first instances of cells processed in an electric field in 2006 that Jurkat cells could survive jetting in a 2 kV/mm electric field with no observable cell damage [65].

This difference in the range of electric fields that cells can sustain during electrospinning may vary among cell types. From electroporation studies with 15 different cell lines, O'Hare et al. reported that the different cell types showed markedly different levels of electrosensitivity, which could not be ascribed to cell size or culture conditions. From this study, they found lymphoid cells to be most sensitive, followed by epithelial and fibroblast cells [66]. However, in another study investigating electropermeabilization and electrosensitivity, no trend in electrosensitivities of specific tissue types was found, instead significant differences in electrosensitivities appeared among different tumor cell lines, even from the same tumor type [67]. However, the electric field strengths reported in the studies listed in this review vary greatly; it is reasonable to question if the difference could lie in other process parameters or composition of electrospinning material as well. There are examples where various field strengths have been employed on the same cell type, such as C2C12 in the studies of Yeo et al. [32] and Dawson et al. [43]. Yeo et al. reported cell viability at >80% when electrospinning a solution of 2% alginate and 3% PEO at up to 0.1 kV/mm while it decreased drastically to around 10% at 0.125 kV/mm (Figure 2a) [32]. Dawson et al. reported on similar viability at 0.1 kV/mm with same cell type in a solution of 7.5% hydrazide functionalized POEGMA (POH) and 2.5% PEO (Figure 2b,c). However, with electrospraying cell suspension in culture medium, even higher electric fields of up to 0.15 kV/mm could be applied without affecting cell viability noticeably (Figure 2d) [43]. This example highlights the importance of evaluating electric field strength effects in combination with other parameters such as solution composition and physical properties. For example, material conductivity and dielectric properties of both the solutes and the solvents are important to consider in relation to electric field strength. At the onset of electrospinning, the taylor cone formation is highly affected by the

availability of free charges in the solution that is further influenced by the dielectric property of the solution. As cell electrospinning is performed in aqueous solution such as medium or PBS buffer which include ionic salts for retaining the correct conditions for living cells, the conductivity is markedly increased compared to water. Cell culture medium and PBS buffer typically have conductivities around 1.5–2 S/m [68,69] and 1.4 S/m [70], respectively, compared to a conductivity of 5.5 µS/m for pure water, and when exposed to air, 0.1–0.2 mS/m [71]. While not directly shown for electrospinning, medium conductivity has shown to negatively influence the survival of Chinese hamster fibroblasts (DC3F) cells in electropermeabilization [69]. The electric field strength is therefore not the only parameter to consider when evaluating the effect of the electric field on living cells; besides affecting the electrospun cells, it also affects the electrospinning process itself, including electrospinnability and fiber morphology [72–74].

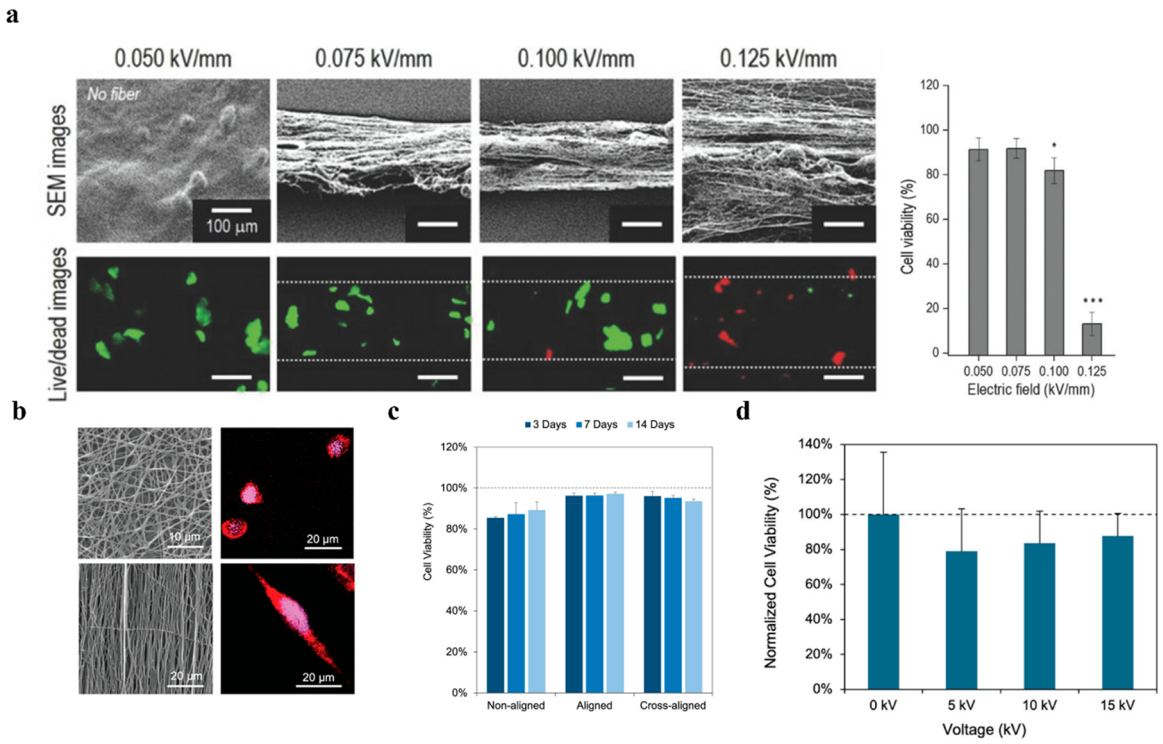

Figure 2. Electric field effects on cell viability. (**a**) C2C12 myoblast viability in increasing electric fields during cell electrospinning. * $p < 0.05$, and *** $p < 0.001$, scale bars = 100 µm [32], (**b**) C2C12 myoblasts electrospun in random and aligned fibers, red: CellTrace CFSE, blue: DAPI, their viabilities (**c**) at day 3, 7 and 14 at 0.1 kV/mm and (**d**) electrospray in cell suspension [43]. (**a**) Reproduced with permission from ref. [32]. Copyright 2018 John Wiley and Sons. (**b**) Reprinted (adapted) with permission from [43]. Copyright 2023 American Chemical Society.

3.3. Viscosity and Shear Force

Viscosity is a critical parameter in electrospinning and fiber formation, however, in the context of cell electrospinning it is even more critical with a smaller process window. A certain viscosity is needed to reach good spinnability, but if the viscosity becomes too high, the charges initiating the spinning may be insufficient for stretching the viscous material into a fiber. At this point, spinning would require higher applied voltage, leading to heterogeneous fibers and would eventually result in a higher shear force which can be damaging to living cells. On the contrary, too low viscosity results in electrosprayed droplets instead of fibers [47]. The viscosity is therefore important to control and monitor, however, only two studies included in this review reports on actual viscosity [25,26]. Instead, polymer concentrations are typically given, but reproducing experiments with electrospinning solely based on published polymer concentrations is challenging. Variations in molecular weight, environmental factors like temperature, which significantly influences viscosity, can lead to unpredictable changes in fiber morphology or even render the results irreproducible [75].

The influence of shear force on cell viability during electrospinning is rather underrepresented. The shear force acting on an object in a viscous solution is partly determined by viscosity of the solution and is proportional to the viscosity at constant flow rate [28]. The higher the viscosity, the greater force is required to extrude the

solution, resulting in higher shear stress. This is also a well-known challenge in extrusion-based bioprinting [17] (Figure 3a). For example, it was observed by Kim et al. that cell viability decreased significantly to below 80% from 93% when the collagen content in their bioink was increased from <5% to >7% [76]. Shear stress effects were also observed biologically by Ang. et al., with upregulation of IL-8 expression in HUVECs endothelial cells post electrospinning (Figure 3b) [28]. Looking across studies using the same polymer such as PVA but achieving very different cell viabilities could also relate to viscosity. In these studies, 8–12% PVA is used either for single needle electrospinning or as the core with cells in coaxial electrospinning. The very low viabilities of 15–25% and 8.38–19.6% obtained in the studies by Canbolat et al. [18] and Zanatta et al. [27], respectively, share the use of higher molecular weight polymers compared to the other two studies by Wu et al. and Das et al. [33,37]. The use of high MW polymers must have resulted in higher viscosities and higher shear stresses on the cells in the electrospinning process. This is further supported by the fact that electrospraying cells in culture medium with low viscosity yielded much better viability (>90%), reported by Canbolat et al. [18]. In addition, these studies [18,27] yielding low cell viabilities used DI water/cell medium and MilliQ-water in the electrospinning solution, respectively, further indicating that an osmotic pressure mismatch could also have negatively influenced the cell viability.

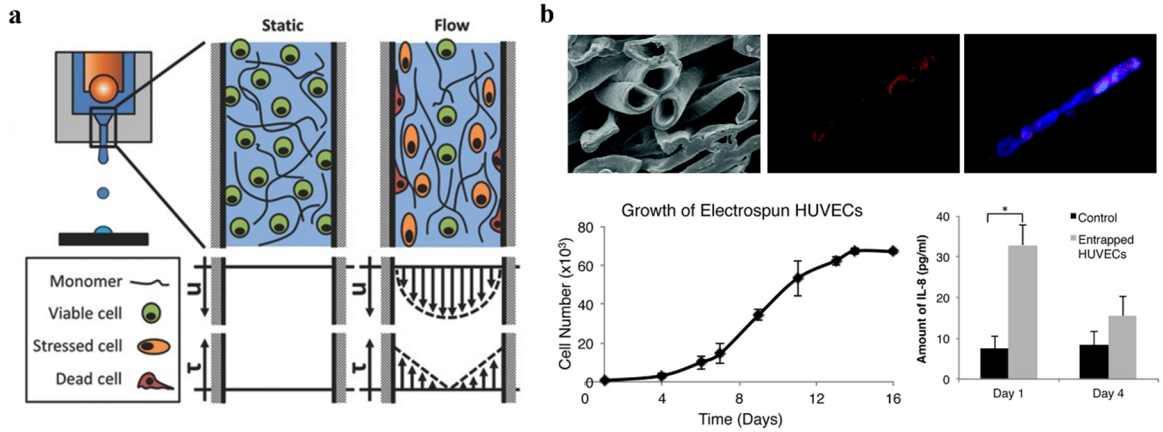

Figure 3. Viscosity and shear stress effects on cells in (**a**) standard extrusion-based bioprinting where flow-induced shear stress influences cell function and viability [77], (**b**) HUVEC cells in coaxial electrospun fibers showing increased shear stress marker, IL-8, expression 1 day post electrospinning, while decreased expression after 4 days of culture indicating cell recovery. Red: DiI (membrane dye), blue: DAPI [28]. (**a**) Reproduced with permission from ref. [77]. Copyright 2018 John Wiley and Sons. Adapted from ref. [28] (Creative Commons CC-BY-NC 3.0).

Coaxial electrospinning could be a solution to isolate cells from the shear stress induced by the polymer solution while extruded, by loading cells into the core in a low viscosity solution or cell medium. The core solution does not need to be electrospinnable, as long as the sheath solution is so and can drag the core solution with it [78]. The compartmentalization further expands the material choice to biocompatible, hydrophobic polymers. For example, PDMS or PCL shell solutions have been shown to successfully assist the electrospinning of cells only cell suspension in medium or a low concentrated polymer solution with cells in the core in only cell suspension. Townsend-Nicholson et al. found that the cell viability remained similar to the control group at 67.6% when locating the cell solution in the core of a coaxial needle with highly viscous PDMS in the shell [25]. Wu et al. reported a 20% PCL shell with a cell-loaded 10% PVA core to be electrospun at 0.1 kV/mm with a cell viability >95% and no reported viability problems even when increasing voltages [33]. It should be noted that they used different cell types and are not fully comparable, however, it still gives a good indication of the protective role of shielding cells in the inner core. At the opposite, a certain viscosity might also be beneficial for protecting cells from the electric field as Wen et al. demonstrated. They observed that better cell viability was obtained when cell electrospinning was carried out with fish gelatin/PBS compared to electrospraying cells in PBS alone [41]. Another benefit of using the coaxial needle system relates back to the challenge of the limited availability of solvents and the need for crosslinking fibers before cell culture (Section 3.1). Studies demonstrated that the use of organic solvents for dissolving e.g., PLLA or PCL in the shell solution did not affect the electrospun cells when they were suspended in aqueous solution in the core [26,33].

3.4. Other Parameters

Flow rate and dehydration time has also been suspected to affect the viability of electrospun cells. Typical flow rates used are in the range of 0.25 to 7.5 mL/h in single needle cell electrospinning according to our review. High flow rates may increase the shear force on the cells, but it was in contrast reported by Semitela et al. that a flow rate of 1 mL/h resulted in much higher cell death compared to flow rates at 2–7 mL/h [40]. It was further found in a study by Guo et al. that increased flow rate for stabler jet formation had a lower negative influence on cell viability than decreasing the distance between the electrode and collector which would directly enhance the electric field strength [34]. In coaxial electrospinning, the flow rates can be controlled separately for core and shell solution leading to increased complexity and a more challenging process. Typically, shell flow rates needs to be higher than core flow rates to draw along the core solution and by varying this ratio, the sizes of core/shell structures can also be manipulated in connection with solution viscosities [78–80]. In practice, the ratio of shell:core flow rates for previous cell electrospinning experiments in literature have varied from 1.2 to 100 (Table 1). Placing living cells in the core could then be a tool to protect cells from the higher flow rate, i.e., larger shear stresses from the sheath fluid.

Dehydration has been suspected to influence viability in electrospinning processes since fibers are often deposited on a dry collector after solvent evaporation [18]. However, Fei Xu et al. tested this with 3T3 fibroblasts and Psi2 12S6 epithelial cells where cell viability was above 80% after 2 h of dehydration, and Dawson et al. tested the same on C2C12 myoblasts with acceptable viability after 1 h of dehydration (Figure 2b) [42,43].

3.5. Summary

As clearly seen from previous sections, there are many variables both in the experimental settings and properties of the cell-containing electrospinning solutions that influence electrospinning performance, cell viability and functionality of post-processed cells. There is of course an operational window of the electric fields strengths and other physical parameters like needle-to-collector distance, flow rate and dehydration time that a cell can tolerate. However, putting emphasis on the physical and chemical properties of the bioinks seems to be even more important. Specifically, one of the main causes of cell death is the high shear stress that cells are experiencing during the process, which is determined by the combination of both the physical process parameters such as electric field strength and the composition and mechanical properties of the bioink. As viscosity and viscoelasticity are important parameters in determining effective shear stress, we believe reporting this parameter is of underestimated value when publishing papers on cell electrospinning.

4. Tissue Engineering Applications

Current applications of cell electrospinning of mammalian cells are mostly in tissue engineering, spanning from wound healing, neuron tissue engineering, to skeletal muscle tissue engineering, where the extracellular matrix and tissue morphology and characteristics are mimicked to regenerate the lost tissue. Here, cell electrospinning benefits from having cells homogeneously localized all over a scaffold instead of only on the top layer.

Wen et al. included mesenchymal stem cells (MSCs) into fish gelatin electrospun fibers for wound healing. The cell-loaded fibers were deposited onto a wound on mouse in vivo and was shown to promote healing by enhancing ECM remodelling with increased collagen deposition and decreased expression of the inflammation marker IL-6. It also promoted angiogenesis by increasing the expression of vascular endothelial growth factor (VEGF) and demonstrated to be an efficient approach for stem cell delivery [41].

Another application is in nerve regeneration as also envisioned with conventional electrospinning [81–83]. Wu et al. successfully incorporated PC12 cells and differentiated them inside hollow coaxial electrospun PVA/PCL fibers without the addition of nerve growth factors NGF) (Figure 4a,b) [33].

Skeletal muscle tissue has also been engineered using cell electrospinning, specifically with a drum collector to facilitate alignment of fibers. Anisotropic cues are often used to mimic muscle tissue [84] and guide the formation of myotubes. Yeo et al. demonstrated cell electrospinning for the same purpose, incorporating C2C12 myoblast cells in electrospun alginate fibers, yielding highly aligned and multinucleated cell morphology that could facilitate myogenic differentiation (Figure 4c) [32].

Embedding cells within single cell-sized electrospun fibers may enable other unexplored functionality. First, fibers with diameters at the cellular scale can provide a more direct 3D localized morphological and mechanical cues for the encapsulated single cells [85–88]. 2D Surface topography is known to influence not only the shape of cells but also intracellular processes such as gene expression. This can happen through focal adhesion assembly change and cytoskeletal reorganization, which can further activate transcription coregulators, e.g., the well-known mechanosensing Yes-Associated Protein (YAP) [89]. 2D surface structures and guidance have been further proven

to direct differentiation of stem cells into specified cell types through mechanobiological pathways [90,91]. Encasing single cells inside a fiber structure is hypothesized to not only induce guided cell alignment but also provide 3D, subcellular mechanical cues around the single cell, potentially providing a new tool of utilizing mechanobiology for the production of novel high resolution 3D tissue models.

On the other hand, electrostatic ejection of a cell-embedded liquid jet in the electrospinning process may affect biophysical functions of the cell and tissue constructs [92]. Apart from mechanical cues, adverse or beneficial effects of electric field could be anticipated. Electrical stimulation of cells has been demonstrated using a variety of techniques, such as electromagnetic stimulation [93,94], piezoelectric scaffolds [95] and hybrid conductive microfibers [96] to affect cell behaviours like differentiation [95,96], proliferation and migration [97], nerve regeneration [98,99] and gene expression [100] etc. Seeing cell electro-spinning and -spraying as another tool for single-pulse electrical stimulation could open new perspectives in the utilization of the technology in tissue engineering.

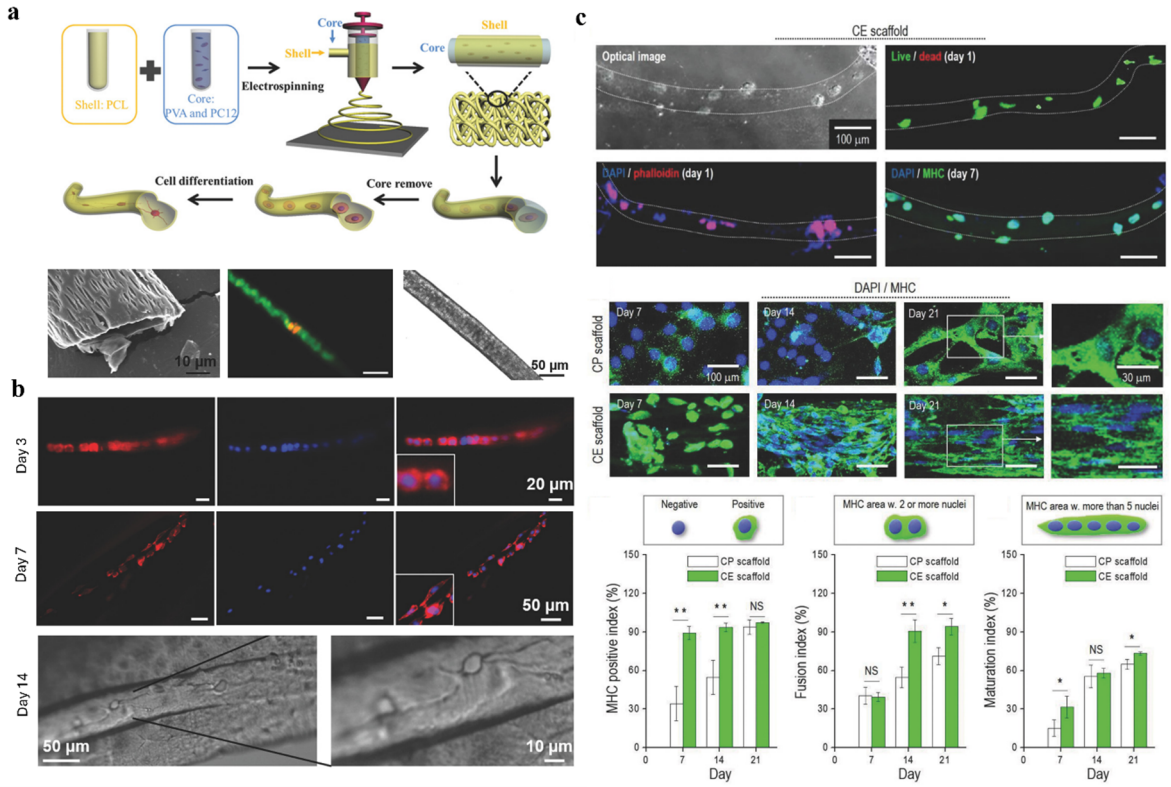

Figure 4. Examples of applications of cell electrospinning. (**a**) Coaxial electrospinning with living PC12 cells suspended in the core with (**b**) most cells surviving (green) and successful differentiation into neuron-like cells obtained after 7 days in culture in the fibers. Red: MAP2; blue: DAPI [33]. (**c**) C2C12 myoblasts encapsulated inside electrospun fibers via cell electrospinning. Myosin heavy chain (MHC) positive staining indicated successful myogenic differentiation, with cell electrospun fibers being superior in performance to a traditional cell printed scaffold. * $p < 0.05$, ** $p < 0.01$ [32]. (**a**,**b**) Reproduced with permission from ref. [33]. Copyright 2018 John Wiley and Sons Copyright. (**c**) Reproduced with permission from ref. [32]. Copyright 2018 John Wiley and Sons.

5. Conclusions and Outlook

While significant progress in cell electrospinning has been achieved, several key areas require further investigation to optimize the process and broaden its applicability. The fact that viscosity was reported in only two of the reviewed studies highlights a significant knowledge gap in technology transfer. Future studies should prioritize characterizing and controlling these key parameters to better understand its impact on cell viability and fiber formation. Furthermore, computational modelling of shear stress effect on cells during the extrusion in electrospinning initiation could help the prediction and optimization of experimental outcomes, leading to more efficient and reproducible results. Achieving a balance between electrospinnability, cell embedding efficiency, and cell viability remains a central challenge, demanding careful consideration of combined material properties and process parameters.

Beyond cell viability, it would also be crucial to study mechanobiological and electrophysiological effects on the cells when being processed through this electrohydrodynamic process. The former addresses the mechanical

influence of the polymer solution with its molecular entanglement, viscosity and resulting shear forces on a cell during syringe flow, Taylor cone formation and jetting. The latter exerts electrical interference on cell membrane. Generally, presenting cells to extracellular physical force such as shear stress, tension or compression has been proved to influence cell behaviour through mechanosensing pathways [101]. For example, cell stretching on a stiff substrate or simply compression of the nucleus using an AFM cantilever can result in translocation of the mechanotransduction regulated transcription factor YAP from cytosol to the nucleus [102]. One could therefore hypothesize that YAP translocation would also be affected by both the shear forces during the electrospinning process and the possible compression force that cells experience inside thin fibers. YAP translocation is known to influence gene transcription and thereby gene expression, potentially leading to interesting biological effects of cell electrospinning. This might open up new applications in the biomedical field.

Besides mechanobiological effect, electrophysiological effects might also lead changes in both cell phenotypes and genetics, for example as reported by Das et al. where global DNA hypomethylation was enhanced in cells subjected to electrical fields during electrospinning [37]. Other desirable electrophysiological effects have been indicated such as differentiation of PC12 cells inside electrospun fibers [33]. Furthermore, it could also be hypothesized that electroporation through cell electrospinning should in principle be possible.

In conclusion, if the ongoing challenges of cell electrospinning in terms of electrospinnability, and cell viability are well addressed, true applications of this technique will be unleashed, providing single cell models for investigating mechanobiological and electrohydrodynamic effects on diverse cell types, as well as contributing to the construction of high-resolution tissue engineering constructs with in-depth cell distribution and mechanobiological/electrohydrodynamic guidance.

Author Contributions: A.-K.K.L.: conceptualization, writing—original draft preparation; M.C.: conceptualization, supervision; writing—reviewing and editing. All authors have read and agreed to the published version of the manuscript.

Funding: This research was funded by Lundbeck Foundation, grant number R400-2022-1232, Marie Skłodowska-Curie Actions programme ENSIGN, grant number 101086226 and L4DNANO, grant number 101086227.

Institutional Review Board Statement: Not applicable.

Informed Consent Statement: Not applicable.

Data Availability Statement: Not applicable.

Conflicts of Interest: The authors declare no conflict of interest.

References

1. Luraghi, A.; Peri, F.; Moroni, L. Electrospinning for drug delivery applications: A review. *J. Control. Release* **2021**, *334*, 463–484. https://doi.org/10.1016/j.jconrel.2021.03.033.
2. Kishan, A.P.; Cosgriff-Hernandez, E.M. Recent advancements in electrospinning design for tissue engineering applications: A review. *J. Biomed. Mater. Res. Part A* **2017**, *105*, 2892–2905. https://doi.org/10.1002/jbm.a.36124.
3. Lu, T.; Cui, J.; Qu, Q.; Wang, Y.; Zhang, J.; Xiong, R.; Ma, W.; Huang, C. Multistructured Electrospun Nanofibers for Air Filtration: A Review. *ACS Appl. Mater. Interfaces* **2021**, *13*, 23293–23313. https://doi.org/10.1021/acsami.1c06520.
4. Mercante, L.A.; Scagion, V.P.; Migliorini, F.L.; Mattoso, L.H.C.; Correa, D.S. Electrospinning-based (bio)sensors for food and agricultural applications: A review. *TrAC Trends Anal. Chem.* **2017**, *91*, 91–103. https://doi.org/10.1016/j.trac.2017.04.004.
5. Taylor, S.G. Disintegration of water drops in an electric field. *Proc. R. Soc. London. Ser. A Math. Phys. Sci.* **1964**, *280*, 383–397. https://doi.org/10.1098/rspa.1964.0151.
6. Baumgarten, P.K. Electrostatic spinning of acrylic microfibers. *J. Colloid Interface Sci.* **1971**, *36*, 71–79. https://doi.org/10.1016/0021-9797(71)90241-4.
7. Boda, S.K.; Li, X.; Xie, J. Electrospraying an enabling technology for pharmaceutical and biomedical applications: A review. *J. Aerosol. Sci.* **2018**, *125*, 164–181. https://doi.org/10.1016/j.jaerosci.2018.04.002.
8. Jansen, K.A.; Donato, D.M.; Balcioglu, H.E.; Schmidt, T.; Danen, E.H.; Koenderink, G.H. A guide to mechanobiology: Where biology and physics meet. *Biochim. Biophys. Acta* **2015**, *1853*, 3043–3052. https://doi.org/10.1016/j.bbamcr.2015.05.007.
9. Maurmann, N.; França, F.S.; Girón, J.; Pranke, P. Cell Electrospinning: A Review of Materials and Methodologies for Biofabrication. *Adv. Biol.* **2023**, *7*, 2300058. https://doi.org/10.1002/adbi.202300058.
10. Nosoudi, N.; Hasanzadeh, A.; Hart, M.; Weaver, B. Advancements and Future Perspectives in Cell Electrospinning and Bio-Electrospraying. *Adv. Biol.* **2023**, *7*, 2300213. https://doi.org/10.1002/adbi.202300213.
11. Elveren, B.; Kurečič, M.; Maver, T.; Maver, U. Cell Electrospinning: A Mini-Review of the Critical Processing Parameters and Its Use in Biomedical Applications. *Adv. Biol.* **2023**, *7*, 2300057. https://doi.org/10.1002/adbi.202300057.
12. Karvinen, J.; Kellomäki, M. Design aspects and characterization of hydrogel-based bioinks for extrusion-based bioprinting. *Bioprinting* **2023**, *32*, e00274. https://doi.org/10.1016/j.bprint.2023.e00274.

13. He, C.-F.; Qiao, T.-H.; Wang, G.-H.; Sun, Y.; He, Y. High-resolution projection-based 3D bioprinting. *Nat. Rev. Bioeng.* **2025**, *3*, 143–158. https://doi.org/10.1038/s44222-024-00218-w.
14. Lee, M.; Rizzo, R.; Surman, F.; Zenobi-Wong, M. Guiding Lights: Tissue Bioprinting Using Photoactivated Materials. *Chem. Rev.* **2020**, *120*, 10950–11027. https://doi.org/10.1021/acs.chemrev.0c00077.
15. Zandrini, T.; Florczak, S.; Levato, R.; Ovsianikov, A. Breaking the resolution limits of 3D bioprinting: Future opportunities and present challenges. *Trends Biotechnol.* **2023**, *41*, 604–614. https://doi.org/10.1016/j.tibtech.2022.10.009.
16. Greiner, A.; Wendorff, J.H. Electrospinning: A Fascinating Method for the Preparation of Ultrathin Fibers. *Angew. Chem. Int. Ed.* **2007**, *46*, 5670–5703. https://doi.org/10.1002/anie.200604646.
17. Boularaoui, S.; Al Hussein, G.; Khan, K.A.; Christoforou, N.; Stefanini, C. An overview of extrusion-based bioprinting with a focus on induced shear stress and its effect on cell viability. *Bioprinting* **2020**, *20*, e00093. https://doi.org/10.1016/j.bprint.2020.e00093.
18. Canbolat, M.F.; Tang, C.; Bernacki, S.H.; Pourdeyhimi, B.; Khan, S. Mammalian Cell Viability in Electrospun Composite Nanofiber Structures. *Macromol. Biosci.* **2011**, *11*, 1346–1356. https://doi.org/10.1002/mabi.201100108.
19. Yeo, M.; Yoon, J.W.; Park, G.T.; Shin, S.-C.; Song, Y.-C.; Cheon, Y.-I.; Lee, B.-J.; Kim, G.H.; Kim, J.H. Esophageal wound healing by aligned smooth muscle cell-laden nanofibrous patch. *Mater. Today Bio* **2023**, *19*, 100564. https://doi.org/10.1016/j.mtbio.2023.100564.
20. Nosoudi, N.; Oommen, A.J.; Stultz, S.; Jordan, M.; Aldabel, S.; Hohne, C.; Mosser, J.; Archacki, B.; Turner, A.; Turner, P. Electrospinning Live Cells Using Gelatin and Pullulan. *Bioengineering* **2020**, *7*, 21. https://doi.org/10.3390/bioengineering7010021.
21. Diep, E.; Schiffman, J.D. Electrospinning Living Bacteria: A Review of Applications from Agriculture to Health Care. *ACS Appl. Bio Mater.* **2023**, *6*, 951–964. https://doi.org/10.1021/acsabm.2c01055.
22. Schulte-Hermann, J.; Riessland, H.; MacKinnon, N.; Korvink, J.G.; Islam, M. Biomineralization of Electrospun Bacteria-Encapsulated Fibers: A Relevant Step toward Living Ceramic Fibers. *ACS Appl. Bio Mater.* **2024**, *7*, 7936–7943. https://doi.org/10.1021/acsabm.4c00715.
23. Zussman, E. Encapsulation of cells within electrospun fibers. *Polym. Adv. Technol.* **2010**, *22*, 366–371. https://doi.org/10.1002/pat.1812.
24. Zhang, Y.-Q.; Wang, P.; Shi, Q.-F.; Ning, X.; Chen, Z.; Ramakrishna, S.; Zheng, J.; Long, Y.-Z. Advances in Wet Electrospinning: Rich Morphology and Promising Applications. *Adv. Fiber Mater.* **2025**, *7*, 374–413. https://doi.org/10.1007/s42765-024-00493-7.
25. Townsend-Nicholson, A.; Jayasinghe, S.N. Cell Electrospinning: a Unique Biotechnique for Encapsulating Living Organisms for Generating Active Biological Microthreads/Scaffolds. *Biomacromolecules* **2006**, *7*, 3364–3369.
26. Shih, Y.-H.; Yang, J.-C.; Li, S.-H.; Yang, W.-C.; Chen, C.-C. Bio-electrospinning of poly(l-lactic acid) hollow fibrous membrane. *Text. Res. J.* **2012**, *82*, 602–612. https://doi.org/10.1177/0040517511420756.
27. Zanatta, G.; Steffens, D.; Braghirolli, D.I.; Fernandes, R.A.; Netto, C.A.; Pranke, P. Viability of mesenchymal stem cells during electrospinning. *Braz. J. Med. Biol. Res.* **2012**, *45*, 125–130. https://doi.org/10.1590/s0100-879x2011007500163.
28. Ang, H.Y.; Irvine, S.A.; Avrahami, R.; Sarig, U.; Bronshtein, T.; Zussman, E.; Boey, F.Y.C.; Machluf, M.; Venkatraman, S.S. Characterization of a bioactive fiber scaffold with entrapped HUVECs in coaxial electrospun core-shell fiber. *Biomatter* **2014**, *4*, e28238. https://doi.org/10.4161/biom.28238.
29. Ehler, E.; Jayasinghe, S.N. Cell electrospinning cardiac patches for tissue engineering the heart. *Analyst* **2014**, *139*, 4449–4452. https://doi.org/10.1039/c4an00766b.
30. Yeo, M.; Kim, G. Fabrication of cell-laden electrospun hybrid scaffolds of alginate-based bioink and PCL microstructures for tissue regeneration. *Chem. Eng. J.* **2015**, *275*, 27–35. https://doi.org/10.1016/j.cej.2015.04.038.
31. Braghirolli, D.; Pranke, P.; Zamboni, F.; Acasigua, G.A.X. Association of electrospinning with electrospraying: A strategy to produce 3D scaffolds with incorporated stem cells for use in tissue engineering. *Int. J. Nanomed.* **2015**, 5159-5170. https://doi.org/10.2147/ijn.s84312.
32. Yeo, M.; Kim, G.H. Anisotropically Aligned Cell-Laden Nanofibrous Bundle Fabricated via Cell Electrospinning to Regenerate Skeletal Muscle Tissue. *Small* **2018**, *14*, 1803491. https://doi.org/10.1002/smll.201803491.
33. Wu, Y.; Ranjan, V.D.; Zhang, Y. A Living 3D In Vitro Neuronal Network Cultured inside Hollow Electrospun Microfibers. *Adv. Biosyst.* **2018**, *2*, 1700218. https://doi.org/10.1002/adbi.201700218.
34. Guo, Y.; Gilbert-Honick, J.; Somers, S.M.; Mao, H.Q.; Grayson, W.L. Modified cell-electrospinning for 3D myogenesis of C2C12s in aligned fibrin microfiber bundles. *Biochem. Biophys. Res. Commun.* **2019**, *516*, 558–564. https://doi.org/10.1016/j.bbrc.2019.06.082.
35. Ranjan, V.D.; Zeng, P.; Li, B.; Zhang, Y. In vitro cell culture in hollow microfibers with porous structures. *Biomater. Sci.* **2020**, *8*, 2175–2188. https://doi.org/10.1039/c9bm01986c.

36. Yeo, M.; Kim, G. Micro/nano-hierarchical scaffold fabricated using a cell electrospinning/3D printing process for co-culturing myoblasts and HUVECs to induce myoblast alignment and differentiation. *Acta Biomater.* **2020**, *107*, 102–114. https://doi.org/10.1016/j.actbio.2020.02.042.
37. Das, P.; Hore, A.; Ghosh, A.; Datta, P. Bone tissue engineering construct fabricated using a cell electrospinning technique with polyglutamic acid biopolymer. *J. Polym. Res.* **2021**, *28*, 255. https://doi.org/10.1007/s10965-021-02612-z.
38. Yang, I.-H.; Chen, Y.-S.; Li, J.-J.; Liang, Y.-J.; Lin, T.-C.; Jakfar, S.; Thacker, M.; Wu, S.-C.; Lin, F.-H. The development of laminin-alginate microspheres encapsulated with Ginsenoside Rg1 and ADSCs for breast reconstruction after lumpectomy. *Bioact. Mater.* **2021**, *6*, 1699–1710. https://doi.org/10.1016/j.bioactmat.2020.11.029.
39. Nosoudi, N.; Hart, C.; Mcknight, I.; Esmaeilpour, M.; Ghomian, T.; Zadeh, A.; Raines, R.; Ramirez Vick, J.E. Differentiation of adipose-derived stem cells to chondrocytes using electrospraying. *Sci. Rep.* **2021**, *11*, 24301. https://doi.org/10.1038/s41598-021-03824-5.
40. Semitela, Â.; Ramalho, G.; Capitão, A.; Sousa, C.; Mendes, A.F.; Aap Marques, P.; Completo, A. Bio-electrospraying assessment toward in situ chondrocyte-laden electrospun scaffold fabrication. *J. Tissue Eng.* **2022**, *13*, 204173142110693. https://doi.org/10.1177/20417314211069342.
41. Wen, Z.; Chen, Y.; Liao, P.; Wang, F.; Zeng, W.; Liu, S.; Wu, H.; Wang, N.; Moroni, L.; Zhang, M.; et al. In Situ Precision Cell Electrospinning as an Efficient Stem Cell Delivery Approach for Cutaneous Wound Healing. *Adv. Healthc. Mater.* **2023**, *12*, 2300970. https://doi.org/10.1002/adhm.202300970.
42. Xu, F.; Dawson, C.; Hoare, T. Multicellular Layered Nanofibrous Poly(Oligo Ethylene Glycol Methacrylate) (POEGMA)-Based Hydrogel Scaffolds via Reactive Cell Electrospinning. *Adv. Biol.* **2023**, *7*, 2300052. https://doi.org/10.1002/adbi.202300052.
43. Dawson, C.; Xu, F.; Hoare, T. Reactive Cell Electrospinning of Anisotropically Aligned and Bilayer Hydrogel Nanofiber Networks. *ACS Biomater. Sci. Eng.* **2023**, *9*, 6490–6503. https://doi.org/10.1021/acsbiomaterials.3c01013.
44. Lu, T.; Yang, L.; Li, Z.; Liu, Y.; Xu, S.E.; Ye, C. Immediate implantation of ultrafine fiber slow-release system based on cell electrospinning to induce osteogenesis of mesenchymal stem cells. *Regen. Biomater.* **2024**, *11*, rbad113. https://doi.org/10.1093/rb/rbad113.
45. Al-Abduljabbar, A.; Farooq, I. Electrospun Polymer Nanofibers: Processing, Properties, and Applications. *Polymers* **2022**, *15*, 65. https://doi.org/10.3390/polym15010065.
46. Lasprilla-Botero, J.; Álvarez-Láinez, M.; Lagaron, J.M. The influence of electrospinning parameters and solvent selection on the morphology and diameter of polyimide nanofibers. *Mater. Today Commun.* **2018**, *14*, 1–9. https://doi.org/10.1016/j.mtcommm.2017.12.003.
47. Xue, J.; Wu, T.; Dai, Y.; Xia, Y. Electrospinning and Electrospun Nanofibers: Methods, Materials, and Applications. *Chem. Rev.* **2019**, *119*, 5298–5415. https://doi.org/10.1021/acs.chemrev.8b00593.
48. Sell, S.A.; Wolfe, P.S.; Garg, K.; Mccool, J.M.; Rodriguez, I.A.; Bowlin, G.L. The Use of Natural Polymers in Tissue Engineering: A Focus on Electrospun Extracellular Matrix Analogues. *Polymers* **2010**, *2*, 522–553. https://doi.org/10.3390/polym2040522.
49. Yang, J.M.; Yang, J.H.; Tsou, S.C.; Ding, C.H.; Hsu, C.C.; Yang, K.C.; Yang, C.C.; Chen, K.S.; Chen, S.W.; Wang, J.S. Cell proliferation on PVA/sodium alginate and PVA/poly(gamma-glutamic acid) electrospun fiber. *Mater. Sci. Eng. C Mater. Biol. Appl.* **2016**, *66*, 170–177. https://doi.org/10.1016/j.msec.2016.04.068.
50. Wang, Y.; Guo, Z.; Qian, Y.; Zhang, Z.; Lyu, L.; Wang, Y.; Ye, F. Study on the Electrospinning of Gelatin/Pullulan Composite Nanofibers. *Polymers* **2019**, *11*, 1424. https://doi.org/10.3390/polym11091424.
51. Seon-Lutz, M.; Couffin, A.C.; Vignoud, S.; Schlatter, G.; Hebraud, A. Electrospinning in water and in situ crosslinking of hyaluronic acid/cyclodextrin nanofibers: Towards wound dressing with controlled drug release. *Carbohydr. Polym.* **2019**, *207*, 276–287. https://doi.org/10.1016/j.carbpol.2018.11.085.
52. Nie, H.; He, A.; Wu, W.; Zheng, J.; Xu, S.; Li, J.; Han, C.C. Effect of poly(ethylene oxide) with different molecular weights on the electrospinnability of sodium alginate. *Polymer* **2009**, *50*, 4926–4934. https://doi.org/10.1016/j.polymer.2009.07.043.
53. Saquing, C.D.; Tang, C.; Monian, B.; Bonino, C.A.; Manasco, J.L.; Alsberg, E.; Khan, S.A. Alginate–Polyethylene Oxide Blend Nanofibers and the Role of the Carrier Polymer in Electrospinning. *Ind. Eng. Chem. Res.* **2013**, *52*, 8692–8704. https://doi.org/10.1021/ie302385b.
54. Kim, M.W. Surface activity and property of polyethyleneoxide (PEO) in water. *Colloids Surf. A Physicochem. Eng. Asp.* **1997**, *128*, 145 154.
55. Bt Ibrahim, S.F.; Mohd Azam, N.A.N.; Mat Amin, K.A. Sodium alginate film: The effect of crosslinker on physical and mechanical properties. *IOP Conf. Ser. Mater. Sci. Eng.* **2019**, *509*, 012063. https://doi.org/10.1088/1757-899x/509/1/012063.
56. Yang, Q.; Guo, J.; Zhang, S.; Guan, F.; Yu, Y.; Feng, S.; Song, X.; Bao, D.; Zhang, X. Development of cell adhesive and inherently antibacterial polyvinyl alcohol/polyethylene oxide nanofiber scaffolds via incorporating chitosan for tissue engineering. *Int. J. Biol. Macromol.* **2023**, *236*, 124004. https://doi.org/10.1016/j.ijbiomac.2023.124004.
57. Huang, C.-Y.; Hu, K.-H.; Wei, Z.-H. Comparison of cell behavior on pva/pva-gelatin electrospun nanofibers with random and aligned configuration. *Sci. Rep.* **2016**, *6*, 37960. https://doi.org/10.1038/srep37960.

58. Kwak, H.W.; Shin, M.; Lee, J.Y.; Yun, H.; Song, D.W.; Yang, Y.; Shin, B.S.; Park, Y.H.; Lee, K.H. Fabrication of an ultrafine fish gelatin nanofibrous web from an aqueous solution by electrospinning. *Int. J. Biol. Macromol.* **2017**, *102*, 1092–1103. https://doi.org/10.1016/j.ijbiomac.2017.04.087.
59. Young, A.T.; White, O.C.; Daniele, M.A. Rheological Properties of Coordinated Physical Gelation and Chemical Crosslinking in Gelatin Methacryloyl (GelMA) Hydrogels. *Macromol. Biosci.* **2020**, *20*, 2000183. https://doi.org/10.1002/mabi.202000183.
60. Xiao, S.; Guo, S.; Nesin, V.; Heller, R.; Schoenbach, K.H. Subnanosecond electric pulses cause membrane permeabilization and cell death. *IEEE Trans. Biomed. Eng.* **2011**, *58*, 1239–1245. https://doi.org/10.1109/TBME.2011.2112360.
61. Kotnik, T.; Rems, L.; Tarek, M.; Miklavcic, D. Membrane Electroporation and Electropermeabilization: Mechanisms and Models. *Annu. Rev. Biophys.* **2019**, *48*, 63–91. https://doi.org/10.1146/annurev-biophys-052118-115451.
62. Zu, Y.; Huang, S.; Lu, Y.; Liu, X.; Wang, S. Size Specific Transfection to Mammalian Cells by Micropillar Array Electroporation. *Sci. Rep.* **2016**, *6*, 38661. https://doi.org/10.1038/srep38661.
63. Harris, E.; Elmer, J.J. Optimization of electroporation and other non-viral gene delivery strategies for T cells. *Biotechnol. Prog.* **2021**, *37*, e3066. https://doi.org/10.1002/btpr.3066.
64. Yang, I.-H.; Chen, Y.-S.; Li, J.-J.; Liang, Y.-J.; Lin, T.-C.; Jakfar, S.; Thacker, M.; Wu, S.-C.; Lin, F.-H. The development of laminin-alginate microspheres encapsulated with Ginsenoside Rg1 and ADSCs for breast reconstruction after lumpectomy. *Bioact. Mater.* **2021**, *6*, 1699–1710. https://doi.org/10.1016/j.bioactmat.2020.11.029.
65. Jayasinghe, S.N.; Eagles, P.A.M.; Qureshi, A.N. Electric field driven jetting: An emerging approach for processing living cells. *Biotechnol. J.* **2006**, *1*, 86–94. https://doi.org/10.1002/biot.200500025.
66. O'Hare, M.J.; Ormerod, M.G.; Imrie, P.R.; Peacock, J.H.; Asche, W. Electropermeabilization and Electrosensitivity of Different Types of Mammalian Cells. In *Electroporation and Electrofusion in Cell Biology*; Springer: Berlin/Heidelberg, Germany, 1989; pp. 319–330.
67. ĈemazˆR, M.; Jarm, T.; Miklavĉiĉ, D.; Lebar, A.M.; Ihan, A.; Kopitar, N.A.; Serŝa, G. Effect of Electric-Field Intensity on Electropermeabilization and Electrosensitmty of Various Tumor-Cell Lines In Vitro. *Electro Magnetobiol.* **1998**, *17*, 263–272. https://doi.org/10.3109/15368379809022571.
68. Lang, Q.; Wu, Y.; Ren, Y.; Tao, Y.; Lei, L.; Jiang, H. AC Electrothermal Circulatory Pumping Chip for Cell Culture. *ACS Appl. Mater. Interfaces* **2015**, *7*, 26792–26801. https://doi.org/10.1021/acsami.5b08863.
69. Pucihar, G.; Kotnik, T.; Kanduser, M.; Miklavcic, D. The influence of medium conductivity on electropermeabilization and survival of cells in vitro. *Bioelectrochemistry* **2001**, *54*, 107–115.
70. Kucernak, A.R.; Wang, H.; Lin, X. Avoid Using Phosphate Buffered Saline (PBS) as an Electrolyte for Accurate OER Studies. *ACS Energy Lett.* **2024**, *9*, 3939–3946. https://doi.org/10.1021/acsenergylett.4c01589.
71. Ageev, I.M.; Rybin, Y.M. Features of Measuring the Electrical Conductivity of Distilled Water in Contact with Air. *Meas. Tech.* **2020**, *62*, 923–927. https://doi.org/10.1007/s11018-020-01714-2.
72. Sun, Z.; Deitzel, J.M.; Knopf, J.; Chen, X.; Gillespie, J.W. The effect of solvent dielectric properties on the collection of oriented electrospun fibers. *J. Appl. Polym. Sci.* **2012**, *125*, 2585–2594. https://doi.org/10.1002/app.35454.
73. Wendorff, J.H.; Agarwal, S.; Greiner, A. *Electrospinning: Materials, Processing and Applications*; Wiley-VCH: Weinheim, Germany, 2012.
74. Angammana, C.J.; Jayaram, S.H. Analysis of the Effects of Solution Conductivity on Electrospinning Process and Fiber Morphology. *IEEE Trans. Ind. Appl.* **2011**, *47*, 1109–1117. https://doi.org/10.1109/tia.2011.2127431.
75. Nezarati, R.M.; Eifert, M.B.; Cosgriff-Hernandez, E. Effects of humidity and solution viscosity on electrospun fiber morphology. *Tissue Eng. Part C Methods* **2013**, *19*, 810–819. https://doi.org/10.1089/ten.TEC.2012.0671.
76. Kim, Y.B.; Lee, H.; Kim, G.H. Strategy to Achieve Highly Porous/Biocompatible Macroscale Cell Blocks, Using a Collagen/Genipin-bioink and an Optimal 3D Printing Process. *ACS Appl. Mater. Interfaces* **2016**, *8*, 32230–32240. https://doi.org/10.1021/acsami.6b11669.
77. Blaeser, A.; Duarte Campos, D.F.; Puster, U.; Richtering, W.; Stevens, M.M.; Fischer, H. Controlling Shear Stress in 3D Bioprinting is a Key Factor to Balance Printing Resolution and Stem Cell Integrity. *Adv. Healthc. Mater.* **2016**, *5*, 326–333. https://doi.org/10.1002/adhm.201500677.
78. Yoon, J.; Yang, H.S.; Lee, B.S.; Yu, W.R. Recent Progress in Coaxial Electrospinning: New Parameters, Various Structures, and Wide Applications. *Adv. Mater.* **2018**, *30*, e1704765. https://doi.org/10.1002/adma.201704765.
79. Han, D.; Steckl, A.J. Coaxial Electrospinning Formation of Complex Polymer Fibers and their Applications. *Chempluschem* **2019**, *84*, 1453–1497. https://doi.org/10.1002/cplu.201900281.
80. Lu, Y.; Huang, J.; Yu, G.; Cardenas, R.; Wei, S.; Wujcik, E.K.; Guo, Z. Coaxial electrospun fibers: Applications in drug delivery and tissue engineering. *WIREs Nanomed. Nanobiotechnol.* **2016**, *8*, 654–677. https://doi.org/10.1002/wnan.1391.
81. Saudi, A.; Amini, S.; Amirpour, N.; Kazemi, M.; Zargar Kharazi, A.; Salehi, H.; Rafienia, M. Promoting neural cell proliferation and differentiation by incorporating lignin into electrospun poly(vinyl alcohol) and poly(glycerol sebacate) fibers. *Mater. Sci. Eng. C Mater. Biol. Appl.* **2019**, *104*, 110005. https://doi.org/10.1016/j.msec.2019.110005.

82. Liu, J.J.; Wang, C.Y.; Wang, J.G.; Ruan, H.J.; Fan, C.Y. Peripheral nerve regeneration using composite poly(lactic acid-caprolactone)/nerve growth factor conduits prepared by coaxial electrospinning. *J. Biomed. Mater. Res. Part A* **2011**, *96A*, 13–20. https://doi.org/10.1002/jbm.a.32946.
83. Xu, H.; Gao, Z.; Wang, Z.; Wu, W.; Li, H.; Liu, Y.; Jia, S.; Hao, D.; Zhu, L. Electrospun PCL Nerve Conduit Filled with GelMA Gel for CNTF and IGF-1 Delivery in Promoting Sciatic Nerve Regeneration in Rat. *ACS Biomater. Sci. Eng.* **2023**, *9*, 6309–6321. https://doi.org/10.1021/acsbiomaterials.3c01048.
84. Zhang, Y.; Zhang, Z.; Wang, Y.; Su, Y.; Chen, M. 3D myotube guidance on hierarchically organized anisotropic and conductive fibers for skeletal muscle tissue engineering. *Mater. Sci. Eng. C Mater. Biol. Appl.* **2020**, *116*, 111070. https://doi.org/10.1016/j.msec.2020.111070.
85. Onoe, H.; Takeuchi, S. Cell-laden microfibers for bottom-up tissue engineering. *Drug Discov. Today* **2015**, *20*, 236–246. https://doi.org/10.1016/j.drudis.2014.10.018.
86. Jana, S.; Levengood, S.K.L.; Zhang, M. Anisotropic Materials for Skeletal-Muscle-Tissue Engineering. *Adv. Mater.* **2016**, *28*, 10588–10612. https://doi.org/10.1002/adma.201600240.
87. Batalov, I.; Jallerat, Q.; Kim, S.; Bliley, J.; Feinberg, A.W. Engineering aligned human cardiac muscle using developmentally inspired fibronectin micropatterns. *Sci. Rep.* **2021**, *11*, 11502. https://doi.org/10.1038/s41598-021-87550-y.
88. Kobayashi, M.; Lei, N.Y.; Wang, Q.; Wu, B.M.; Dunn, J.C. Orthogonally oriented scaffolds with aligned fibers for engineering intestinal smooth muscle. *Biomaterials* **2015**, *61*, 75–84. https://doi.org/10.1016/j.biomaterials.2015.05.023.
89. Nardone, G.; Oliver-De La Cruz, J.; Vrbsky, J.; Martini, C.; Pribyl, J.; Skládal, P.; Pešl, M.; Caluori, G.; Pagliari, S.; Martino, F.; et al. YAP regulates cell mechanics by controlling focal adhesion assembly. *Nat. Commun.* **2017**, *8*, 15321. https://doi.org/10.1038/ncomms15321.
90. Teo, B.K.K.; Wong, S.T.; Lim, C.K.; Kung, T.Y.S.; Yap, C.H.; Ramagopal, Y.; Romer, L.H.; Yim, E.K.F. Nanotopography Modulates Mechanotransduction of Stem Cells and Induces Differentiation through Focal Adhesion Kinase. *ACS Nano* **2013**, *7*, 4785–4798. https://doi.org/10.1021/nn304966.
91. Von Erlach, T.C.; Bertazzo, S.; Wozniak, M.A.; Horejs, C.-M.; Maynard, S.A.; Attwood, S.; Robinson, B.K.; Autefage, H.; Kallepitis, C.; Del Río Hernández, A.; et al. Cell-geometry-dependent changes in plasma membrane order direct stem cell signalling and fate. *Nat. Mater.* **2018**, *17*, 237–242. https://doi.org/10.1038/s41563-017-0014-0.
92. Iranshahi, K.; Defraeye, T.; Rossi, R.M.; Müller, U.C. Electrohydrodynamics and its applications: Recent advances and future perspectives. *Int. J. Heat Mass Transf.* **2024**, *232*, 125895. https://doi.org/10.1016/j.ijheatmasstransfer.2024.125895.
93. Wang, Z.; Li, S.; Wu, Z.; Kang, Y.; Xie, S.; Cai, Z.; Shan, X.; Li, Q. Pulsed electromagnetic field-assisted reduced graphene oxide composite 3D printed nerve scaffold promotes sciatic nerve regeneration in rats. *Biofabrication* **2024**, *16*, 035013. https://doi.org/10.1088/1758-5090/ad3d8a.
94. Jensen, B.N.; Wang, Y.; Le Friec, A.; Nabavi, S.; Dong, M.; Seliktar, D.; Chen, M. Wireless electromagnetic neural stimulation patch with anisotropic guidance. *NPJ Flex. Electron.* **2023**, *7*, 34. https://doi.org/10.1038/s41528-023-00270-3.
95. Liu, Z.; Cai, M.; Zhang, X.; Yu, X.; Wang, S.; Wan, X.; Wang, Z.L.; Li, L. Cell-Traction-Triggered On-Demand Electrical Stimulation for Neuron-Like Differentiation. *Adv. Mater.* **2021**, *33*, 2106317. https://doi.org/10.1002/adma.202106317.
96. Guo, W.; Zhang, X.; Yu, X.; Wang, S.; Qiu, J.; Tang, W.; Li, L.; Liu, H.; Wang, Z.L. Self-Powered Electrical Stimulation for Enhancing Neural Differentiation of Mesenchymal Stem Cells on Graphene-Poly(3,4-ethylenedioxythiophene) Hybrid Microfibers. *ACS Nano* **2016**, *10*, 5086–5095. https://doi.org/10.1021/acsnano.6b00200.
97. Hu, W.; Wei, X.; Zhu, L.; Yin, D.; Wei, A.; Bi, X.; Liu, T.; Zhou, G.; Qiang, Y.; Sun, X.; et al. Enhancing proliferation and migration of fibroblast cells by electric stimulation based on triboelectric nanogenerator. *Nano Energy* **2019**, *57*, 600–607. https://doi.org/10.1016/j.nanoen.2018.12.077.
98. Choe, G.; Han, U.G.; Ye, S.; Kang, S.; Yoo, J.; Cho, Y.S.; Jung, Y. Effect of Electrical Stimulation on Nerve-Guided Facial Nerve Regeneration. *ACS Biomater. Sci. Eng.* **2023**, *9*, 3512–3521. https://doi.org/10.1021/acsbiomaterials.3c00222.
99. He, L.; Xiao, Q.; Zhao, Y.; Li, J.; Reddy, S.; Shi, X.; Su, X.; Chiu, K.; Ramakrishna, S. Engineering an Injectable Electroactive Nanohybrid Hydrogel for Boosting Peripheral Nerve Growth and Myelination in Combination with Electrical Stimulation. *ACS Appl. Mater. Interfaces* **2020**, *12*, 53150–53163. https://doi.org/10.1021/acsami.0c16885.
100. Huang, J.; Xue, S.; Buchmann, P.; Teixeira, A.P.; Fussenegger, M.; Huang, J.; Xue, S.; Buchmann, P.; Teixeira, A.P.; Fussenegger, M. An electrogenetic interface to program mammalian gene expression by direct current. *Nat. Metab.* **2023**, *5*, 1395–1407. https://doi.org/10.1038/s42255-023-00850-7.
101. Argentati, C.; Morena, F.; Tortorella, I.; Bazzucchi, M.; Porcellati, S.; Emiliani, C.; Martino, S. Insight into Mechanobiology: How Stem Cells Feel Mechanical Forces and Orchestrate Biological Functions. *Int. J. Mol. Sci.* **2019**, *20*, 5337 https://doi.org/10.3390/ijms20215337.
102. Elosegui-Artola, A.; Andreu, I.; Beedle, A.E.M.; Lezamiz, A.; Uroz, M.; Kosmalska, A.J.; Oria, R.; Kechagia, J.Z.; Rico-Lastres, P.; Le Roux, A.L.; et al. Force Triggers YAP Nuclear Entry by Regulating Transport across Nuclear Pores. *Cell* **2017**, *171*, 1397–1410.e1314. https://doi.org/10.1016/j.cell.2017.10.008.

Article

Angle-Independent Surface-Instability Hydrogel Sensors Enabled by Thickness Control

Ruoyi Ke †, Imri Frenkel †, Zixiao Liu, Chuan Wei Zhang, Ping He, Pengju Shi, Abdullatif Jazzar, Yousif Alsaid, Yingjie Du, Sidi Duan, Dong Wu, Mutian Hua, Shuwang Wu, and Ximin He *

Department of Materials Science and Engineering, University of California, Los Angeles, CA 90095, USA
* Correspondence: ximinhe@ucla.edu
† These authors contributed equally to this work.
Received: 9 July 2025; Revised: 26 August 2025; Accepted: 1 September 2025; Published: 4 September 2025

Abstract: Surface instability-based hydrogel sensors offer equipment-free visual detection but suffer from severe angle-dependent visibility that limits practical applications. Here we demonstrate that film thickness serves as a critical fourth design parameter—beyond elastic modulus, swelling ratio, and stimulus concentration—to achieve omnidirectional optical readout. Through systematic optimization across poly(2-(dimethylamino) ethyl methacrylate) (PDMAEMA), poly(acrylamide-co-acrylic acid) (P(AAm-*co*-AAc)), and poly(N-isopropylacrylamide-co-acrylamide) (P(NIPAm-*co*-Am)) systems, we identify an operational thickness window of 160–1300 μm, with 300 μm producing wrinkle dimensions that match visible light wavelengths for angle-independent scattering. This morphological control reduces viewing angle effects by >80%, enabling reliable naked-eye detection across a wide viewing angle range (0–60°), representing an >80% improvement over previous angle-dependent sensors. We validate this design framework through enzyme-coupled glucose sensors operating across clinical ranges (200–1000 mg/dL) and direct polarity sensors with binary discrimination at Polarity Index (PI) ~3.5. Exploiting the threshold nature of instability-induced scattering (IIS), we further demonstrate soft material logic gates (AND, OR, XOR) that process environmental stimuli and autonomously control LCE actuators within 15 s—establishing the examples of hydrogel-based Boolean computation without electronic components. These advances transform IIS sensors from laboratory curiosities into practical platforms for soft robotics and autonomous systems.

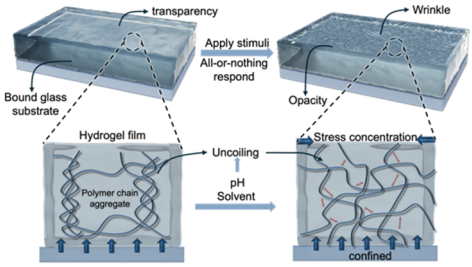

Keywords: hydrogel sensors; surface instability; angle-independent detection; material-based computation; soft robotics

1. Introduction

Intelligent responsive materials capable of sensing environmental changes and transducing them into measurable outputs have emerged as transformative alternatives to traditional rigid electronic sensors [1–4]. Among these, hydrogel-based smart sensors offer unprecedented advantages through their unique combination of high water content (up to 99%) [5], mechanical flexibility, and stimuli-responsive behavior [6,7], enabling seamless integration with biological systems while achieving molecular-level detection capabilities and maintaining mechanical compliance similar to soft tissues [8]. Unlike conventional electronic sensors that require complex fabrication processes, external power sources, and suffer from biocompatibility issues, hydrogel sensors leverage volume phase transitions (VPT) [9,10] to achieve detection sensitivities down to femtomolar concentrations [11] through simple swelling/deswelling mechanisms. Pioneering work on pH-responsive hydrogels has demonstrated remarkable volume changes, with poly(2-hydroxyethyl methacrylate) systems exhibiting swelling ratios from 40% to 80% under alkaline conditions [12], while temperature-responsive poly(N-isopropylacrylamide) systems show sharp transitions at physiologically relevant temperatures [13], and glucose-

sensing hydrogels incorporating enzymes enable continuous monitoring [14]. Notably, fiber-optic interferometric sensors incorporating responsive hydrogels have demonstrated detection limits down to nanomolar concentrations [15], with some systems achieving refractive index sensitivities surpassing 0.001 RIU resolution [16], representing orders of magnitude improvement over conventional methods by exploiting optical interference patterns in hydrogel matrices. Beyond sensing, these materials have enabled remarkable advances in soft robotics, with light-guided swimming robots achieving speeds up to 19.2 mm/s through photothermal Marangoni effects while incorporating multi-band electromagnetic stealth capabilities [17]. These developments have addressed fundamental challenges in the sensor field by combining the biocompatibility and flexibility of hydrogels with detection sensitivities that match or exceed traditional electronic sensors, paving the way for applications in wearable health monitoring [18], environmental sensing [19], and biomedical diagnostics [20] where rigid electronics would be impractical.

Among the diverse landscape of smart material sensors, self-reporting capability represent a critical advancement by fundamentally solving the instrumentation dependency [21] that has limited practical deployment of responsive hydrogels. Traditional hydrogel sensors, despite their excellent sensitivity and biocompatibility, typically require external equipment such as spectrophotometers, electrochemical analyzers, or mechanical testing apparatus to transduce and quantify their responses, adding cost, complexity, and limiting portability [22–24]. Self-reporting sensor address this challenge by integrating both sensing and signaling functions within a single material platform, producing visually observable outputs—such as color changes [25,26], fluorescence modulation [27,28], or transparency-to-opacity transitions [29]—that can be interpreted with the naked eye. Frenkel et al. [30] exemplified this approach by developing self-reporting hydrogel sensors based on surface IIS, establishing a three-parameter design space encompassing elastic modulus, critical swelling ratio, and stimulus concentration, where hydrogel films transition from transparent to opaque states upon reaching critical analyte concentrations. This capability is particularly transformative for point-of-care diagnostics, environmental monitoring in resource-limited settings, and wearable health devices where conventional readout equipment would be impractical or prohibitively expensive, demonstrating that sophisticated sensing can be achieved without any external power or readout devices.

However, when integrating self-reporting sensors into intelligent systems for autonomous decision-making and actuation, a critical challenge emerges: angle-dependent visibility that compromises reliable signal interpretation [31–33]. This limitation, inherent to many optical self-reporting mechanisms including surface instability-based sensors [34], arises from the wavelength-dependent light scattering of surface features that vary with observation angle—a well-documented phenomenon in rough surface optics where the angular dependence of scattered light intensity can vary significantly with viewing geometry [35]. Studies on rough surfaces have demonstrated that the intensity of scattered radiation generally decreases with increasing reflection angle [36], with some systems showing variations in optical response that can compromise measurement reliability when the observation angle deviates from normal incidence [37]. Such angle sensitivity severely restricts practical applications where consistent readout is essential, particularly in soft robotic systems [38,39], wearable devices [40], or automated monitoring platforms [41] where sensor orientation cannot be precisely controlled. Previous IIS sensors required oblique viewing angles to confirm wrinkled states, as surface instabilities were not discernibly opaque when observed head-on [30], fundamentally limiting their integration into autonomous systems that rely on unambiguous binary signals. We propose that systematic optimization of film thickness—a previously overlooked fourth design parameter—can fundamentally resolve this angle-dependency by tuning the characteristic wavelength of surface features to match visible light wavelengths, thereby achieving robust omnidirectional visibility essential for intelligent system integration.

Here, we present a comprehensive design strategy that advances IIS sensors from angle-dependent reporters to omnidirectional smart material computing elements suitable for autonomous soft robotic systems. By systematically investigating the role of film thickness across multiple stimuli-responsive polymer systems—including cationic PDMAEMA for pH sensing and P(NIPAm-*co*-Am) for solvent polarity detection—we establish that thickness optimization within the 160–1300 μm range enables angle-independent visibility through precise matching of wrinkle wavelengths with visible light. We demonstrate that this fourth design parameter not only resolves the fundamental optical limitations but also enables the construction of soft material logic gates (AND, OR, XOR) by exploiting the discrete threshold-dependent transitions inherent to IIS sensors. Furthermore, we integrate these logic elements with liquid crystal elastomer (LCE) actuators to create fully autonomous soft robotic systems capable of sensing environmental stimuli, processing information through material-based computation, and executing mechanical responses without any electronic components—achieving the first demonstration of closed-loop intelligent behavior in purely soft material systems. This work establishes a new paradigm where

materials themselves become autonomous agents capable of sophisticated decision-making, opening unprecedented possibilities for soft robotics, biomedical devices, and adaptive systems.

2. Experimental Methods

2.1. Chemicals and Materials

2-(dimethylamino)ethyl methacrylate (DMAEMA), acrylamide, acrylic acid, N-isopropyl acrylamide (NIPAm), N,N′-Methylenebisacrylamide (Bis), poly(ethylene glycol) diacrylate (PEGDA) (Mn = 250; 525; and 700), Lithium phenyl-2,4,6-trimethylbenzoylphosphinate (TPO-Li), 1-[4-(2-Hydroxyethoxy)-phenyl]-2-hydroxy-2-methyl-1-propane-1-one (Irgacure 2959), 2-hydroxy-2-methylpropiophenone (Darocur 1173), azobisisobutyronitrile (AIBN), glucose oxidase, glucose. Citric acid, monosodium phosphate, disodium phosphate, trisodium phosphate. dimethyl formamide (DMF), dimethylsulfoxide (DMSO), methanol, 2-propanol, hexane, ethyl acetate. 3-trimethyoxysilyl propyl methacrylate, acetic acid, ethanol were purchased from Sigma-Aldrich (St. Louis, MO, USA). 2-Methyl-1,4-phenylene bis(4-(3-(acryloyloxy)propoxy)benzoate) (RM 257) was purchased from Shijiazhuang Sdyano Fine Chemical, Co., Ltd. (Shijiazhuang, Hebei, China). 1,6-hexanedithiol (HDT), pentaerythritol tetrakis (3-mercaptopropionate) (PETMP), dipropylamine (DPA) and toluene were purchased from Sigma-Aldrich (St. Louis, MO, USA). Polydimethylsiloxane (PDMS) (Sylgard 184) was purchased from Dow Inc. (Midland, MI, USA). Silicone adhesive was purchased from Loctite (Düsseldorf, Germany). These chemicals were used directly as purchased, unless further specified.

UV LED (Dymax, Torrington, CT, USA), pH meter (Thermo Scientific, Waltham, MA, USA), Vacuum Oven (VWR, Radnor, PA, USA), Freeze Dryer (Labconco, Kansas City, MO, USA), Arduino (Arduino, Somerville, MA, USA), Profilometer (Bruker, Billerica, MA, USA), SEM (JEOL, Tokyo, Japan), FTIR (PerkinElmer, Waltham, MA, USA), Critical CO2 dryer (Tousimis, Rockville, MD, USA), Laser (green, 532 nm) and Laser (red, 650 nm) (Thorlabs, Newton, NJ, USA).

2.2. Synthesis of IIS Sensors

Hydrogel sensors were prepared by photopolymerization of aqueous monomer solutions following the fabrication process illustrated in Supplementary Figure S1. Monomers (acrylamide, N-isopropylacrylamide, acrylic acid, or 2-(dimethylamino)ethyl methacrylate) were combined with crosslinkers (Bis, PEGDA250, PEGDA525, or PEGDA700) and photoinitiators (Irgacure 2959, Darocur 1173, or TPO-Li) in deionized water. Formulations contained 10–60% *w*/*w* monomer and 1–4% *w*/*w* crosslinker relative to total solution mass.

For acrylamide-acrylic acid and NIPAm-Am systems, Bis crosslinker and Irgacure 2959 were maintained at 1% *w*/*w*. DMAEMA formulations utilized 0.7% *w*/*w* TPO-Li with various crosslinkers tested. PEGDA700 at 3% *w*/*w* was selected for final device fabrication based on consistent homogeneous polymerization and favorable swelling characteristics. Formulations with Bis crosslinker produced fragile gels, while those exceeding 60% monomer or 3% crosslinker content were excessively rigid despite ready polymerization.

For enzyme-responsive sensors, urease (Sigma-Aldrich, St. Louis, MO, USA) (0.4% *w*/*w*) or glucose oxidase (0.1–1% *w*/*w*) was dissolved in the monomer solution. Solutions were homogenized by stirring for 15 min. Aliquots of 160–500 µL were dispensed into PDMS molds (60–1500 µm depth) and covered with functionalized glass slides, avoiding air bubble entrapment. Acrylamide-based formulations were polymerized under 400 W UV illumination for 60 s using a Dymax 2000-EC Series flood lamp (Dymax, Torrington, CT, USA). DMAEMA formulations required 600 W UV LED exposure for 20 min. Polymerized films remained adhered to glass substrates upon demolding.

2.3. Functionalized Substrates

Glass substrates were cut to size and cleaned by sequential sonication in ethanol, acetone, and water (15 min each) using a Branson 5800 sonicator (Branson Ultrasonics, Danbury, CT, USA). After N_2 drying, substrates underwent O_2 plasma treatment (3 min, high power) in a Harrick Plasma PDC-001 cleaner (Harrick Plasma, Ithaca, NY, USA) (115V). Immediately following plasma exposure, substrates were immersed in a silanization solution containing ethanol (600 mL), acetic acid (18 mL, 10%), and 3-(trimethoxysilyl)propyl methacrylate (6 mL) for 48 h. Functionalized substrates were stored in a desiccator until use.

The silanization treatment with 3-(trimethoxysilyl)propyl methacrylate creates covalent bonds between the glass substrate and hydrogel network through copolymerization of the methacrylate groups during UV polymerization. This chemical anchoring mechanism has been demonstrated to provide exceptional interfacial stability, withstanding repeated swelling-deswelling cycles and long-term aqueous immersion without delamination [42]. Previous studies have shown that silanized interfaces maintain adhesion strength above 100

kPa even after 6 months of continuous water exposure, far exceeding the ~10 kPa stress generated during hydrogel swelling [43]. Furthermore, the transparent glass substrate requirement can be addressed through alternative transparent polymeric substrates (e.g., silanized PET or PMMA) that offer similar optical clarity while enabling flexible device architectures [44].

2.4. Soft Robotic LCE-Based Actuator

Liquid crystal elastomer (LCE) actuators were prepared following the protocol of Shi et al. [38]. Candle soot (CS) was collected on aluminum foil from burning paraffin candles. The LCE matrix was synthesized via two-step thiol-acrylate Michael addition. RM 257 monomer and Irgacure 2959 (0.6% *w*/*w*) were dissolved in toluene (30% *w*/*w*) and combined with PETMP (13 mol% of thiol groups), HDT (2.5% molar excess of acrylate), and CS (1.0% *w*/*w*). The mixture was stirred at 80 °C and 500 rpm, then sonicated for 20 min in a Branson 5800 bath sonicator.

DPA catalyst solution (1 mol% based on thiol groups, 2% *w*/*w* in toluene) was added dropwise with continuous stirring. The reaction mixture was cast between glass plates coated with Kapton tape (DuPont, Wilmington, DE, USA) and reacted at room temperature for 24 h, followed by 55 °C curing for an additional 24 h. The partially crosslinked film was stretched to 60% strain, clamped in the extended state, and exposed to 365 nm UV light for 30 min to complete crosslinking.

2.5. Characterization

Swelling ratios and surface morphologies were analyzed using a Nikon camera with Tracker (version 6.0.1) and ImageJ software (version 1.53) for image analysis. Elastic moduli were determined by dynamic mechanical analysis (DMA 850, TA Instruments, New Castle, DE, USA) at 8%/min strain rate and 25 °C. Optical properties were characterized using a Shimadzu UV-3101-PC UV-Vis-NIR (Shimadzu Corporation, Kyoto, Japan) spectrophotometer for transmission and reflectance measurements. Solution pH was monitored with a Thermo Scientific pH meter (Thermo Fisher Scientific, Waltham, MA, USA).

3. Result and Discussion

3.1. Surface Instability-Induced Optical Switching in Constrained Hydrogels

Substrate-constrained hydrogel films undergo surface instability formation when exposed to environmental stimuli (Figure 1a). In our PDMAEMA system, acidic conditions protonate tertiary amine groups, enhancing hydrophilicity and generating osmotic pressure that drives water uptake. The polymer network attempts to expand isotropically, but substrate adhesion prevents lateral expansion at the bottom interface. This geometric constraint converts volumetric swelling into compressive stress within the film plane. Once this stress exceeds the critical buckling threshold—determined by the film's elastic modulus and thickness—the surface spontaneously forms periodic wrinkles to minimize elastic energy [45–47]. Optical measurements reveal a dramatic transformation (Figure 1b,c): smooth films with >80% transmission at 650 nm suddenly develop light-scattering surface textures, reducing transmission below 20%. This transition occurs within 0.5 pH units, producing an unambiguous visual change from transparent to opaque states. The cooperative nature of polymer volume phase transitions ensures no intermediate states exist—sensors are either fully transparent or completely opaque, enabling reliable binary detection without instrumentation. Importantly, hysteresis characterization revealed minimal differences between forward and reverse pH sweeps (Supplementary Figure S2), with both normalized transmission and mass changes showing nearly overlapping profiles during acidification and alkalinization cycles. The sensors maintained consistent critical pH thresholds (pH 7–8.0) regardless of sweep direction, ensuring reliable and reproducible detection without drift in activation points—a critical requirement for practical sensing applications.

The robust substrate-hydrogel interface achieved through silane coupling ensures long-term operational stability of IIS sensors. The covalent Si-O-Si bonds formed during silanization are hydrolytically stable at pH 3–9, covering the entire operational range of our sensors. Wang et al. demonstrated that hydrogels anchored to glass substrates through siloxane bonds maintained firm adhesion in purified water and acidic solutions for over 36 days, only detaching in strongly alkaline conditions (pH > 9) [48]. This chemical anchoring prevents the interfacial failure modes commonly observed in physically adhered hydrogel films, such as delamination, edge lifting, or catastrophic peeling during volume phase transitions. Additionally, the constrained swelling mechanism inherently protects the interface—while unconstrained hydrogels can experience 300–400% volume changes that generate destructive stresses, substrate-constrained films redirect expansion perpendicular to the interface, minimizing shear forces that could compromise adhesion [49].

Systematic characterization across multiple hydrogel formulations revealed the parameter space governing instability formation (Figure 1d). Elastic modulus measurements using dynamic mechanical analysis showed values ranging from 65 kPa for 40%-3% monomer-crosslinker compositions to 425 kPa for 50%-2% formulations. Critical swelling ratios varied from 1.5 to 4.5, inversely correlating with crosslink density. For PDMAEMA systems, critical pH values shifted from 5.5 to 9.0 with increasing polymer content, while P(AAm-*co*-AAc) exhibited opposite trends due to anionic carboxylic groups [30]. P(NIPAm-*co*-Am) hydrogels responded to solvent polarity rather than pH, with critical transitions occurring at polarity indices between 3.8 and 4.5. Despite these diverse chemical mechanisms, all systems followed similar mechanical principles—surface instability occurred when swelling-induced stress exceeded approximately 0.3 times the elastic modulus. However, experimental testing revealed a critical limitation: wrinkled surfaces showed strong angular dependence in visibility. Sensors appearing transparent when viewed at oblique angles (e.g., 45°) displayed opaque wrinkled textures under perpendicular observation. Quantitative measurements confirmed transmission could vary by over 50% depending on observation angle, severely limiting applications where sensor orientation cannot be controlled [39,40].

Film thickness emerged as the key parameter determining both wrinkle formation and optical performance (Figure 1e). Finite element analysis revealed thickness controls surface pattern characteristics through two mechanisms. First, bending stiffness scales with thickness cubed, establishing the minimum stress required for buckling. Second, thickness determines the characteristic length scale of instability patterns. Simulations showed 300 μm films produce high-frequency wrinkles with 50–100 μm wavelengths, while 1500 μm films generate low-frequency undulations exceeding 200 μm wavelength. Experimental validation confirmed only films within 160–1300 μm thickness successfully formed visible wrinkles—thinner films experienced uniform stress preventing localized buckling, while thicker films required stresses beyond what swelling could generate. Most critically, spectroscopic analysis across 400–800 nm revealed that 300 μm thickness produces optimal light scattering (Figure 1f). At this thickness, wrinkle dimensions match visible light wavelengths, generating Mie scattering that appears uniformly opaque over a wide range of viewing angles. Combined transmission and 90° reflectance measurements showed angle-independent visibility metrics reached minimum values at 300 ± 50 μm thickness, reducing observation angle effects by over 80% compared to unoptimized sensors. This morphological control transforms IIS sensors into robust optical indicators suitable for integration with autonomous soft robotic systems.

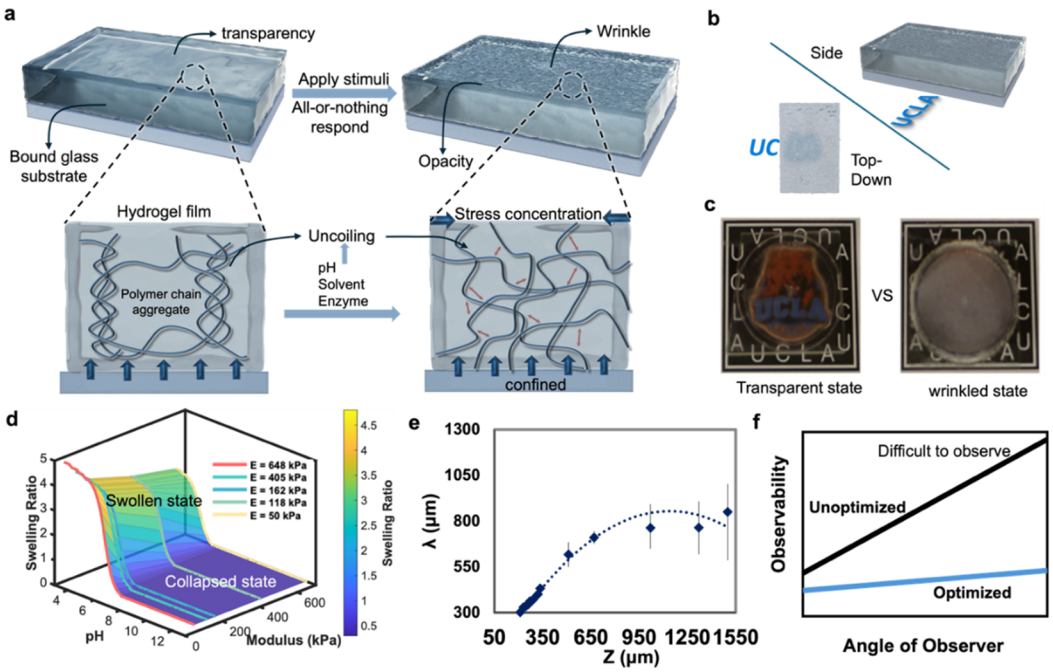

Figure 1. Fundamental mechanisms and design principles of IIS sensors. (**a**) Stimulus-induced transformation from coiled to confined polymer chains generating surface instabilities. (**b**) Fabricated IIS sensor with visual contrast indicator. (**c**) Transparent-to-opaque transition demonstrating naked-eye readability. (**d**) Three-parameter design space of modulus-pH-swelling relationships. (**e**) Finite element analysis of thickness-dependent wrinkle wavelength evolution. (**f**) Angular observability enhancement through thickness optimization.

3.2. Thickness-Mediated Transition from Angle-Dependent to Omnidirectional Visibility

Systematic variation of monomer-crosslinker ratios in PDMAEMA hydrogels produced sensors with distinct pH response thresholds (Figure 2a). Visual inspection revealed wrinkle formation occurring at pH values ranging from 3.5 to 10.0 across different formulations (Supplementary Figure S3). Quantitative transmission measurements at 650 nm confirmed these observations, showing sharp optical transitions within 0.5 pH units (Figure 2b). Each sensor formulation exhibited characteristic critical pH values: 40%-3% M-CL compositions activated at pH 3.5, while 50%–2% formulations required pH 8.0 for wrinkle formation (Figure 2c). These extracted parameters, combined with elastic modulus measurements (65–425 kPa from DMA analysis) (Supplementary Figure S4) and swelling ratio determinations (1.5–4.5), enabled construction of a comprehensive design space (Figure 2d). The normalized pH metric (pHBP) successfully integrated data from both cationic PDMAEMA and anionic P(AAm-*co*-AAc) systems, which exhibit opposite pH responses [30]. This three-dimensional parameter space accurately predicted instability thresholds across diverse polymer chemistries. However, sensors with identical polymer compositions occasionally showed inconsistent optical responses, suggesting additional factors influenced performance.

Film thickness emerged as the critical factor explaining performance variations. Systematic studies across 60–1500 μm thicknesses revealed that only films within 160–1300 μm consistently produced visible wrinkles upon pH stimulation (Figure 2e). Time-resolved transmission measurements demonstrated distinct thickness-dependent behaviors: 160 μm films showed rapid but modest transmission changes (ΔT ~20%), 300–650 μm films exhibited pronounced drops (ΔT > 70%), while 1300 μm films displayed delayed, gradual responses. Films thinner than 160 μm failed to wrinkle due to substrate constraint dominating the entire film thickness, preventing stress localization necessary for buckling. Films exceeding 1300 μm required prohibitively high stresses for instability formation, as bending rigidity scales with thickness cubed [50]. Additionally, thicker films suffered from extended diffusion times that prevented sharp pH gradients needed for localized stress generation. Within the operational range, another critical issue emerged: sensors showed strong viewing angle dependence. Films appearing transparent at 45° oblique angles displayed opaque wrinkled textures under perpendicular observation, with transmission varying by over 50% based on viewing geometry.

Finite element analysis provided mechanistic insights into thickness-dependent wrinkle formation (Figure 2f). The coupled diffusion-deformation model incorporated hygroscopic swelling:

$$\varepsilon_{hs} = \beta M_m (C - C_{ref}) \quad (1)$$

where ε_{hs} represents the hygroscopic strain, M_m is the molar mass, and C and C_{ref} are the concentrations inside the hydrogel and reference concentration, respectively [51–53]. Simulations revealed systematic evolution of surface morphology with thickness: 300 μm films produced high-frequency wrinkles (λ = 50–100 μm) with modest amplitudes (~50 μm), 650 μm films showed intermediate patterns (λ = 100–150 μm), and 1500 μm films generated low-frequency undulations (λ > 200 μm) with amplitudes exceeding 200 μm. The wavelength-thickness relationship followed $\lambda \propto h^{0.8}$, consistent with elastic instability theory. Experimental profilometry confirmed these predictions (Supplementary Figure S5). Interestingly, wrinkle morphology transitioned from herringbone patterns in 180–250 μm films to labyrinthine structures in 280–350 μm films (Supplementary Figure S6), though both geometries produced equivalent light scattering. Wavelength-resolved transmission measurements across 400–800 nm showed thickness-dependent kinetics, with 300 μm films achieving 90% of their final opacity within 2 min, compared to over 10 min for 1300 μm films (Figure 2g).

Comprehensive optical characterization revealed the mechanism underlying angle-independent detection. While transmission measurements alone suggested multiple potentially optimal thicknesses, incorporating 90° reflectance data provided the complete picture (Figure 2h). Thin films (160 μm) showed minimal reflectance changes despite transmission drops, indicating light passed through wrinkled regions rather than scattering. Thick films (1300 μm) exhibited high baseline reflectance that masked wrinkle-induced changes. Films near 300 μm thickness demonstrated maximum changes in both transmission (ΔT = 75%) and reflectance (ΔR = 45%), indicating efficient multi-directional light scattering. The combined angle independence metric:

$$\text{Angle Independence} = (R_f + T_f)/(R_i + T_i) \quad (2)$$

where subscripts f and i denote final (wrinkled) and initial (clear) states, reached its minimum at 300 ± 50 μm thickness (Figure 2i). This optimal performance arises from wrinkle dimensions at this thickness matching visible light wavelengths, producing Mie scattering that appears uniformly opaque regardless of observation angle [54–57]. Temperature-controlled experiments confirmed these films maintained consistent visibility from 0° to 60° viewing angles, substantially reducing the orientation constraints that limited previous IIS sensors. Visual comparison of sensors with different thicknesses clearly demonstrates this thickness-dependent angular visibility

(Supplementary Figure S7). Sensors with non-optimal thicknesses (160 μm and 650 μm) exhibit pronounced transparency variations when viewed from different angles—appearing transparent at certain viewing angles while showing partial opacity at others. In contrast, the optimized 300 μm thickness sensors maintain consistent opacity across the entire 0°–60° viewing range, with minimal variation in visual appearance regardless of observation angle. While not achieving complete omnidirectional visibility (360°), this represents a significant advancement over our previous work [26] which required precise oblique viewing angles (45° ± 5°) for reliable detection. This four-parameter framework—incorporating elastic modulus, swelling ratio, critical stimulus concentration, and film thickness—enables rational design of sensors with predetermined thresholds and reliable omnidirectional visibility.

Long-term cycling tests further validated the practical viability of these sensors (Supplementary Figure S8). Over 100 operational cycles, sensors demonstrated exceptional durability with >85% retention of their initial transmission range. Specifically, sensors cycled between water (pH = 1) and hexane maintained 91.0% of their optical response range, while those alternating between pH 7 and pH 8 environments retained 92.6% of their performance metrics. The minimal performance degradation and consistent activation thresholds throughout extended cycling confirm that the surface instability mechanism remains robust despite repeated mechanical deformations, supporting applications in reusable logic gates and autonomous control systems.

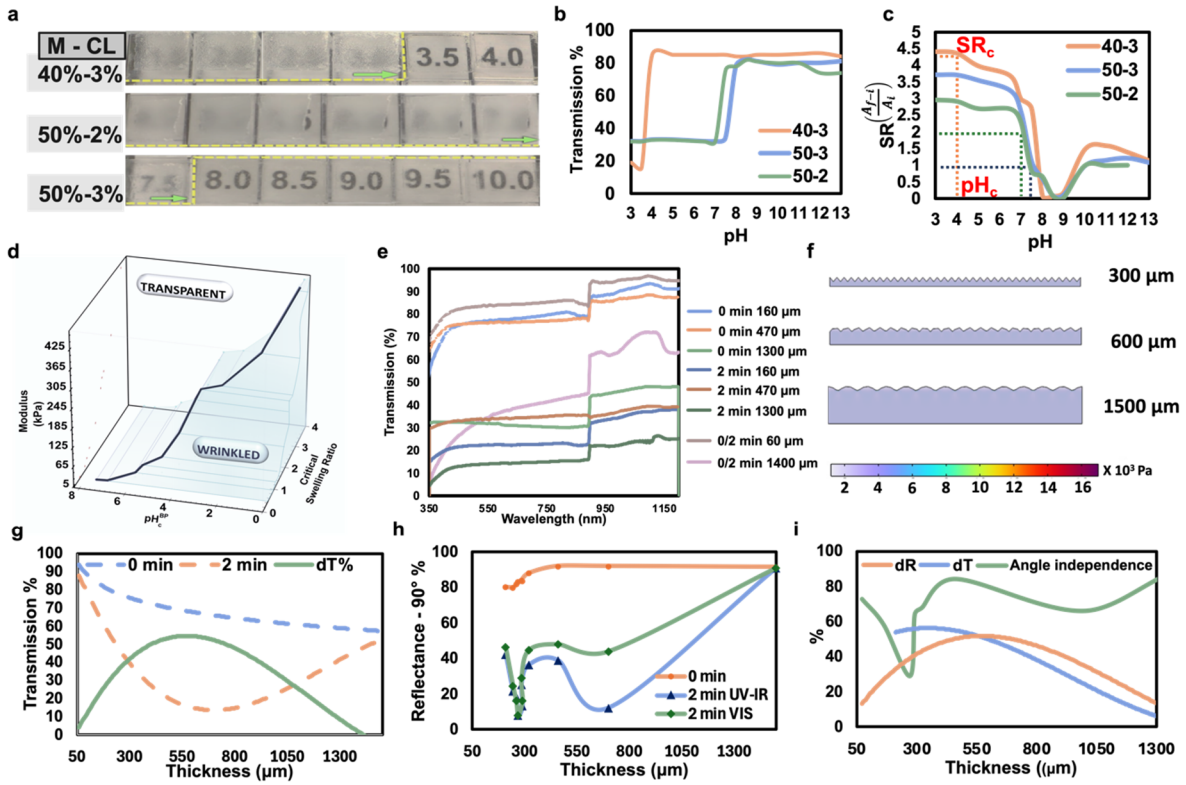

Figure 2. Systematic optimization of IIS sensor parameters. (**a**) Photographic array of pH-responsive sensor strips with varied monomer-crosslinker formulations displaying concentration-dependent opacity. (**b**) UV-Vis transmission spectra demonstrating abrupt intensity drops at formulation-specific pH thresholds. (**c**) Critical pH thresholds and corresponding swelling ratio determinations. (**d**) Normalized three-dimensional design space for universal polymer systems. (**e**) Temporal evolution of optical transmission across thickness range. (**f**) Finite element simulations of surface displacement profiles across three representative thicknesses. (**g**) Spectral transmission data comparing wavelength-independent responses. (**h**) Reflectance measurements at 90-degree collection angle for comprehensive optical characterization. (**i**) Angle-independence optimization revealing optimal 300 μm thickness.

3.3. Enzymatic pH Modulation and Polymer-Solvent Interaction-Based Detection Systems

Enzyme-coupled IIS sensors exploit a unique signal amplification mechanism where single glucose molecules generate multiple protons through Glucose Oxidase (Gox) catalysis (Figure 3a) [58,59]. The enzymatic cascade (glucose + O_2 → gluconic acid + H_2O_2) creates steep pH gradients within the hydrogel matrix, dropping from physiological pH to ~2 near enzyme sites [49,50]. This localized acidification is crucial—bulk pH changes would require impractically high glucose concentrations, but compartmentalized reactions within the polymer network achieve threshold swelling at clinically relevant levels. Unexpectedly, enzyme loading showed biphasic

effects on sensor performance: swelling increased until 0.2% *w*/*w* GOx, then declined at higher loadings (Supplementary Figure S9). This counterintuitive behavior reveals competing mechanisms—while more enzyme generates more acid, excessive protein content creates physical crosslinks that restrict polymer chain mobility. The optimal 0.2% *w*/*w* loading balances catalytic activity with mechanical compliance, enabling sensors to detect glucose across 200–1000 mg/dL ranges relevant to diabetes monitoring (Figure 3b).

The power of array-based sensing lies not in individual sensor precision but in collective information encoding. Each sensor element functions as a chemical comparator, switching states only when glucose exceeds its preset threshold (Figure 3c). By engineering systematic threshold variations through polymer content (40–50% *w*/*w*), we created a biological analog-to-digital converter: continuous glucose concentrations transform into discrete visual patterns. The array's stepped activation profile (Figure 3d) mirrors clinical glucose ranges—single sensor activation (200–400 mg/dL) indicates hypoglycemia requiring immediate intervention, two sensors (600–800 mg/dL) confirm normal fasting levels, while complete activation (>1000 mg/dL) warns of dangerous hyperglycemia. This design philosophy prioritizes actionable information over numerical precision. Unlike digital glucometers providing exact values that users must interpret, IIS arrays directly communicate clinical status through intuitive visual patterns, particularly valuable in resource-limited settings where device maintenance and user training present barriers.

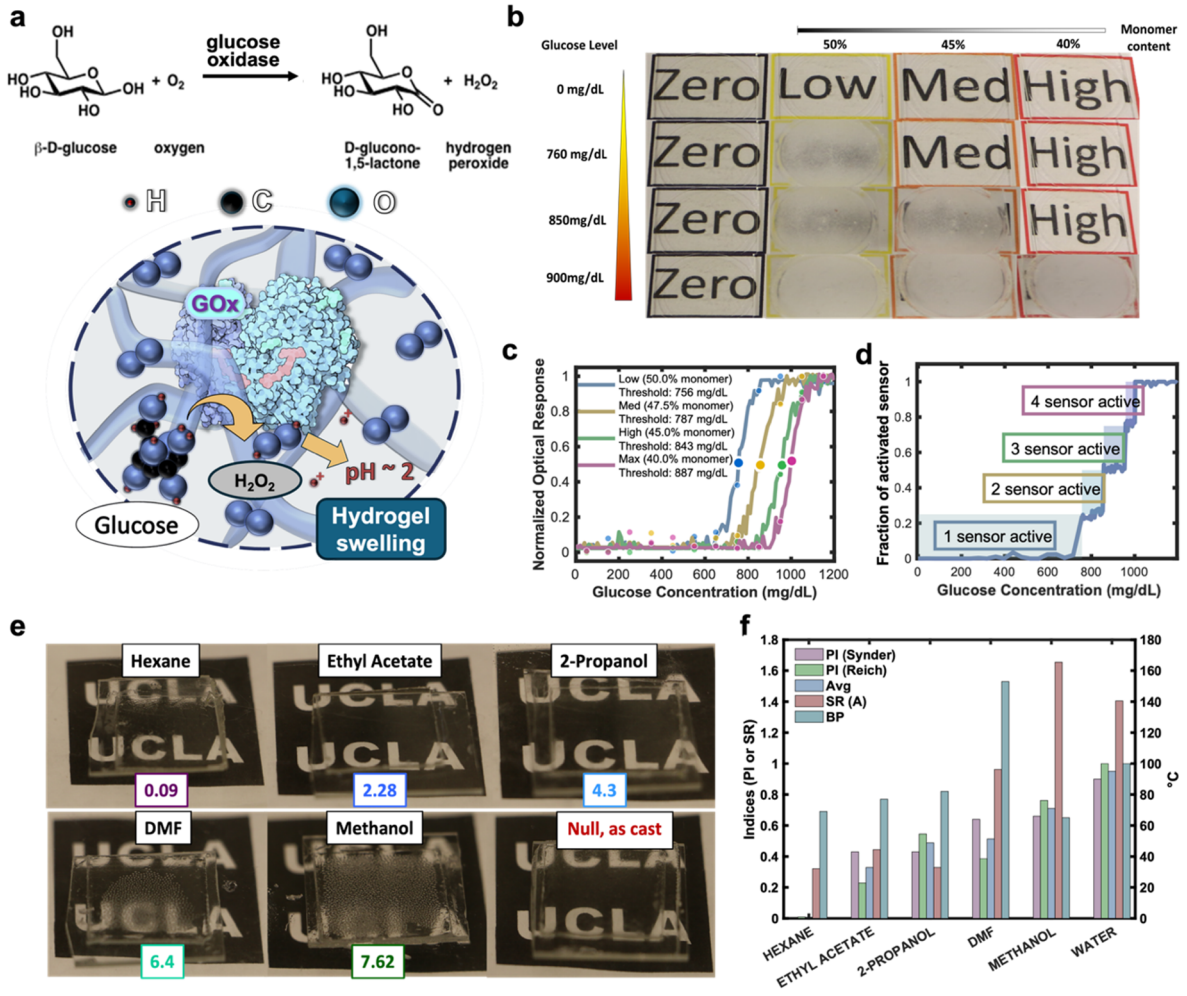

Figure 3. Multi-stimuli sensing applications. (**a**) Glucose oxidase-catalyzed conversion of glucose to gluconic acid inducing pH-triggered hydrogel swelling. (**b**) Semi-quantitative glucose detection array with differential activation thresholds across clinical concentration ranges. (**c**) Normalized optical responses of sensors with systematically varied glucose sensitivities. (**d**) Collective sensor activation pattern for concentration range identification. (**e**) Selective optical response to solvents of varying polarity indices. (**f**) Quantitative correlation between solvent polarity parameters and hydrogel swelling behavior.

Direct polarity sensing reveals fundamental differences in stimulus-response mechanisms between enzyme-coupled and physical detection modalities (Figure 3e). P(NIPAm-*co*-Am) hydrogels exhibit threshold behavior at PI ~3.5 [60,61], below which polymer-polymer interactions dominate, maintaining collapsed conformations

despite solvent exposure. Above this threshold, solvent molecules disrupt hydrophobic associations, triggering cooperative swelling transitions. The sharp discrimination between transparent (PI < 3.5) and opaque (PI > 3.5) states enables binary solvent classification without gradual transitions (Figure 3f). Remarkably, this threshold remains consistent across diverse solvent classes—alcohols, amides, and water—suggesting the response depends on general solvation power rather than specific molecular interactions (Supplementary Figure S10). This universality extends to mixed solvents, where sensors respond to volume-averaged polarity rather than preferentially interacting with either component (Supplementary Figure S11). The ability to transduce both biochemical reactions and physical properties through identical optical outputs demonstrates the versatility of surface instability as a signal transduction mechanism, enabling multiplexed arrays that simultaneously monitor diverse environmental parameters (Supplementary Figure S12).

3.4. Soft Material Logic Gates for Autonomous Control of LCE Actuators

IIS sensors exhibit intrinsic Boolean behavior through their threshold-dependent optical transitions, making them natural candidates for material-based computation (Figure 4a). Unlike gradual responses that require complex signal processing, the abrupt transparent-to-opaque switching at critical stimuli concentrations creates unambiguous binary states. This eliminates the need for analog-to-digital conversion—the material itself performs the digitization. Environmental stimuli (pH changes, solvent exposure) replace voltage inputs in classical logic gates, while optical transmission substitutes for current output. The fundamental advantage lies in passive operation: no power supply, clock signals, or refresh cycles are required. Ambient light serves as both the signal carrier and energy source, with hydrogel states storing information through mechanical deformation rather than charge separation. This approach transforms traditionally active electronic components into passive material elements that compute through their physical response to environmental conditions.

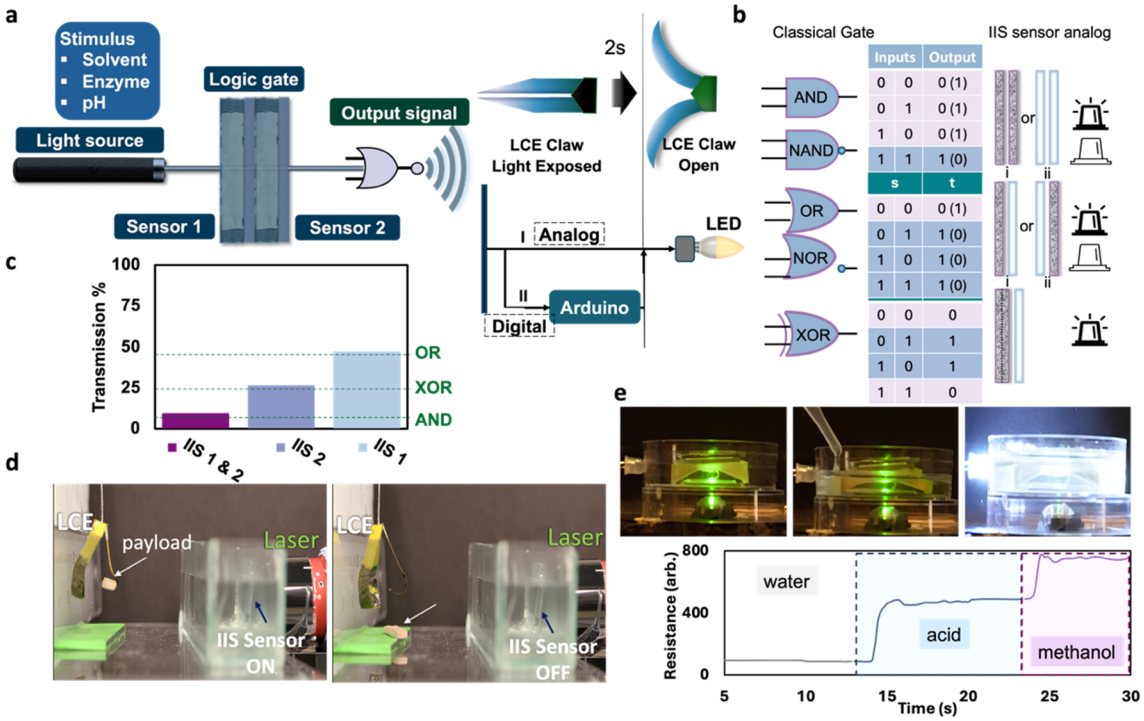

Figure 4. Logic gate implementation and autonomous control. (**a**) Integration of IIS sensors as computational elements for stimulus-responsive actuation of soft robotic and electronic systems. (**b**) Boolean operation mapping from voltage-based to environment-based logic gates. (**c**) Threshold-dependent optical transmission establishing distinct logic states for OR, XOR, and AND operations. (**d**) Autonomous LCE gripper actuation via laser transmission modulation through IIS optical switching. (**e**) Sequential environmental stimuli processing in pH-polarity AND gate configuration with conditional LED activation.

Systematic optical characterization established the transmission thresholds required for different Boolean operations (Figure 4b,c). Single IIS sensors functioning as pass-through elements maintained 80% transmission in the OFF state, dropping to 20% when activated. Stacking sensors in series created AND gate functionality, with combined transmission falling to 10% only when both sensors activated. Parallel sensor arrangements with partial

overlap produced OR gates exhibiting 50% transmission when either sensor triggered. Most intriguingly, offset sensor pairing generated XOR behavior—25% transmission occurred when only one sensor activated, while dual activation restored higher transmission through spatial light redistribution. These distinct optical signatures remained consistent across 400–800 nm wavelengths (Supplementary Figure S13b), ensuring robust operation under varied lighting conditions. The 15 s switching time, limited by polymer swelling kinetics rather than electronic delays, proves adequate for environmental monitoring applications where stimuli change over minutes to hours.

Autonomous actuation demonstrations validated practical implementation in both soft robotic and electronic systems. LCE grippers programmed with nematic-to-isotropic transition temperatures of 45 °C responded to 650 nm laser heating modulated by IIS optical gates (Figure 4d). In the wrinkled ON state, sensors blocked laser transmission, maintaining gripper closure and payload retention. Environmental stimuli switching sensors to transparent OFF states enabled laser penetration, heating LCE above transition temperature to induce 40% contraction and payload release. This configuration achieved stimulus-triggered mechanical work without control circuitry, batteries, or wireless communication. Electronic integration through photoresistor interfaces demonstrated more complex operations (Figure 4e). An AND gate combining pH-sensitive (threshold pH 6) and polarity-sensitive (threshold PI 4.0) sensors required both acidic conditions and polar solvent exposure to activate LED output. Sequential exposure to water (pH 7, PI 9), acid (pH 3, PI 9), and finally acid plus methanol (pH 3, PI 5) confirmed proper AND logic—only the dual-stimulus condition triggered the 760-unit resistance threshold for LED activation. The modular architecture enables construction of multi-input gates and cascaded logic circuits through standardized sensor elements (Supplementary Figure S13c,d), suggesting pathways toward fully soft, environmentally responsive computational systems.

4. Conclusions

The discovery that film thickness controls both wrinkle morphology and optical scattering in IIS sensors resolves a fundamental limitation of surface instability-based detection—angle-dependent visibility that has restricted practical deployment. By optimizing thickness to 300 μm, where wrinkle dimensions match visible light wavelengths, omnidirectional sensors emerge that maintain consistent appearance regardless of viewing geometry. This morphological control, combined with the intrinsic threshold response of stimuli-responsive hydrogels, enables a conceptual leap from passive indicators to active computational elements. The demonstration of soft material logic gates—while currently limited by 15 s switching speeds suitable for environmental monitoring rather than rapid computation—establishes that information processing need not require electrons, power supplies, or rigid semiconductors. Instead, mechanical deformation can encode binary states, ambient light can carry signals, and polymer swelling can execute Boolean operations. The enzymatic glucose sensors achieving clinical range detection (200–1000 mg/dL) and solvent polarity discriminators operating at PI ~3.5 thresholds validate the versatility of this approach across biochemical and physical sensing modalities. Most significantly, integrating these capabilities with autonomous LCE actuators proves that entirely soft systems can sense, decide, and respond without electronic mediation. Future advances will focus on reducing response times through thinner active layers, expanding stimulus vocabulary through multi-responsive polymers, and developing hierarchical architectures where local material computations coordinate to produce emergent behaviors.

Supplementary Materials: The following supporting information can be downloaded at: https://media.sciltp.com/articles/others/2509041550542777/MI-1420-SI-revised.pdf, including additional characterization data, Supplementary Figures S1–S13.

Author Contributions: R.K. and I.F. contributed equally to this work. R.K. assisted with data interpretation, and contributed to manuscript writing. I.F. conceived the concept, designed experiments, performed mechanical characterization, performed synthesis, developed the multi-stimuli systems, and conducted data analysis. Z.L. assisted with COMSOL simulations and theoretical modeling. C.W.Z. and P.H. assisted with data interpretation. P.S. developed the LCE actuator system and performed soft robotic demonstrations. Y.A. contributed to the initial pH-responsive system development. Y.D., S.D. and D.W. performed supporting experiments and characterization. A.J. assisted with data collection and provided support in materials preparation. M.H. and S.W. provided technical guidance on hydrogel synthesis and characterization methods. X.H. supervised the project, secured funding, and edited the manuscript. All authors reviewed and approved the final manuscript.

Funding: This research was funded by the American Chemical Society, grant number 66747-ND7; Johnson & Johnson, grant number 20231448; Inventor Fellow, grant number 12072; National Institutes of Health (NIH), grant number R01DK132319; Gordon and Betty Moore Foundation, grant number 12072; Semiconductor Research Corporation, grant number 2023-JU-3136; and the Office of Naval Research (ONR), grant numbers N000142412187 and N000142212595.

Data Availability Statement: Not applicable. Requests for data may be made to the corresponding author under appropriate justification.

Acknowledgments: The authors gratefully acknowledge financial support from the American Chemical Society, Johnson & Johnson, Inventor Fellow program, NIH, the Moore Foundation, Semiconductor Research Corporation, and the Office of Naval Research.

Conflicts of Interest: The authors declare no conflict of interest.

References

1. Ates, H.C.; Nguyen, P.Q.; Gonzalez-Macia, L.; Morales-Narvaez, E.; Guder, F.; Collins, J.J.; Dincer, C. End-to-end design of wearable sensors. *Nat. Rev. Mater*. **2022**, *7*, 887–907.
2. Zhao, D.; Zhu, Y.; Cheng, W.; Chen, W.; Wu, Y.; Yu, H. Cellulose-Based Flexible Functional Materials for Emerging Intelligent Electronics. *Adv. Mater*. **2021**, *33*, e2000619.
3. McEvoy, M.A.; Correll, N. Materials science. Materials that couple sensing, actuation, computation, and communication. *Science* **2015**, *347*, 1261689.
4. Qian, X.; Zhao, Y.; Alsaid, Y.; Wang, X.; Hua, M.; Galy, T.; Gopalakrishna, H.; Yang, Y.; Cui, J.; Liu, N.; et al. Artificial phototropism for omnidirectional tracking and harvesting of light. *Nat. Nanotechnol*. **2019**, *14*, 1048–1055.
5. Pedro, D.I.; Nguyen, D.T.; Trachsel, L.; Rosa, J.G.; Chu, B.; Eikenberry, S.; Sumerlin, B.S.; Sawyer, W.G. Superficial Modulus, Water-Content, and Mesh-Size at Hydrogel Surfaces. *Tribol. Lett*. **2021**, *69. 160.*
6. Zhao, Y.; Lo, C.Y.; Ruan, L.; Pi, C.H.; Kim, C.; Alsaid, Y.; He, X. Somatosensory actuator based on stretchable conductive photothermally responsive hydrogel. *Sci. Robot.* **2021**, *6*, eabd5483.
7. Zhao, Y.; Hua, M.; Yan, Y.; Wu, S.; Alsaid, Y.; He, X. Stimuli-Responsive Polymers for Soft Robotics. *Annu. Rev. Control Robot. Auton. Syst*. **2022**, *5*, 515–545.
8. Hoffman, A.S. Hydrogels for biomedical applications. *Adv. Drug Deliv. Rev.* **2012**, *64*, 18–23.
9. Cai, Z.; Luck, L.A.; Punihaole, D.; Madura, J.D.; Asher, S.A. Photonic crystal protein hydrogel sensor materials enabled by conformationally induced volume phase transition. *Chem. Sci*. **2016**, *7*, 4557–4562.
10. Dušková-Smrčková, M.; Dušek, K. How to Force Polymer Gels to Show Volume Phase Transitions. *ACS Macro Lett*. **2019**, *8*, 272–278.
11. Walker, J.P.; Asher, S.A. Acetylcholinesterase-Based Organophosphate Nerve Agent Sensing Photonic Crystal. *Anal. Chem*. **2005**, *77*, 1596–1600.
12. Ferreira, L.; Vidal, M.M.; Gil, M.H. Evaluation of poly(2-hydroxyethyl methacrylate) gels as drug delivery systems at different pH values. *Int. J. Pharm*. **2000**, *194*, 169–180.
13. Nakayama, M.; Yamada, N.; Kumashiro, Y.; Kanazawa, H.; Yamato, M.; Okano, T. Thermoresponsive poly(N-isopropylacrylamide)-based block copolymer coating for optimizing cell sheet fabrication. *Macromol. Biosci.* **2012**, *12*, 751–760.
14. Yetisen, A.K.; Jiang, N.; Fallahi, A.; Montelongo, Y.; Ruiz-Esparza, G.U.; Tamayol, A.; Zhang, Y.S.; Mahmood, I.; Yang, S.-A.; Kim, K.S.; et al. Glucose-sensitive hydrogel optical fibers functionalized with phenylboronic acid. *Adv. Mater*. **2017**, *29*, 1606380.
15. Choi, M.; Humar, M.; Kim, S.; Yun, S.-H. Step-Index Optical Fiber Made of Biocompatible Hydrogels. *Adv. Mater*. **2015**, *27*, 4081–4086.
16. Wang, Z.; Zhang, W.; Liu, X.; Li, M.; Lang, X.; Singh, R.; Marques, C.; Zhang, B.; Kumar, S. Novel Optical Fiber-Based Structures for Plasmonics Sensors. *Biosensors* **2022**, *12*, 1016.
17. Ling, Z.; Chen, J.; Li, S.; Lu, H.; Du, J.; Liu, Z.; Qiu, J. A multi-band stealth and anti-interference superspeed light-guided swimming robot based on multiscale bicontinuous three-dimensional network. *Chem. Eng. J*. **2024**, *485*, 150094.
18. Zhang, C.W.; Chen, C.; Duan, S.; Yan, Y.; He, P.; He, X. Hydrogel-based soft bioelectronics for personalized healthcare. *Med-X* **2024**, *2*, 20.
19. Yang, S.; Sarkar, S.; Xie, X.; Li, D.; Chen, J. Application of Optical Hydrogels in Environmental Sensing. *Energy Environ. Mater*. **2024**, *7*, e12646.
20. Cao, H.; Duan, L.; Zhang, Y.; Cao, J.; Zhang, K. Current hydrogel advances in physicochemical and biological response-driven biomedical application diversity. *Signal Transduct. Target. Ther*. **2021**, *6*, 426.
21. Yetisen, A.K.; Butt, H.; Volpatti, L.R.; Pavlichenko, I.; Humar, M.; Kwok, S.J.J.; Koo, H.; Kim, K.S.; Naydenova, I.; Khademhosseini, A.; et al. Photonic hydrogel sensors. *Biotechnol. Adv*. **2016**, *34*, 250–271.
22. Wang, M.; Yang, Y.; Min, J.; Song, Y.; Tu, J.; Mukasa, D.; Ye, C.; Xu, C.; Heflin, N.; McCune, J.S.; et al. A wearable electrochemical biosensor for the monitoring of metabolites and nutrients. *Nat. Biomed. Eng.* **2022**, *6*, 1225–1235.
23. Sun, S.; Chen, J. Recent Advances in Hydrogel-Based Biosensors for Cancer Detection. *ACS Appl. Mater. Interfaces* **2024**, *16*, 46988–47002.
24. Shen, P.; Li, M.; Li, R.; Han, B.; Ma, H.; Hou, X.; Zhang, Y.; Wang, J.-J. Aptamer-functionalized smart photonic hydrogels: application for the detection of thrombin in human serum. *NPG Asia Mater*. **2022**, *14*, 94.

25. Qin, M.; Sun, M.; Hua, M.; He, X. Bioinspired structural color sensors based on responsive soft materials. *Curr. Opin. Solid State Mater. Sci*. **2019**, *23*, 13–27.
26. Qin, M.; Sun, M.; Bai, R.; Mao, Y.; Qian, X.; Sikka, D.; Zhao, Y.; Qi, H.J.; Suo, Z.; He, X. Bioinspired Hydrogel Interferometer for Adaptive Coloration and Chemical Sensing. *Adv. Mater*. **2018**, *30*, 1800468.
27. Yang, S.; Tang, Z.; Tian, Y.; Ji, X.; Wang, F.; Xie, C.; He, Z. Dual-Color Fluorescent Hydrogel Microspheres Combined with Smartphones for Visual Detection of Lactate. *Biosensors* **2022**, *12*, *802.*
28. Li, W.; Zhang, X.; Hu, X.; Shi, Y.; Li, Z.; Huang, X.; Zhang, W.; Zhang, D.; Zou, X.; Shi, J. A smartphone-integrated ratiometric fluorescence sensor for visual detection of cadmium ions. *J. Hazard. Mater.* **2021**, *408*, 124872.
29. Wang, Q.; Zhao, X. Beyond wrinkles: Multimodal surface instabilities for multifunctional patterning. *MRS Bull*. **2016**, *41*, 115–122.
30. Frenkel, I.; Hua, M.; Alsaid, Y.; He, X. Self-Reporting Hydrogel Sensors Based on Surface Instability-Induced Optical Scattering. *Adv. Photonics Res*. **2021**, *2*, 2100058.
31. Fan, W.; Zeng, J.; Gan, Q.; Ji, D.; Song, H.; Liu, W.; Shi, L.; Wu, L. Iridescence-controlled and flexibly tunable retroreflective structural color film for smart displays. *Sci. Adv.* **2019**, *5*, eaaw8755.
32. Lee, K.-L.; Chang, C.-C.; You, M.-L.; Pan, M.-Y.; Wei, P.-K. Enhancing Surface Sensing Sensitivity of Metallic Nanostructures using Blue-Shifted Surface Plasmon Mode and Fano Resonance. *Sci. Rep*. **2018**, *8*, 9762.
33. Zhang, R.; Yang, Z.; Wang, Q.; Li, W.; Xu, H.; Li, L. Angle dependent structural colors with full-visible-spectrum and narrow-angle change properties for anti-counterfeiting. *Dyes Pigm*. **2023**, *208*, 110794.
34. Chung, J.Y.; Nolte, A.J.; Stafford, C.M. Surface Wrinkling: A Versatile Platform for Measuring Thin-Film Properties. *Adv. Mater*. **2011**, *23*, 349–368.
35. Warren, T.J.; Bowles, N.E.; Donaldson Hanna, K.; Bandfield, J.L. Modeling the Angular Dependence of Emissivity of Randomly Rough Surfaces. *J. Geophys. Res. Planets* **2019**, *124*, 585–601.
36. Gross, P.; Störzer, M.; Fiebig, S.; Clausen, M.; Maret, G.; Aegerter, C.M. A precise method to determine the angular distribution of backscattered light to high angles. *Rev. Sci. Instrum*. **2007**, *78*, 033105.
37. Considine, P.S.; Cronin, D.J.; Reynolds, G.O. Angular Dependence of Radiance of Rough Surfaces in Imaging Systems. *J. Opt. Soc. Am*. **1966**, *56*, 877–883.
38. Chen, C.; Shi, P.; Liu, Z.; Duan, S.; Si, M.; Zhang, C.; Du, Y.; Yan, Y.; White, T.J.; Kramer-Bottiglio, R.; et al. Advancing physical intelligence for autonomous soft robots. *Sci. Robot*. **2025**, *10*, eads1292.
39. Zhao, Y.; Li, Q.; Liu, Z.; Alsaid, Y.; Shi, P.; Jawed, M.K.; He, X. Sunlight-powered self-excited oscillators for sustainable autonomous soft robotics. *Sci. Robot*. **2023**, *8*, eadf4753.
40. Liu, Y.; Tian, G.; Du, Y.; Shi, P.; Li, N.; Li, Y.; Qin, Z.; Jiao, T.; He, X. Highly Stretchable, Low-Hysteresis, and Adhesive TA@MXene-Composited Organohydrogels for Durable Wearable Sensors. *Adv. Funct. Mater*. **2024**, *34*, 2315813.
41. Zhao, K.; Cao, X.; Alsaid, Y.; Cheng, J.; Wang, Y.; Zhao, Y.; He, X.; Zhang, S.; Niu, W. Interactively mechanochromic electronic textile sensor with rapid and durable electrical/optical response for visualized stretchable electronics. *Chem. Eng. J.* **2021**, *426*, 130870.
42. Liu, Q.; Nian, G.; Yang, C.; Qu, S.; Suo, Z. Bonding dissimilar polymer networks in various manufacturing processes. *Nat. Commun*. **2018**, *9*, 846.
43. Yuk, H.; Zhang, T.; Lin, S.; Parada, G.A.; Zhao, X. Tough bonding of hydrogels to diverse non-porous surfaces. *Nat. Mater*. **2016**, *15*, 190–196.
44. Wirthl, D.; Pichler, R.; Drack, M.; Kettlguber, G.; Moser, R.; Gerstmayr, R.; Hartmann, F.; Bradt, E.; Kaltseis, R.; Kaltenbrunner, M. Instant tough bonding of hydrogels for soft machines and electronics. *Sci. Adv*. **2017**, *3*, e1700053.
45. Vandeparre, H.; Gabriele, S.; Brau, F.; Gay, C.; Parker, K.K.; Damman, P. Hierarchical wrinkling patterns. *Soft Matter*. **2010**, *6*, 5751–5756.
46. Li, B.; Cao, Y.-P.; Feng, X.-Q.; Gao, H. Mechanics of morphological instabilities and surface wrinkling in soft materials: a review. *Soft Matter*. **2012**, *8*, 5728–5745.
47. Kim, H.S.; Crosby, A.J. Solvent-Responsive Surface via Wrinkling Instability. *Adv. Mater*. **2011**, *23*, 4188–4192.
48. Liu, J.; Jiang, Z.; Li, Y.; Kang, G.; Qu, S. Stability of hydrogel adhesion enabled by siloxane bonds. *Eng. Fract. Mech*. **2022**, *271*, 108662.
49. Kang, M.K.; Huang, R. Effect of surface tension on swell-induced surface instability of substrate-confined hydrogel layers. *Soft Matter*. **2010**, *6*, 5736–5745.
50. Auguste, A.; Yang, J.; Jin, L.; Chen, D.; Suo, Z.; Hayward, R.C. Formation of high aspect ratio wrinkles and ridges on elastic bilayers with small thickness contrast. *Soft Matter.* **2018**, *14*, 8545–8551.
51. Zhou, Y.; Chen, Y.; Jin, L. Three-dimensional postbuckling analysis of thick hyperelastic tubes. *J. Mech. Phys. Solids* **2023**, *173*, 105202.
52. Kang, C.; Liu, Z.; Chen, S.; Jiang, X. Circular trajectory weaving welding control algorithm based on space transformation principle. *J. Manuf. Process*. **2019**, *46*, 328–336.

53. Jin, L.; Takei, A.; Hutchinson, J.W. Mechanics of wrinkle/ridge transitions in thin film/substrate systems. *J. Mech. Phys. Solids* **2015**, *81*, 22–40.
54. Lynch, D.K. Snell's window in wavy water. *Appl. Opt*. **2015**, *54*, B8–B11.
55. Young, A.T. Rayleigh scattering. *Appl. Opt*. **1981**, *20*, 533–535.
56. Schwartz, C.; Dogariu, A. Conservation of angular momentum of light in single scattering. *Opt. Express*. **2006**, *14*, 8425–8433.
57. Mansuripur, M. Angular Momentum Exchange Between Light and Material Media Deduced from the Doppler Shift. *Proc. SPIE* **2012**, *8458*, 20–27.
58. Zia, M.A.; Khalil Ur, R.; Kamal, S.M.; Andaleeb, F.; Mahmood, I.R.; Ahmad, S.M.; Khan, I.A.; Ahmad, I.K. Thermal Characterization of Purified Glucose Oxidase from A Newly Isolated Aspergillus Niger UAF-1. *J. Clin. Biochem. Nutr*. **2007**, *41*, 132–138.
59. Bright, H.J.; Appleby, M. The pH Dependence of the Individual Steps in the Glucose Oxidase Reaction. *J. Biol. Chem.* **1969**, *244*, 3625–3634.
60. Snyder, L.R. Classification of the solvent properties of common liquids. *J. Chromatogr*. *A* **1974**, *92*, 223–230.
61. Acree, W.E.; Lang, A.S.I.D. Reichardt's Dye-Based Solvent Polarity and Abraham Solvent Parameters: Examining Correlations and Predictive Modeling. *Liquids* **2023**, *3*, 303–313.

Editorial

Responsive Materials—Designing the Future of Dynamic Functionality

Yadong Yin [1,*], Hiroshi Fudouzi [2,*], and Takashi Nakanishi [3,*]

[1] Department of Chemistry, University of California, Riverside, CA 92521, USA
[2] National Institute for Materials Science, 1-2-1 Sengen, Tsukuba 305-0047, Japan
[3] National Institute for Materials Science (NIMS), Namiki 1-1, Tsukuba 305-0044, Japan
* Correspondence: yadong.yin@ucr.edu (Y.Y.); fudouzi.hiroshi@nims.go.jp (H.F.); nakanishi.takashi@nims.go.jp (T.N.)

Welcome to this Thematic Collection of *Materials and Interfaces*, dedicated to the fascinating and rapidly expanding field of *responsive materials*. These "smart" materials are revolutionizing technology by seamlessly integrating dynamic and adaptive functionalities into a wide range of applications, from medical devices and displays to soft robotics and environmental sensors. The ability of these materials to change their properties, including color, shape, or wettability, in response to external stimuli such as light, temperature, or magnetic fields, represents a paradigm shift from passive components to active systems.

The articles in this Thematic Collection highlight the breadth and ingenuity of current research in responsive materials. We begin with innovations in electrochromic and photochromic technologies, which are crucial for next-generation displays and smart windows. The work by Sean Xiao, An Zhang and coworkers on an intrinsically multi-color electrochromic device, as well as the research by Yun Zhang, Wenshou Wang, and coworkers on visible-light-driven black coloration, demonstrates significant strides in achieving stable, high-contrast, and fast-acting color-changing systems.

Itthen delves into the world of mechanical and structural responsiveness. The research by Hiroshi Fudouzi and coworkers on mechanochromic colloidal crystal sheets and by Yasuhiro Ishida and coworkers on anisotropic hydrogels for directional sensing demonstrates how mechanical deformation can be harnessed to create visual indicators or flexible sensors. Furthermore, the work by Ximin He and coworkers explores the development of angle-independent hydrogel sensors for autonomous soft actuator control, pushing the boundaries of integrated sensing and actuation.

Moving beyond simple sensing, several contributions explore how responsive materials can be used for more complex, controlled actions. Yuhan Zhang, Bo Li, Shichao Niu and coworkers present a magnetically-driven cilium array for precise droplet manipulation, which has profound implications for microfluidics and dynamic displays. Christopher J. Bardeen and coworkers introduce a novel approach to photochemical bubble generation from polymer films, which opens new avenues for applications in medical ultrasound imaging. The article by Toshimitsu Kanai and coworkers highlights the development of chameleon-inspired color-changeable films that are sensitive to human body temperature, expanding the potential for biomimetic applications.

This collection also highlights current research that bridges fundamental material science with innovative applications. The work of Jianping Ge and coworkers on the synthesis of liquid photonic crystals and of Kyosuke Isoda and coworkers on thermally responsive liquid materials showcases the development of new material platforms with versatile functionalities. The articles by Yukikazu Takeoka and coworkers, as well as Keita Kuroiwa and coworkers, further illustrate the molecular-level design of temperature-responsive polymers and spin crossover complexes, respectively, to achieve desired properties.

This collection further features articles reviewing cutting-edge research in responsive materials with diverse applications. The article by Younan Xia and coworkers provides a comprehensive overview of light-driven soft actuators, which are distinguished by their ability to undergo significant changes in shape or volume in response to light, offering effective methods for wireless control in soft robotics and advanced manufacturing. The article by Yadong Yin and coworkers reviews the use of colorimetric plasmonic nanosensors for environmental pollution monitoring, demonstrating their potential for rapid and cost-effective detection. The paper by Yanzhao Yang, Wei Feng, Ling Wang, and coworkers provides an up-to-date review on the additive manufacturing of bioinspired structural-color materials, showcasing how new fabrication techniques are enabling complex, durable designs.

These papers collectively illustrate the dynamism and interdisciplinary nature of responsive materials research. They not only present cutting-edge findings but also lay the groundwork for future advancements. As we look ahead, the integration of these smart materials into functional systems promises to address some of the most

pressing challenges in technology, healthcare, and environmental science. We are honored to present this collection of work and hope it inspires further research and collaboration in this exciting field.

Conflicts of Interest: The authors declare no conflict of interest.

Biographies of Authors

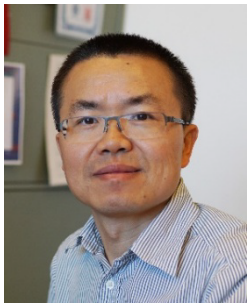

Yadong Yin is a Chemistry Professor at the University of California, Riverside, with an affiliate appointment in Materials Science and Engineering. He earned his B.S. and M.S. in Chemistry from the University of Science and Technology of China in 1996 and 1998, respectively, and his Ph.D. in Materials Science and Engineering from the University of Washington in 2002. In 2003, he worked as a postdoctoral fellow at the University of California, Berkeley, and later at Lawrence Berkeley National Laboratory, before becoming a staff scientist at LBNL in 2005. He joined the faculty at UC Riverside in 2006. His research interests include synthesis, self-assembly, interfacial manipulation, and applications of nanostructured materials.

Hiroshi Fudouzi is a Chief Researcher at the National Institute for Materials Science, NIMS. He earned his B.S. and M.S. in Chemistry from the Kyushu Institute of Technology in 1991 and 1993, respectively, and his Doctor of Engineering from Kyushu University in 2004. In 1993, he worked as a researcher at the National Research Institute of Metals (NRIM), and in 2001, he joined NIMS. He was a visiting scholar in the Department of Chemistry, University of Washington (2002-2003). Since 2019, he has concurrently held the position of Visiting Professor at Nagoya Institute of Technology. His research interests include colloidal crystals, self-assembly, structural color, smart materials that respond to external stimuli, and their applications to address social issues.

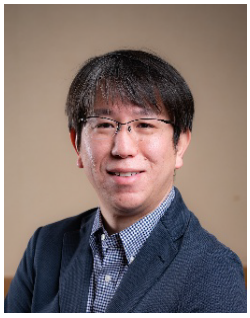

Takashi Nakanishi is a Group Leader at the Research Center for Materials Nanoarchitectonics (MANA), National Institute for Materials Science (NIMS), Japan. He received his Ph.D. Degree within a short period from Nagasaki University in 2000. He was awarded a JSPS Postdoctoral Fellowship (DC1 and PD) and worked at Houston University and Oxford University. He started his research career at NIMS in 2004. Since 2016, he has been in his current position. In 2007–2010, he was also a group leader at the Max Planck Institute of Colloids and Interfaces. He is currently a visiting professor at Hokkaido University. His research focuses on organic/polymer soft materials, particularly optoelectronically functional molecular liquids and their applications in security inks and healthcare sensors.

Article

Growth of NiAl-LDH Nanoplates on NiFe Foam and Their Enhanced Electrochemical Properties for Oxygen Evolution Reaction

Jaeyoung Lee [1,2,†], Jae Ryeol Jeong [3,†], Yoojin Lee [4,†], Jinhoon Jang [1,†], Hongdeok Park [3], Yonghwan Jo [1], Jeong Woo Han [4,*], Min Hyung Lee [3,*], and Taekyung Yu [1,*]

[1] Department of Chemical Engineering, College of Engineering, Integrated Engineering Major, Kyung Hee University, Yongin 17104, Republic of Korea
[2] School of Earth and Atmospheric Sciences, Georgia Institute of Technology, Atlanta, GA 30332, USA
[3] Department of Applied Chemistry, Kyung Hee University, Yongin 17104, Republic of Korea
[4] Department of Materials Science and Engineering, Research Institute of Advanced Materials, Seoul National University, Seoul 08826, Republic of Korea
* Correspondence: jwhan98@snu.ac.kr (J.W.H.); minhlee@khu.ac.kr (M.H.L.); tkyu@khu.ac.kr (T.Y.)
† These authors contributed equally to this work.
Received: 1 September 2025; Revised: 19 September 2025; Accepted: 29 September 2025; Published: 30 September 2025

Abstract: The development of sustainable energy that does not emit carbon pollutants is a major research topic toward minimizing waste generation and ecosystem degradation caused by the use of fossil fuels. Electrochemical water splitting is a semipermanent cycle that produces energy with zero carbon emissions. It is an innovative science and technology for a sustainable future for humanity and nature. However, its high operating potential due to the four-electron transfer process of the oxygen evolution reaction (OER) at the anode is the main factor hindering the overall reaction rate. Thus, given the importance of operating this cycle with high efficiency, studies have been extensively conducted to enhance the activity of transition-metal-based layered double hydroxide (LDH) catalysts. The use of metal foam as a substrate for LDH growth is considered the most effective method. However, most studies aimed at improving the performance of heterostructured catalysts have generally focused on controlling the active materials grown on the foam rather than the foam itself. Herein, we propose a new perspective on the role of foam, emphasizing that it is more than a mere supporting medium for growth. Density functional theory (DFT) calculations were performed to investigate the effects of NiFe foam (NFF) by modeling a heterostructure comprising NiAl-LDH and NFF. The calculation results demonstrated electron redistribution at the NiAl-LDH@NFF interface, which effectively influenced the OER performance and interfacial binding energy. Furthermore, we obtained insights into the role of foam by investigating changes in the OER overpotential caused by differences in the elements comprising the foam (Ni foam, 327 mV at 10 mA cm^{-2}; NFF, 214 mV at 10 mA cm^{-2}). This study affords flexibility in the utilization of metal foam-based heterostructured catalysts.

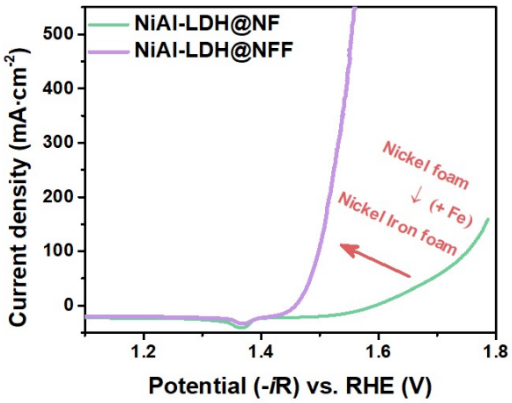

Keywords: NiFe foam; NiAl-LDH; oxygen evolution reaction; heterostructure modeling; density functional theory; substrate effect

1. Introduction

Fossil fuels have been a key resource for the advanced development of humanity worldwide. The ongoing development of highly efficient technologies for the production of shale gas has led to a continuous rise in the global production of fossil fuels [1–3]. Nevertheless, fossil fuels present a significant drawback—the substantialemission of carbon dioxide, a major contributor to global warming. Consequently, it is imperative to explore and implement clean energy alternatives for the sustainable development of humanity [4–6].

Among various eco-friendly energies, hydrogen is the most promising candidate. It is abundant on Earth, exhibits no regional scarcity, and has a higher energy density than fossil fuels. The energy density of hydrogen, petroleum, and coal is 120, 44, and 25 MJ/kg, respectively. Nevertheless, the delay in the replacement of fossil fuels by hydrogen is primarily attributed to the limited efficiency of water electrolysis, which is the predominant carbon-neutral production method for hydrogen [7]. The bottleneck is the oxygen evolution reaction (OER), a crucial half-reaction of water electrolysis characterized by inherently sluggish kinetics. Previous studies have frequently used noble-metal-based (Ru, Ir, Pt, etc.) electrocatalysts to enhance the OER efficiency [7–9]. However, these materials have failed to significantly improve the efficiency of water electrolysis, largely due to cost implications from the finite availability of noble metals. Thus, current studies have intensified their focus on materials with layered structures, particularly those comprising four-period transition metals [10–12].

Among these materials, NiAl-layered double hydroxide (NiAl-LDH) is a highly promising electrocatalyst. The incorporation of Al has been observed to be advantageous because it enhances the structural stability of Ni-based catalysts and increases the proportion of low-coordinated Ni species [13]. Furthermore, using foam as the growth environment for electrocatalysts offers significant advantages, including a high specific surface area, efficient material utilization, low mass density, versatile porous channels, and good conductivity [14–16]. The use of foam comprising well-established elements, such as Ni and Fe, which have been extensively validated, is a robust strategy for maximizing the potential of NiAl-LDH. In addition, it simultaneously addresses the limitations associated with the existing rotating disk electrode configurations.

Previous studies on electrocatalysis using density functional theory (DFT) calculations have focused on understanding the interaction between catalyst materials and their interfaces [17,18]. However, recent studies involving catalysts directly grown on substrates, such as single-atom catalysts [19,20], have revealed that changes in catalytic activity can arise from interactions between reactants and the catalyst surface, as well as from interactions between the substrate and catalyst [21–23]. Thus, this study was aimed at investigating the effect of foam on electrocatalytic reactions and examining the interface between LDH and foam. This was achieved by meticulously modeling a heterostructure comprising LDH and foam.

Herein, we present a paper detailing the direct growth of catalysts on metal foams and the resulting alterations in catalytic activity induced by the charge structure modification facilitated by the metal foam. The NiFe foam (NFF) used remarkably enhanced the catalytic activity of NiAl-LDH in the OER. The OER overpotential at 10 mA cm^{-1} using the NiAl-LDH@NFF (214 mV) as a catalyst was significantly reduced compared with that of the NiAl-LDH@Ni foam (NF) (327 mV). The activity trend was elucidated by calculating the interaction between the well-modeled NFF and NiAl-LDH. The investigation revealed that the interactions between catalysts and substrates can control the electronic structures of catalysts through charge transport from the metal substrate. This phenomenon is similar to the charge transport-induced enhancement of catalytic activity observed for single-atom catalysts. These findings provide a promising approach to the rational design of OER catalysts, wherein electronic structure control through interactions with metal substrates is leveraged at the atomic scale and at larger scales, rendering them applicable for practical implementation.

2. Experimental Section

2.1. Materials and Methods

Nickel chloride ($NiCl_2$; 98%), aluminum chloride ($AlCl_3 \cdot 6H_2O$; 99%), urea (99%), ruthenium oxide (RuO_2, 99.9%), and hydrochloric acid (HCl; 37%) were purchased from Sigma-Aldrich (St. Louis, MO, USA). NFF and NF were purchased from Medipl and 4science (Seoul, Korea), respectively. Nafion solution (D520, DuPont) was used as received. All the reagents were of analytical grade and used without further purification.

2.1.1. Synthesis of NiAl-LDH@NFF and NiAl-LDH@NF

NiAl-LDH@NFF was synthesized following a reported method that was optimized to suit the present experimental conditions [24]. The NFF (1.4 × 1.4 cm) was pretreated in HCl (3 M) for 10 min to remove the surface oxide layer. It was subsequently rinsed twice with a water and ethanol solution and dried at room temperature for 3 h. Next, $NiCl_2$ (1.6 mmol) and $AlCl_3 \cdot 6H_2O$ (0.8 mmol) were dissolved in distilled water (12 mL) with continuous magnetic stirring at 450 rpm for 10 min. Thereafter, urea (1.2 mmol) was added. The acid-treated NFF and mixed solution were transferred into a Teflon-lined stainless-steel reactor, sealed, and maintained at 120 °C for 12 h in a convection oven. Afterward, the synthesized NiAl-LDH@NFF was sonicated thrice for 2 min in a mixture of water and ethanol and dried at room temperature for future use. NiAl-LDH@NF was synthesized using the same method, except for the replacement of NFF with NF.

2.1.2. Characterization

Transmission electron microscopy (TEM) was performed using a JEM-2100F microscope (Jeol, Osaka, Japan) at 200 kV. Scanning electron microscopy (SEM) images were obtained using a LEO SUPRA 55 microscope (Zeiss, Dublin, CA, USA). Powder X-ray diffraction (XRD) patterns were recorded at room temperature using a D/MAX-2200PC X-ray diffractometer (Rigaku, Tokyo, Japan) equipped with graphite-monochromatized Cu Kα radiation (λ = 1.5418 Å). The step scan mode was employed in the 2θ range of 10–90°, with a step size of 0.02° and a counting time of 4 s per step. An inductively coupled plasma (ICP) spectrometer (Direct Reading Echelle ICP, Leeman, Hudson, NH, USA) was used to determine the Al/Ni molar ratio in the LDH. The X-ray photoelectron spectroscopy (XPS, K-Alpha, Thermo Fisher Scientific, Waltham, MA, USA) was employed to investigate the oxidation states of NiAl-LDH@NF and NiAl-LDH@NFF

2.1.3. Electrochemical Measurement

Electrochemical measurements were conducted using an SP300 electrochemical workstation (BioLogic Science Instruments, Seyssinet-Pariset, France) in a standard three-electrode configuration with a 1 M KOH electrolyte. The reference and counter electrodes were an Hg/HgO electrode and Pt mesh, respectively. To assess the electrocatalytic activity of NiAl-LDH toward OERs, linear sweep voltammetry (LSV) was performed at a sweep rate of 2 mV s^{-1}. Electrochemical impedance spectroscopy (EIS) was conducted at an amplitude of 0.01 V over a frequency range of 0.01–100,000 Hz under a bias of 0.6 V vs. Hg/HgO. The potential of the working electrode was converted into the reversible hydrogen electrode (RHE) using the following equation:

$$E_{RHE} = 0.098 + (0.0592 \cdot pH) + E_{Hg/HgO}.$$

The OER overpotential (η) was determined by subtracting 1.23 V, the theoretical potential for water oxidation, as shown in the following equation:

$$\eta = E_{RHE} - 1.23.$$

The Tafel slopes, as per the LSV curve, were fitted using the following equation:

$$\eta = a + b \log J,$$

where a represents a constant, b is the Tafel slope, and J denotes the current density. Chronopotentiometry was performed to evaluate long-term stability.

The electrochemically active surface area (ECSA) was estimated based on the electrochemical capacitance of the double layer. Cyclic voltammetry was performed to determine the capacitance of the double layer (C_{dl}) by extracting the slope of the geometric current density vs. the scan rate (5–30 mV s^{-1}). No peaks were observed in the non-Faradaic potential range of 0–0.2 vs. RHE owing to the absence of kinetic polarization. The linear slope was equivalent to twice the C_{dl}, representing the ECSA [25].

The turnover frequency (TOF) was calculated using the following equation:

$$TOF = J/(4 \times n \times F),$$

where J represents the current density at a given potential, 4 is the number of electrons transferred during the OER, n is the number of active sites of all the metal ions available for the OER (including Ni and Al), and F is Faraday's constant (96,485 C mol^{-1}) [26,27].

2.1.4. Computational Methods

Spin-polarized DFT calculations were performed using the Vienna Ab initio Simulation Package (VASP) [28,29]. The projector augmented wave (PAW) method was employed to efficiently represent the interaction between valence electrons and the ion core. The generalized gradient approximation with the Perdew, Burke, and Ernzerhof functional (GGA-PBE) was employed to describe the exchange-correlation energy [30,31]. The cutoff energy was set to 400 eV for the plane-wave expansion, and the convergence criteria were set to 0.03^{-1} and 10^{-4} eV for the residual force and energy, respectively. The Monkhorst–Pack schemes of the k-point grid for the LDH, NFF, NF slab and LDH@NFF, and LDH@NF heterostructure supercells were sampled by 2 × 2 × 1 for geometry optimization and Bader charge calculations [32].

Prior to modeling the heterostructure, NiFe(111), Ni(111) and NiAl-LDH(001) slabs were constructed. The optimized lattice parameters of the $FeNi_3$ and Ni bulks were 3.55 and 3.52 Å, respectively, similar to previous experimental and theoretical reports [33,34]. The NiFe(111) and Ni(111) surfaces were modeled with three atomic layers, where the bottom layer was fixed to describe the bulk positions. For the $Ni(OH)_2$ monoclinic bulk structure,

the optimized lattice parameters were 3.16, 3.16, and 4.64 Å for the x-, y-, and z-directions (α = β = 90°, γ = 120°), respectively. To simplify the heterostructure, the original unit cells of NiFe(111), Ni(111), and $Ni(OH)_2$ were converted into an orthorhombic unit cell. To mimic the experimental ratio of Ni and Al (Ni:Al = 3:1), NiAl-LDH was constructed by replacing one Ni atom with one Al atom in the (2 × 2) $Ni(OH)_2$ unit cell (Figure S1). For the heterostructure modeling, a (2 × 3) surface unit cell of the NiAl-LDH slab was attached to a (3 × 2) surface unit cell of NiFe(111) and Ni(111), to minimize the strain induced by the lattice mismatch. The NiFe(111) and Ni(111) slabs of the heterostructure were compressed by as much as 4.31% and 3.51% in the y-direction, respectively. The NiFe(111), Ni(111) and NiAl-LDH(001) slabs had vacuum thicknesses of 15 Å to avoid artificial interactions between its periodic images in the z-direction (Figure S2).

According to the widely accepted OER mechanism that involves the elementary steps of the four-electron mechanism, the OER occurs via three oxygen-containing intermediates as follows (Equations (1)–(4)):

$$H_2O + {}^* \rightarrow {}^*OH + H^+ + e^-, \quad (1)$$

$${}^*OH \rightarrow {}^*O + H^+ + e^-, \quad (2)$$

$$H_2O + {}^*O \rightarrow {}^*OOH + H^+ + e^-, \quad (3)$$

$${}^*OOH \rightarrow O_2(g) + {}^* + H^+ + e^-, \quad (4)$$

where the asterisk denotes an active site [35]. Under standard conditions (T = 298.15 K, p = 1 bar, pH = 0), the energy of $H^+ + e^-$ was represented by 1/2 H_2 using the standard hydrogen electrode (SHE) [36]. The Gibbs free energies of each step $\Delta G_i (i = 1, 2, 3, 4)$ were calculated by correcting the DFT energy (E) with the zero-point energy (ZPE) and entropy (S) as follows:

$$\Delta G_i = \Delta E + \Delta ZPE - T\Delta S,$$

where T = 298.15 K. The ZPE correction and S calculations used the vibrational frequencies obtained by applying the finite difference method in the DFT. The thermodynamic entropy was referenced to H_2O (g) under a pressure of 0.035 bar because it was in equilibrium with H_2O (l) at 298.15 K.

During the OER process, the step with the highest free energy change is referred to as the potential determining step (PDS). The theoretical overpotential (η) can be expressed as

$$\eta = \max(\Delta G_i)/e - 1.23\ V$$

The charge distributions of the heterostructures were evaluated using the Bader charge analysis method [37].

The interfacial binding energy between NiAl-LDH(001) and NiFe(111), Ni(111) was determined using the following equation:

$$E_b = \frac{E_{LDH@foam} - E_{LDH} - E_{foam}}{S_{interface}},$$

where $E_{LDH@foam}$, E_{LDH}, and E_{foam} denote the total energies of the LDH@foam heterostructure, LDH, and foam, respectively, and $S_{interface}$ denotes the surface area of the unit cells.

2.2. Results and Discussion

Figure 1 shows the morphology and crystal structure of NiAl-LDH@NFF prepared using an aqueous phase hydrothermal synthesis method. Figure 1a shows a low-magnification SEM image, revealing its three-dimensional macroporous structure and rough surface features. This was attributed to the formation of plate-shaped NiAl-LDH on the NFF surface. To confirm the microstructure of the NiAl-LDH@NFF, we observed the yellow dotted box in Figure 1a using field-emission (FE)SEM and measured its thickness at random points (Figure 1b). Through these measurements, we determined that NiAl-LDH nanoplates with an average thickness of 41.6 ± 7.9 nm were formed on the NFF. Figure 1c shows a TEM image of the NiAl-LDH@NFF, indicating the formation of plate morphology. This corresponds to the SEM images in Figure 1a,b. Diffraction peaks at 44.28°, 51.53°, and 75.87° from the XRD patterns of NiAl-LDH@NFF and NFF corresponded to the (111), (200), and (220) planes of $FeNi_3$ (JCPDS #38-0419), respectively (Figure 1d) [38]. Contrarily, diffraction peaks at 11.73°, 23.58°, 35.12°, and 39.71° observed for NiAl-LDH@NFF, which were not observed for NFF, could correspond to the (003), (006), (012), and (015) planes of NiAl-LDH (JCPDS #15-0087), respectively [39,40]. Based on the crystal structure analysis, it is necessary to double-check NiAl-LDH by measuring the lattice distance in the white dotted square in Figure 1c. After sufficiently increasing the magnification to investigate the lattice distance in the white dotted

square, the length of 10 spacing was measured to be 2.55 nm (Figure S3). One spacing was 2.55 Å, corresponding to the (015) plane of NiAl-LDH, evidencing the NiAl-LDH, as typically observed by high-resolution (HR) TEM [24,41]. In addition, after the hydrothermal reaction, the color of the NFF and NF changed to greenish-gray, indicating the formation of NiAl-LDH (Figure S4) [42]. The sequential comparison of low-magnification SEM images of the samples prior to (Figure S5a,b) and after the hydrothermal reaction confirmed the morphological evolution of the foam surface after the reaction (Figure S5c,d). Moreover, energy-dispersive spectroscopy (EDS) mapping images of NiAl-LDH@NFF demonstrated an even distribution of Ni, Fe, and Al on the foam surface, revealing that NiAl-LDH was well-grown on the entire NFF surface (Figure S6a).

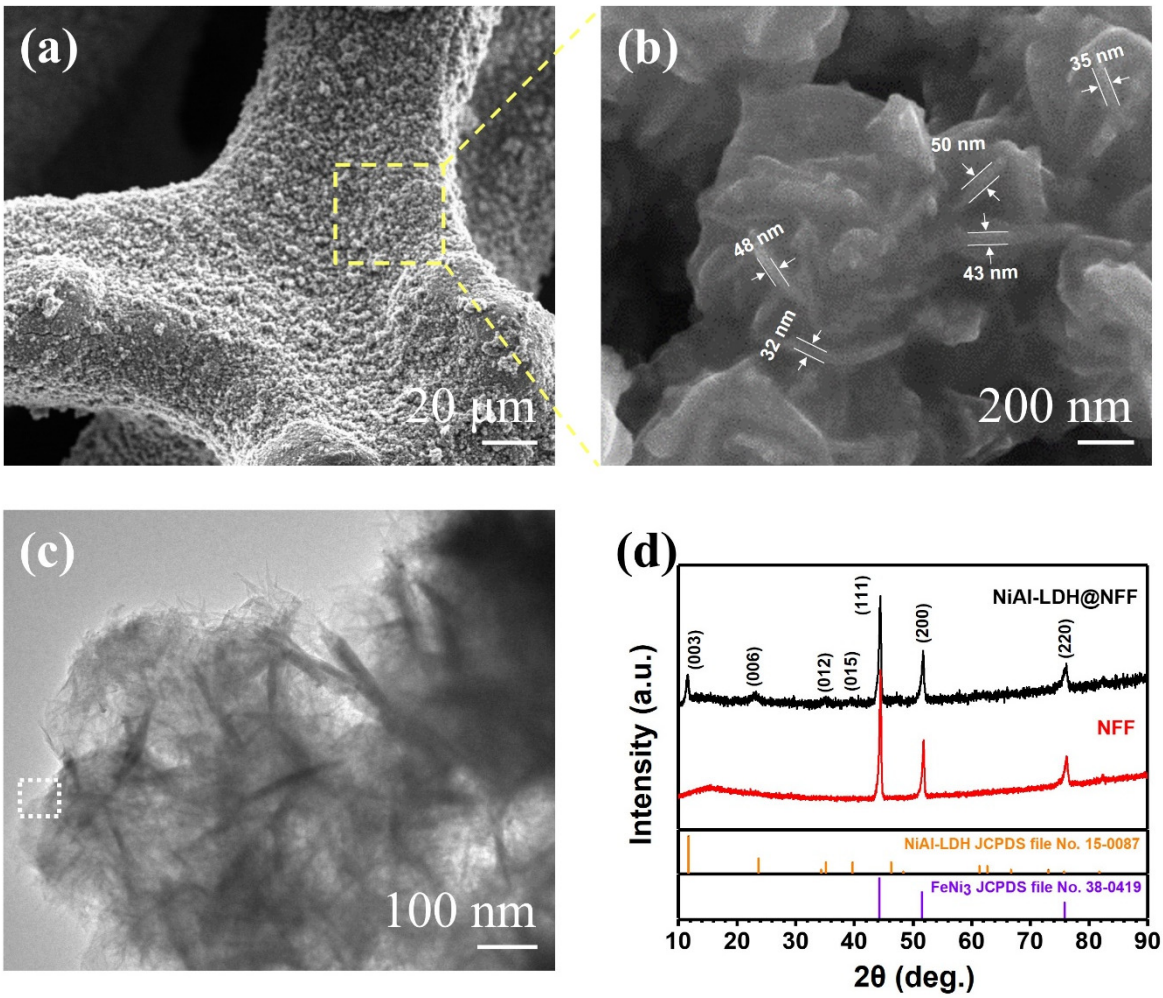

Figure 1. Characterization of NiAl-LDH@NFF. (**a**) Low (×1000) and (**b**) high (×100,000) magnification SEM images of NiAl-LDH@NFF including thickness measurements at several points. (**c**) TEM image of NiAl-LDH grown on NFF. The white dotted square corresponds to the area for measuring *d*-spacing of NiAl-LDH in Figure S3. (**d**) XRD patterns of NiAl-LDH@NFF and NFF with reference XRD patterns.

For comparison, NiAl-LDH@NF was prepared using the same synthesis method except that the procedure was conducted with NF instead of NFF. A low-magnification SEM image of NiAl-LDH@NF (Figure 2a) revealed that the foam surface was relatively smoother than that of NiAl-LDH@NFF. The average thickness of the NiAl-LDH nanoplates was 21.2 ± 2 nm, thinner than the nanoplates on NFF (Figure 2b). We believe that a relatively insufficient growth of the nanoplate could have led to the reduced thickness and blunt interface of NiAl-LDH@NF. Figure 2c shows a TEM image, indicating the formation of a small nanoplate, compared with that of NiAl-LDH@NFF, which corresponded with the SEM results (Figure 2b). The XRD patterns of NiAl-LDH@NF exhibited 44.5°, 51.85°, and 76.38° peaks corresponding to the (111), (200), and (220) planes of metallic Ni (JCPDS #87-0712), respectively (Figure 2d) [43–45]. Diffraction peaks were not observed for NiAl-LDH, potentially attributed to its low concentration on NF.

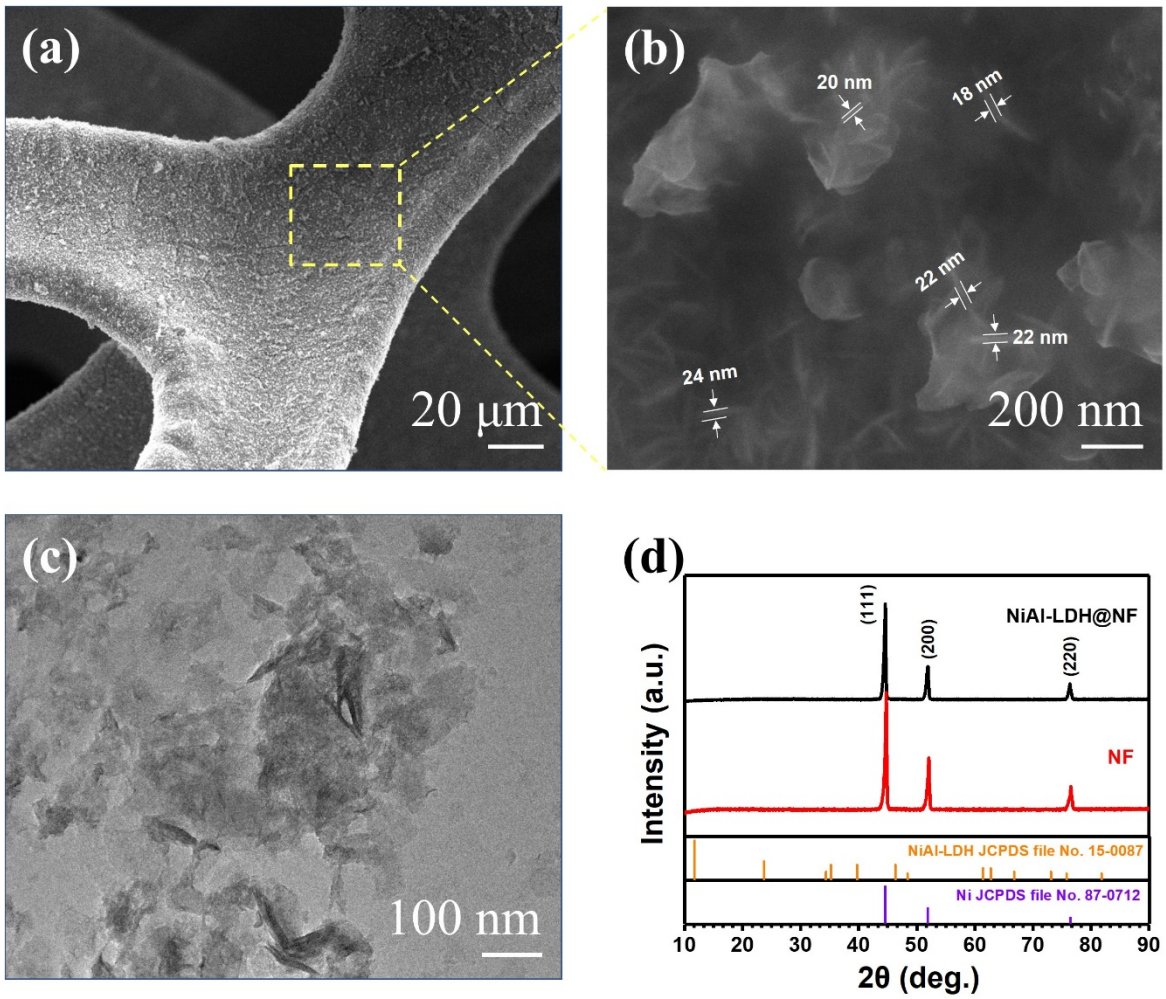

Figure 2. Characterization of NiAl-LDH@NF. (**a**) Low (×1000) and (**b**) high (×100,000) magnification SEM images of NiAl-LDH@NF including thickness measurement at several points. (**c**) TEM image of NiAl-LDH grown on NF. (**d**) XRD patterns of NiAl-LDH@NF and NF with reference XRD patterns.

However, the EDS mapping analyses confirmed that Ni and Al were evenly distributed over the entire sample area, supporting the formation of NiAl-LDH (Figure S6b). To quantitatively analyze Ni and Al in NiAl-LDH@NF, an ICP analysis was performed (Table 1). It was observed that the amount of NiAl-LDH synthesized on NF was lower than the amount of LDH on NFF. The amount of NiAl-LDH on NFF was 1.86 times that of the LDH on NF, as determined by the calculation based on Al content (0.0179 mmol for NiAl-LDH@NFF and 0.0096 mmol Al for NiAl-LDH@NF). In addition, the amount of NiAl-LDH on NF did not significantly increase when the amount of Al precursor was increased three and five times, demonstrating that the use of NFF was key in increasing the amount of NiAl-LDH on the foam (Figure S7). XPS analysis was additionally conducted to examine the oxidation states of NiAl-LDH deposited on different substrates. The Ni 2p spectra of NiAl-LDH@NF showed Ni $2p_{3/2}$ and Ni $2p_{1/2}$ peaks at 855.8 eV and 873.5 eV, respectively, while those of NiAl-LDH/NFF exhibited a slight positive shift to 856.2 eV and 874.0 eV, indicating a minor oxidation of Ni species upon changing the substrate from NF to NFF (Figure S8a). In contrast, the Al 2p binding energy decreased from 74.5 eV in NiAl-LDH@NF to 74.3 eV in NiAl-LDH@NFF, suggesting a slight reduction of Al species (Figure S8b). The Fe $2p_{3/2}$ peak at 711.3 eV confirmed the presence of oxidized Fe species (Figure S8c), while the O 1s spectra revealed contributions from M–OH groups at 531.4–531.5 eV and adsorbed H_2O near 533 eV (Figure S8d). These findings indicate that the oxidation state of NiAl-LDH is affected by the substrate, which is likely due to the NFF substrate serving as an Fe source that promotes the formation of oxidized Fe species.

To evaluate the electrocatalytic characteristics of NiAl-LDH@NF and NiAl-LDH@NFF, LSV measurements were performed. The LSV curves revealed that the overpotential of the NiAl-LDH@NFF electrode was considerably lower than that of NiAl-LDH@NF (Figure 3a). At a current density of 10 mA cm^{-2}, NiAl-LDH@NF and NiAl-LDH@NFF exhibited overpotentials of 327 and 214 mV, respectively. For comparison, the bare NF, RuO_2@NF, bare NFF, and RuO_2@NFF electrodes showed overpotentials of 400, 344, 294, and 254 mV,

respectively. Notably, NiAl-LDH demonstrated higher activity than the commercial RuO_2 catalyst, and both NiAl-LDH and RuO_2 exhibited enhanced performance when supported on NFF compared to NF. This indicated a substantial improvement in the OER activity attributable to the critical function of the NFF.

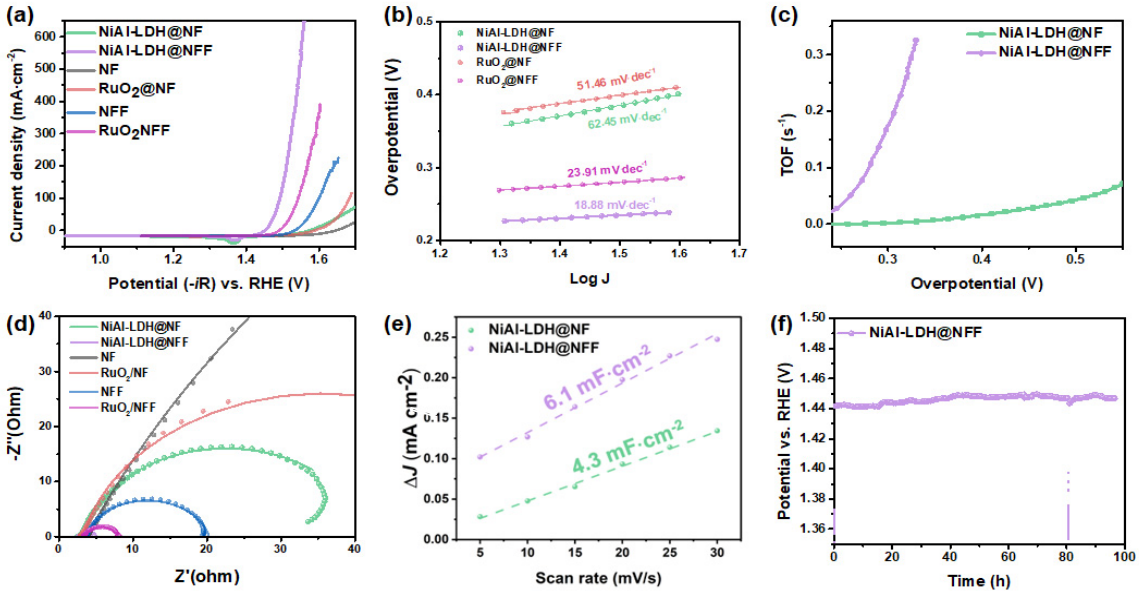

Figure 3. (**a**) LSV curves in the 1 M KOH electrolyte at a scan rate of 2 mV s^{-1}, (**b**) Tafel slopes, (**c**) TOF curves, (**d**) Nyquist plots, (**e**) linear fitting of capacitive currents of the electrocatalysts vs. scan rate, and (**f**) Chrono potentiometric stability test of NiAl-LDH@NFF recorded at a constant current density. The sharp potential drop observed around 80 h is attributed to the replenishment of electrolyte.

Furthermore, to determine the catalytic activity per amount of Ni active site, the mass activities of NiAl-LDH@NF and NiAl-LDH@NFF were investigated based on the ICP results (Table 1, Figure S9). The mass activity of NiAl-LDH@NFF exhibited an overpotential of 270 mV at 100 mA mg_{Ni}^{-1}, significantly higher than that of NiAl-LDH@NF (1.54 mA mg_{Ni}^{-1}) at the same potential.

Tafel plots derived from the LSV data were scrutinized to further assess the electrocatalytic kinetics of NiAl-LDH@NF and NiAl-LDH@NFF (Figure 3b). NiAl-LDH@NFF exhibited a significantly lower Tafel slope (18.88 mV dec^{-1}), whereas NiAl-LDH@NF exhibited 62.45 mV dec^{-1}. For comparison, RuO_2@NF and RuO_2@NFF showed Tafel slopes of 51.46 and 23.9 mV dec^{-1}, respectively. These values implied that NiAl-LDH@NFF significantly reduced the OER overpotential and augmented the reaction kinetics. The Tafel slope was substantially lower than that of other reported transition-metal-based catalysts and superior to those of noble-metal-based catalysts. This extremely low Tafel slope observed for NiAl-LDH@NFF, indicating a significantly less overpotential at a high current density, highlights its potential application as an anode for industrial-scale green hydrogen production via water electrolysis. Moreover, it can function as a counter electrode for other catalytic reactions, such as CO_2 reduction reactions.

TOF values were estimated to compare the intrinsic catalytic activities of NiAl-LDH@NF and NiAl-LDH@NFF for OERs (Figure 3c). The TOF of NiAl-LDH@NFF (0.1 s^{-1} at an overpotential of 280 mV) exceeded that of NiAl-LDH@NF (0.1 s^{-1} at an overpotential above 550 mV). This indicated an enhancement of the intrinsic catalytic properties through efficient charge transport with NFF. The EIS results corroborated the catalytic performance trend for the NiAl-LDH (Figure 3d). NiAl-LDH@NF and NiAl-LDH@NFF exhibited similar solution resistance (R_s) values of 2.5 and 2.6 W, respectively. The charge transport resistance (R_{ct}) of NiAl-LDH@NFF was significantly lower at 31.8 W, compared with that of NiAl-LDH@NF (2.3 W), corresponding with the LSV trend. In addition, the bare NF, RuO_2@NF, bare NFF, and RuO_2@NFF electrodes exhibited R_{ct} values of 340, 65, 16.7, and 4.7 Ω, respectively. These findings suggest that the NFF substrate can enhance electrical conductivity and improve charge transport, resulting in a substantially higher OER catalytic performance.

As shown in Figure 3e, the C_{dl} of the catalysts was obtained from CV curves at various scan rates within the non-Faradaic potential range (Figure S10). The C_{dl} values of NiAl-LDH@NF and NiAl-LDH@NFF were estimated at 4.3 and 6.1 mF cm^{-2}, respectively. This observation implied that the number of active sites in NiAl-LDH@NFF exceeded that in NiAl-LDH@NF.

To evaluate the durability of each catalyst, chronopotentiometry was measured at a current density of 10 mA cm^{-2} (Figure 3f). Notably, the NiAl-LDH@NFF electrode exhibited long-term stability with a slight change in potential (ΔV = 0.006 V for 97 h). The sudden potential drop observed around the 80 h mark was not indicative of catalyst degradation, but was instead a direct result of electrolyte replenishment. Furthermore, the electrochemical durability of NiAl-LDH@NFF was confirmed by TEM and XRD (Figure S11). Considering that the electrochemical reaction is fundamentally destructive, the edge of the NiAl-LDH surface became slightly blunt. However, XRD did not reveal a significant difference prior to and after the reaction, thereby demonstrating excellent stability.

Table 1. ICP analysis of NiAl-LDH@NFF and NiAl-LDH@NF.

Sample	Element	Amount (mmol)
NiAl-LDH@NFF	Ni	0.4106
	Al	0.0179
	Fe	1.3161
NiAl-LDH@NF	Ni	0.7156
	Al	0.0096

DFT calculations were performed to elucidate the origin of the improved OER activity of NiAl-LDH@NFF and to clarify the role of NFF in catalytic performance. A heterostructure model of NiAl-LDH supported on NFF was constructed and compared with that on NF, a conventional substrate for LDH synthesis (Figure 4a,b). The OER pathway was analyzed by calculating the adsorption energies of key intermediates (*OH, *O, and *OOH). The potential-determining step (PDS) was identified as the first proton-electron transfer for NiAl-LDH@NFF, in contrast to the third step for NiAl-LDH@NF (Figure 4c). The corresponding overpotentials were 0.40 eV for NiAl-LDH@NFF and 0.64 eV for NiAl-LDH@NF, demonstrating a substantial decrease of 0.24 eV in favor of the NFF-supported system. This improvement indicates enhanced OER activity, in agreement with the experimentally observed lower overpotential of NiAl-LDH@NFF.

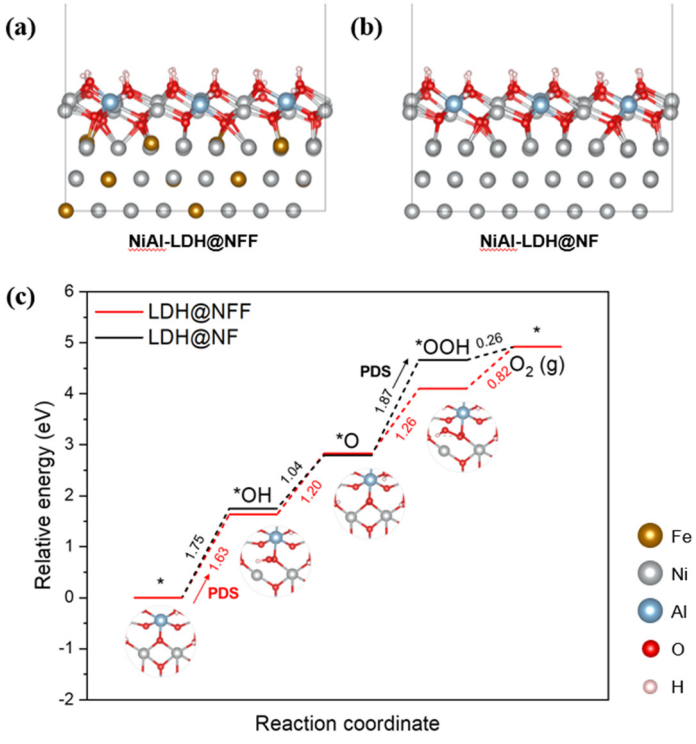

Figure 4. Model systems of (**a**) NiAl-LDH@NFF and (**b**) NiAl-LDH@NF for DFT calculations. (**c**) Gibbs energy profiles of the four-electron OER mechanism and corresponding top-view intermediate structures on the LDH@NFF surfaces. Here, PDS denotes potential-determining step.

Bader charge analysis was conducted to probe interfacial electronic interactions. In the NiAl-LDH@NFF heterostructure, Fe atoms in the foam donated electrons while Ni atoms in the NiAl-LDH layer accepted electrons. The net charge transfer to NiAl-LDH was 0.32 e^- higher in NiAl-LDH@NFF compared with NiAl-LDH@NF

(Table 2, Figure 5), indicating that Fe provides electrons to NiAl-LDH across the interface. The interfacial binding energy was further examined to assess the thermodynamic stability of the heterostructures. The calculated binding energies were −121.5 meV Å^{-2} for NiAl-LDH@NFF and −111.4 meV Å^{-2} for NiAl-LDH@NF, indicating that both foams can stabilize the NiAl-LDH layer. The more negative binding energy of NiAl-LDH@NFF suggests a stronger interfacial interaction, as reflected in the thicker growth of NiAl-LDH on NFF (Figures 1 and 2).

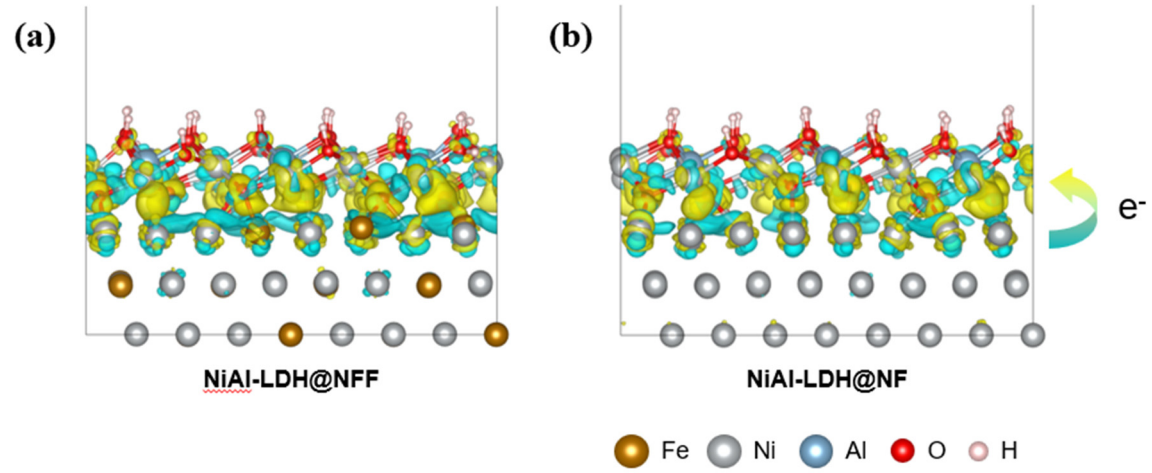

Figure 5. Charge density redistribution at the interface of NiAl-LDH and (**a**) NFF, and (**b**) NF. The yellow and cyan colors represent charge accumulation and depletion, respectively.

The number of electrons gained by LDH was 0.32 e$^-$ more in the LDH@NFF model than in the LDH@NF model, attributable to the increased supply of electrons in the foam owing to the influence of Fe. We investigated the interfacial binding energy of a heterostructure to elucidate the thermodynamic stability of the heterostructure. We calculated the interfacial binding energies of the heterostructure as −121.5 and −111.4 meV Å^{-2} for LDH@NFF and LDH@NF, respectively, indicating that NFF and NF can form stable heterostructures with NiAl-LDH. Furthermore, the stronger energy of LDH@NFF, compared with that of LDH@NF, demonstrated that a greater amount of LDH can be generated in NFF. This shows that NiAl-LDH grows thicker on NFF than on NF (Figures 1 and 2).

Table 2. Calculated Bader charge changes of Ni, Fe, and Al ions on heterostructured NiAl-LDH@NFF and NiAl-LDH@NF. The negative and positive value represents electron rich and poor, respectively.

Total Bader Charge Change			
Analyzed Component		**LDH@NFF**	**LDH@NF**
LDH	Ni	−2.37	−2.05
	Al	0.06	0.06
Foam	Ni	7.03	8.65
	Fe	2.75	-

The OER overpotential of LDH@NFF was lower than that of LDH@NF. Through the Bader charge analysis of the heterostructure on which LDH was formed on foam, it was confirmed that charge transfer occurred at the interface. More electron transfer occurred at the interface of LDH@NFF than that of LDH@NF because of the electron supply from Fe in NFF. In conclusion, it was observed that the LDH was better formed on NFF with stronger interfacial binding energy, leading to a better OER performance.

3. Conclusions

The study successfully synthesized NiAl-LDH@NFF through a hydrothermal procedure, using NFF as the growth substrate for NiAl-LDH. The heterostructured NiAl-LDH@NFF exhibited outstanding performance as an OER catalyst. Notably, NiAl-LDH@NFF exhibited a significantly denser growth (more than thrice) compared with cases where NF was employed as the growth substrate, leading to improved electrochemical performance (overpotentials of 214 and 327 mV at 10 mA cm^{-2}). DFT calculations revealed a higher electron transfer from the foam to LDH in the LDH@NFF model compared with the LDH@NF model, thereby enhancing the electrochemical performance. Moreover, the interfacial binding energy was stronger, providing evidence

supporting the enhanced LDH growth on NFF. Consequently, this study emphasized the importance of the growth substrate over the catalyst. Furthermore, this study suggests a more flexible and scalable approach in catalyst development for large-scale hydrogen generation through water electrolysis in the future, with NiAl-LDH@NFF as a promising initial step.

Supplementary Materials: The following supporting information can be downloaded at: https://media.sciltp.com/articles/others/250930153659061 9/MI-25090007-Supplementary_Materials.pdf.

Author Contributions: J.L.: Conceptualization, Data Curation, Formal Analysis, Investigation, Methodology, Writing—Original Draft Preparation; J.R.J.: Data Curation, Formal Analysis, Investigation, Methodology, Writing—Original Draft Preparation; Y.L.: Data Curation, Formal Analysis, Investigation, Methodology, Software, Writing—Original Draft Preparation; J.J.: Conceptualization, Data Curation, Formal Analysis, Investigation, Methodology, Validation; H.P.: Formal Analysis, Investigation, Methodology, Validation; Y.J.: Investigation, Validation, Writing—Review & Editing; J.W.H.: Funding Acquisition, Project Administration, Resources, Supervision, Writing—Review & Editing; M.H.L.: Funding Acquisition, Project Administration, Resources, Supervision, Writing—Review & Editing; T.Y.: Conceptualization, Funding Acquisition, Project Administration, Resources, Supervision, Writing—Review & Editing. All authors have read and agreed to the published version of the manuscript.

Funding: This work was funded by the Nano & Material Technology Development Program (RS-2024-00450102) and the Basic Research Program (RS-2021-NR059373) through the National Research Foundation of Korea (NRF) funded by the Ministry of Science and ICT. This work was (partially) funded by the BK21 FOUR program of National Research Foundation of Korea (GS-5-JO-NON-20232970). This research was (partially) funded by the BK21 FOUR program of National Research Foundation of Korea (GS-5-JO-NON).

Data Availability Statement: The authors confirm that the data supporting the findings of this study are available within the article and its supplementary materials.

Conflicts of Interest: The authors declare no conflict of interest.

References

1. Bhattacharya, M.; Paramati, S.R.; Ozturk, I.; Bhattacharya, S. The effect of renewable energy consumption on economic growth: Evidence from top 38 countries. *Appl. Energy* **2016**, *162*, 733–741.
2. Olatomiwa, L.; Mekhilef, S.; Ismail, M.S.; Moghavvemi, M. Energy management strategies in hybrid renewable energy systems: A review. *Renew. Sustain. Energy Rev.* **2016**, *62*, 821–835.
3. Chu, S., Cui, Y., & Liu, N. The path towards sustainable energy. *Nature materials*. **2017**, *16*(1), 16-22.
4. Vesborg, P.C.; Jaramillo, T.F. Addressing the terawatt challenge: Scalability in the supply of chemical elements for renewable energy. *RSC Adv.* **2012**, *2*, 7933–7947.
5. Fajrina, N.; Tahir, M. A critical review in strategies to improve photocatalytic water splitting towards hydrogen production. *Int. J. Hydrogen Energy* **2019**, *44*, 540–577.
6. Jeevanandam, J.; Barhoum, A.; Chan, Y.S.; Dufresne, A.; Danquah, M.K. Review on nanoparticles and nanostructured materials: History, sources, toxicity and regulations. *Beilstein J. Nanotechnol.* **2018**, *9*, 1050–1074.
7. Jiao, Y.; Zheng, Y.; Davey, K.; Qiao, S.Z. Activity origin and catalyst design principles for electrocatalytic hydrogen evolution on heteroatom-doped graphene. *Nat. Energy* **2016**, *1*, 16130.
8. Reier, T.; Pawolek, Z.; Cherevko, S.; Bruns, M.; Jones, T.; Teschner, D.; Selve, S.; Bergmann, A.; Nong, H.N.; Schlögl, R.; et al. Molecular insight in structure and activity of highly efficient, low-Ir Ir–Ni oxide catalysts for electrochemical water splitting (OER). *J. Am. Chem. Soc.* **2015**, *137*, 13031–13040.
9. Forgie, R.; Bugosh, G.; Neyerlin, K.C.; Liu, Z.; Strasser, P. Bimetallic Ru electrocatalysts for the OER and electrolytic water splitting in acidic media. *Electrochem. Solid-State Lett.* **2010**, *13*, B36.
10. Li, B.Q.; Xia, Z.J.; Zhang, B.; Tang, C.; Wang, H.F.; Zhang, Q. Regulating p-block metals in perovskite nanodots for efficient electrocatalytic water oxidation. *Nat. Commun.* **2017**, *8*, 934.
11. Grimaud, A.; May, K.J.; Carlton, C.E.; Lee, Y.L.; Risch, M.; Hong, W.T.; Zhou, J.; Shao-Horn, Y. Double perovskites as a family of highly active catalysts for oxygen evolution in alkaline solution. *Nat. Commun.* **2013**, *4*, 2439.
12. Karmakar, A.; Karthick, K.; Sankar, S.S.; Kumaravel, S.; Madhu, R.; Kundu, S. A vast exploration of improvising synthetic strategies for enhancing the OER kinetics of LDH structures: A review. *J. Mater. Chem. A* **2021**, *9*, 1314–1352.
13. Liu, H.; Wang, Y.; Lu, X.; Hu, Y.; Zhu, G.; Chen, R.; Ma, L.; Zhu, H.; Tie, Z.; Liu, J.; et al. The effects of Al substitution and partial dissolution on ultrathin NiFeAl trinary layered double hydroxide nanosheets for oxygen evolution reaction in alkaline solution. *Nano Energy* **2017**, *35*, 350–357.
14. Yang, G.W.; Xu, C.L.; Li, H.L. Electrodeposited nickel hydroxide on nickel foam with ultrahigh capacitance. *Chem. Commun.* **2008**, 6537–6539.
15. Li, Y.; Yang, S.; Li, H.; Li, G.; Li, M.; Shen, L.; Yang, Z.; Zhou, A. Electrodeposited ternary iron-cobalt-nickel catalyst on nickel foam for efficient water electrolysis at high current density. *Colloids Surf. A Physicochem. Eng. Asp.* **2016**, *506*, 694–702.

16. Lu, X.; Zhao, C. Electrodeposition of hierarchically structured three-dimensional nickel–iron electrodes for efficient oxygen evolution at high current densities. *Nat. Commun.* **2015**, *6*, 6616.
17. Huang, L.A.; Shin, H.; Goddard III, W.A.; Wang, J. Photochemically deposited Ir-doped NiCo oxyhydroxide nanosheets provide highly efficient and stable electrocatalysts for the oxygen evolution reaction. *Nano Energy* **2020**, *75*, 104885.
18. Huang, H.; Jung, H.; Park, C.Y.; Kim, S.; Lee, A.; Jun, H.; Choi, J.; Han, J.W.; Lee, J. Surface conversion derived core-shell nanostructures of Co particles@ RuCo alloy for superior hydrogen evolution in alkali and seawater. *Appl. Catal. B Environ.* **2022**, *315*, 121554.
19. Park, B.J.; Wang, Y.; Lee, Y.; Noh, K.J.; Cho, A.; Jang, M.G.; Huang, R.; Lee, K.S.; Han, J.W. Effective screening route for highly active and selective Metal—Nitrogen-doped carbon catalysts in CO_2 electrochemical reduction. *Small* **2021**, *17*, 2103705.
20. Liu, J.; Bak, J.; Roh, J.; Lee, K.S.; Cho, A.; Han, J.W.; Cho, E. Reconstructing the coordination environment of platinum single-atom active sites for boosting oxygen reduction reaction. *Acs Catal.* **2020**, *11*, 466–475.
21. Guo, C.; Jiao, Y.; Zheng, Y.; Luo, J.; Davey, K.; Qiao, S.Z. Intermediate modulation on noble metal hybridized to 2D metal-organic framework for accelerated water electrocatalysis. *Chem* **2019**, *5*, 2429–2441.
22. Hong, Y.R.; Dutta, S.; Jang, S.W.; Ngome Okello, O.F.; Im, H.; Choi, S.Y.; Han, J.W.; Lee, I.S. Crystal facet-manipulated 2D Pt nanodendrites to achieve an intimate heterointerface for hydrogen evolution reactions. *J. Am. Chem. Soc.* **2022**, *144*, 9033–9043.
23. Du, F.; Ling, X.; Wang, Z.; Guo, S.; Zhang, Y.; He, H.; Li, G.; Jiang, C.; Zhou, Y.; Zou, Z. Strained heterointerfaces in sandwich–like NiFe layered double hydroxides/Co1-xS for highly efficient and superior long–term durable oxygen evolution reaction. *J. Catal.* **2020**, *389*, 132–139.
24. Feng, L.; Du, Y.; Huang, J.; Cao, L.; Feng, L.; Feng, Y.; Liu, Q.; Yang, D.; Kajiyoshi, K. Nanoporous NiAl-LDH nanosheet arrays with optimized Ni active sites for efficient electrocatalytic alkaline water splitting. *Sustain. Energy Fuels* **2020**, *4*, 2850–2858.
25. McCrory, C.C.; Jung, S.; Peters, J.C.; Jaramillo, T.F. Benchmarking heterogeneous electrocatalysts for the oxygen evolution reaction. *J. Am. Chem. Soc.* **2013**, *135*, 16977–16987.
26. Anantharaj, S.; Kundu, S. Do the evaluation parameters reflect intrinsic activity of electrocatalysts in electrochemical water splitting? *ACS Energy Lett.* **2019**, *4*, 1260–1264.
27. Dang Van, C.; Kim, S.; Kim, M.; Lee, M.H. Effect of rare-earth element doping on NiFe-layered double hydroxides for water oxidation at ultrahigh current densities. *ACS Sustain. Chem. Eng.* **2023**, *11*, 1333–1343.
28. Grenier, P.; Houde, D.; Jandl, S.; Boatner, L.A. Soft-mode studies in KTa 0.93 Nb 0.07 O 3 with use of the time-resolved third-order optical susceptibility χ^3. *Phys. Rev. B* **1993**, *47*, 1.
29. Kresse, G.; Furthmüller, J. Efficient iterative schemes for ab initio total-energy calculations using a plane-wave basis set. *Phys. Rev. B* **1996**, *54*, 11169.
30. Blöchl, P.E. Projector augmented-wave method. *Phys. Rev. B* **1994**, *50*, 17953.
31. Perdew, J.P.; Burke, K.; Ernzerhof, M. Generalized gradient approximation made simple. *Phys. Rev. Lett.* **1996**, *77*, 3865.
32. Monkhorst, H.J.; Pack, J.D. Special points for Brillouin-zone integrations. *Phys. Rev. B* **1976**, *13*, 5188.
33. Pandya, N.Y.; Mevada, A.D.; Gajjar, P.N. Lattice dynamical and thermodynamic properties of $FeNi_3$, FeNi and Fe_3Ni invar materials. *Comput. Mater. Sci.* **2016**, *123*, 287–295.
34. Wang, C.; Wang, C.Y. Ni/Ni_3Al interface: A density functional theory study. *Appl. Surf. Sci.* **2009**, *255*, 3669–3675.
35. Nørskov, J.K.; Rossmeisl, J.; Logadottir, A.; Lindqvist LR, K.J.; Kitchin, J.R.; Bligaard, T.; Jonsson, H. Origin of the overpotential for oxygen reduction at a fuel-cell cathode. *J. Phys. Chem. B* **2004**, *108*, 17886–17892.
36. Valdés, Á.; Qu, Z.W.; Kroes, G.J.; Rossmeisl, J.; Nørskov, J.K. Oxidation and photo-oxidation of water on TiO_2 surface. *J. Phys. Chem. C* **2008**, *112*, 9872–9879.
37. Henkelman, G.; Arnaldsson, A.; Jónsson, H. A fast and robust algorithm for Bader decomposition of charge density. *Comput. Mater. Sci.* **2006**, *36*, 354–360.
38. Liu, G.; Wang, B.; Wang, L.; Wei, W.; Quan, Y.; Wang, C.; Zhu, W.; Li, H.; Xia, J. MOFs derived FeNi3 nanoparticles decorated hollow N-doped carbon rod for high-performance oxygen evolution reaction. *Green Energy Environ.* **2022**, *7*, 423–431.
39. Hu, X.; Li, P.; Zhang, X.; Yu, B.; Lv, C.; Zeng, N.; Luo, J.; Zhang, Z.; Song, J.; Liu, Y. Ni-based catalyst derived from NiAl layered double hydroxide for vapor phase catalytic exchange between hydrogen and water. *Nanomaterials* **2019**, *9*, 1688.
40. Zhang, X.; Chen, X.; Jin, S.; Peng, Z.; Liang, C. Ni/Al2O3 catalysts derived from layered double hydroxide and their applications in hydrodeoxygenation of anisole. *ChemistrySelect* **2016**, *1*, 577–584.
41. Jo, W.K.; Moru, S.; Tonda, S. A green approach to the fabrication of a TiO 2/NiAl-LDH core–shell hybrid photocatalyst for efficient and selective solar-powered reduction of CO_2 into value-added fuels. *J. Mater. Chem. A* **2020**, *8*, 8020–8032.
42. Koilraj, P.; Takemoto, M.; Tokudome, Y.; Bousquet, A.; Prevot, V.; Mousty, C. Electrochromic thin films based on NiAl layered double hydroxide nanoclusters for smart windows and low-power displays. *ACS Appl. Nano Mater.* **2020**, *3*,

6552–6562.

43. Yan, X.; Zhang, W.D.; Hu, Q.T.; Liu, J.; Li, T.; Liu, Y.; Gu, Z.G. Defects-rich nickel nanoparticles grown on nickel foam as integrated electrodes for electrocatalytic oxidation of urea. *Int. J. Hydrogen Energy* **2019**, *44*, 27664–27670.
44. Zhu, W.; Yue, X.; Zhang, W.; Yu, S.; Zhang, Y.; Wang, J.; Wang, J. Nickel sulfide microsphere film on Ni foam as an efficient bifunctional electrocatalyst for overall water splitting. *Chem. Commun.* **2016**, *52*, 1486–1489.
45. Wang, Z.; Wang, F.; Tu, J.; Cao, D.; An, X.; Ye, Y. Nickel foam supported hierarchical mesoporous MnO_2/$Ni(OH)_2$ nanosheet networks for high performance supercapacitor electrode. *Mater. Lett.* **2016**, *171*, 10–13.